Accurate fault location in low voltage underground cables using advanced signal processing and artificial intelligence

Moshtagh, Jamal

Award date:
2006

Awarding institution:
University of Bath

Accurate Fault Location in Low Voltage Underground Cables Using Advanced Signal Processing and Artificial Intelligence

Submitted by Jamal Moshtagh for the degree of Doctor of Philosophy
University of Bath
Department of Electrical and Electronic Engineering

July 2006

COPYRIGHT

ProQuest LLC
789 East Eisenhower Parkway
P.O. Box 1346
Ann Arbor, MI 48106-1346

SYNOPSIS

The use of underground systems has increased extensively in recent years and many cities in the world have installed underground distribution cables. This is partly due to the need for preserving the landscape, and partly due to the fear of adverse biological effects on health resulting from electrical fields in the vicinity of overhead lines. The other reasons for using cables in preference to overhead lines are high reliability and low voltage regulation associated with the former. However, underground transmission is more expensive than the overhead alternative. Nowadays significant advancement in cable insulation has resulted in a variety of cables to be manufactured for employment in distribution systems.

In underground residential distribution cable systems, the cables have begun to experience an increasing rate of failure as they near the end of their useful life. Many of the cable systems installed in the 1960's and early 1970's are now experiencing failures, and many are being replaced. These failures are causing problems for utilities, more so due to the fact that very often, failures can culminate into cable faults which must then be accurately located. Accurate fault location is vitally important which are due to a number of key factors namely, reliability of supply, quality of supply, reducing operating costs of repairs and low tariff charges to maintain a competitive edge in the market. Nowadays, increased competition due to the deregulation of the power industry and the desire to provide better services to the customers having more and more sensitive loads, makes the development of faster, reliable and accurate fault location methods for distribution systems an important issue.

One of the most important factors in accurate fault location is to develop an accurate model of a cable which then needs to be integrated into an overall distribution system model; this is essentially to determine accurately, the per unit length impedance and admittance of a network which determine the relationships between current, voltage, attenuation and velocity of travelling wave in the transient state.

In addition to an accurate model, there are other factors that affect such parameters as current, voltage, etc, in a distribution system under disturbances, these being fault

resistance, fault incidence angle, type of fault and load taps with different types of load. Such factors have a highly complex and non-linear interaction amongst themselves and they influence the nature of the voltage and current waveforms under faults. In this respect, artificial intelligence (AI) offers a very attractive tool for accurately deducing Fault location and this is by virtue of the fact that AI has the attribute of accurately mapping highly complex and non-linear input/output patterns.

The work presented in this thesis is essentially in two parts. The first part investigates the methodology of accurately modelling low voltage (LV) underground (UG) cables, in particular under the fault transient phenomena. The resultant method is then integrated into a practical LV cable distribution system (DS) using the well known EMTP software, for the purposes of simulating the requisite voltage and current signals under a whole variety of practically encountered different system and fault conditions. The fault data is then utilised to research and effect, using advanced signal processing and AI technologies, a novel and accurate fault location technique for low voltage DS.

Acknowledgement

I would like to thank Prof. R.K. Aggarwal for the great supervision as well as the enlightening comments and tireless support during the whole course of this research. I am deeply indebted to him for all the help and advice that I have received.

I wish to express my appreciation to all the academic and technical staff in the department of Electrical and Electronic Engineering and all the friends for their help and support.

I gratefully acknowledge the receipt of a generous scholarship from my employer, the Kurdistan University, Sanandaj, I.R. Iran, and without whose financial support this research would not have been possible.

I would like to express the greatest love to my wife, Mozhgan, and my daughter, Tina, who cope with me during my course. Without your love, support, patient and encouragement this would not have been possible.

Finally, I owe my deepest gratitude to my parents and my family for their continuous and enduring love, encouragement and support through my study.

CONTENTS

CHAPTER 3 NEW CABLE MODEL

CHAPTER 4 TRANSIENT DATA SIMULATION UNDER FAULTS

CHAPTER 5 SIGNAL PROCESSING

CHAPTER 6 Fault Location Technique Based on Artificial Neural Network

Index to Figures

CHAPTER 2

CHAPTER3

CHAPTER4

CHAPTER 5

CHAPTER 6

Index to Tables

List of Parameters

A , A_i Magnetic vector potential
B Magnetic flux density
C Capacitance
E Electric field intensity
E_x Axial Electric field intensity
f Frequency
G Conductance
H Magnetic field intensity
I Current
I_i Modified Bessel function of the first kind of order i
J_i Bessel function of the first kind of order i
J_x Axial electric current density
K_i Modified Bessel function of the second kind of order i
L Inductance
m Reciprocal of the complex depth of penetration
P Potential coefficient
R Resistance
Rf Fault resistance
r Radius of circle
t Time
V Voltage
Y Admittance
Y_c Characteristic admittance
Z Impedance
ω Angle frequency
λ Magnetic flux
μ_r Permeability of the material
μ_o Permeability of free space
ε_r Relative permittivity of the insulation material
ε_o Absolute permittivity of free space
ρ Resistivity
σ conductivity
δ Euler's constant
γ Propagation constant
$[T_i]$, $[T_v]$ Transformation matrix
$[\Lambda]$ Diagonal matrix
λ_k k-th eigenvalue
α_k Attenuation constant of mode k
β_k Phase constant of mode k
v_k Phase velocity of mode k

List of Abbreviations

ACI	Average Confidence Index
ADALINE	Adaptive Linear Neuron Network
ADC	Analogue Digital Converter
AI	Artificial Intelligence
ANNs	Artificial neural networks
A/D	Analogue to Digital
CC	Cable Constant
CM	Conformal Mapping
CTs	Current Transformers
CWT	Continuous Wavelet Transform
DFR	Digital Fault Recorder
DFT	Discrete Fourier Transform
DS	Distribution System
DWT	Discrete Wavelet Transform
EMTP	Electro-Magnetic Transient Programming
FD	Frequency Dependence
FDTD	Finite Difference Time Domain
FDTM	Frequency-Dependent Transformation Matrix
FFT	Fast Fourier Transform
FRED	Fault Re-Energising Device
FT	Fourier Transform
GIS	Gas Insulation System
HV	High Voltage
LM	Levenberg-Marquardt
LMS	Least Mean Square
LV	Low Voltage
MFN	Multi-layer Feed-forward Network
MRI	Misclassification Rate Index
MV	Medium Voltage
O/E	Optical to Electrical
PSD	Power Spectral Density
SCI	Single Confidence Index
SD	Standard Deviation
STFT	Short Time Fourier Transform
TDR	Time Domain Reflectometery
UG	Underground
UGDS	Underground Distribution System
ULVDNs	Underground Low Voltage Distribution Networks
VTs	Voltage Transformer
WT	Wavelet Transform
WDFT	Windowed Discrete Fourier Transform
a_ppv/a_ppi	Ratio of peak-peak voltage approximation to peak-peak current approximation at level 5
sin(φi-φv).v/I	Sine of phase-shift between current and voltage approximate at level 5 multiplied by a_ppv/a_ppi
SDv/SDi	Ratio of SD of voltage to SD of current approximate at level 5
cos(φv)	Cosine of phase of voltage approximate signal at level 5 correspond

	to second peak
cos(φi)	Cosine of phase of current approximate signal at level 5 correspond to second peak
Mabs_coev	The mean of absolute of coefficients 102 to 125 for voltage approximate signal at level 5
Mabs_coei	The mean of absolute of coefficients 102 to 125 for current approximate signal at level 5
SPH-G-SC	Single-Phase to Ground Short Circuit Fault
2PH-G-SC	Two-Phase to Ground Short Circuit Fault
2PH-SC	Phase to Phase Short Circuit Fault
3PH-SC	Three-Phase Short Circuit Fault
SPH-OC	Single Phase Open Circuit Fault
2PH-OC	Two-Phase Open Circuit Fault
3PH-OC	Three-Phase Open Circuit Fault
ag-sc	'a' Phase to Ground Short Circuit Fault
bg-sc	'b' Phase to Ground Short Circuit Ground Fault
cg-sc	'c' Phase to Ground Short Circuit Ground Fault
abg-sc	'a' and 'b' Phases to Ground Short Circuit Ground Fault
acg-sc	'a' and 'c' Phases to Ground Short Circuit Ground Fault
bcg-sc	'b' and 'c' Phases to Ground Short Circuit Ground Fault
ab-sc	'a' Phase to 'b' Phase Short Circuit Ground Fault
ac-sc	'a' Phase to 'c' Phase Short Circuit Ground Fault
bc-sc	'b' Phase to 'c' Phase Short Circuit Ground Fault
abc-sc	Three-Phase Short Circuit Ground Fault
a-oc	'a' Phase Open Circuit Fault
b-oc	'b' Phase Open Circuit Fault
c-oc	'c' Phase Open Circuit Fault
ab-oc	'a' and 'b' Phases Open Circuit Fault
ac-oc	'a' and 'c' Phases Open Circuit Fault
bc-oc	'b' and 'c' Phases Open Circuit Fault
abc-oc	Three-Phase Open Circuit Fault

CHAPTER 1

INTRODUCTION

1.1 Challenges for Accurate Cable Model

There has been an upsurge in the usage of underground distribution systems in recent years. In this respect, increased competition due to the deregulation of the power industry and the demand to provide better service to the customers having increasingly sensitive loads, makes the development of reliable and accurate fault location methods for distribution systems an important issue. As a pre-requisite, one of the most important factors in accurate fault location is to develop an accurate model of a cable which then needs to be integrated into an overall distribution system model. Essentially, there is a need to determine accurately, the per unit length impedance and admittance of a cable, which in turn determine the relationships between current, voltage, attenuation and velocity of travelling waves in the transient state.

A number of models have been proposed to date. These models can be classified into the following two main groups; time domain and frequency domain models. With regard to the advantages and disadvantages of these techniques, in reference [1], the presented model belongs to the class of time-domain, frequency-dependent methodology. It overcomes the main limitations of existing time-domain cable models, that is, it takes into account the frequency dependence of the modal transformation matrices. This model is compatible with the time domain solution, such as the one used in the EMTP. A general method based on constrained optimization for evaluating the modal transformation matrices for overhead transmission lines and underground cables has been developed and tested in reference [2]. The method guarantees in the methodology adopted, the smoothness of all the eigenvectors and modal characteristic impedances over a wide range of frequencies. This method can be used in the EMTP software in which the eigenvalues and eigenvectors of a complex upper Hessenberg matrix are found by the modified LR-method due to Rutishauser [3]. In many analyses of overhead line parameters, approximations ignoring eddy currents in conductors can be assumed. However, in close conductors, such as underground cables, the AC

parameters vary significantly with frequency and conductor spacing. In references [4] and [5], on which the EMTP model is based, the distributions of current density due to proximity and skin effects are determined analytically by solving the differential equation for penetration of currents in the conducting material and appropriately applying boundary conditions. However, for eccentric conductors such as a three-phase cable, inner conductors are replaced with an assumed small circle which is concentric with the outer conductor such as pipe or armour. In all the aforementioned methods and also in the EMTP model, it is assumed that permeability μ for conductors and pipe is constant. Thus in order to determine μ throughout the pipe, in reference [6], the magnetic field intensity in each element of the pipe is solved using the finite-element method. In reference [7], the cable is divided into a large number of cells as the field is assumed to be constant within each cell and a linear integration is performed for the voltage using Finite-Difference Time Domain (FDTD) method.

In the modelling of a three-phase cable or pipe type cable, the main problem arises by virtue of the fact that the three conductors are positioned off centre within the pipe or armour and it is principally due to this that some estimations and approximations are made in the EMTP model; a direct consequence of the latter is that the mathematical representation of the impedance and admittance in a pipe type cable in the EMTP software includes infinite series formulations of the flux linkage and the proximity effects; this of course is based on some approximations in the configuration of cable. However, with regard to the conformal mapping (CM) ability to transform an isotropic region into a symmetrical and much simpler region, the mathematical equations for the calculation of series impedance Z and shunt admittance Y take a simplified form and eliminate such approximations which mathematically change the configuration of the cable and then increase the accuracy, as shown in this research.

1.2 Challenges for Accurate Fault Location Technique

With increased environmental concern, there is an increase in demand for underground distribution system (UGDS). It is thus very likely that more and more distribution system (DS) comprising underground cables will be built. UGDS has to be highly reliable and efficient under normal and contingency conditions. In the event of a fault

there should be exact information available about the type of fault and its location. This information is required to initiate network reconfiguration as soon as possible and restore normal electrical power supply. The type of method employed in fault location is very much dependent upon the purpose of fault location and hence these techniques can be classified into a number of categories. There are essentially two categories; on-line and off-line associated with the protection and operation of power systems, respectively. Fault location for repair and inspection purposes requires very high accuracy, while the speed of the fault location is not as critical; the computations completed in minutes or even slower are acceptable. Thus, more accurate phasor calculation can be applied in conjunction with the best available data window and filtering techniques. Use of all locally available information and also that obtained via communication systems is relevant for accurate fault location. However, the location for protective relaying purposes is entirely different as the speed of the fault location is a critical factor; accuracy is not that important so long as the technique retains its discriminatory property.

Many off-line fault location techniques involve patrolling along the lines or cables. In overhead distribution lines, most of the failures can be located quickly by visual inspection without the aid of special equipment. However, locating a fault in an underground cable system is more difficult. It involves additional equipments (e.g., thumpers, radar, etc.) to transform the invisibility of the cable into other forms of signals, such as acoustic sound and electromagnetic pulses. Trained operators must carry the equipment above the ground, follow the path of the signal, and draw lines on their maps in order to locate the fault. Sometimes, even smelling the burnt cable faults is a way to detecting the problem. These techniques are time consuming, not always reliable and, as in the case of high-voltage DC thumpers, can cause additional damage to the healthy parts of the cable circuit.

Methods of accurate location of power system faults can also be broadly classified into two categories; one based on the power frequency components (low frequency), and the other utilizing the higher frequency contents of the transient fault signals. In the case of latter, according to the travelling wave theory, fault transients will have different signatures at the substation terminals and these in turn very much depend on the number of network junctions they pass through as they travel towards the substation. These

signatures which in essence can contain much useful and important information to enhance the accuracy in fault location only show up at the high frequency end of the spectrum and will be missed by most methods based on the power frequency signals. Thus in order to effect a very accurate method to locate faults, it would appear that a transient-based technique would be better suited than the traditional power-frequency – based methods. Chapter 2 summarises all the work reported to date in the area of fault location in UG cable systems; this includes the advantages/disadvantages (including limitations and drawbacks) of some of the existing techniques employed by Distribution companies and also the advantages that have taken place in fault location and those that have been reported in the upon literature.

1.3 Objectives of the Work

The principal technologies achievements of this research are:

1. To research a very accurate model for underground cables; this will then be integrated into a low voltage (LV) distribution network model Using the EMTP software for the purposes of generating voltage and current signals across the frequency spectra under different system and fault conditions. One of the main purposes of this section is to compare different cable models in existence, particularly their limitations and drawbacks. As part of this research, a new cable model using CM is introduced as a more accurate model. Also, a comparison is done between EMTP and CM model for a typical distribution network.

2. Data simulation under different system and faults conditions in a practical UGDS, including a radial and double-end fed systems, transformers and different load taps.

3. Extraction of useful and significant information from the simulated waveforms using advanced signal processing techniques. In this respect, a number of signal processing methods such as the Fast Fourier Transform (FFT), Short Time Fourier Transform (STFT) and the Wavelet Transform (WT) are reviewed, particularly their advantages and disadvantages. The optimal signal processing technique is then selected.

4. To research an artificial intelligence-based technology in order to identify/classify and locate the disturbances in underground cables through pattern recognition. In this respect, the main thrust is on the employment of artificial neural networks (ANNs) which have the attribute of mapping highly complex, non-linear input/output patterns and importantly, to be able to deal with the interaction amongst a large number of variables associated with cable faults.

5. To test the accuracy and robustness of the affected fault location method including the number of sources, variation in the length of cables and the sensitivity to the number of load taps and the types of load.

1.4 Scope of the Thesis

Chapter 2

In this chapter, a review of the cable modelling and fault location techniques developed to date, is presented. In the first part; a comparison is made between different cable models particularly in their limitations and drawbacks. The second part gives an overview of fault location techniques for underground transmission and distribution networks.

Chapter 3

This chapter is concerned with an outline of mathematical analysis associated with the calculation of the per unit length series impedance Z and shunt admittance Y within the well established and powerful EMTP software widely employed for modelling the transient phenomena in power systems. The various assumptions and approximations made within the EMTP giving rise to inaccuracies in the transient waveforms in cables, are detailed and a new cable model based on CM is then introduced as a more accurate model. Also, a comparison is made between the EMTP and CM model for a typical distribution network comprising of UG cables.

Chapter 4

This chapter describes in detail data simulation under different system and fault conditions in a practical UGDS, either radial or double-end fed, transformers and different load taps using EMTP in conjunction with the modified cable model. Here also, the simulated raw data (voltage and current signals) is conditioned through an emulation of practical CTs and VTs, anti-aliasing filters and A/D converter in preparation for the digital processing through the fault-location algorithm, as detailed in the next chapter.

Chapter 5

In this chapter, the digitised signals are processed using advanced signal processing techniques for the extraction of the most significant features from the signals. In this respect, some signal processing methods such as the FFT, STFT and the WT are reviewed, particularly their advantages and disadvantages. Then useful information is extracted by selecting the most appropriate method. A set of input variables (based on feature extraction) are then selected to set up data set vectors for training ANNs, as detailed in the next chapter.

Chapter 6

This chapter briefly reviews the ANNs concepts and then based on this technology a new and novel approach to fault classification and fault location in LV underground distribution systems are presented. In this respect, the type of ANNs, the training algorithm, transfer function, the number of neurons in the hidden layer and the other specifications of ANNs are determined. Then the effective ANNs architectures are trained based on previously mentioned features inputs attained via signal processing and finally, the developed fault location algorithm is tested by three different data tests; the first one is concerned with the test data which is not used during training of ANNs. The second data test evaluates the accuracy of the algorithm as applied to the chosen DS but under fault conditions different from those used in the training of the ANNs. By the third data test, the sensitivity and the robustness of the algorithm to small changes in the DS configuration (different types of loads including the location, variation in cable length, connection of remote source, etc) are tested and the outcomes presented.

Chapter 7

Chapter 7 presents an overall summary of the work presented in this thesis and the conclusions. Some suggestions for future work are also outlined.

CHAPTER 2

LITERATURE REVIEW OF CABLE MODEL AND FAULT LOCATION TECHNIQUES FOR UGDS

In this chapter, a review of the work is presented. This can be essentially divided into two categories: (i) the first one is to compare different cable models in existence, particularly their limitations and drawbacks. (ii) The second one is an overview of fault location techniques for underground transmission and distribution networks.

2.1 Cable Model

The increasing use of cable systems and the growing levels of capacity make the analysis of wave propagation and determining an accurate model for cables as an important branch in Electrical Power Engineering. Because XLPE insulated cable is now well established in most European countries at low voltages and up to 35 kV, a review of the various cable modelling techniques covering the XLPE type is very useful. XLPE now constitutes 90% of all distribution cables installed up to 35KV [14]. Numerous papers on this type of cable have been written. In this respect, The EMTP software is a very powerful tool in the modelling of electromagnetic transients in power system networks as a whole. The EMTP software is particularly attractive for developing accurate cable models by virtue of the fact that it has a number of different methods for determining the cable parameters and characteristics. The main purpose of this section is to compare different cable models in existence, particularly their limitations and drawbacks and also some important points are assessed as a basic to modify the EMTP software based cable model. A number of models have been proposed to date. These models can be classified into the following two main groups:

a) **Time domain model:** In this model, the solution is carried out in the time domain without using the inverse Fourier or Laplace transformation. Within this group, two types of models are considerable:

1) Lumped-parameters models: The validity of these models is restricted to relatively short lines or cables and, in general, their frequency response is only good in the neighbourhood of the frequency at which the parameters are evaluated.

2) Distributed-parameters, frequency-dependent model: The solution is performed in the modal domain. The frequency dependence and the distributed nature of the line or cable parameters are taken into account. The validity of these models is restricted because the modal transformation matrices are assumed to be constant, although they are heavily dependent on frequency particularly in the case of underground cables. Thus it produces unsatisfactory results.

b) **Frequency domain models**: In these models, the frequency dependence of the line or cable parameters and of the modal transformation matrices is taken into account. The applicability of these models is restricted by the limitations of their host programs. Also sudden changes in the network configuration (such as faults) and the modelling of non-linear elements cannot be handled easily with frequency-domain solution methods.

2.1.1. Optimization Methods for Modal Transformation Matrices

In spite of the strong frequency dependence (FD) of the parameters of underground cables in power system, there are not as yet fully satisfactory models that are simple and reliable for general-purpose electromagnetic transient simulators, like the EMTP. A number of well-established models can be found in the literature [1], [15]-[18] for the frequency-dependent modelling of lines and cables. Most of these models use modal decomposition theory to decouple the physical system (phase domain) into mathematically equivalent decoupled system (modal domain) in order to solve a multiphase line by considering a number of single-phase lines.

One of the most widely used transmission line models is the FD line model proposed by J. Marti [15]. This model includes the FD of the line parameters and the distributed nature of the line losses. The transformation matrix used in this model is, however, assumed to be real and constant. This model is very reliable and the assumption of a real constant transformation matrix is generally accurate for overhead lines as long as there are not very strong asymmetries. However, for underground cables, the transformation matrix depends strongly on frequency. The FD model developed by L. Marti [1] overcomes this restriction by synthesizing the frequency-dependent transformation matrix (FDTM) with rational functions in the frequency domain. This model has worked well for cable simulations for both high and low frequency phenomena. Also, by being compatible with the solution algorithm of EMTP, only the updating of the history of the current sources at each time step, and the value of Y_{eq} are different. However lossless lines and frequency-dependent lines are the same in the updating of the history of the current sources and the value of Y_{eq} [1].

A general method based on constrained optimization for evaluating the modal transformation matrices for overhead transmission lines and underground cables have been developed and tested by T. Nguyen & H.Y. Chan [2]. The method guarantees in the calculation, the smoothness of all of the eigenvectors and modal characteristic impedances over a wide range of frequencies. The convergence to valid eigenvectors and eigen-values has been proved mathematically and confirmed with evaluations in practical cases. The method is applicable to the preparatory phase of evaluation for any time-domain electromagnetic transient program that implements the distributed parameter models for lines and cables and uses the modal domain form of analysis.

A line or cable can be characterized by two matrix transformation functions including the propagation γ and the characteristic admittance Y_c. These are frequency dependent quantities and can in practice only be calculated as discrete functions in the frequency domain. A time domain simulation can be carried out using convolutions involving the time domain counter parts of γ and Y_c , which are obtained via an inverse Fourier transform. A critical part is the accurate fitting of γ and Y_c with rational functions. The elements of Y_c are in general very

smooth functions of frequency and can easily be fitted. The fitting of γ is more difficult because its elements are composed of modal components, which in general have different time delays. In the case of overhead lines, the modal time delays are not very different, which makes it possible to take these into account by a common factor $\exp(-j\omega\tau)$ corresponding to the fastest mode. However, in the case of cables, the modal time delays may be widely different. The fitting is done in the frequency domain by A. Moched et. al. [19], as γ first, is fitted in the modal domain. The resulting poles and time delays are then used for fitting γ in the phase domain under the assumption that all poles contribute to all elements of γ. By using this method, very high accuracy can be achieved with a low number of poles per mode, as compared to currently used models.

A major difficulty in multiphase cable modelling with traditional electromagnetic transient program like the EMTP is the synthesis of the FDTM which relates modal and phase domain variables. Ting-Chung Yu & J. R. Marti [20] present a new model (Zcable) to represent the FD of cable parameters directly in phase coordinates, thus avoiding the problems related to FDTM. The cable model is split into two parts: 1) a constant ideal line section, which represents the electric and magnetic fields outside the conductors and 2) a loss section which includes the losses and internal inductance inside the conductors and ground which depend on the skin effect and are, therefore, frequency-dependent. Assuming the permittivity and permeability of the external media constant, the parameters of the ideal line section are constant with frequency and depend exclusively on the geometry of the system. A pi-correction is proposed to solve the problem of different travelling times in the ideal line section. The main advantage of the proposed model as compared to existing FDTM models is the model's absolute numerical stability for strongly asymmetrical cable configurations and for arbitrary fault conditions. In addition, the model parameters are easy to obtain with robust algorithms and the model can be efficiently implemented in the context of a real-time PC-cluster simulator within the software.

2.1.2. Skin and Proximity Effects

In several applications of cylindrical symmetry, it is desirable to know the distribution of eddy currents in conducting media of a cylindrical form i.e. shells, when there exists an AC excitation of low frequency and the axial direction. Also it is necessary to know the distribution of the current flowing axially in the shell itself. These two current distributions, known also as proximity effect and skin effect respectively, constitute a problem which has been of interest to engineers for a long time. There are several applications in the power system where proximity effect and skin effect in cylindrical shells appear. The most important of them is the sheaths of cables. The main reason for knowing these current distributions in cylindrical shells is the evaluation of losses and as a result, the determination of an accurate cable model. The problem is approached by electromagnetic theory as a two-dimensional boundary value problem by J.A. Tegopoulos & E.E. Kriezis [4,5]. The distributions of current density due to proximity and skin effects are determined analytically by solving the differential equation for penetration of currents in the conducting material and appropriately applying boundary conditions. This approach seems to be more systematic and general in treating all related problems. There are essentially two configurations dealt with in ref. [4]. Firstly, a cylindrical shell of infinite thickness and infinite length i.e. a hole in a material filling all space with the current is assumed to flow in a filament placed inside the shell as being parallel to its axis. Secondly, a solid cylinder of infinite length with the current assumed to flow in a filament, outside the solid cylinder and being parallel to its axis. In the ref. [5], the method is applied rigorously to the thickness of the shell. The method also allows the treatment of the same problem but with the shell having a finite length. In this case, the problem becomes 3-dimensional. The following assumptions are made in refs. [4,5]:

- Displacement current is neglected
- μ is constant
- The excitation current is assumed to flow in a filament
- The length of shell and filament are infinite, straight line and parallel to each other

- Finite thickness [4] and infinite thickness [5]
- The return of the current in the filament is assumed to flow in the cylindrical shell

2.1.3. Improved Modelling of the Nonlinear B-H Curve

As mentioned above, in the majority of methods such as [1]-[4], μ has been considered constant. However, an improved modelling of the nonlinear B-H curve of ferromagnetic material is introduced by G. Lio in ref. [21]; the B-H curve is represented by a Fourier series, based on a set of measurement data. With the Fourier series expression, the magnetic energy density can be calculated and then used in an iterative procedure for determining μ everywhere within the ferromagnetic material. To validate the model's accuracy, it is employed, together with the finite-element method, to investigate the zero-sequence impedance of an underground pipe-type cable and the magnetic field in its vicinity. The computational results have a good agreement with the measurement data. To determine μ throughout the pipe, at first the magnetic field intensity in each element of the pipe is solved using finite-element method by X.B. Xu et. al. [6]. Subsequently, an iterative procedure is carried out using the following steps:

- An initial value of μ is assumed for each element of the pipe. By using μ and the results of [6], magnetic field intensity in each element of the pipe is calculated.
- Using the calculated magnetic field intensity, the magnetic energy density W in the nonlinear steel is obtained from Eq. (6) in ref.[21].
- The magnetic energy density W_f in the fictitious material is calculated as: $W_f = \frac{1}{2}\mu_p\left[H_{\max}^{p\ 2} - H_{\min}^{p\ 2}\right]$ Where P is referred to the P_{th} term
- In each element, the relative difference of W and W_f is compared with a small quantity ε. If $\left|(W - W_f)/W\right| < \varepsilon$ in every element, the iterative procedure is stopped and μ_p is determined by $\mu_p = \frac{2W}{H_{MAX}^{p^2} - H_{\min}^{p^2}}$

- If $\left|(W - W_f)/W\right| > \varepsilon$ somewhere, then obtained μ_p will be used as the new permeability in the first step of the next iteration.

By using this method and calculating μ throughout the pipe, the aforementioned method that employs μ as a constant value can be modified.

Xiao-Bang Xu et. al. [6] present a numerical method for computing the zero-sequence impedance of an underground Pipe-type cable. This method is based on finite element analysis, which is employed to determine the source current density in the conducting regions and magnetic vector potential everywhere in the pipe-type cable. Special attention is paid to the nonlinear B-H characteristic of the steel pipe and an iterative procedure is employed to determine the varying permeability of the steel pipe. Then, based on the knowledge of the source current density in the conducting regions, it obtains the zero-sequence impedance corresponding to various current levels. Since the zero-sequence impedance varies with the magnitude of the zero-sequence current, therefore, the solution of the zero-sequence impedance corresponding to different current levels presented in this reference should be useful for the fault analysis in pipe-type cables.

2.1.4. Finite-Difference Time-Domain (FDTD) method

D.L. paul et. al. [7] employ FDTD method to obtain magnetic and electric field intensities. The cable is divided into a large number of cells as the field is assumed to be constant within each cell and a linear integration is performed for the voltage. The contour of integration of the H magnetic field intensity is squared. Also for the wire formulation, a hybrid approach is considered. In particular, the nearest cells to the wire are assumed to have electric field intensity with 1/r dependence and thus the voltage for these cells is calculated by integrating this function from the wire surface to the cell boundary. The voltage across the remaining cell is calculated using linear integration between the cell boundary and the outer conductor surface. Similarly, the H is assumed to have radial symmetry, so that circular contour is used to calculate the current using Ampere's law. By using the FDTD, the magnetic field H, the

electric field E, the cable current vector [I] and the cable voltage vector [V] are obtained iteratively by M. Feliziani & F. Maradei [22]. The magnetic field H and the cable current vector [I] are updated at time $t=(n+1/2)\Delta t$, while the electric field E and the cable voltage vector [V] are updated at time $t=(n+1)\Delta t$. The main steps of the iterative procedure can be summarized as follows:

Time $(n+1/2)\Delta t$

a) H is updated by standard FDTD expressions.
b) The tangential electric field vector $[E_i]^n$ is evaluated on the cable shield surface at any I_{th} point of the cable axis by interpolating the E^n.
c) $[I_i]^{n+1/2}$ is updated.
d) $J_s^{n+1/2}$ (current density) is evaluated (only in the FDTD cubic cells with embedded cable section) by partitioning the $[I_i]^{n+1/2}$ under the assumption that the current density in the cell is parallel to the cable axis.

Time $(n+1)\Delta t$

e) E^{n+1} is updated by standard FDTD expressions.
f) $[V_i]^{n+1}$ is updated.

The results of FDTD method should be compared with the other methods used in EMTP, and probably, EMTP methods can be modified to increase accuracy.

2.1.5. High-Frequency Models and Frequency Responses for Cables

For the power cable, it is well known that distributed parameter representation provides more accurate results in the study of high frequency transients than the lumped parameter models. The parameters of the cable model are calculated by analyzing the behaviour of the short circuit impedance (Z_{sc}) and open circuit impedance (Z_{oc}) over a broad range of frequencies by A.F. Moreira et. al. [23]. As frequency responses are obtained experimentally, suitable models are developed to match the experimental results. Fig.(1) represents per-phase high frequency model of the power cable per-unit length. R_s and L_s are associated with the behaviour of Z_{sc}, while the parallel parameters R_{p1}, R_{p2}, C_{p1} and C_{p2} are associated with the behaviour of Z_{oc}. This model in over voltage phenomena is more accurate than in transient states.

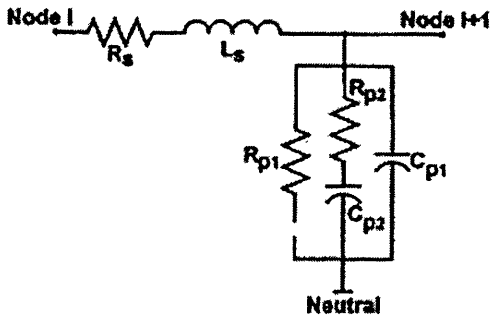

Fig.1- per-phase high frequency cable model

2.1.6. The Effects of Semi-Conducting Screens on Cables

Although the use of semiconductors in a power cable for underground transmission and distribution has been increased, the effects of these are not considered on the cable parameters, such as propagation constant and wave velocity. In this type of cables, the insulation is sandwiched between two black semi-conducting layers having mechanical properties almost identical to the insulation.

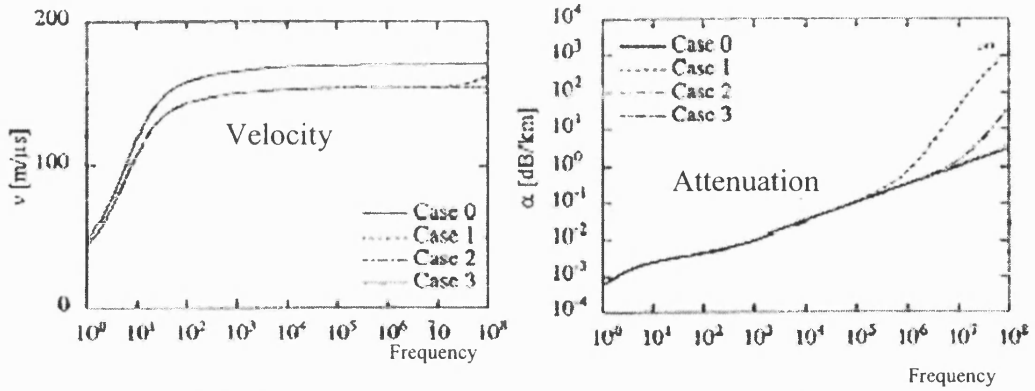

Fig.2- Velocity and attenuation of wave propagation

The two semi- conducting layers are often referred to as the conductor screen and the insulation screen, respectively. Even with perfect conductors, these layers influence the propagation characteristics. Experiments have shown that the speed of propagation in 15kV concentric neutral 175 mile XLPE cable, for example, is consistently much lower than would be that calculated from the standard formula. The effects of semi-conducting layers have been taken into account by A Ametani et. al. in Ref. [24]. Fig. (2) shows the attenuation and the velocity of wave propagation at different frequencies. From the data presented, the following observations can be made concerning wave propagation in a power cable.

- Wave speed is reduced by the semi-conducting screen layers at frequencies below about 10^9 Hz. At frequencies below about 10^4 Hz, the conductivity of the conductors and surrounding earth reduce the speed significantly. Especially for small diameter cables, the speed is dependent upon the screen thickness and the relative thickness of insulation and screens.

- Wave attenuation is increased by the semi-conducting screens but less than one might expect for typical screens.

- The cut-off frequency is higher for higher values of semi-conducting screen conductivity.

In spite of these important effects of semi-conducting on the propagation characteristics of a cable, unfortunately support routines (cable constants) in EMTP do not allow explicit representation of the semi-conducting screen. Thus an

approximate data conversion procedure must be applied. B. Gustavsen in ref. [25] describes the necessary procedures for converting the available cable data into a new set of data which can be used as input for cable constants. In particular, it demonstrates how to handle the semi-conducting screens of single core coaxial type cables. The effect of inaccurate data on a time domain simulation is also shown. Some important points that have been referred to are as follows:

a) Core:

The cable constant (CC) support routine requires the core data to be given by the resistivity ρ_c and the radius r_1; however, the core conductor is often out of the stranded design, where CC assumes a homogenous (solid) conductor. So the equal resistivity ρ_c will be:

$$\rho_c = \rho_c' \frac{\pi r_1^2}{A_c} \quad \text{or} \quad \rho_c = R_{DC} \frac{\pi r_1^2}{l} \tag{2-1}$$

Where ρ'_c is annealed copper or hard drawn aluminium.

b) Insulation and semi-conducting screen:

The permittivity ε_r will be $\varepsilon_r = \varepsilon_{rins} \dfrac{\ln\left(\frac{r_2}{r_1}\right)}{\ln\left(\frac{b}{a}\right)}$ (2-2)

Where the ε_{rins} is the main insulation permittivity [for XLPE ε_{rins} equals 2.3], r_1 is core radius, r_2 is r_1 plus the sum of the thickness of the semi-conducting screens and the main insulation, a and b are the insulation inner and outer radii respectively. The conductivity of the semi-conducting screen is much lower than the core and the sheath conductors and so it does not have an important effect on the longitudinal current conduction. However, because its permittivity is very high, the capacitance of the screen is much higher than the insulation and will tend to act as a short circuit when calculating the shunt admittance

between the core and sheath. Thus in order to consider these effects, the user should let the XPLE insulation extend to the surface of the core and sheath and increase the relative permittivity to leave the capacitance unaltered. It should be noted that this modelling technique neglects the possible attenuation caused by the semiconductor.

c) Wire screen:

When the sheath consists of a wire screen, the most practical procedure is to replace the screen with a tubular conductor having a cross sectional area equal to the total wire area A_s. With an inner sheath radius of r_2, the outer radius r_3 becomes: $r_3 = \sqrt{\frac{A_s}{\pi} + r_2^2}$. A model that considers the effect of semi-conducting screen is shown in Fig (3).

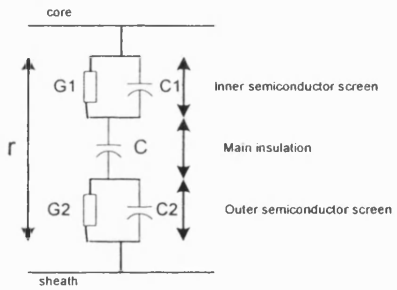

Fig.3- Improved model of insulation screens

As mentioned before, having increasingly sensitive loads makes the development of reliable and accurate fault location methods for distribution systems an important issue. One of the most important factors in accurate fault location is to develop an accurate model of a cable which then needs to be integrated into an overall distribution system model. Essentially, there is a need to determine accurately, the per unit length impedance and admittance of a cable, which in turn determine the relationships between current, voltage, attenuation and velocity of travelling waves in the transient state. As mentioned before, the EMTP software is particularly attractive for developing accurate cable models by virtue of the fact that it has a number of different methods for determining the cable parameters and characteristics. However,

in the modelling of a three-phase cable using EMTP, the main problem arises by virtue of the fact that the three conductors are positioned off centre within the pipe or armour and it is principally due to this that some estimations and approximations are made in the EMTP model; a direct consequence of the latter is that the mathematical representation of the impedance and admittance in a pipe type cable in the EMTP software includes infinite series formulations of the flux linkage and the proximity effects; this of course is based on some approximations in the configuration of cable. In order to affect a more accurate cable model devoid of many of the approximations associated with the EMTP model, the CM-based approach, the discussion of the next chapter, is much better suited; this is due to its ability to transform an isotropic region into a symmetrical and much simpler region.

2.2 Fault Location Techniques

The development of fault location techniques in transmission systems has been identified as an essential requirement for power companies. However, until recently, relatively little work has been done in the development of fault locating techniques for distribution systems; this stems from the fact that fault locators on such systems have been considered useful but not essential. However, the demand and importance for a cost effective method for accurately locating fault on distribution systems has increased in many part of the world; a major cause of this is the challenge facing many utilities resulting from deregulation, the privatisation of the electricity supply industry in Britain being one example. The consequences of the latter are resulting in a need to effect repairs more quickly through locating of faults via purpose-built fault locators.

The current practice in fault location within the electricity distribution companies in the UK, involves three main stages: diagnosis, prelocation and pinpoint. In the diagnosis stage, the existence and characteristics of the fault are confirmed. This takes the form of cable insulation resistance and continuity tests. The prelocation stage requires tests from cable terminals to obtain the distance to the fault. In the pinpoint stage, some methods are carried out in the locality indicated by the prelocation stage to confirm the precise location of the fault. Currently in the UK, the

impulse current method is used to prelocate faults, prior to using acoustic methods to pinpoint the fault location. The impulse current method is heavily dependent on the engineer's knowledge and experience in recognising/interpreting the transient waveforms produced by the fault.

The purpose of this section is an overview of existing fault location techniques for underground transmission and distribution networks. These techniques are currently available to utilities. An overview of some fault location methods more recently developed by other researcher is then presented, with particular explanation on their advantages and disadvantages.

2.2.1 Fault Location Stages:

a- Fault Diagnosis

Compared to low voltage distribution cables, fault location on high voltage cables is straight forward as the cables can be completely isolated for testing. However, in low voltage cables since consumers' apparatus is connected across the conductors therefore it is often impossible to enter all the consumers' buildings to disconnect it. Also in high voltage networks, each transmission cable may be equipped with its own relay and fault locator and this relay can detect the fault and inform the operators automatically, but in low voltage cable network, the fault is usually reported by customers. Whenever a fault is reported, diagnostic tests are performed to confirm its existence as well as to distinguish the faulty and healthy cores of the cable. This is done by measuring the continuity and insulation resistance of the cable. For example, a sound cable will have a high continuity as well as a high insulation resistance with other conductors and earth.

b- Fault Prelocation

The purpose of fault prelocation is to locate the section of cable in which the fault has occurred. The current prevalent practice for the prelocation of faults on both high voltage and low voltage (LV,HV) underground cables is the use of the impulse current method. The method has the advantage of locating with accuracy, all types of cable faults irrespective of their parameters. The method is based on travelling wave principles and uses the current transients which occur when a cable breaks down on

the application of high voltage DC or when a surge is fired into a faulty cable in the case of HV networks, but it is impossible to employ HV burning equipment on LV networks for several reasons, including the risk of damaging customers' equipment. In this respect, another form of fault processing has been developed as fault blasting which uses heavy current to obtain the necessary damage in the case of LV networks that is dealt with later.

c- Fault Pinpointing

The purpose of pinpointing is to locate precisely the fault from the fault distance estimated at the prelocation stage. An impulse DC voltage is applied to the faulty core of cable. When the spark gap breaks down, an acoustic signal is created. This acoustic signal can be detected as a loud 'bang' using a cable fault locator in the vicinity of the cable fault. The exact location of the fault is then identified and the minimum of excavation done to expose and repair the cable.

2.2.2 Type of Cable Faults:

The two major categories of faults that occur in underground distribution networks are series and shunt faults. A series fault occurs when one or more of conductors, including the sheath, lose continuity, partially or totally. Usually a series fault becomes dominant and develops in to an open-circuit fault when at least one of the conductors loses its continuity completely. Series fault comprises single phase, double phase and three-phase open circuit. A shunt fault occurs when the insulation of one or more conductors fails. The single phase to earth fault is the most common type of shunt fault. The shunt cable fault is represented by the simple equivalent circuit of Fig. (4) by K.K. Kuan & K. Warwick as in ref. [18].

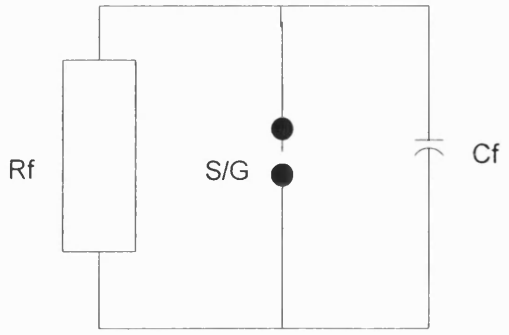

Fig.4- The model of a shunt fault

In Fig.(4) R_f, S/G and C_f represent the fault resistance, spark gap and capacitance in parallel with the fault resistance, respectively. The values of all the elements can vary widely and are independent of each other. Typically, the value of fault resistance can vary from zero to infinity, depending on the degree of carbonisation of the dielectric. The capacitance depends on the percentage of moisture present. The breakdown voltage across the spark gap can vary from a few hundred to a few thousand volts. Shunt faults are normally divided into low and high resistance types. Low and high resistance faults are when the fault resistance is lower and higher than ten times the characteristic surge impedance of the cable, respectively. Shunt faults are divided into balanced and unbalanced faults; the former consist of three phase direct and three phase to earth faults and the latter comprise of single phase to earth, double phase to earth and phase to phase faults.

2.2.3 Basic Principles in Fault Location:

The economic and reliable operation and protection of power systems requires the exact and fast determination of the point where a fault occurs. The following section determines some important and basic principles in fault location and is then dealt with an overview of the fault location techniques currently available to utilities.

2.2.3.1- On-line and Off-line Techniques

Generally one type of classification is based on the main purpose of fault location and is divided into two categories - on-line and off-line - which are associated with protection and operation of power systems, respectively. In respect of operation, fault location techniques are used for accurately pinpointing the fault position. Benefits of accurate fault location in the operating state are as follows:

- Fast repair to restore power system.
- Improves system availability and performance as well as reduces operating costs.
- Saves time and expense of crew searching in bad weather and difficult terrain.
- Aid crew in disturbance diagnostics by identifying temporary faults and detecting weak spots.

Fault location for repair and inspection purposes requires very high accuracy, while the speed of the fault location is not so critical and computations completed in minutes or even slower are acceptable. Thus, more accurate phasor calculation can be applied with use of the best available data window and filtering techniques. Use of all locally available information and also data obtained via communication systems is relevant for accurate fault location. However, the location for protective relaying purposes is entirely different as the speed of the fault location is a critical factor.

2.2.3.2- High and Low Frequency Techniques

Methods of locating power system faults can also be broadly classified under two categories: one based on the power frequency components (low frequency components), and the other utilizing the higher frequency contents of the transient fault signals. The latter is also referred to as travelling wave or ultra high speed fault location method, due to its use of travelling wave theory and shorter sampling windows. According to the travelling wave theory, fault transients will have different signatures at the substation terminals depending on the number of network junctions they pass through as they travel towards the substation. These signatures only show up at the high frequency end of the spectrum and will be missed by most methods based on the power frequency signals. Thus in order to effect an accurate method to locate faults, on the face of it, it would appear that this can be better achieved by utilising the high frequency information in the fault transient signals rather than the power frequency data.

2.2.3.3- Voltage Class

Another approach used by utilities for fault location depends on the types of insulation. Underground distribution circuit routes are less well defined than underground transmission circuits and affect the performance of fault location methods. The details required to locate the fault vary with the types of installation. In practice, utilities use some form of prelocation followed by one or more fault location methods to pinpoint the location of the cable fault.

One method of classification can be achieved via voltage class [8]. There are differences in the application of techniques between transmission and distribution cables (high, medium and low voltages networks; HV, MV and LV). Many utilities have field crews which perform all types of work, with fault location as one part. When the fault's location is determined for a distribution network, one of the field crew replaces or splices the cable without assistance from other personnel. A timely repair of the cable system is required since, unlike transmission cables, a faulted distribution cable means that customers are out of service and the faulty cable should be repaired as soon as possible. For a transmission cable, a failure investigation, including fault location, involves an engineer or senior technician since the cost and importance of a transmission cable is greater than for distribution. More time is spent on locating transmission cable faults because the cable needs be isolated without interrupting service to customers.

The following are the main difficulties which make fault location on LV cables more difficult than on HV cables:

- Most HV cables have only two ends, or a few ends, with no consumers' apparatus directly connected to the conductors. However, LV cables have a large number of tee branches. Also consumers' apparatus is connected across the conductors and it is often impossible to enter all the consumers' buildings to disconnect it. All these factors usually make classical tests with bridge methods (which are dealt with later) impossible.

- The extra electrical complexity caused by the presence of many branches and joints due to the connection of consumers' apparatus across conductors, made the pulse-echo or radar techniques (which are dealt with later) impossible to use in the past; any resulting oscilloscope trace was so complex that the fault was impossible to observe.

- Shock-discharge tests (that is explained later) for pinpointing faults were normally impossible for several reasons. The low operating-voltage of the cables and the presence of consumers' apparatus across the conductors

prevented the application of high-voltage shock-waves similar to those use on HV cables.

- Many LV cable faults are not permanent but intermittent or self-sealing.
- Probably the most successful techniques in HV fault location are pulse-echo and shock-discharge. These have now been successfully adapted for LV cables but changes have had to be made. Pulse-echo depends on first burning or processing the original fault until it possesses suitable characteristics, mainly low resistance. However, it is impossible to employ HV burning equipment on LV networks for several reasons, including the risk of damaging customers' equipment. Another form of fault processing has been developed as fault blasting which uses heavy current to obtain the necessary damage.

- Because of economical reasons, feeder-dedicated fault locators can hardly be applied in MV and LV networks. However, substational monitoring using digital fault recorders is a common utility practice in most countries. Moreover, fault recording function is available in new installed digital relays.

- In HV networks, each transmission cable or line may be equipped with its own fault locator. In contrast, in MV networks, fault locators are usually assumed to be a centralised type, i.e., they measure the quantities common for the whole substation (busbar voltages and transformer currents) and this makes accurate fault location more difficult.

- The MV networks are non-homogeneous, loads are tapped at different nodes and line configuration could be different between each pair of adjacent nodes.

2.2.3.4- Terminal and Tracer methods

The next classification technique which has been dealt with in some research and papers associated with cables is divided into two categories of fault location as follows; terminal methods and tracer methods. Reference [8] gives an overview of this classification method. Terminal fault location methods are techniques which are performed from one or both ends of the cable system. In general, these methods are

most useful in prelocating the cable fault. However, cable fault location with tracer techniques requires 'walking the route' to locate an audible or electromagnetic signal. These methods are most useful for pinpointing the fault location after the approximate location has been determined. Generally, two people are required to use the tracer techniques, one to operate the signal generation equipment (thumper, tone set, etc.) and another to traverse the cable route. To detect the tracer signal along the cable route, a field crewman must follow the cable or enter manholes to gain access to the cable. Some tracer fault location techniques can also be used to locate the cable. Knowledge of the cable route is important since many of the tracer techniques produce signals which can only be detected within a limited range of the cable. Large deviation from the route during tracer fault location can make finding the fault, difficult.

2.2.4 **Existing Fault Location Techniques**:

With regard to the aforementioned classifications of the fault location in transmission and distribution networks, the following section deals with some existing fault location methods which are employed in practice.

2.2.4.1- Bridge Techniques:

Bridge techniques are based on off-line, steady state, DC source and terminal method and require the use of a resistive bridge to determine the location of the fault and are useful only for poly-phase cable systems. In the past, bridges were useful for locating cable faults although the accuracy of common null detectors (galvanometer or other means) was poor. With the advent of digital multimeters and other devices that may be accurate to 4-5 digits, several utilities are revisiting the use of bridges for cable fault location. A generic bridge is shown in Fig. (5), [8].

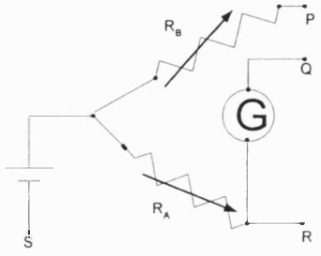

Fig.5- Typical electrical bridge

In the bridge, R_A and R_B are variable resistors that are adjusted until the galvanometer, G, indicates a null. Under this condition, the bridge is balanced. Several bridge techniques are dealt with in the following:

I- Hillborn loop

This method is valid for shorted and high impedance (shunt) faults on shielded cables. The length and/or resistance of the faulted and unfaulted cables do not have to be the same. In this method, the bridge is connected to the cable as shown in Fig. (6) and with R_A and R_B known, the distance to the fault can be found as follows:

$$Dis\_to\_fault = \frac{R_A}{R_A + R_B + (r_d)(length_{un-faulted-cable})} .length_{faulted-cable}$$

Where r_d is the unfaulted conductor resistance in ohms/unit length.

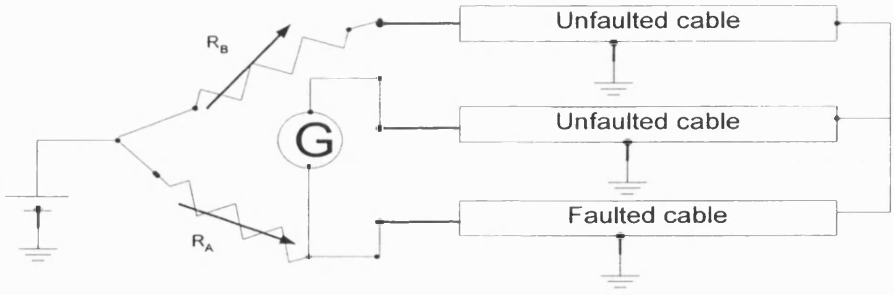

Fig.6- Hillborn Loop connection

II- Murray loop

This method is valid for shorted and high impedance (shunt) faults on shielded cables or for phase to phase faults on belted cables. The Murray loop is the most commonly used bridge technique by utilities. By making the measurement with the bridge connections shown in Fig. (7), resistances R_A and R_B can be used in the following equation to find the cable fault.

$$Dis\_to\_fault = \frac{R_A}{R_A + R_B} * 2L$$ as L is the cable length.

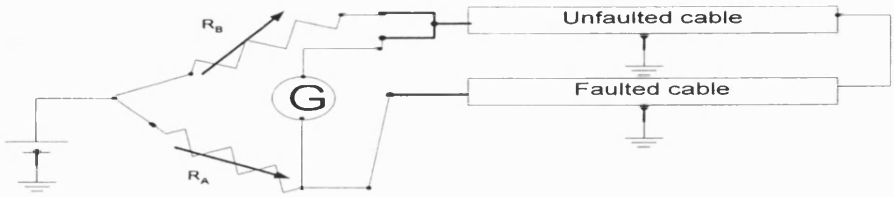

Fig.7- Murray Loop connection

The Murray Bridge is difficult to apply if one of the end terminals of the cable line is connected to a GIS. In addition, in the case of XLPE cables, the resistance at the fault is often very high, which makes detection by the Murray loop very difficult.

III- Murray Loop Two-End

This method is valid for shorted and high impedance (shunt) faults on shielded cables or for phase to phase faults on bolted cables. The Murray Loop can be applied to both ends of a cable circuit for enhanced accuracy in locating the cable fault. The benefit of the two-end method is that it is not sensitive to variations in length between the faulted and unfaulted cables. For the two-end method, a test is performed at each end of the cable with the bridge connected as shown for the Murray Bridge. The location of the fault can then be approximated with the following equation (primed values are for the second test):

$$Dis\_to\_fault = \frac{R_A(R'_A + R'_B)}{R_B R'_B - R_A R'_A} * unfaulted\_cable\_length$$

IV- Murray-Fisher Loop

This method is valid for shorted and high-impedance (shunt) faults with an available unfaulted phase conductor on shielded cables. Like the two-end Murray Loop, the Murray-Fisher Loop can be used to locate a cable fault when the faulted and unfaulted cable lengths are not the same. Two tests are required (the connection for test 1 is similar to Fig. (7) and for test 2 has been shown in Fig. (8)). Test 1 providing R_A and R_B and test 2 providing R'_A and R'_B which can then be used in the following equation:

$$Dis\_to\_fault = \frac{R_A(R'_A + R'_B)}{R'_B(R_A + R_B)} * unfaulted\_cable\_length$$

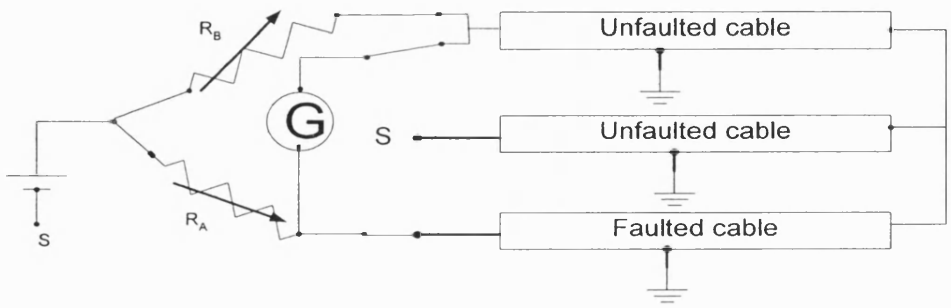

Fig.8- Test 2 connections for the Murray-Fisher Loop

V- Open & Closed Loop

This method is valid for shorted and high-impedance (shunt) faults on shielded cables when two phases are faulted. The faulted conductors must be of the same length and have the same construction as the unfaulted cable. The test is applied with the far end open and closed. R_A and R_B are produced by test 1 (fig.(9)) and R'_A and R'_B are provided from test 2 (fig.(10)). These values can then be applied in the following equation:

$$Dis\_to\_fault = \frac{R'_A R_B - R_A R'_B}{(R'_A + R'_B)(R_B - R_A)} * 2 * (total\_cable\_length)$$

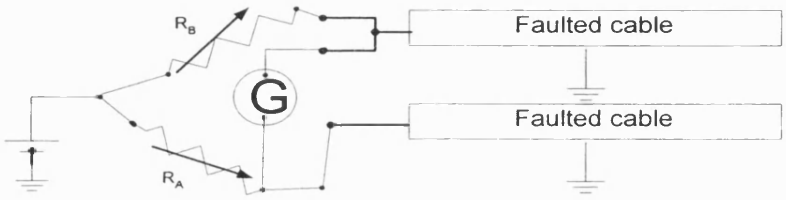

Fig.9- Connection for test 1 of open Loop

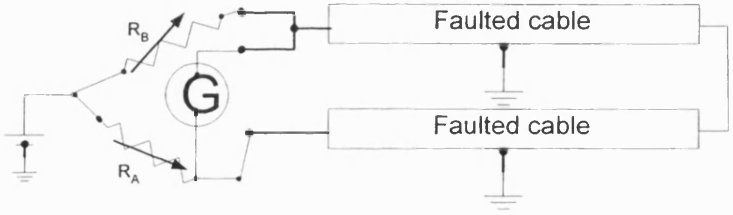

Fig.10- Test 2 of Closed Loop and connection for Werren Loop

VI- Varley Loop

This method is valid for phase to phase short-circuit faults on shielded cables. The method can be applied when the lengths of the faulted and unfaulted cables are not equal. Two tests are required, the first to determine the length of the faulted conductor from the length of the unfaulted conductor (fig.(11)) and the second to determine the distance to the fault on the faulted conductor (fig.(12)). R_A and R_B are set to equivalent values for the first test and the variable resistance, R' is determined. The length of the faulted conductor can be found as follows:

$$faulted\_cable\_length = \frac{R' - (resistance_{unfaulted-cable})(length_{unfaulted-cable})}{resistance_{faulted-cable}}$$

The distance to the fault can then be found using the results of Test 2 which produces variable resistance, R''.

$$Dis\_to\_fault = \frac{R' - R''}{2 * (resis\tan ce_{faulted-cable})} * (faulted\_cable\_length)$$

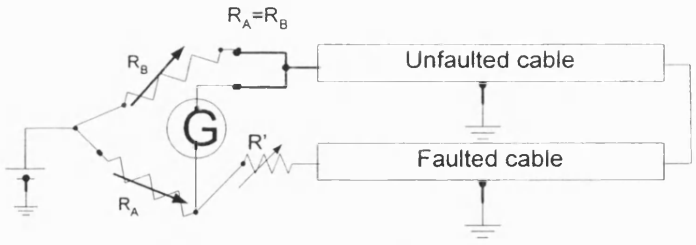

Fig.11- Test 1 connections for Varley Loop

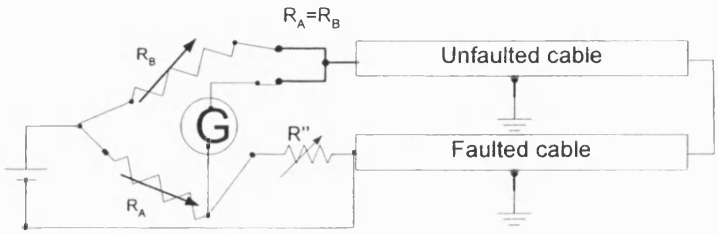

Fig.12- Test 2 connections for Varley Loop

VII- Werren Loop

This method is valid for shorted and high-impedance line to line to ground faults on shielded cables. The Werren Loop employs the bridge in the same way as Test 2 for the Closed Loop (Fig. (10)). Two tests are performed using this configuration, one from each end of the cable circuit. R_A and R_B are obtained from Test 1, and R'_A and R'_B are obtained from Test 2. These values are then used in the following equation to approximate the fault location:

$$Dis\_to\_fault = \frac{(R_A + R_B)(R'_A - R'_B)}{2.(R_A R'_A - R_B R'_B)} * total\_cable\_length$$

Because bridge techniques always require a sound phase, three-phase faults are not detectable by using the aforementioned bridges.

2.2.4.2- Capacitance Ratio:

This method is employed in off-line and low frequency categories and valid for open conductor faults on shielded cables in HV and MV. Since the fault is open, it is possible to measure the capacitance C_1 of the cable section from one terminal to the fault and

compare this value to the capacitance C_2 of an unfaulted cable. The measurement made from both ends if an unfaulted cable is not available. The distance to the fault can be determined as follows:

$$Dis\_to\_fault = \frac{C_1}{C_2} * total\_cable\_length$$

2.2.4.3- Insulation Resistance Ratio:

This method is employed in off-line and low-frequency categories and valid for open conductor faults on shielded cables in HV and MV. An insulation resistance measurement is made on a faulted and unfaulted cable and the ratio determines the fault location. The unfaulted cable resistance is smaller than the faulted cable since the cable effectively has more parallel resistance-to-ground than in the faulted cable. An additional measurement from the opposite end may improve accuracy; R_1 is the insulation resistance measured on the faulted cable and R_2 is the insulation resistance on the un-faulted cable. The distance to the fault can be approximated by:

$$Dis\_to\_fault = \frac{R_2}{R_1} * total\_cable\_length$$

2.2.4.4- Time Domain Reflectometery (TDR):

TDR is one of the most commonly used methods for locating faults on underground cables and transmission lines. TDR based fault location techniques were developed and successfully applied in high or medium voltage cable or overhead transmission networks, but not for low voltage networks; this is due to multiple 3-phase and single-phase tee joints in the LV systems. Due to the multiple tees, the TDR recorded signals are more complex than those obtained from high and medium voltage underground cables, and overhead transmission lines. In the TDR initially, a pulse is launched into the cable network from an accessible point. This pulse is partially or completely reflected by any impedance mismatches in the cable network. These impedance mismatches can be a short circuit or an open circuit or tee joint. The reflected pulses (signals) are recorded for both faulty and sound phases. These reflected signals are then used to locate any fault in the cable network either by visual comparison or by subtracting one from the other. This method is used in many commercial underground

low voltage distribution networks (ULVDNs) fault location instruments such as Edgcume E2760 [9], Hathaway P240 [10], and Biccotest T510 [11]. The main disadvantage of the TDR method when used for ULVDNs is the need for experienced engineers to interpret the results due to the complexity of the reflected signals. Some of the key issues in ULVDNs faults using the TDR are as follows:

- TDR recorder signals are not easy to interpret due to reflections from the many tee connections in the network.
-single-phase tees may produce reflections similar to short circuits; therefore it is difficult to distinguish between single-phase tee and short circuit fault from the reflections recorded.

-when fault location is carried out on live lines, non of the access points for fault recordings are isolated from the busbar. If the access point is not isolated from the busbar then it is not possible to record good sound phase reflected signals. This is because the pulse launched into the cable travels into other feeders as well. Therefore, the recordings are reflected in to the faulty phase. To record a sound phase reflected signal, additional fuses need to be taken off which will lead to power outages to customers.

With regard to the aforementioned points, an automatic system based on intelligent processing of the TDR signals for locating faults on ULVDNs has been presented by S. Navaneethan et. al. in ref. [12]. The presented method not only locates a fault but also differentiates between single-phase tees and faults. This method is evaluated relative to current practice, using fault data that was obtained from real ULVDNs. In addition to the above points, it should be noted that the TDR is effective only when the fault resistance is low enough to produce a pulse or standing wave reflection.

C.M. Ho et. al. in ref. [26] show how the position and the magnitude of the pulses in a pulse-echo response are related to the topology and the dimensions of the cable; the terms topology and dimensions refer to the relative positions of the tee joints in a cable, and the lengths of cable sections between joints and cable ends, respectively. Also it considers the inverse problem as to how one may deduce the topology and the dimensions of the cable from its pulse-echo response.

2.2.4.5- Shock Methods:

Shock methods are used for pinpointing the fault in cable networks. In the following, some shock methods are explained.

I- pulse discharge detection:

This method is valid for shorted and open faults on shielded cables in HV networks [8]. This method employs the use of an impulse generator or capacitor discharge device (thumper) to cause a breakdown at the cable fault. The breakdown produces a travelling wave in the cable. When the first reflection reaches a voltage coupler at the test location, the time period until the second reflection arrives, is monitored. By knowing the velocity of propagation, the distance to the fault is determined from the time difference between the two reflections.

When the fault breaks down, a transient is induced in the cable which, when properly analyzed, gives the location of the fault. In practice, the physical phenomena associated with this process affect the location procedure. Break down phenomena are statistical in nature and influence the received transients. The propagation characteristics of the cable are also an important factor in the analysis. When voltage is applied to the cable, the damaged portion of the cable begins to conduct. The conduction process is random and depends on the geometry of the faulted portion of the cables as well as the properties of the materials present at the fault site. In the case of open-circuited fault, the conduction process does not begin immediately; there is a statistical time lag. This time lag can extend from tens of nanoseconds to many microseconds and depends heavily on the over voltage applied to the equivalent gap, modelling the fault. A less understood phenomenon also occurs. If the rise time of the high voltage is too slow, the fault gradually progresses into conduction. In this case, a fault transient is still generated, but a sharp breakdown is not observed. The implication of this slow conduction process is that the fault transient does not contain much of the high frequency energy necessary for effective fault location. From empirical evidence, it is clear that as long as the rise time of excitation voltage exceeds the statistical time lag of the break down, there is little effect on the frequency content of the fault transient. In other words, the power source must be able to bring the cable to full voltage before the conduction process begins.

II- Low Voltage Radar Detection:

This method is valid for shorted and open faults on shielded cables. A signal is sent down the cable which produces reflections at the fault location. The far end of the cable is left open during use of the radar and is indicated by an upward sweep in the radar trace on a scope. A shorted fault will be indicated by a downward deflection in the trace. In addition to locating cable faults, the radar may approximate the location of splices. It can be difficult to distinguish a cable fault from splices. When this is a problem, a comparison of an unfaulted cable radar trace is helpful.

III- Radar with High Voltage Pulse:

This method is valid for shorted and high-impedance faults on shielded cables in HV networks. Where conventional radar does not sufficiently indicate the location of a cable fault, a capacitive discharge device may enhance the radar trace. When a thumper is applied to the cable with a radar set, a coupler is used to protect the radar set. During the breakdown of the insulation, the resistance to ground at the fault is momentarily reduced. The radar set can then obtain a better reflection at the fault. Radar scopes with a storage display are especially useful for this method since an easier comparison of two radar traces is possible.

IV- Fault Blasting and the Shock-Switching Test:

In the first instance, it is necessary to explain the difference between fault burning and fault blasting. Fault burning is a highly controlled technique entailing the application of high voltages and small currents for long periods to HV cable faults. However, it is not applicable to LV networks. In this case, the necessary damage is achieved by switching heavy current straight into the fault from the power system for periods which may extend over many 50 Hz cycles and if necessary, the process can be repeated several times. The current used can range from a few hundred amps to several thousands amps. Its duration can range from many seconds to a fraction of a cycle. The principle has been used very successfully for several years. High-resistance shunt faults are soon turned into low-resistance faults or the cable conductor is blown apart at the fault, making a clean open-circuit [27]. The necessary switching device is called FRED (fault re-energising device). The shock-switching test is the LV equivalent of the HV pulse-discharge test. FRED switches the LV busbar source into the fault and engineers detect a thump at the fault position. In the shock-switching test it is possible to produce a

heavy mechanical and acoustic shock at the fault position at LV; this is normally done by using a FRED. One recloses the FRED a number of times and the engineers detect the shock at the fault position. They can do so by using similar equipment (special microphones and so on) as with the HV pulse-discharge test. However, frequently, on LV the shock is big enough to be felt by the feet or heard through the air; this is because LV cables are nearer the surface.

2.2.4.6- Impedance Technique:

The principle of fault location based on impedance technique is quite simple. According to ohm's law, the impedance from a measuring point to a faulted point is determined by the quotient of the measured voltage and the measured current during the fault. This ratio will be constant for any particular fault position, irrespective of the magnitude of fault current and will only vary if the distance between the fault and the measuring point varies. This technique is more complex in practice. It may be important to incorporate the influence of the existing pre-fault load current. Also the resistance of the fault itself is not known. Since the reactance of the fault is known to be zero and the cable reactance are well known and not current dependent, therefore in developed impedance technique the fault locator works with the reactance only and the resistance will not be used. According to some publications it is recommended to disregard the resistance part of the fault impedance.

Impedance technique is employed for protection of systems and diagnosis of faults. This technique is in on-line and power frequency categories of fault location techniques. Under ideal conditions, impedance is directly proportional to the fault distance. If the fault is located within the relay's protection zone, the relay must generate a trip signal. There are a few impedance algorithms, two of which are; the algorithm by the Bornard/Bastide [11] and the Phadke/Ibrahim [11].

The algorithm by Bornard/Bastide is based on the solution of differential equations. It shown that this method is reliable in the presence of harmonics because of error minimisation. However, it requires more than 15 input samples which results in long computation times and the effects of CTs lead to estimation error in the detected distance.

The algorithm by Phadke/Ibrahim determines the fundamental wave phasors of I and V signals by using digital filters and thus, the Fourier analysis is employed. This method is particularly reliable against distortion by harmonics. However, DC components cannot be taken into consideration by the analysis associated with this method. Additionally, it needs I or V signals with a width of one period in order to solve the requisite equations, which lead to computational times greater than 20ms (if f_n=50Hz).

Because much useful information in transient fault signals are associated with high frequency components, impedance techniques using power frequency components are not in essence, satisfactory methods for accurately locating faults.

2.2.5-An Overview of some Developments in Fault Location Techniques

Modern electrical supply systems require efficient methods for fault location, supply restoration and high quality customer service, which reduce the overall costs. In recent years, many techniques for the fault location have been reported. This part of thesis deals with results of some researched algorithms and publication papers associated with fault location techniques in underground transmission and distribution networks.

An on-line fault location system for 66 kV underground cables with fast optical to Electrical (O/E) and fast A/D technique is reported by N. Inoue et. al. in ref. [28]. Location test is carried out on single phase coaxial cable of 1000m long. The average location error of the system is below 10m. Operational principles of the system are summarized as follows:

- A fast optical CT of 1-MHz bandwidth is attached to each end of a transmission line and detects surge current which flows from the point of fault to each end following a ground fault.

- A surge current waveform detected by an optical CT is converted to electrical signals by a fast O/E converter of 1-MHz bandwidth.

- After O/E conversion, electrical signals are converted into digital data by a fast 16-bit A/D converter.

- The point of rise of the surge waveform is determined from digital data, and the distance to point of fault is calculated.

- All such processing is performed automatically under the control of a 16-bit CPU.

However, since this method is based on travelling wave theory and in view of the limitation in frequency bandwidth for CT (1 MHz), the sample rate of data recording must be more than 2 MHz. Thus, with regard to the velocity of wave propagation (about $2*10^8$ m/s), the minimum distance which can be detected is 100m (10% of total distance) and this error is unacceptably large. Another drawback of this method is that the data is recorded from two ends which makes synchronisation of data recording rather difficult in practice, particularly in distribution systems. Also the effects of load taps have not been considered and only a single phase to ground fault is presented in a subtransmission system (66 kV).

J. Zhu et. al. [29] describe an automated distribution fault location and diagnosis system. This system integrates information available from a substation digital transient recording device with knowledge of the feeder configuration and protection coordination contained in a distribution database. The proposed fault location and diagnosis scheme is based on the steady state analysis and involves three sequential processes using; signal processing, fault location and fault diagnosis. Firstly, a signal processing algorithm is used to estimate the voltage and current phasor quantities and extract the sequence of events from the recorded digital waveforms. With the estimated phasor quantities, a fault location algorithm is then applied to locate the fault distance. To allow for the uncertainties inherent in the system modelling and the phasor estimation, this algorithm has been adopted to estimate the error bounds for the calculated fault distance, based on probabilistic modelling and analysis. Since the distribution feeder is a radial network, with measurements normally available only at the substation, multiple possibilities of fault location can result. Using additional information related to protection coordination and system loading, a fault diagnosis algorithm is finally used to prune down and rank the possible fault locations. However, a drawback of this method is that the information about the operation of the feeder's protective devices and/or the protection coordination schemes may not be accurate or

even not available at all the substations. Also since this method is based on steady state, some high frequency transient information due to a fault is missed.

As mentioned before, since the Murray Bridge, which is one of the most popular fault location method accurately employed in practice, is difficult to apply if one of the end terminals of the cable line is connected to a GIS and also because the conventional pulse radar method is difficult to apply if the cable line is branched or crossbonded, a fault locating instrument based upon travelling wave current detection has been developed by M. Komoda et. al. in ref. [30]. Measurement is automated and the distance to the fault point is displayed by merely pushing a switch. In a branched or crossbonded line, the fault point can be located without interference from the branched or the crossbonded point. The method is applicable even if the resistance at the fault point is high. However, one drawback of this method similar to the previous method [28] which is based on travelling wave, is that it is not accurate in DS for short distances (a few hundred metres) and sampling rate for data recording must be very high (> MHz). Furthermore, this method has three main disadvantages. Firstly, the amplitude variation may cause problems in interpreting the reflected signals. Secondly, this method can only deal with two signals at any instant. This may cause a problem if the faulty phase signal is not known. Thirdly, the reflected signals recording in ULVDN are restricted; this is due to live line testing and hence, it is not always possible to record healthy and faulty phase reflected signals without customer power outage.

S. Navaneethan in ref. [12] has explained an automatic fault location technique for permanent faults in underground low voltage distribution networks (ULVDNs). It uses signals from an existing Time Domain Reflectometry (TDR) instrument. It pre-processes the TDR signals to eliminate reflections due to single-phase tee-offs and to locate 3-phase open or short circuit faults and also uses adaptive filtering to compare the TDR signals to locate faults. This method uses the existing TDR signals together with advanced signal processing techniques which increases the accuracy and automate the fault location process. The key characteristic of this approach is the way these signals are compared to each other and it is not vital to record the reflected signals between non-faulted phases to locate faults. This method can solve the three aforementioned disadvantages in ref. [30]. However, it is still based on travelling wave theory and needs very high sample rate to record data that can have practical difficulties in DS.

F. H. Magnago & Ali Abour in ref. [31] present a new, wavelet transform based fault location method. Using the travelling wave theory of transmission lines, the transient signals are first decoupled into their modal components. Modal signals are then transformed from the time domain into the time-frequency domain by applying the wavelet transform. The wavelet transform coefficients at the two lowest scales are then used to determine the fault location for various types of faults and line configurations. The proposed fault location method is independent of the fault impedance and is shown to be suitable for mutually coupled tower geometries as well as series capacitor compensated lines. The method can be used both with single ended and also synchronized two ended recording of fault transients. The fault location estimation error is related to the sampling time used in recording the fault transient. This method shows the ability of the wavelet signal processing to locate the fault, but because it is based on travelling wave, in underground DS with short distances, it requires very high sample rate, posing practical difficulties. Also in the case of two sources, it requires data from two ends and this poses further practical problems of data synchronisation from the two ends of the DS.

F. H. Magnago & Ali Abour in ref. [32] describe a single-ended fault location technique for radial distribution feeders based on the information provided by the measurements and the feeder configuration. The proposed method firstly identifies the fault path, based on the travelling wave information provided by the high frequency components of the recorded fault transient signals. It then calculates the exact fault location along the identified path based on the power frequency signals. The multiphase transient signals are firstly decomposed into their modal components. Then, the modal signals are decomposed into their wavelet components to obtain the corresponding wavelet coefficients. These wavelet coefficients are used to extract the relevant signal features which are subsequently used to identify the branch or path where the fault is located. Finally, the fault distance from the main substation is deduced using the information provided by the power frequency signal. The main advantages of this method are as follows: firstly, the identification of the faulted phase is based on the voltage signal decomposition in the frequency spectrum 12 to 25 kHz and hence voltage transducers with a bandwidth of 50 kHz are needed and this is acceptable in practice; secondly, in contrast to the technique presented in ref. [33], in addition to identifying the path of a fault in a radial DS with some branches, this method can find the exact location of fault

(pinpointing); thirdly, all processes are based on measurements at the substation only not at all ends, as is the case in ref. [33]. However, this method can only process a radial DS (one source) and although pinpointing is based on the power frequency signals, thus some useful information related to high frequencies is missed and this event decreases the accuracy of the method.

A conventional method to locate a fault in a radial network involves placing current detectors along each feeder. The measured currents indicate if the fault is above or below each sensor. The proposed method by P. Bastard et. al. in ref. [33] is not based on current measurements, but on voltages measurements located in MV/LV stations. This method may be particularly interesting if LV voltage transformers are already available. The method is divided into two steps; the first step involves determining whether each sensor is upstream or downstream the fault. The second step involves determining the faulted section, using a topological method. It pre-supposes that each end of this feeder is equipped with a sensor associated with an algorithm making it possible to determine if the sensor is upstream or downstream the fault. A sensor located downstream the fault will be called "active sensor". If all the active sensors on a given feeder are known, it is possible to determine in a systematic way the faulted section. Despite the problem of measuring accuracy, the proposed fault location algorithm has two interesting advantages. Firstly, it can be easily used in networks where voltage sensors have already been installed in MV/LV stations, for instance to control the voltage available on the LV network. Secondly, it is very efficient in locating open-circuit faults. In such a case, the measured precision is not a problem anymore and the faulted section can be determined very easily. However, this method has some drawbacks as follows: it requires a significant number of sensors (for all ends) and only covers radial DS. Also, only the faulted section can be detected (pre-location with small accuracy) but precise location has not been presented.

A fault locating system is developed and tested by P.M.V. Oirsouw & F. Provoost in ref. [34]. It is able to identify the fault location using the measured voltage and current time series of the fault sequence. The measurements are provided by an extra function in the protection system. It is shown that the method is able to identify the fault location within the required accuracy within 100 metres for two and three phase faults and 1000 metres for a single phase to ground fault. The soundness of the system is heavily

dependent on a good realistic network model and this modelling of the positive and zero sequence network impedances to be more precise. The total time for determining a fault location is less than 5 minutes. This time largely depends on the data collection and transmission time from the substation to the dispatch centre. The actual calculation time is less than 20 seconds. This method is based on an impedance technique, as the impedance is determined from a measuring point to a fault point by the quotient of the measured voltage and current during the fault. This method has two drawbacks; 1) the influence of load taps is not considered. 2) it is based on power frequency signals and it misses out some useful information related to high frequencies in the transient condition.

M.M. Saha et. al. in ref. [35] present a method for estimating the location of faults on radial medium voltage (MV) systems, which can include many intermediate load taps. In this method non-homogeneity of the feeder sections is also taken into account. Performance of the technique is investigated using data obtained from the EMTP simulation. The data recorded during faults in a real MV network is also used. Distribution utility MV networks are used as an example. The voltage and current data samples obtained from the EMTP simulation or delivered by digital fault recorder are converted into the MATLAB format. The 1 kHz sampled data are then used in the MATLAB fault locator model. This method is based on impedance technique similar to that in ref. [34], but, load taps have been taken into account. Although it is based on power frequency signals, some useful information associated with high frequencies in transient condition is missed.

Aggarwal et. al. in ref. [36] present a new technique in single-ended fault location for overhead distribution systems, which is based on the concept of superimposed components of voltages and currents rather than total quantities and also special filtering techniques have been utilised to accurately extract the fundamental phasors from the measured fault signals. It has been shown that the fault locator is highly insensitive to variations in local and remote sources and to the presence of taps with variable loads. The results presented also show the locator's robustness to large errors in the estimation of load taps and remote source capacity (if present). However, this method does not consider open-circuit faults and is based on power frequency signals only; some useful information associated with high frequencies in transient condition is thus lost, as in the case also in ref. [35].

A novel technique for locating faults in underground cable systems is presented by M.T. Glinkowski & N.C. Wang in ref. [37]. The technique utilizes the concept of artificial neural networks. During a system fault, a set of measurements of voltages and currents at various locations in the distribution circuit is used as a "pattern" that is applied to a specially trained neural network (NN). This pattern is then compared with the library of training patterns (cases) to recognize the location of the fault. The output of the neural network is graphically displayed as a simple 3-D chart that provides an operator with an instantaneous indication of the location of the fault. The last section of the paper illustrates sample results for two typical distribution circuits and discusses the sensitivity analysis of the new method. In this reference, many important facts have been established during the study as follows:

- Artificial neural networks can be successfully used to recognize the location of faults in distribution cable circuits with different interconnections and topology where the conventional fault locating techniques do not yield satisfactory results. Simultaneous measurements of V and I at various circuit points during the fault condition obtain the information about the fault location. This information can be processed using a ANN.
- Neural networks have to be trained to recognize the faults. The training cases can be generated using short circuit studies, EMTP or actual field data if available.

- When properly trained the ANN can recognize the faults even when V and I data contain the noise of up to 10%.

- The ANN can generalize its knowledge of the faults and in many instances give the indication of the fault point within a cable section.

- The results of the ANN calculations can be displayed using 3-D charts that provide immediate and simple indication of the fault location even for untrained personnel.

- The ANN method of fault location is generally applicable to other circuits such as overhead lines. The main drawback of this method is that a large number of measurements (at all ends, at location of loads and junctions) have to be implemented.

In this section four basic principles in fault location techniques have been outlined including; (i) on-line or off-line methods; (ii) high or low frequency techniques (iii)

voltage level and (iv) terminal and tracer methods. Some existing methods and their abilities and drawbacks are then explained. The following chapters deal with a new method in fault location which is based on off-line, high frequency, 11 kV system and terminal categories. In this respect, some important practical factors are considered and the proposed method presented is under a much wider range of system and fault conditions than has hitherto been possible.

CHAPTER 3

NEW CABLE MODEL

3.1- Introduction

The EMTP programme includes dedicated support routines (cable constants) for calculating an electrical representation of a cable system in terms of a series impedance matrix Z and a shunt admittance matrix Y, based on cable data defined by geometry and material properties. Z and Y are the basic inputs of the various cable models which are used in the EMTP. This chapter presents the calculations of Z and Y in the EMTP for single-core, three-phase and multi-core pipe type cables, by considering the various assumptions and approximations. Then a new cable model using conformal mapping (CM) is introduced as a more accurate model. Also, a comparison is done between the EMTP and CM models in for a typical distribution network.

3.2- Cable Model in EMTP

There are a vast variety of cables in the power distribution system. Thus it is not possible to develop one generic computer program which can calculate the parameters of all types. The three commonly employed cable models, namely the coaxial single-core, three–phase and multi-core pipe type cables have been modelled by various researchers using the EMTP by making the following assumptions:

I) The displacement current is neglected.
II) The excitation current is assumed to flow in a filament.
III) The length of the shell as well as of the filament is infinite and both follow a straight line, being parallel to each other.
IV) The return of the current in the filament is assumed to flow in the cylindrical shell.
V) μ is constant.

3.2.1- Single-phase cable

This type of cable (Fig.(13)) consists of tubular conductors inside a metallic sheath and armour with insulation between them. In this model, series impedances and shunt admittances per unit length are represented by the following equations and appendix-1 deals with these equations in detail.

$$-\begin{bmatrix} \frac{dv_{core}}{dx} \\ \frac{dv_{sheath}}{dx} \\ \frac{dv_{armour}}{dx} \end{bmatrix} = \begin{bmatrix} z_{cc} & z_{cs} & z_{ca} \\ z_{sc} & z_{ss} & z_{sa} \\ z_{ac} & z_{as} & z_{aa} \end{bmatrix} \times \begin{bmatrix} I_{core} \\ I_{sheath} \\ I_{armour} \end{bmatrix} \qquad (3\text{-}1)$$

Where v_{core} = voltage from core to ground

v_{sheath} = voltage from sheath to ground

v_{armour} = voltage from Armour to ground

$I_{core} = I_1$

$I_{sheath} = I_2 - I_1$

$I_{armour} = I_3 - I_2$

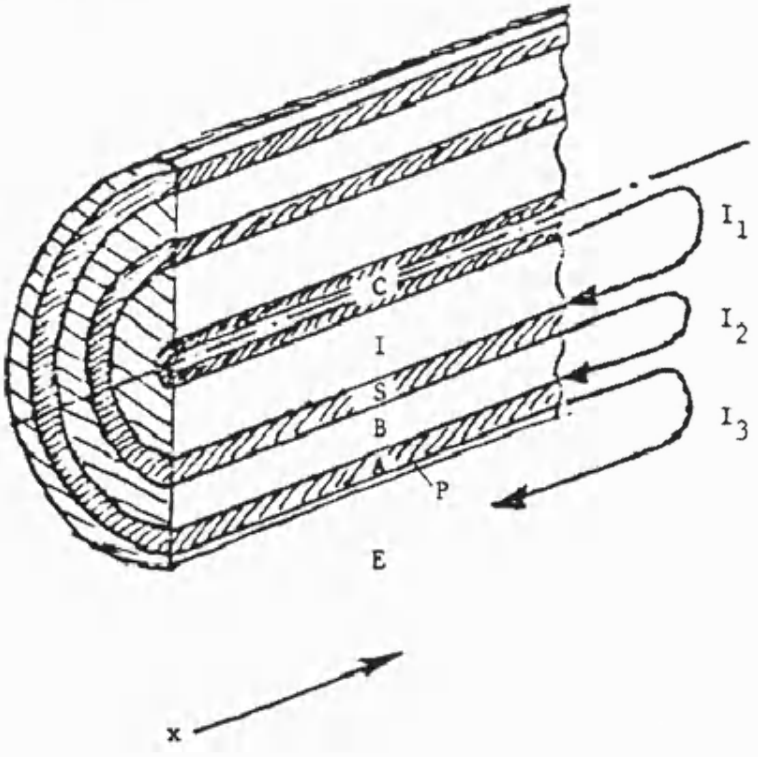

Fig.13- Single core self-contained cable (C=core, I=paper insulation, S=metallic sheath, B=bedding, A=armour, p=plastic sheath)

Appendix-1 shows that:

$$z_{insulation} = \frac{1}{2\pi} j\omega\mu_o\mu_r \ln\left(\frac{r}{q}\right) \quad (3\text{-}2)$$

$\mu_{r=}$ permeability of insulation

$\mu_o = 2*10^{-4}$ H/Km

r=outside radius of insulation (or tube)

q=inside radius of insulation (or tube)

$$z_{tube-in} = \frac{\rho m}{2\pi q D}[I_O(mq)*k_1(mr)+k_o(mq)*I_1(mr)] \quad (3\text{-}3)$$

$$z_{tube-out} = \frac{\rho m}{2\pi r D}[I_O(mr)*k_1(mq)+k_o(mr)*I_1(mq)] \quad (3\text{-}4)$$

$$z_{tube-mutual} = \frac{\rho}{2\pi r q D} \quad (3\text{-}5)$$

With $D=I_1(mr)*k_1(mq)-I_1(mq)*k_1(mr)$ (3-6)

$$m = \sqrt{j\omega\mu/\rho} \quad (3\text{-}7)$$

Where the I_O,I_1,K_0 and K_1 are Bessel functions.

For the current changes along the cable:

$$-\begin{bmatrix} \frac{-dI_{core}}{dx} \\ \frac{dI_{sheath}}{dx} \\ \frac{dI_{armour}}{dx} \end{bmatrix} = \begin{bmatrix} Y_1 & -Y_1 & 0 \\ -Y_1 & Y_1+Y_2 & -Y_2 \\ 0 & -Y_2 & Y_2+Y_3 \end{bmatrix} * \begin{bmatrix} v_{core} \\ v_{sheath} \\ v_{armour} \end{bmatrix} \quad (3\text{-}8)$$

With $Y_i=G_i+j\omega C_i = j\,2\pi\omega\varepsilon_0\varepsilon_r/\ln(r/q)$ (3-9)

$$\varepsilon_r = 2.5 + \frac{0.94}{\left(1+j\omega 6*10^{-9}\right)^{315}} = \varepsilon' - j\varepsilon'' \quad (3\text{-}10)$$

The support routine cable constants now assume $\varepsilon''=0$, ε' being constant. The dielectric losses are of little importance for the attenuation [3], and using a constant ε' with $\varepsilon''=0$ should therefore give acceptable results in most cases.

3.2.2- Three-phase cable

With minor changes in the aforementioned formulas, a parallel single-core cable model can be effected for three single-core cables (Fig.(14)); the coupling terms among of the three phases and the mutual impedances between the three outer loops have to be taken into account. The symmetrical $[Z_{phase}]$ in Eq.(3-1) will be :

$$[Z_{phase}] = \begin{bmatrix} [Z_{self-a}] & [Z_{mutual-a-b}] & [Z_{mutual-a-c}] \\ [Z_{mutual-a-b}] & [Z_{self-b}] & [Z_{mutual-b-c}] \\ [Z_{mutual-a-c}] & [Z_{mutual-b-c}] & [Z_{self-c}] \end{bmatrix} \tag{3-11}$$

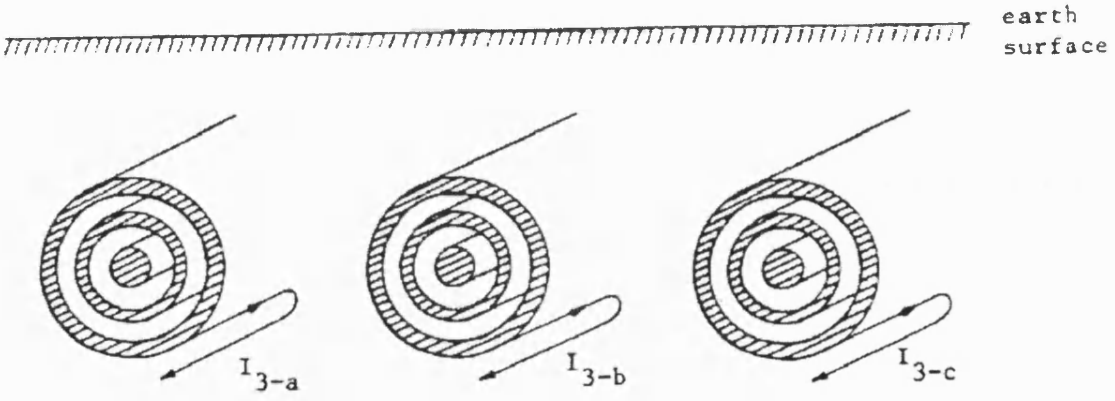

Fig.14- Three single-core cables

As :
$$[Z_{mutual-a-b}] = \begin{bmatrix} Z_{ab} & Z_{ab} & Z_{ab} \\ Z_{ab} & Z_{ab} & Z_{ab} \\ Z_{ab} & Z_{ab} & Z_{ab} \end{bmatrix} \tag{3-12}$$

Z_{ab} is the mutual impedance between cables a and b. There is no coupling amongst the three phases in the case of shunt admittances. Thus, the shunt admittance matrix for the three-phase system is simply given as

$$[y_{phase}] = \begin{bmatrix} [y_a] & 0 & 0 \\ 0 & [y_b] & 0 \\ 0 & 0 & [y_c] \end{bmatrix} \tag{3-13}$$

Where $[y_a]$ is the 3*3 matrix of Eq.(3-8) for phase a, and so on. It should be noted that in a parallel status, if the sheath and armours are ungrounded and open-circuited , then the full current will flow in the outer loop for each cable and this will produce maximum induced voltages in the neighbouring cable. However, if both the sheath and armour are grounded at both ends, then the induced voltage would be small. For the practical example of a 500 kV AC submarine cable at 60 Hz, 14% of the core current would return through the sheath, 87.8% through armour and only 5.6% through the outermost loop (the total of three mentioned value are more than 100 because they have a minor phase difference due to different R and X [3]), with ground or sea water return. If the cable is buried in infinite or semi-infinite earth, in addition to core, sheath and armour, earth also has to be taken into account. See Fig(15).

The Wedepohl's approximate formulas for semi-infinite earth are:

$$z_{earth} = \frac{\rho m^2}{2\pi}\{\ln(\delta mR/2) + 0.5 - 4/3 \times mh\} \tag{3-14}$$

$$z_{mutual} = \frac{\rho m^2}{2\pi}\{\ln(\delta md/2) + 0.5 - 2/3 * ml\} \tag{3-15}$$

With δ=Euler's constant

l=sum of the depths of burial of the two conductors

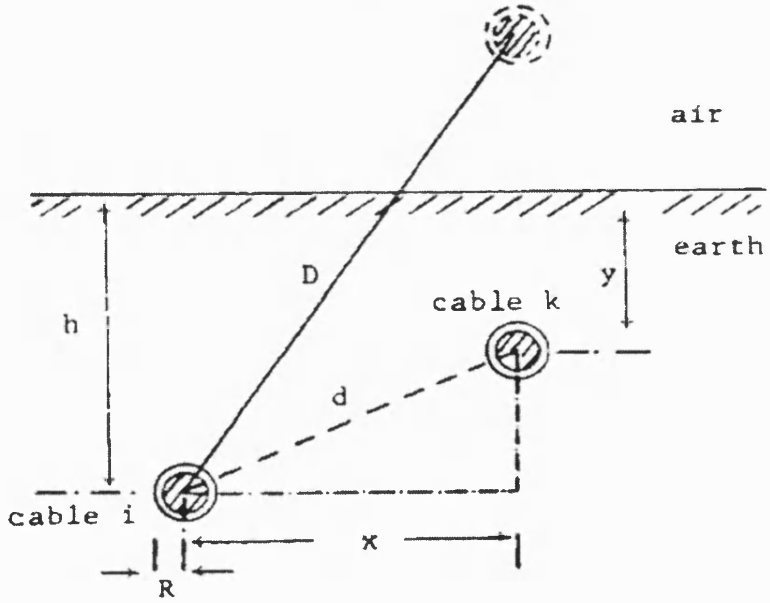

Fig.15- Geometric configuration of two cables

And also the depth of penetration in the earth is:

$$d_{earth} = \frac{\sqrt{2}}{|m|} = 503 * \sqrt{\frac{\rho_{earth}(\Omega m)}{\mu_r f(Hz)}} \tag{3-16}$$

This becomes much smaller than the depth of burial and the earth impedances will be:

$$z_{earth} = \frac{\rho m}{2\pi R_i} * \frac{k_0(mR_i)}{k_1(mR_i)} \tag{3-17}$$

$$z_{mutual} = \frac{\rho k_0(md)}{2\pi R_i R_k k_1(mR_i) k_1(mR_k)} \tag{3-18}$$

3.2.3- Multi-Conductor Pipe-Type Cable

Compared to the geometry of the single-core cable, the geometry of the pipe-type cable is more complex Fig.(16) for two reasons:

a) The single-core cables inside the pipe are not concentric with respect to the pipe.
b) The steel pipe is magnetic and subject to current-dependent saturation effects.

Depending on the thickness of pipe, the two states can be evaluated as follows:

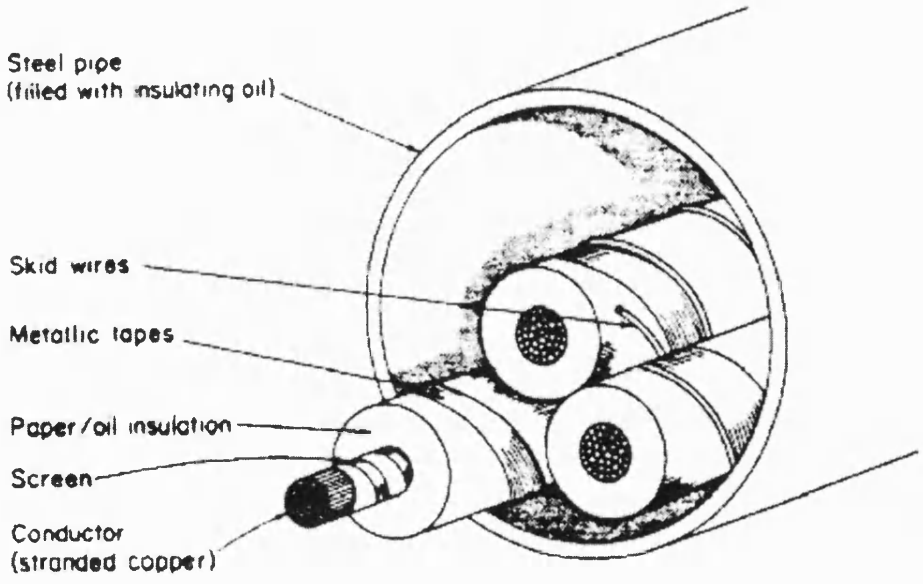

Fig.16- Pipe-type oil-filled cable

I) - Infinite pipe thickness

If the depth of penetration is less than the pipe thickness, then no voltage will be induced on the outside of the pipe and consequently, the loop current pipe/earth return will be zero. The configuration is the same as that for three single-core cables in fig(14), except that this pipe is the return path instead of earth (fig.(17)).

The self impedance of the loop between the armour (skid wire) and the pipe consists of three terms as in Eq.(A1-5). The first term $z_{armour\text{-}out}$ is the same as Eq.(3-4), but the second term becomes:

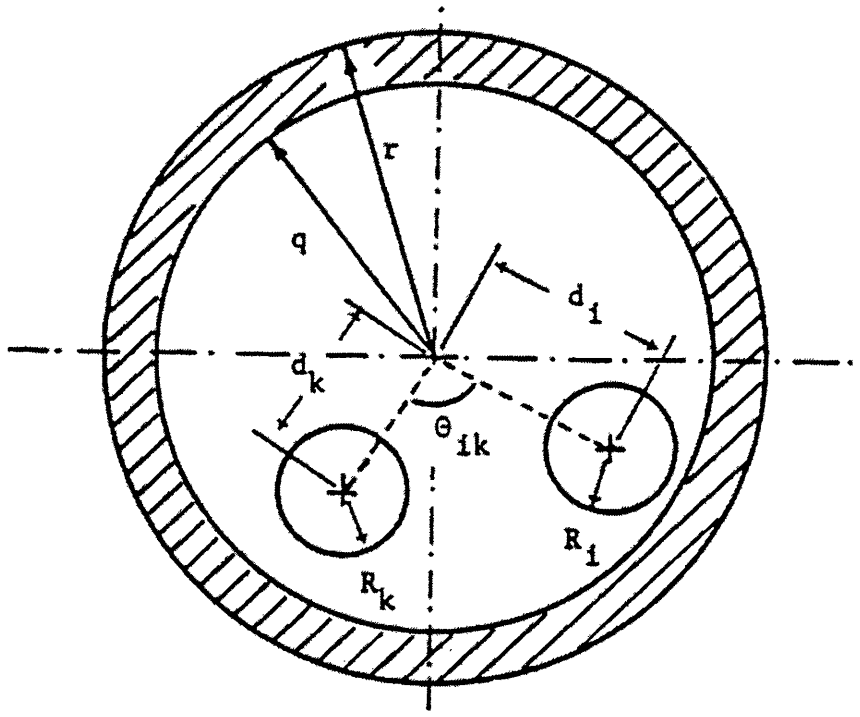

Fig.17- Pipe-type multi single core cables

$$z_{insulation} = \frac{j\omega\mu_0}{2\pi} \ln\left[\frac{q}{R_i} * \left(1 - \left(\frac{d_i}{q}\right)^2\right)\right] \qquad (3\text{-}19)$$

And the third term is equal to:

$$z_{pipe-in} = \frac{j\omega\mu_0\mu_r}{2\pi}\left\{\frac{k_0(mq)}{mqk_1(mq)} + 2 * \sum_{n=1}^{\infty}\left(\frac{d_i}{q}\right)^{2n} \frac{k_n(mq)}{n\mu_r k_n(mq) - mqk'_n(mq)}\right\} \qquad (3\text{-}20)$$

m is from Eq.(3-7), and $\mu = \mu_o * \mu_r$=permeability of the pipe,

k_i=modified Bessel function of the second kind of order i

k_i'=derivative of k_i

For the concentric case with $d_i=0$ and with reference to Eq.(3-7), Eq.(3-20) becomes identical to Eq.(3-17) (it should be noted that $q=R_i$.).

The mutual impedance Z_{ab} (mentioned in Eq.(3-12)) between the two outermost loops formed by armour and pipe becomes eq.(3-21).

The magnetic properties of the steel pipe are taken into account by using the correct values for the relative permeability μ_r in Eq.(3-17). However μ_r depends on current because of saturation effects. To model saturation effects accurately is not simple because even at one frequency, the permeability would not remain constant over one cycle. The admittances for pipe-type cables according to Fig.(16) configuration become those shown by Eq.(3-22).

$$z_{mutual} = \frac{j\omega\mu_0}{2\pi}\left\{\begin{array}{l} \ln\dfrac{q}{\sqrt{d_i^2 + d_k^2 - 2d_i d_k \cos\Theta_{ik}}} + \mu_r \dfrac{k_0(mq)}{mqk_1(mq)} \\ +2*\sum_{n=1}^{\infty}\left(\dfrac{d_i.d_k}{q^2}\right)^n \cos(n\Theta_{ik})[2\mu_r \dfrac{k_n(mq)}{n\mu_r k_n(mq) - mqk'_n(mq)} - \dfrac{1}{n}] \end{array}\right\} \quad (3\text{-}21)$$

$$[y_{phase}] = j\omega[P_{phase}]^{-1} \quad (3\text{-}22)$$

Where $[P_{phase}]$ is a potential coefficient matrix given as:

$$[p_{phase}] = \begin{bmatrix} [p_a] & 0 & 0 \\ 0 & [p_b] & 0 \\ 0 & 0 & [p_c] \end{bmatrix} + \begin{bmatrix} [p_{aa}] & [p_{ab}] & [p_{ac}] \\ [p_{ab}] & [p_{bb}] & [p_{bc}] \\ [p_{ac}] & [p_{bc}] & [p_{cc}] \end{bmatrix} \quad (3\text{-}23)$$

$$[P_a] = \begin{bmatrix} p_1+p_2+p_3 & p_2+p_3 & p_3 \\ p_2+p_3 & p_2+p_3 & p_3 \\ p_3 & p_3 & p_3 \end{bmatrix} \quad (3\text{-}24)$$

$p_i = \frac{1}{c_i}$ and c_i is the same as Eq.(3-9) with G=0, and also $[p_{ii}]$ and $[p_{ik}]$ in the second term is a 3*3 matrix with 9 equal elements given as:

$$p_{ii} = \frac{1}{2\pi\varepsilon_0\varepsilon_r}\ln\left[\frac{q}{R_i}*\left(1-\left(\frac{d_i}{q}\right)^2\right)\right] \tag{3-25}$$

$$p_{ik} = \frac{1}{2\pi\varepsilon_0\varepsilon_r}\ln\left[\frac{q}{\sqrt{d_i^2 - d_k^2 - 2d_i d_k\cos\theta_{ik}}}\right] \tag{3-26}$$

The admittance matrix is then found by inverting $[p_{phase}]$, as has been shown in Eq.(3-22).

In the modelling of a three-phase cable or pipe type cable, the main problem arises by virtue of the fact that the three conductors are positioned off centre within the armour or pipe and it is principally due to this that some estimations and approximations are made in the EMTP model; a direct consequence of the latter is that the mathematical representation of the impedance and admittance in a pipe type cable in the EMTP software includes infinite series formulations of the flux linkage and the proximity effects; this of course is based on some approximations in the configuration of the cable.

II) - Finite pipe thickness with earth return

At lower frequencies, there is mutual coupling between the inner and outer surfaces of the pipe. The induced voltage on the outer surface will then produce a circulating current through the pipe and earth return. This extra loop must be added to the loop impedance matrix, but, because the current research is processed at a higher frequency, the work to date has not dealt with the aforementioned state.

3.3- Modal Parameters

It is obvious that the solution of M-phase cable equations becomes simpler if the M coupled equations can be transformed to M decoupled equations. These decoupled equations can then be solved as if they were single-phase equations. For balanced cables, this transformation is achieved with Eq(A2-1) which is shown in appendix-2.

However, many cables are with ungrounded sheath or armour and thus they are unbalanced cables. Fortunately, the matrices of an unbalanced cable can be diagonalized as well, with transformations to modal parameters derived from eigenvalue/eigenvector theory. To explain the theory, the two system of equations (3-1) & (3-8) can be used as a starting point:

$$-[\frac{dV_{phase}}{dx}] = [Z_{phase}].[I_{phase}] \tag{3-27}$$

$$-[\frac{dI_{phase}}{dx}] = [Y_{phase}].[V_{phase}] \tag{3-28}$$

Where $[Y_{phase}]=j\omega[C_{phase}]$ if shunt conductances are ignored, as is customarily done.

Appendix-2 depicts that with eigenvalue theory, it becomes possible to transform the two coupled Eqs (3-27) & (3-28) from phase quantities to modal quantities in such a manner that the equations become decoupled, or in terms of matrix algebra, that the associated matrices become diagonal e.g., for the voltage:

$$[\frac{d^2V_{mode}}{dx^2}] = \begin{bmatrix} \lambda_1 & 0 & 0 \\ 0 & \lambda_2 & 0 \\ 0 & 0 & \lambda_3 \end{bmatrix} [V_{mode}] = [\Lambda][V_{mode}] \tag{3-29}$$

And for current:

$$[\frac{d^2I_{mode}}{dx^2}] = [\Lambda][I_{mode}] \tag{3-30}$$

With the same diagonal matrix ([Λ]) as in Eq. (3-29).

With the decoupled equations of (3-29) & (3-30) in modal quantities, each mode can be analyzed as if it were a single-phase cable. Comparing the modal equation:

$$-\frac{d^2V_{mode-k}}{dx^2} = \lambda_{.k} V_{mode-k} \tag{3-31}$$

With the well-known equation of a single-phase line,

$$-\frac{d^2V}{dx^2} = \gamma^2 V \tag{3-32}$$

Where the propagation constant γ defined in Eq.(3-33)

$$\gamma = \sqrt{(R + j\omega L)(G + j\omega C)} \qquad (3\text{-}33)$$

This shows that the modal propagation constant $\gamma_{mode\text{-}k}$ is the square root of the eigenvalue:

$$\gamma_{mode\text{-}k}=\alpha_k+j\beta_k=\sqrt{\lambda_k} \qquad (3\text{-}34)$$

Where α_k = attenuation constant of mode k in Np/km, or 20log(exp(α_k)) in db/km,

β_k = phase constant of mode k in rad/km.

The phase velocity of mode k is: $v_k=\omega/\beta_k$ (3-35)

And the wave length is: wave length$=2\pi/\beta_k$ (3-36)

While the modal propagation constant is always uniquely defined, the modal series impedance and shunt admittance as well as the modal characteristic impedance are not, because of the ambiguity in the eigenvectors. Thus, the modal impedances and admittances only make sense if they are specified, together with the eigenvectors used in their calculations. To find them, Eq.(3-27) is transformed to modal quantities as:

$$[\frac{dV_{mode}}{dx}] = -[T_v]^{-1}[Z_{phase}][T_i][I_{mode}] \qquad (3\text{-}37)$$

Where T_v and T_i are matrix transformations for voltage and current, respectively.

The triple matrix product in Eq. (3-37) is diagonal and the modal series impedances are diagonal elements of the matrix given as:

$$[Z_{mode}] = [T_v]^{-1}[Z_{phase}][T_i] \qquad (3\text{-}38)$$

Similarly, Eq.(3-28) can be transformed into modal quantities and the modal shunt admittances are then the diagonal elements of the matrix:

$$[Y_{mode}] = [T_i]^{-1}[Y_{phase}][T_v] \qquad (3\text{-}39)$$

Finally, the modal characteristic impedance can be found from the scalar equation:

$$Z_{char-\mathrm{mod}-k} = \frac{\sqrt{Z_{\mathrm{mod}\,e-k}}}{\sqrt{Y_{\mathrm{mod}\,e-k}}} \tag{3-40}$$

All the aforementioned parameters are calculated by the LCC support routine in the EMTP software and the new proposed model presented herein is based on these parameters.

3.4- The Theory of Surge Propagation to Find Z and Y

The key to analyzing surge propagation for any type of configuration is the determination of the propagation factor. For an infinitely long cable, the sinusoidal components of the wave (after travelling a distance x metres) can be described by Eq. (3-41) as:

$$V(z,\omega)=V(0,\omega)e^{-\gamma(\omega)x} \tag{3-41}$$

Where γ is the propagation factor as has been shown in Eq.(3-33); R and L are both frequency dependent. The geometry for any off-centred conductor in a pipe is shown in Fig.(18). It should be noted that point P(r,φ) is related to such cases that the depth of penetration of the pipe is more than the thickness of pipe.

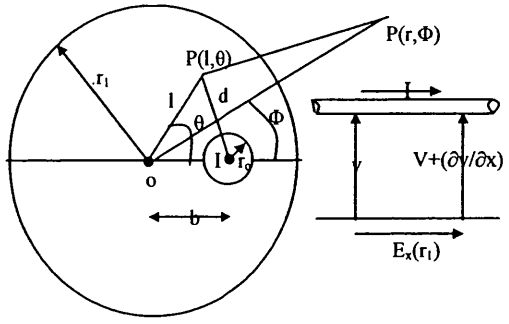

Fig.18- Off-centred conductor in a pipe

The incremental R and L can be determined by calculating the incremental axial voltage drop by applying Faraday's law, and is shown in Eq. (3-42):

$$\frac{\partial V}{\partial x} = -I(R + j\omega L) = -\frac{d\lambda}{dt} + E_x(r_1) \tag{3-42}$$

Since the capacitance is considered ideal, it is related to inductance at infinite frequency by:

$$C = \frac{\mu_0 . \varepsilon_0}{L} \tag{3-43}$$

Thus the propagation factor for any cable can be determined from the flux linkage and the axial electric field at the pipe wall. With a knowledge of the current distribution in the pipe and the vector potential between the conductor and the pipe, the propagation factor can be determined. The current density in the pipe wall is:[38]

$$J_x(r,\phi) = -\sum_{n=0}^{\infty} C_n K_n(m.r).\cos(n\phi) \tag{3-44}$$

and the vector potential within the pipe($l \leq r_1$ in Fig. (18)) is:

$$A_i(l,\theta) = \frac{\mu_0 . I}{4\pi} \ln(l^2 + b^2 - 2lb\cos\theta) + \frac{\mu_0 . L_0}{m}([r_1 \ln(r_1) K_1(mr_1)] - [\frac{1}{m} K_0(mr_1)]) - \frac{\mu_0 r_1}{2m} \sum_{n=1}^{\infty} L_n \frac{1}{n} (\frac{l}{r_1})^n \cos(n\theta) \tag{3-45}$$

Where m is as shown in Eq.(3-7), and L_n and C_n are as follows:

$$L_n = \frac{2n\mu_r C_n K_n(mr_1)}{mr_1} - \frac{mI}{\pi r_1} (\frac{b}{r_1})^n \tag{3-46}$$

$$C_n = \frac{\mathrm{Im}^2}{\pi[n\mu_r K_n(mr_1) - r_1 K_n'(mr_1)}} \tag{3-47}$$

K_n is a Bessel function of the second kind.

First, the flux linkage is determined from the following equation:

$$\frac{d\lambda}{dt} = j\omega \oint A.dl = j\omega[A_i(r_1,\theta) - A_i(b,\theta)] \tag{3-48}$$

Next, the axial electric field at the pipe wall boundary can be determined from the current density as follows:

$$E_x(r_1,\phi) = \frac{J_x(r_1,\phi)}{\sigma} \tag{3-49}$$

Substituting Eqs.(3-44),(3-45),(3-48) &(3-49) into Eq. (3-42) and eliminating the current I, the impedance for a general case becomes:

$$R + j\omega L = \frac{1}{2\pi}\sqrt{\frac{j\omega\mu}{\sigma}}\cdot\frac{-K_0(mr_1)}{r_1 K_0'(mr_1)} + \frac{1}{\sigma}\sum_{n=1}^{\infty}(\frac{b}{r_1})^n C_n K_n(mr_1) + \frac{j\omega\mu_0}{2\pi}\ln[\frac{r_1^2 - b^2}{r_1 r_0}] \quad (3\text{-}50)$$

By substituting Eqs. (3-47) and (3-7) into Eq. (3-50), Eqs.(3-20) and (3-50) become identical (r_1 in Eq. (3-50) and q in Eq. (3-20) are inside the radius of the pipe and they are equal).

Most pipe-type cable applications have more than one conductor in the pipe (three phase system) and most three-phase cables have an armour that acts similar to a pipe. To compute the propagation factor for a multi-conductor system, it is convenient to determine an impedance matrix. The self-impedance term is known from the previous analysis. The mutual impedance terms are derived in a similar manner and the two conductor system in Fig.(19) is analysed.

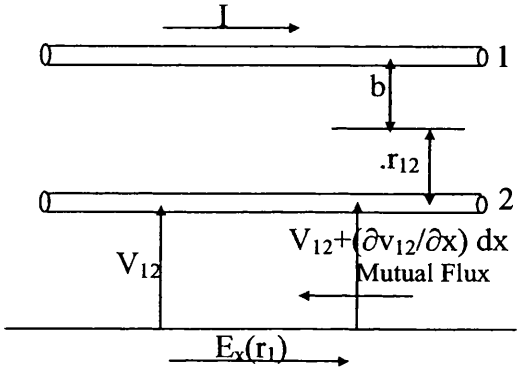

Fig.19- Two conductor system

If conductor 1 is carrying a current that is returning in the pipe, the mutual flux linkage with conductor 2 is in the region between conductor 2 and the pipe. The flux linkage becomes:

$$\frac{d\lambda_{2(1)}}{dt} = j\omega\oint A_{2(1)}.dl_2 = j\omega[A_1(r_1,\theta) - A_1(r_{12},\theta_{12})] \quad (3\text{-}51)$$

Where θ_{12} is as shown in Fig. (17).

By substituting Eqs.(3-44) & (3-47) into Eq. (3-49), Eq. (3-45) into Eq. (3-51) and Eqs. (3-49) & (3-51) into Eq. (3-42) and eliminating current I, the mutual impedance shown in Eq. (3-21) is extracted.

As is apparent from Eq.(3-42) that the voltage drop comprises of two terms including the flux linkage and the axial electric field. Because of eccentric conductors and the

pipe, the results are very complex. In this report, eccentric conductors are transformed into concentric conductors by using CM and the modifications are shown in two different states. The first state is concerned with the modification of the flux linkage based on concentric conductors and in the second state, both of terms of Eq. (3-42) are simplified and modified.

With regard to the third term of Eq. (3-50) that is equal to jωL, the capacitance for the general configuration is determined from Eq.(3-43) as follows:

For single conductor in pipe (Fig. (18)) this is:

$$C = \frac{2\pi\varepsilon_0}{\ln[\frac{r_1^2 - b^2}{r_1 r_0}]} \tag{3-52}$$

And for multi-conductor (Fig. (17)) it is:

$$C = \frac{2\pi\varepsilon_0}{\left\{\ln\frac{q}{\sqrt{d_i^2 + d_k^2 - 2d_i d_k \cos\Theta_{ik}}} - 2*\sum_{n=1}^{\infty}\left(\frac{d_i.d_k}{q^2}\right)^n \cos(n\Theta_{ik})\frac{1}{n}\right\}} \tag{3-53}$$

The main subject that has been dealt with in the first state is to deduce C and L. Eq.(3-52) and the third term of Eq.(3-50) are modified in a single conductor pipe type cable as well as Eq.(3-53) and the first & fourth terms of Eq.(3-21) are modified in a multi-conductor pipe type cable by transforming eccentric circles into concentric circles using CM. In the second state of the CM method, transformation into concentric circles allows the usage of Eqs. (3-3) & (3-5) instead of rather complex Eqs.(3-20) & (3-21), thus R, C and L are obtained.

3.5- The New Cable Model Based on Conformal Mapping

Several cable models have been implemented in the commonly available EMTP which can accurately represent the frequency dependence of cable systems. All of these models require the same type of input parameters, namely the series impedance matrix Z and the shunt admittance matrix Y. In the single-core cable, all conductors (core, sheath and armour) are concentric and related equations are simple and accurate, but, in

the modelling of a three-phase cable or pipe type cable, the main problem arises by virtue of the fact that the three conductors are positioned off centre within the armour or pipe and it is principally due to this that some estimations and approximations are made in the EMTP model; a direct consequence of the latter is that the mathematical representation of the impedance and admittance in a pipe type cable in the EMTP software includes infinite series formulations of the flux linkage and the proximity effects; this of course is based on some approximations in the configuration of cable.

With regard to CM's ability in transforming an isotropic region into a symmetrical and simpler region, the employed equations for Z and Y within the EMTP are simplified and they become more accurate. In the first instance, a single-phase pipe type cable is analysed followed by a multi-conductor cable.

3.5.1- CM Method for a Single-Phase Pipe Type Cable

In order to modify Z and Y, in this section Eqs. (3-19,3-20,3-25) are modified in a single conductor pipe type cable by transforming eccentric circles into concentric circle by using the CM method. It should be mentioned that in ref. [39], for a limited range of eccentric conductor locations, this transformation has been achieved by CM. However, firstly, only a single conductor pipe type cable has been considered and secondly, the depth of penetration of the pipe and the thickness of the outer layer of conductor (e.g. armour) have been neglected and thirdly, the employed conformal transformation has some limitations, as the distance between the centre of two eccentric circles depends on the radii of the circles. The transformation employed in ref. [39] is: $W = \frac{Z-a}{Z+a}$

In this research, one of the objectives is to investigate a conformal transformation that is independent of cable and pipe specifications. Moreover, a three phase pipe type cable and the depth of penetration of the pipe and the thickness of the outer layer of the conductor have been considered. This is essentially to avoid any complexities and approximations (as in other methods) in determining Z and Y. The following sections explain in detail how this is achieved for both single and three-phase cables.

As a first step, a conformal transformation is found that transfers eccentric circles into concentric circles. The first transformation is: $Z = \frac{Z_1}{R_1}$ that transforms Fig. (20) into Fig. (21). Thus:

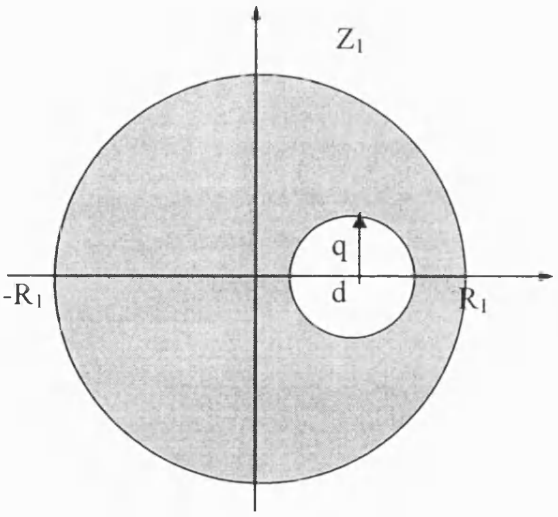

Fig.20- Pipe type single core cable

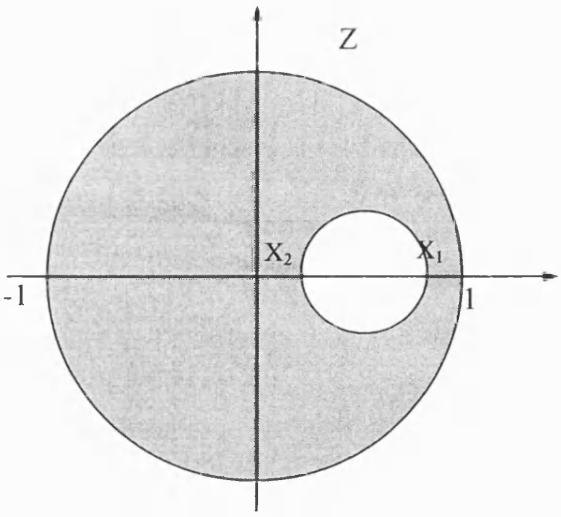

Fig.21- pipe type (unit radius) single core

$$X_1 = \frac{d+q}{R_1} \quad \& \quad X_2 = \frac{d-q}{R_1} \tag{3-54}$$

The second transformation is: $W_1 = \frac{Z-a}{aZ-1}$; this transforms Fig. (21) into the Fig. (22).

Also the transformation $W_2=\ln W_1$ transforms Fig.(22) to Fig.(23).

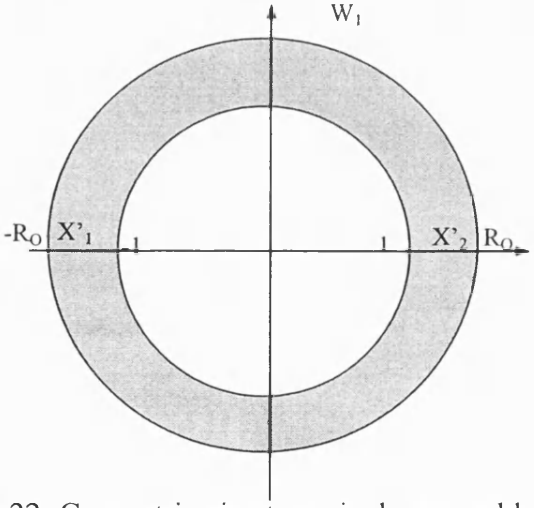

Fig.22- Concentric pipe type single core cable

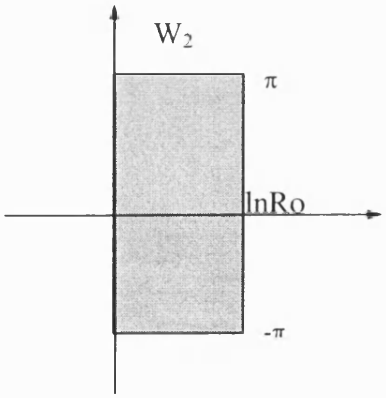

Fig.23- Two parallel lines

As Figs. (21) & (22) show the transformation $W_1 = \frac{Z-a}{aZ-1}$ transforms x_1 to $-R_o$ and x_2 to R_o ; Thus it follows:

$$R_o = \frac{X_2 - a}{aX_2 - 1} \text{ and } -R_o = \frac{X_1 - a}{aX_1 - 1}$$

And hence:

$$a = \frac{1 + X_1 X_2 + \sqrt{(1 - X_1^2)(1 - X_2^2)}}{X_1 + X_2} \tag{3-55}$$

$$R_o = \frac{1 - X_1 X_2 + \sqrt{(1 - X_1^2)(1 - X_2^2)}}{X_1 - X_2} \tag{3-56}$$

Also from Fig. (23) that shows a cross section of two parallel plate, the capacitance per unit length C is:

$$C_{equal} = \frac{\varepsilon_o . A}{D} = \frac{2\pi\varepsilon_o}{\ln R_o} \ (\frac{F}{m}) \tag{3-57}$$

Thus: $$Z_{insulation} = \frac{j\omega\mu_0}{2\pi} \ln R_0 \tag{3-58}$$

Therefore, Eq. (3-52) and the third term of Eq. (3-50) can replaced by Eq. (3-57) and Eq. (3-58), respectively. However, since the core in the pipe is normally insulated as shown in Fig. (24), the permittivity between circle C1 and C2 is $\varepsilon_0\varepsilon_r$ and between circle C2 and C3 is ε_0. In this respect, four aforementioned equations namely the third term of Eq.(3-50) and Eqs(3-52,57,58), change.

With regard to Fig. (24), the capacitance between circles C_1 & C_3 is deduced from Eq. (3-57) and the capacitance between circles C_1 & C_2 becomes:

$$C_{1\_2} = \frac{2\pi\varepsilon_o}{\ln \frac{r}{q}} \tag{3-59}$$

Since r is the radius of circle C2 and q is the radius of circle C1, the capacitance between circles C_2 & C_3 becomes:

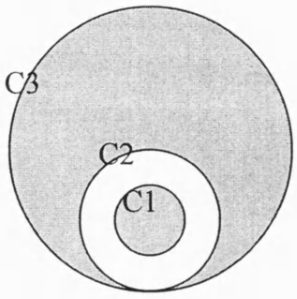

Fig.24- Three eccentric circle

$$C_{2\_3} = \frac{2\pi\varepsilon_o}{\ln \frac{R_0 q}{r}} \tag{3-60}$$

The radius of circle C_3 is unit (equal to one). From Eqs. (3-43) & (3-60), the $Z_{insulation}$ and the capacitance for a single-phase pipe type cable become:

$$Z_{insulation} = \frac{j\omega\mu_0\mu_r \ln\frac{r}{q}}{2\pi} + \frac{j\omega\mu_0 \ln\frac{R_o q}{r}}{2\pi} \quad (3\text{-}61)$$

$$C = \frac{2\pi.\varepsilon_o.\varepsilon_r}{\ln[(\frac{r}{q}).(\frac{R_o q}{r})^{\varepsilon_r}]} \quad (3\text{-}62)$$

In EMTP model these two equations become:

$$Z_{insulation} = \frac{j\omega\mu_0\mu_r \ln\frac{r}{q}}{2\pi} + \frac{j\omega\mu_0 \ln[\frac{r_1^2 - b^2}{r_1 r}]}{2\pi} \quad (3\text{-}63)$$

$$C = \frac{2\pi.\varepsilon_o.\varepsilon_r}{\ln[(\frac{r}{q}).[\frac{r_1^2 - b^2}{r_1 r}]^{\varepsilon_r}]} \quad (3\text{-}64)$$

In the second state associated with the new cable model and with regard to the concentric circles, Eqs.(3-63), (3-64) and (3-20) are replaced by Eqs.(3-61), (3-62) and (3-4) respectively, but it should be noted that the parameters in Eq. (3-4) are changed, based on the results of the transformation. If the depth of penetration of the pipe and the thickness of the outside of the conductor is taken into account, the aforementioned transformation transforms Fig.(25) into Fig.(26). As it can be observed from these figures, the inside of the pipe is transformed into outside of the pipe ($R \rightarrow r$, $R_1 \rightarrow 1$, $X_2 \rightarrow R_0$ and $X_4 \rightarrow rr$) and hence $Z_{pipe\text{-}in}$ is obtained from Eq. (3-4) by replacing r (the outside radius of pipe) to N*1 (N is scale factor) and q (the inside radius of pipe) to N*r. Fig.(19) shows the r. Thus $Z_{pipe\text{-}in}$ instead of Eq.(3-20) becomes:

$$z_{pipe-in} = \frac{\rho m}{2\pi N D}\left[I_O(mN) * k_1(mNr) + k_o(mN) * I_1(mNr)\right] \quad (3\text{-}65)$$

Where D is: $D = I_1(mN)*k_1(mNr) - I_1(mNr)*k_1(mN)$ (3-66)

Also, because the inner conductor is transferred into an outer conductor, thus $Z_{conductor\text{-}out}$ is obtained from the Eq.(3-3) by replacing q (outside radius of conductor) to $N*R_0$ and r

(inside radius of conductor) to N*rr; rr has been shown in Fig.(19). Therefore $Z_{conductor-out}$ becomes:

$$z_{conductor-out} = \frac{\rho m}{2\pi N.R_0 D}\left[I_O(mN.R_0) * k_1(mN.rr) + k_o(mN.R_0) * I_1(mN.rr)\right] \qquad (3\text{-}67)$$

Where D is: $D = I_1(m*N*rr)*k_1(m*N*R_0) - I_1(m*N*R_0)*k_1(m*N*rr)$ (3-68)

It should be noted that when Eq.(3-67) is used, the radii obtained via CM have to be used in Eq.(3-5). Also the scale factor N is determined as shown in Eq. (3-72) and subsequent equations.

Although we can see from Fig.(26) that all circles are not completely concentric, since the depth of penetration in a pipe at power frequency is less than 3mm, and the thickness of the armour or sheath is much smaller than its outer radius, Fig.(26) is a good approximation of four concentric circles and is more accurate than neglecting the effect of the depth of penetration in a pipe and the thickness of the armour (or sheath).

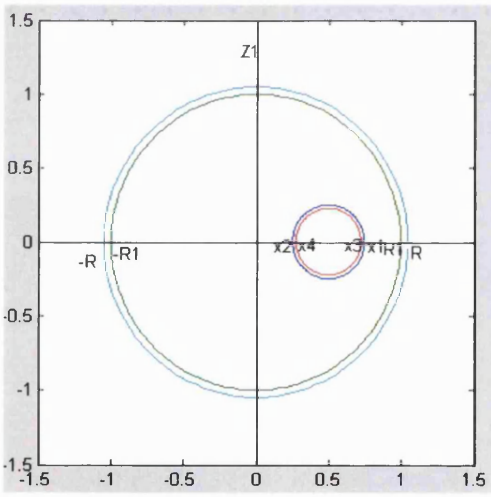

Fig.25- Two eccentric circles (comprised thickness)

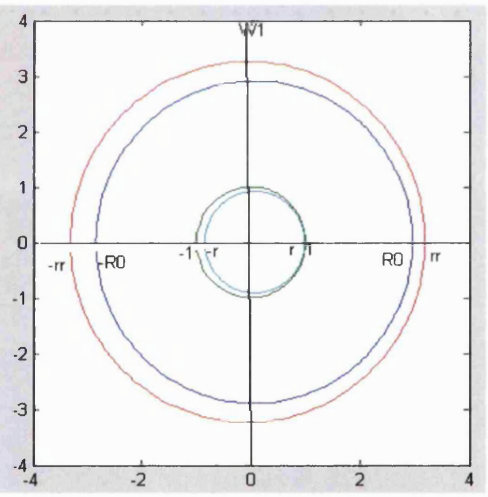

Fig.26- CM transformation of Fig. (25)

In order to find the maximum matching between the four circles in Fig.(26) and consequently the most accurate result in the second state of the CM model, a coefficient k is introduced in the transformation. Thus we have: $W_i = \frac{Z - ka}{kaZ - 1}$; k causes the transformation of the inner circle of the conductor to be concentric with unit circle. If the thickness of conductor is b, k is calculated from Eq.(3-69) as follows:

$$\frac{x_1 - b - ka}{ka(x_1 - b) - 1} = \frac{x_2 + b - ka}{ka(x_2 + b) - 1} \qquad (3\text{-}69)$$

Therefore: $$k = M + \sqrt{M^2 - \frac{1}{a^2}} \quad (3\text{-}70)$$

As: $$M = \frac{(x_1 - b)(x_2 + b) + 1}{a(x_1 + x_2)} \quad (3\text{-}71)$$

In view of such transformations which have been used to transform Fig.(25) into Fig.(26), with an effect on the scaling of Z_{pipein} [39], a scale factor or metric coefficient N should be taken into account. N is the ratio of the distances in the original Z_1-plane to the corresponding distances in the transformed W_1-plane. Hence it is defined by:

$$N = \left|\frac{dZ_1}{dW_1}\right| = \left|\frac{dZ_1}{dZ} \cdot \frac{dZ}{dw_1}\right| \quad (3\text{-}72)$$

With regard to : $Z = \frac{Z_1}{R_1}$ and $W_1 = \frac{Z - ka}{kaZ - 1}$ therefore : $Z_1 = R_1 Z$ or $\frac{dZ_1}{dZ} = R_1$ (3-73)

Also : $kaZW_1 - W_1 = Z - ka$ or $Z = \frac{W_1 - ka}{kaW_1 - 1}$ since this is an analytical function, it can be differentiated directly with respect to W_1, giving: $\frac{dZ}{dW_1} = \frac{(ka)^2 - 1}{(kaW_1 - 1)^2}$ (3-74)

In order to find the absolute value of $\frac{dZ}{dW_1}$, W_1 is expressed as: $W_1 = \cos\theta + j\sin\theta$ and because the radius of the pipe in W_1-plane is unit, it leads to the following:

$$\left|\frac{dZ}{dW_1}\right| = \left|\frac{(ka)^2 - 1}{1 + (ka)^2 - 2ka\cos\theta}\right| \quad (3\text{-}75)$$

Thus: $$N = R_1\left|\frac{(ka)^2 - 1}{1 + (ka)^2 - 2ka\cos\theta}\right| \quad (3\text{-}76)$$

N is seen to be a function of θ. With N appearing as a dominant factor in the denomination of Eqs.(3-65) & (3-67), an average values of $\frac{1}{N}$ should be used where point by point evaluations of N are not undertaken [39]. In this case, the cosθ term vanishes so that N takes the form:

$$N = R_1\left|\frac{(ka)^2 - 1}{(ka)^2 + 1}\right| \quad (3\text{-}77)$$

3.5.2 A Comparison in Results between the EMTP and CM models (single-phase)

1) Calculation of Z and Y parameters

It is important of this stage to do a comparison between the attained Z and Y via the equations in the EMTP and CM methods and for this, a network shown in Fig.(27) has been considered. Specifications of elements in the network are as follows:

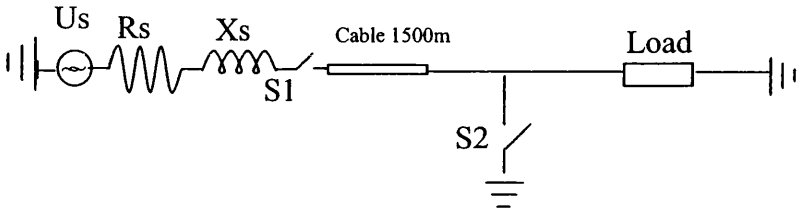

Fig.27- A single phase underground cable system

Source: 11kV $_{rms}$, f=50Hz, R_s=1Ω, X_s=0.7Ω

Switch1: closure time=.1ms

Switch2: closure time=1.5ms

Load : R_L=12Ω, X_L=10Ω

Cable: core+sheath ungrounded, length=1500m

Core: r_{in}=0, r_{out}=6.9mm, ρ=2.3*10^{-8} Ω.m, μ_r=1

Sheath: r_{in}=12.5mm, r_{out}=14.5mm, ρ=17*10^{-8} Ω.m, μ_r=1

Insulator between core and sheath: thickness=5.6mm, ε_r=2.3

Insulator on the sheath: thickness=3mm, ε_r=8

Condition 1: Pipe; r_{in}=5cm, r_{out}=7cm, ρ=5*10^{-8} Ω.m, μ_r=1

Condition 2: Pipe; r_{in}=20cm, r_{out}=25cm, ρ=5*10^{-8} Ω.m, μ_r=1

The results have been obtained using the EMTP software. Table 3-1 shows such cable data which is employed in .lib file in the EMTP for both models and both conditions, as it determines cable specifications in the aforementioned network. R is the modal resistance, Z_s is modal surge impedance, v is velocity of propagation, DIST is length of the line in $vintage,1 (a function in EMTP) as well as T_i matrix in $vintage,0 (a function in EMTP); real part is in row 2i-1 and the imaginary part is in 2i (i is changed from 1 to the number of the mode). It should be noted that because of the ambiguity in the eigenvectors, modal impedances and admittances only make sense if they are

specified together with the eigenvectors used in their calculations. Thus a comparison between the velocities of propagation in the aforementioned methods in Table 3-1 is important. All curves of the voltage in the CM model are computed by replacing modal parameters of the CM model in .lib file of EMTP.

Since Eqs.(3-20) & (3-21), are more accurate when the radius of a cable is much smaller than the inner radius of the pipe, the following two conditions have been considered for the pipe type cable; 1) the cable radius is relatively large compared to the radius of the pipe; this is more commonly the case in practice, 2) the cable radius is too small compared to the radius of the pipe. In this condition, in view of the fact that the approximations and estimations considered due to conductors being off-centre, are reduced in the EMTP; thus the EMTP model is closer to a perfect model. It would thus appear that the results obtained from the CM and EMTP models would be much closer for the second condition (condition 2 above); this is by virtue of the fact that the CM model eliminates altogether any errors arising due to the conductors being off-centre and within the EMTP model, some of the approximations associated with condition are reduced.

Table 3-1 depicts that the velocity of wave propagation of two modes in the EMTP model and in condition 1, these are 4.90295E+07 and 1.71645E+08 while those in the CM model are 4.5937E+07 and 1.366E+08 respectively. As it can be seen, the differences between velocities related to the two models are almost 6% and 20% for two modes. However, in the case of condition 2, the velocities of wave propagation for EMTP and CM models are 5.45899E+07, 2.5547E+08, 5.459E+07 and 2.5426E+08 respectively. And these are much closer to each other. It can thus be concluded that the CM cable model is better suited for cable systems in which the pipe is a much smaller radius i.e., condition 1.

2) Switching and fault transients

Figs. (28) to (31) show the voltage signals measured after the switching point S1 for both models and both conditions 1 and 2. These figures involve two parts; the first part is associated with reclosing S1 on to the load without a fault and the time is between 0.1ms to 1.5ms. The second part is related to the fault that occurs at time 1.5ms. Both

parts are in relation to the velocity of wave propagation of the modes i.e., the higher the velocity, the higher is the frequency of distortion. Figs.(28,29) which are for condition 1, clearly shows that the frequency of distortion on the voltage waveform simulated via the EMTP model is higher in comparison to that for the CM model; this is by virtue of the higher velocity of wave propagation of the modes in the EMTP model, as shown in Table 3-1. Furthermore, because of approximations and estimations associated with the EMTP model, the voltage signal is somewhat smoother in comparison with the CM model.

ATP model condition 1

	R(ohms/meter)	Z_s (ohms)	v(m/s)	DIST(m)
$VINTAGE, 1				
-1IN___AOUT__A	6.42475E-04	1.46860E+01	4.90295E+07	-1.50000E+03 1 2
-2IN___BOUT__B	1.47743E-04	7.09619E+01	1.71645E+08	-1.50000E+03 1 2
$VINTAGE, 0				
-.63385277 .90543937				
-.00439074 -.01681574				
.90559527 .13528443				
-.00065603 .02402491				

C.M model condition 1

	R(ohms/meter)	Z_s (ohms)	v(m/s)	DIST(m)
$VINTAGE, 1				
-1IN___AOUT__A	2.70030e-04	6.52650e+01	1.36600e+08	-1.50000E+03 1 2
-2IN___BOUT__B	5.73200e-04	1.11930e+01	4.59370e+07	-1.50000E+03 1 2
$VINTAGE, 0				
.99732000 -.51360000				
.00000000 -.00402770				
.07008900 .85802000				
.02085500 .00000000				

ATP model condition 2

	R(ohms/meter)	Z_s (ohms)	v(m/s)	DIST(m)
$VINTAGE, 1				
-1IN___AOUT__A	5.96616E-04	1.81472E+01	5.45899E+07	-1.50000E+03 1 2
-2IN___BOUT__B	1.31645E-04	1.81158E+02	2.55470E+08	-1.50000E+03 1 2
$VINTAGE, 0				
-.77556197 .84334175				
-.00235418 -.03484819				
.84406130 .17063135				
-.00047632 .03792606				

C.M model for condition 2

	R(ohms/meter)	Z_s (ohms)	v(m/s)	DIST(m)
$VINTAGE, 1				
-1IN___AOUT__A	1.81330e-04	2.44560e+02	2.54260e+08	-1.50000E+03 1 2
-2IN___BOUT__B	4.54200e-04	1.38130e+01	5.45900e+07	-1.50000E+03 1 2
$VINTAGE, 0				
.97931000 -.67658000				
.00000000 -.00242790				
.19557000 .73636000				
.51936000 .00000000				

Table 3.1- Cable specifications in EMTP and CM models

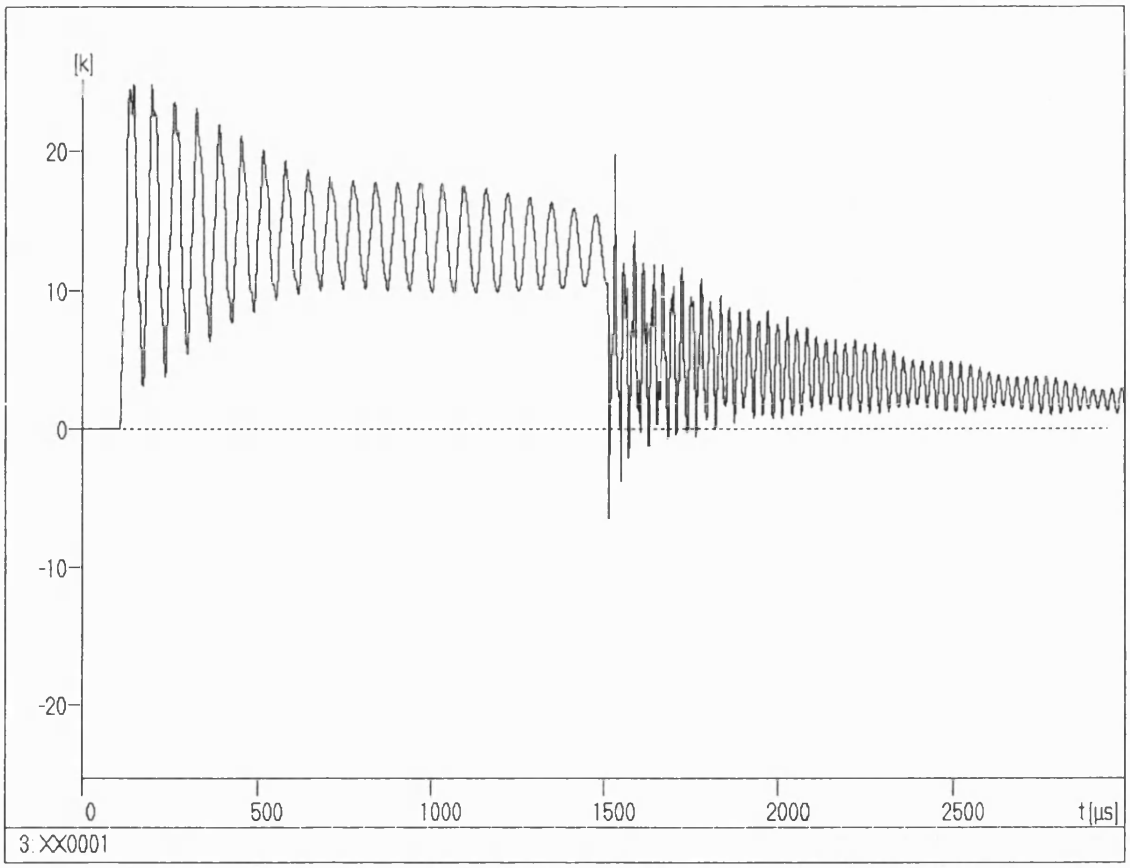

Fig.28- Voltage based on the EMTP model (condition 1)

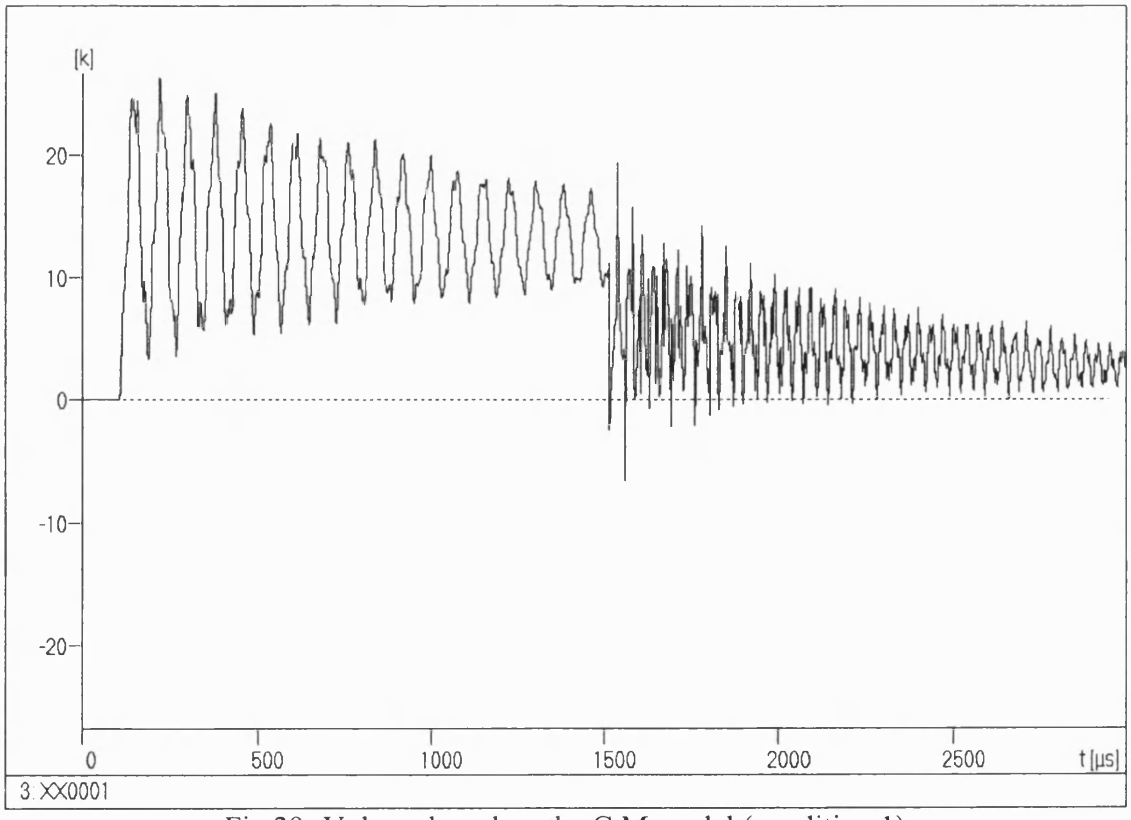

Fig.29- Voltage based on the C.M model (condition 1)

Figs. (30,31) are associated with condition 2 and show that the signals are almost identical to each other for both models. Importantly, the frequency of distortion both during the switching transient and the fault transient periods are much higher in comparison to condition 1; this is due to the higher velocity of wave propagation of the modes for condition 2, as shown in Table 3-1.

A comparison of the transient voltage waveforms attained via the two models- EMTP and CM, clearly shows that the waveforms are very close to each other for condition 2 in which the ratio between pipe and cable radii are much higher (20cm and 6.9mm) than is the case for condition 1 in which the correspond radii are 5cm and 6.9mm. It should be noted that in the case of smaller cables (as in the case in condition1) the approximations with the EMTP-based cable model manifest themselves into producing errors in the simulation of the transients; this of course is not the case in the CM-based technique which overcomes the errors through a series of transformations as outlined previously. Here, it should also be emphasised that the study relating to the larger ratio between the radii is not very common but is simply presented to illustrate the limitation of the EMTP model.

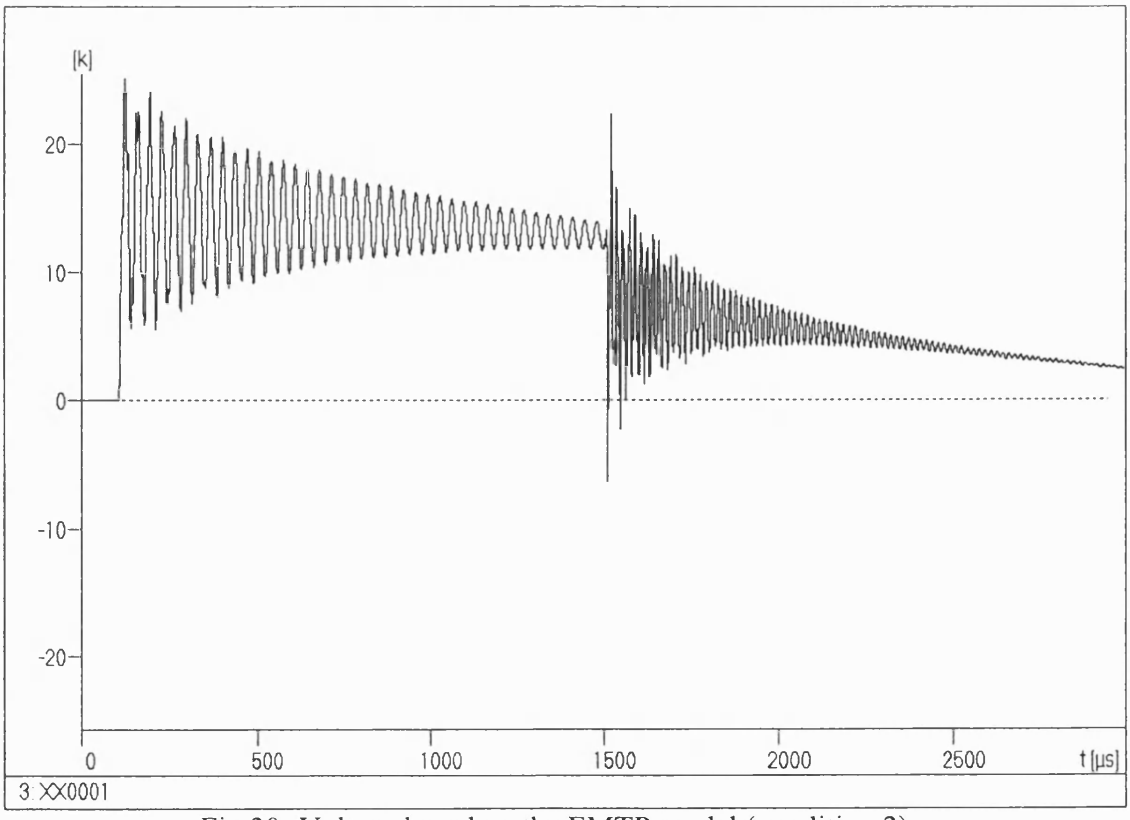

Fig.30- Voltage based on the EMTP model (condition 2)

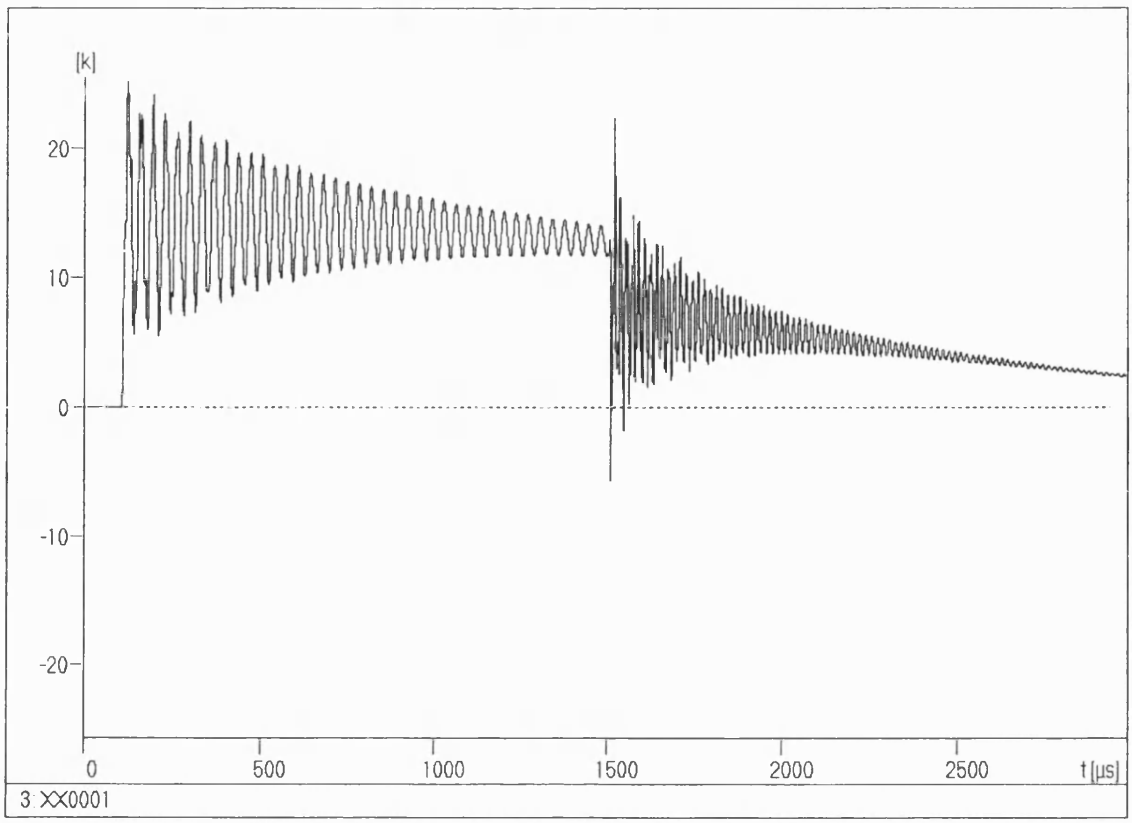

Fig.31- Voltage based on the C.M model (condition 2)

3.5.3-.Multi-Conductor Pipe Type Cable Model Using CM

As mentioned before, in order to modify the equations for Z and Y in a multi-conductor pipe type cable and with regard to the methods for three-phase cable and multi-conductor pipe type cable, further modifications over and above the previously mentioned ones for single phase pipe type cable. Herein, only the commonly employed three-conductor pipe type cable is discussed. It is apparent that a three-phase cable is a symmetrical three-conductor pipe type cable the only difference being that is instead of a pipe, armour is used. The requisite modifications are done by achieving concentric circles (through transformations) as, Eq.(3-53) (capacitance) and first and fourth terms of Eq.(3-21) (inductance) are modified. It is apparent that the modification of Z and Y follows the modification of C and L.

As mentioned before, the axial voltage drop (Eq.(3-42)) depends on the flux linkage and the axial electrical field at the pipe wall. This section will deal with the flux linkage and the modification of C (Eq.(3-53)) and L (the first and fourth terms of Eq.(3-21)) and hence Y and Z, respectively. A three-phase pipe type cable is shown in Fig.(32).

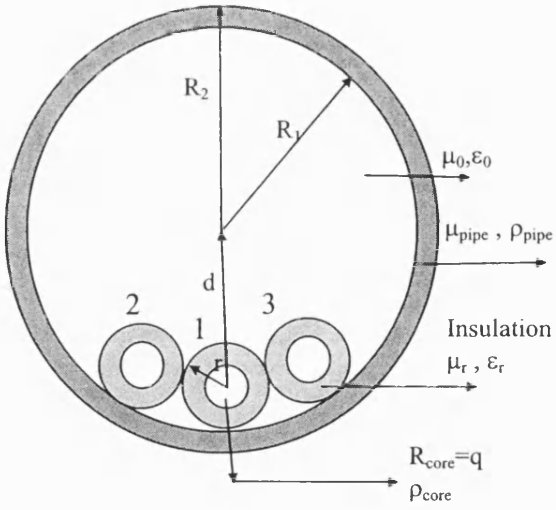

Fig.32- Three-phase pipe type cable

To determine the impedance and admittance matrices for a multi-conductor system, both self and mutual terms should be computed (Eqs(3-11 and 3-23)). The self impedance and admittance terms are known from the previous analysis. The mutual terms are derived as follows:

With reference to Eq.(3-51) and in order to find the level of the mutual flux linkage between conductor 2 and the armour associated with conductor 1, reference should be made to Fig.(33);

As can be seen, fluxes generated by conductor 1 produce a set of circles in which the centre moves from α_1 to 0 on the axis x. Thus in order to find the amount of the flux generated by conductor 1 that flows between conductor 2 and the armour, there is a need to find a circle with centre α_4 and radius R_4.

Referring to Eqs.(3-42 & 3-58) and the CM method, the first and fourth terms of Eq. (3-21) :

$$Ij\omega L = \frac{d\lambda}{dt} = Ij\omega \frac{\mu_o \mu_r}{2\pi} \ln R_o(X_{14}, X_{24}) \tag{3-78}$$

Then, the potential coefficient P_{12} which is $1/C_{12}$ is derived as follows:

$$P_{12} = \frac{1}{2\pi.\varepsilon_o.\varepsilon_r} \ln R_o(X_{14}, X_{24}) \tag{3-79}$$

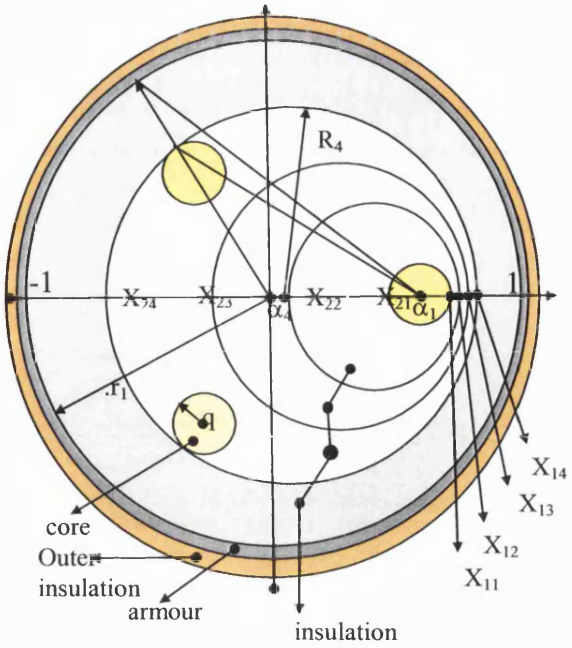

Fig.33- Representation of the flux linkage in a three-phase cable

In order to find the circle(α_4,R_4) in Fig.(33), there is a need to do the following calculations:

$$x_{14}=x_{11}+k.(1-x_{11}) \quad (3\text{-}80\text{-a})$$

$$x_{24}=x_{21}-k.(1+x_{21}) \quad (3\text{-}80\text{-b})$$

$$\alpha_1=(x_{11}+x_{21})/2 \quad (3\text{-}80\text{-c})$$

$$\alpha_4=\alpha_1-k.\alpha_1 \quad (3\text{-}80\text{-d})$$

k is percentage of the full distance between the origin to the centre as shown in Fig. (33); for example $X_{11} \to 1$, $X_{12} \to -1$ or $\alpha_1 \to 0$.

From Fig. (33), it can be concluded that:

$$R_4 = X_{11}^2 + \alpha_4^2 - 2\alpha_4.x_{11}\cos 120 \quad (3\text{-}81\text{-a})$$

$$R_4 = X_{14} - \alpha_4 \quad (3\text{-}81\text{-b})$$

from Eq.(81) k is obtained as follows:

$$k^2 - Mk + N = 0 \Rightarrow k = \frac{M}{2} - \sqrt{\frac{M^2}{4} - N} \quad (3\text{-}82\text{-a})$$

As :

$$M = \frac{2d^2 + X_{11}(d-1) + d + 1}{d^2} \qquad (3\text{-}82\text{-b})$$

and

$$N = \frac{X_{11}^2 + d^2 + X_{11}(d-1) + d}{d^2} \qquad (3\text{-}82\text{-c})$$

After calculating k, x_{14} and x_{24} can be derived from Eq.(3-80). In conclusion, P_{12} is obtained from Eq.(3-79) that R_0 has been shown in Eq.(3-56), but instead of x_1 and x_2, x_{14} and x_{24} should be used respectively. Also Z_{12} is derived by modifying Eq.(3-21) as follows:

$$Z_{12} = \frac{j\omega.\mu_o.\mu_r}{2\pi} \ln R_0(X_{14}, X_{24}) + \frac{c_o k_o(\delta.r_1)}{\sigma} + \frac{1}{\sigma}\sum_{n=1}^{\infty} c_n.k_n(\delta.r_1)(\frac{r_{12}}{r_1})^2.\cos(n.\theta_{12}) \qquad (3\text{-}83)$$

3.5.4 A Comparison in Results between the EMTP and CM models (three-phase)

In order to do a comparison of the Z and Y parameters between the EMTP and CM methods, a practical three-phase underground distribution network shown in Fig. 34 has been considered.

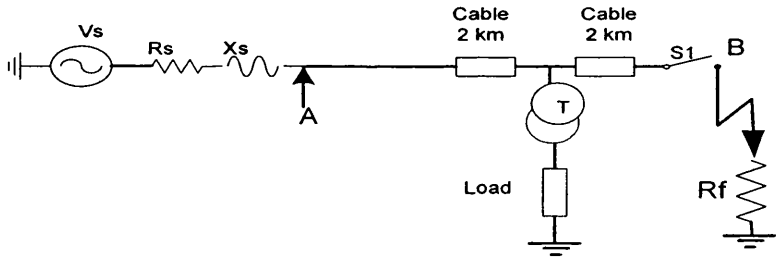

Fig.34- Practical 3-phase underground distribution network

The specifications of the various elements in Fig (34) are as follows:

Source: V_L = 11kV, f=50Hz, X_s:R_s=10, X_s=2Ω, R_s=0.2Ω

Switch1: closing time =5 ms

Fault resistance R_f=0.1 ohms,

Step time for sampling =10 μs i.e. F=100kHz.

Cables: XLPE, Three-phase pipe type cable (core + grounded sheath)

Core: r_{in}=0, r_{out}=6.1mm, ρ=2.3*10^{-8} Ω.m, μ_r=100

Sheath: r_{in}=10mm, r_{out}=11mm, ρ=17*10^{-8} Ω.m, μ_r=100

Insulation between core and sheath: thickness=3.9mm, ε_r=3

Insulator between pipe and sheath: ε_r=8

Pipe: r_{in}=4cm, r_{out}=4.5cm, $\rho=25*10^{-8}$ Ω.m, μ_r=100

Transformer: S=315 kVA

Winding 1 : V_L=11kV, R_p=1Ω ., X_p= 9 . Ω

Winding 2 : V_L=400V, R_s= 0.44 mΩ., X_s= 3.6 mΩ

Magnetizing Branch: R_M=1000 GΩ

Load= V_L=400 Vrms , 3phase λ, P_L=102.626 kW, Q_L=76.733 kVAR,

It should be noted that all voltage and current signals are simulated using the EMTP software employed for setting up the distribution network model (Fig. 34) into which is embedded the CM-based 3-phase cable model.

The comparison comprises of two parts. In the first part, a comparison is made between the various cable parameters, principally to highlight the differences observed between the two types of cable models using, the EMTP and the CM models. The results shown in Table 2 typify the differences experienced in some of the important parameters of a 3-phase pipe type symmetrical cable. It should be mentioned that although the three conductors are symmetrically placed, they are nonetheless eccentric resulting in a complex and non-linear interaction amongst the various electrical variables.

First of all considering the symmetrical components (both series and shunt impedances), it is apparent that the resistive elements of the series impedances are relatively much higher in the case of the CM model compared to the EMTP model. This can be directly attributed to the fact that unlike the EMTP model, the depth of penetration in the pipe has been taken into account in the CM model; this is particularly important from a practical point of view, in view of the fact that the depth of penetration is less than the thickness of the pipe. However, there is only a small difference between the reactive elements of both the series and shunt impedances. Modal parameters are a very important indicator of the behaviour of a cable (or line) particularly under transient conditions. It is clearly evident from Table 3-2 that whilst the velocity of propagation of the three modes (one earth and two aerial) are little different in the two models, the attenuation is significantly higher in the case of the CM model compared to the EMTP

model. Although not shown here, similar differences in the cable characteristics were also observed in the case of an asymmetrical cable.

Table 3.2 - Characteristic of three-phase cable

	EMTP Model	CM Model
R_1 ohm/meter	6.8e-4	10.1803e-4
R_0 ohm/meter	6.78e-4	10.1584e-4
XL_1 ohm/meter	1.2654e-3	1.16085e-3
XL_0 ohm/meter	1.2734e-3	1.1652e-3
XC_1 mho/meter	1.0607e-7	1.0607e-7
XC_0 mho/meter	1.0607e-7	1.0607e-7
Velocity Mode1	2.6175e+7	2.62e+7
Velocity Mode2	2.6243e+7	2.623e+7
Velocity Mode3	2.6243e+7	2.623e+7
Attenuation Mode1	2.60193e-2	3.9027e-2
Attenuation Mode2	2.61673e-2	3.9156e-2
Attenuation Mode3	2.61673e-2	3.9156e-2

In order to ascertain the effect of the aforementioned differences in the cable parameters on both voltage and current signals under faults, an extensive series of fault studies were carried out by integrating the two cable models into a typical 11 kV distribution system as shown in Fig 34. In all cases, the point of observation of the waveforms is 'A' and all faults considered are at point 'B' in Fig. (34). The sampling rate is 100 kHz and for all faults involving earth, the fault resistance is 0.1 Ω.

First of all considering an a-phase-earth fault at voltage maximum, Figs (35)-(38) show a comparison in the voltage and current waveforms attained via the two models. Comparing the voltage waveforms (Figs (35) and (37)) it is apparent that the initial distortion on the faulted a-phase is much the same for the two models. Importantly, the transients in the case of the CM model die down much faster than in the case in the EMTP model; this clearly shows the effect of higher attenuation associated with the CM model (as discussed previously) which manifests itself into the increased damping effect. Interestingly, some distortion is also observed on the two healthy phases b and c in the

case of the CM model. When considering the current waveforms (Figs (36) and (38)), the transients are significantly smaller than those on the voltage waveforms and importantly, there is little difference in distortion between the two models; this is somewhat expected by virtue of the fact that in a highly inductive circuit (cable or line) current signals are predominantly power frequency and swamp over any high frequency distortions.

When considering a b-c-phase fault, Figs (39)-(42) depict the differences observed in the waveforms for the two models considered. First of all looking at the voltage waveforms (Figs (39) and (41)), it is apparent that although the initial distortion is nearly the same for the two models, the transients take significantly longer to die down in the case of the EMTP cable model. In the absence of the earth resistivity playing a part in this type of a fault, the differences in the attenuation constants between the two models (these are higher for the CM model), manifest themselves into the increased damping effect in the case of the CM model. Here again like the single phase to ground fault, there is also distortion on the healthy 'a' phase in the case of the latter. The current waveforms are little different for the two models as shown by Figs (40) and (42).

In the case of b-c-G fault with a small fault resistance, the transients on the faulted waveforms die down much faster in the case of the CM cable model compared to the EMTP cable model (Figs (43) and (45)). Interestingly, when comparing the voltage waveforms with the previous phase-phase fault (Figs (39) and (41)), the high frequency distortion on the faulted phases in the case of CM model persists for a much shorter period in the case of the phase-phase-earth fault; this would be expected by virtue of the fact that for this type of a fault, the higher attenuation factor associated with the CM model is further accentuated by the earth resistivity thereby producing a more profound effect on the damping of the transients. Again as expected, there is little difference in the corresponding current waveforms attained for the two models, as evident from Figs (44) and (46).

In the case of three-phase fault with a small fault resistance, similar to the previous cases, the transients on the faulted phases die down much faster in the case of the CM model compared to the EMTP model in voltage signals as it can be seen from Figs. (47) and (49). Again as expected, there is little difference in the corresponding current

waveforms attained for the two models in terms of distortion but, since the resistive elements of the series impedances are relatively much higher in the case of the CM model compared to the EMTP model, magnitudes of the peak to peak of current signals are larger in EMTP model compared to the CM model, as evident from Figs (48) and (50). Although not shown herein, similar observations to the foregoing have been made in the case of a system employing an asymmetrical cable i.e there is much faster attenuation on the fault phases in the case of the CM cable model in all fault cases.

In conclusion, it can be ascertained that there are quite significant differences in the level of distortion in the simulated voltage and current waveforms between the two approaches, one based on the EMTP cable model and the other based on the CM method; like in the case of the single-phase pipe-type cable, these differences can be directly attributed to the a number of approximations associated with the EMTP-based model; such approximations of course have been significantly minimised through a series of transformations in the case of the CM method, thereby making the latter approach more accurate and hence better suited for research and investigation of a new fault location technique for UG cables, the subject of the next chapter.

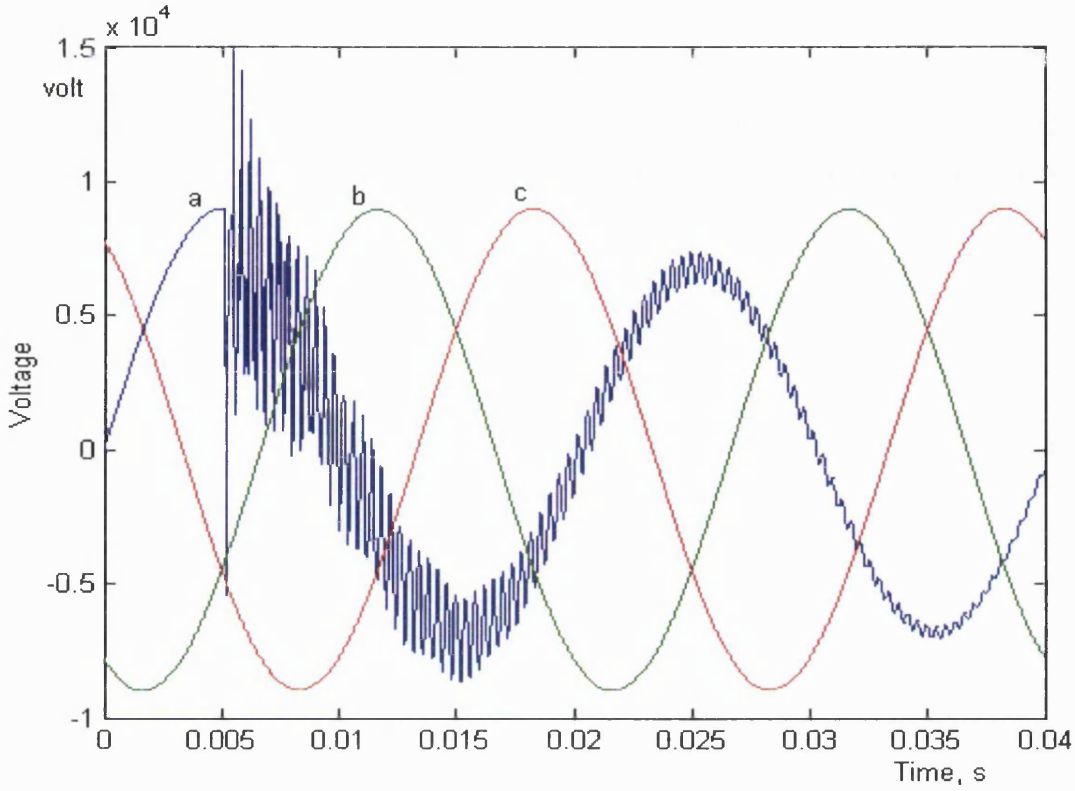

Fig.35- Three-phase Voltage signals, phase a-earth fault EMTP model

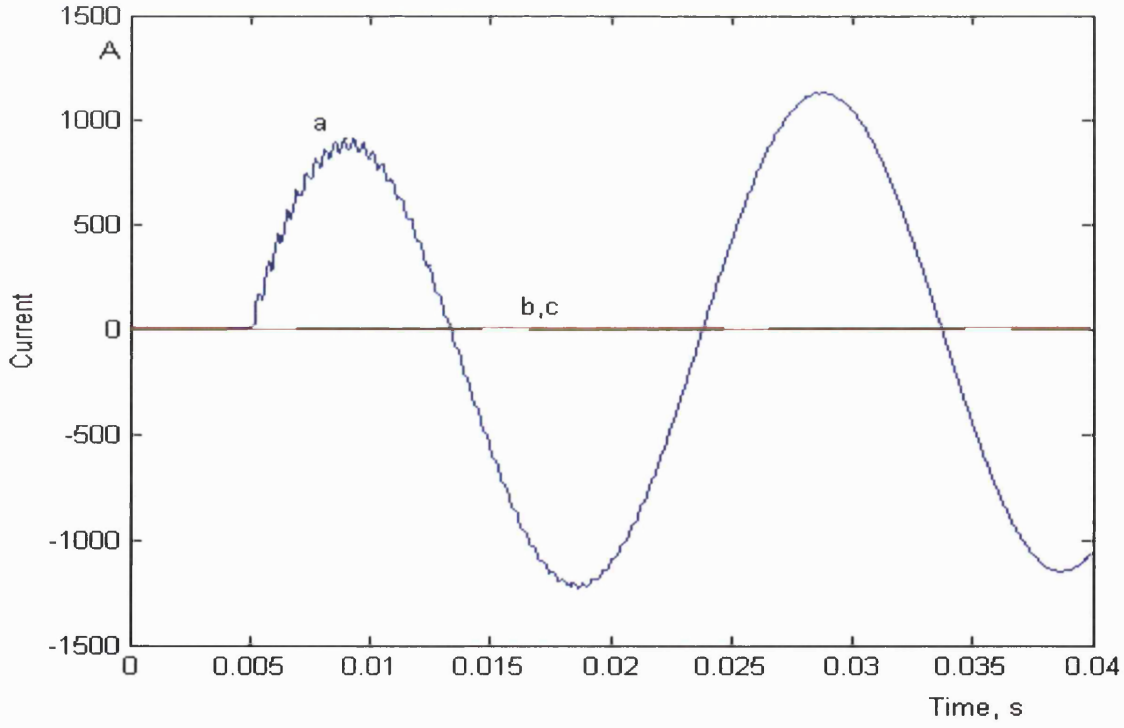

Fig.36- Three-phase Current signals, phase a-earth fault EMTP model

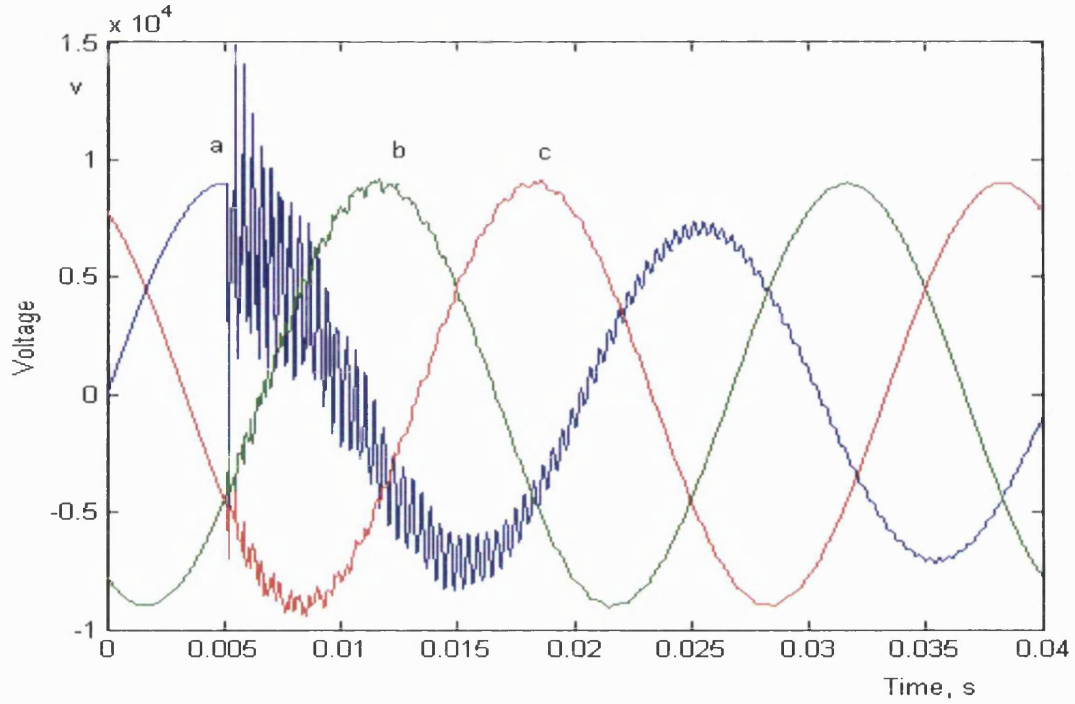

Fig.37- Three-phase Voltage signals, phase a-earth fault CM model

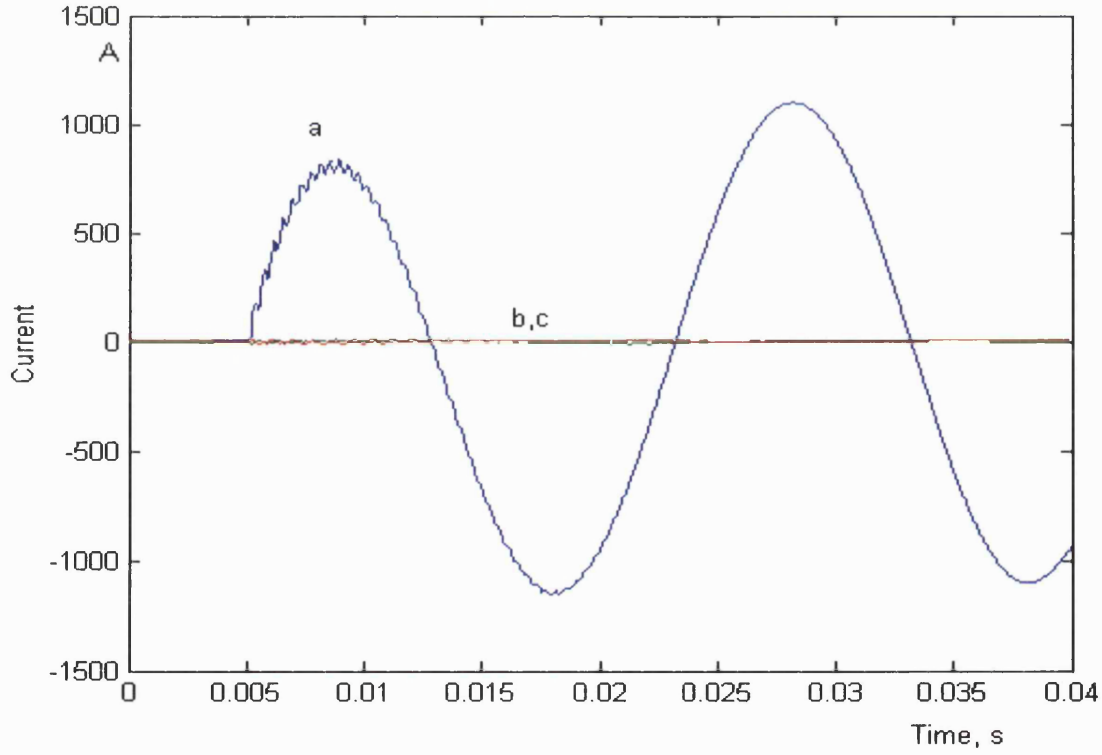

Fig.38- Three-phase Current signals, phase a-earth fault CM model

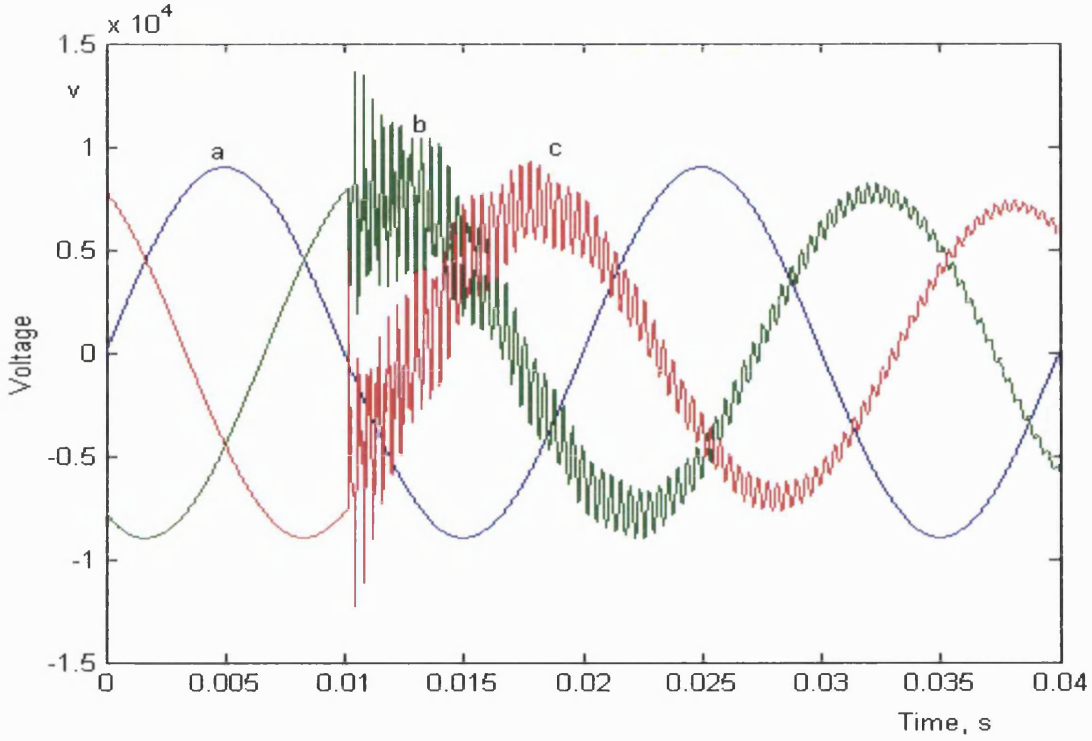

Fig.39- Three-phase Voltage waveforms, b-c fault, EMTP model

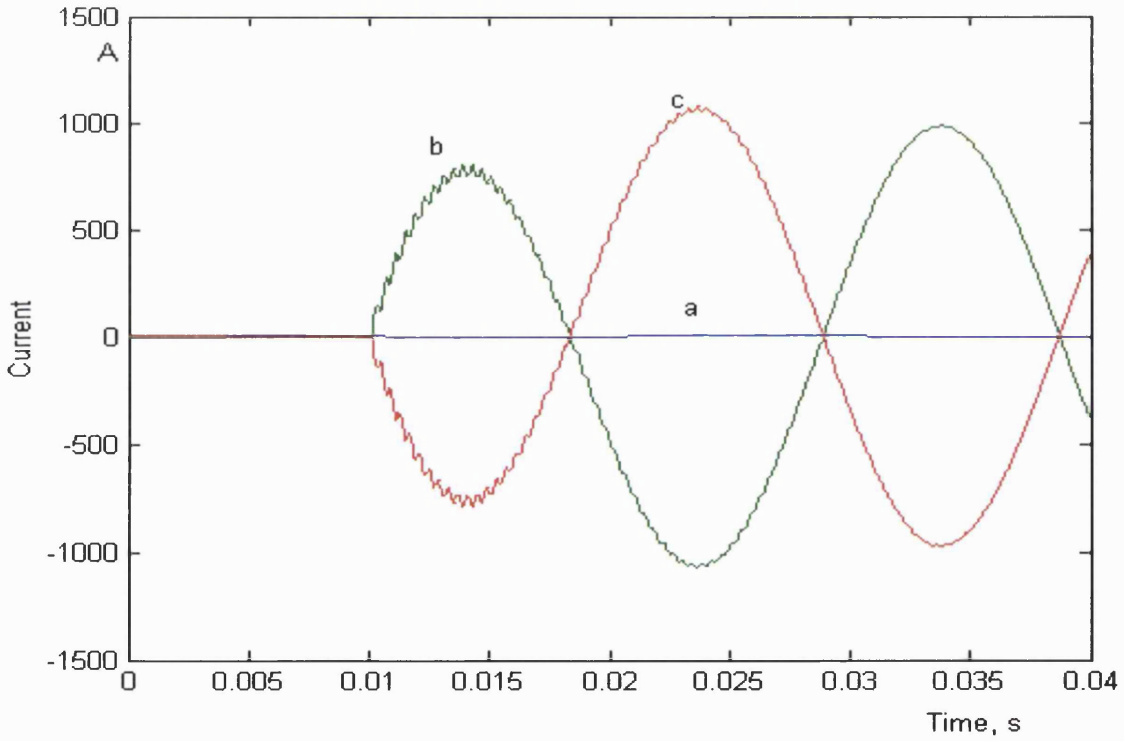

Fig.40- Three-phase Current waveforms, b-c fault, EMTP model

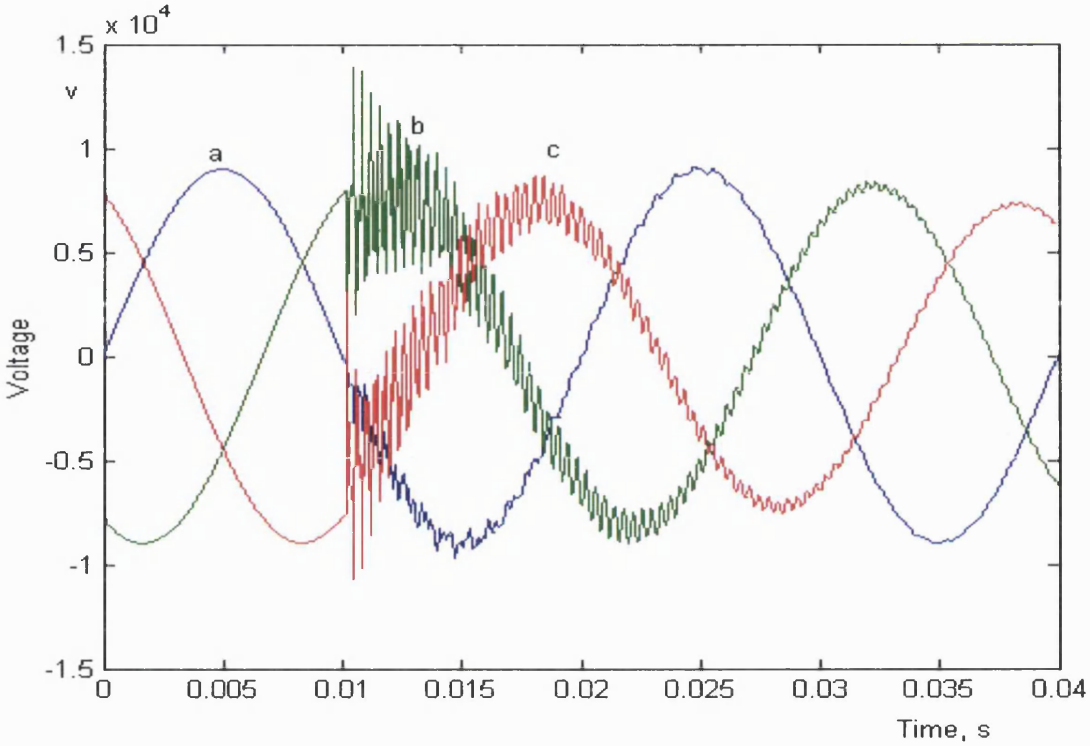

Fig.41- Three-phase Voltage waveforms, b-c fault, CM model

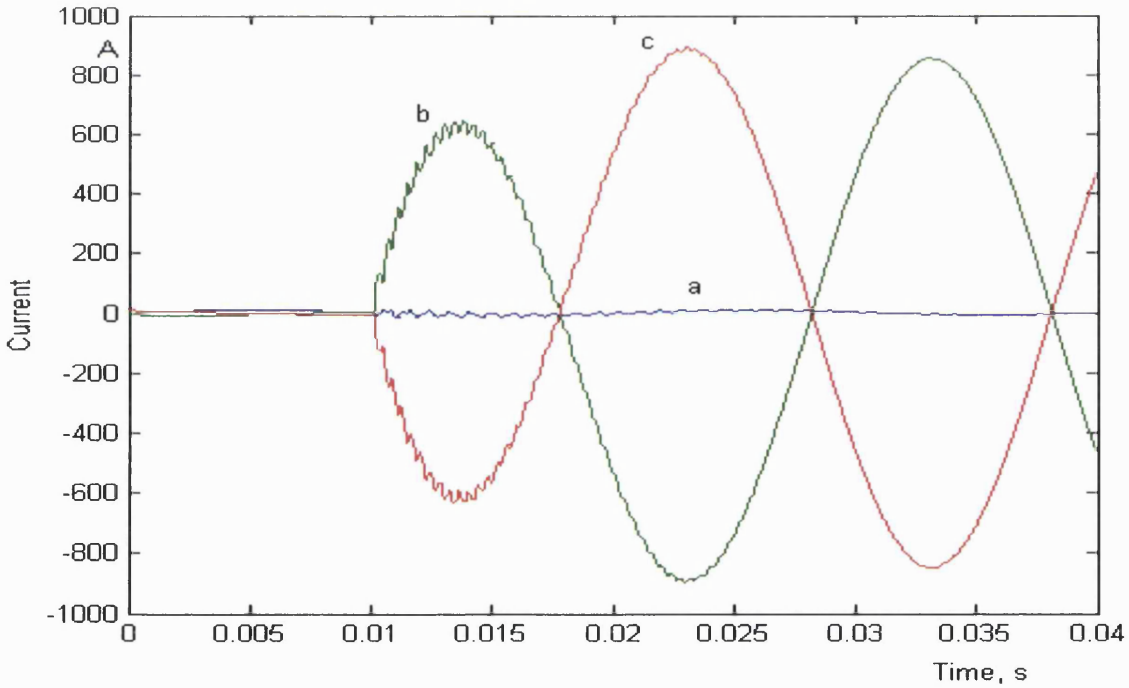

Fig.42- Three-phase Current waveforms, b-c fault, CM model

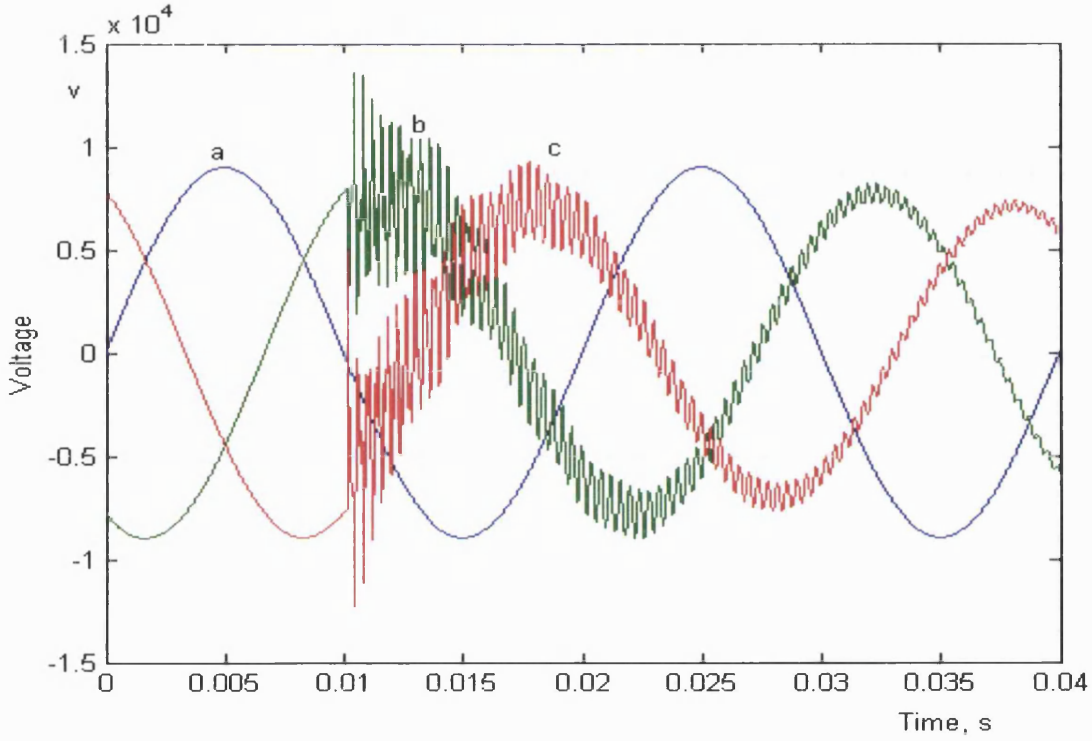

Fig.39- Three-phase Voltage waveforms, b-c fault, EMTP model

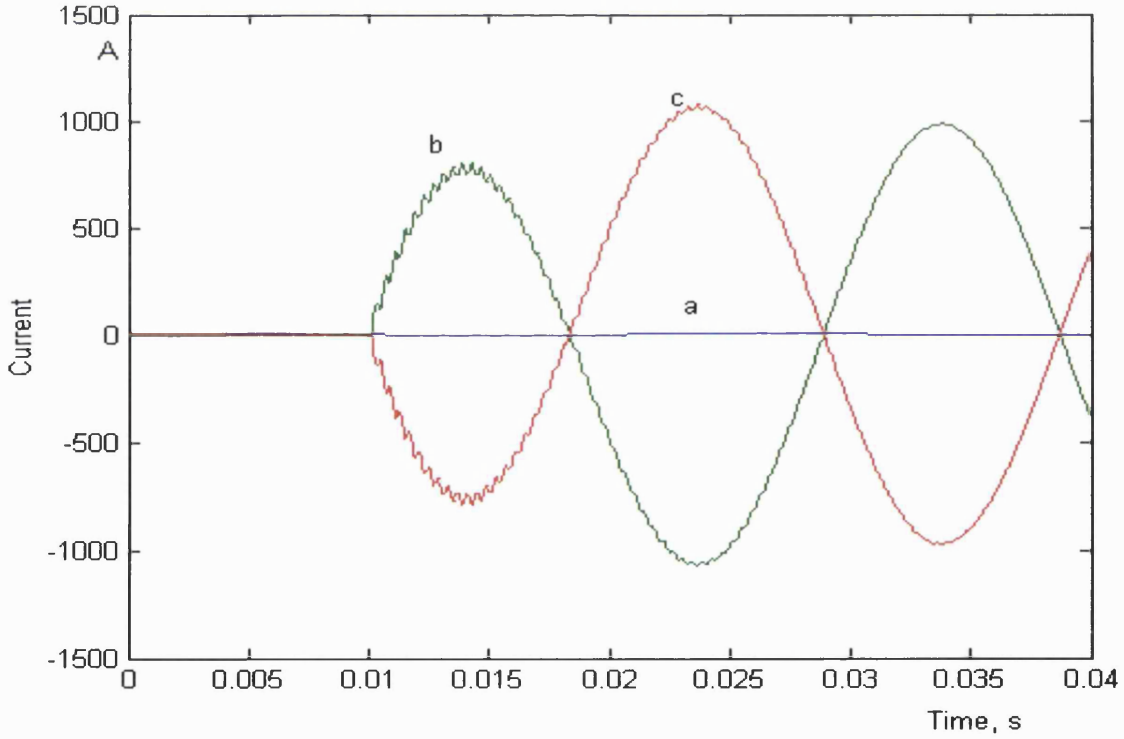

Fig.40- Three-phase Current waveforms, b-c fault, EMTP model

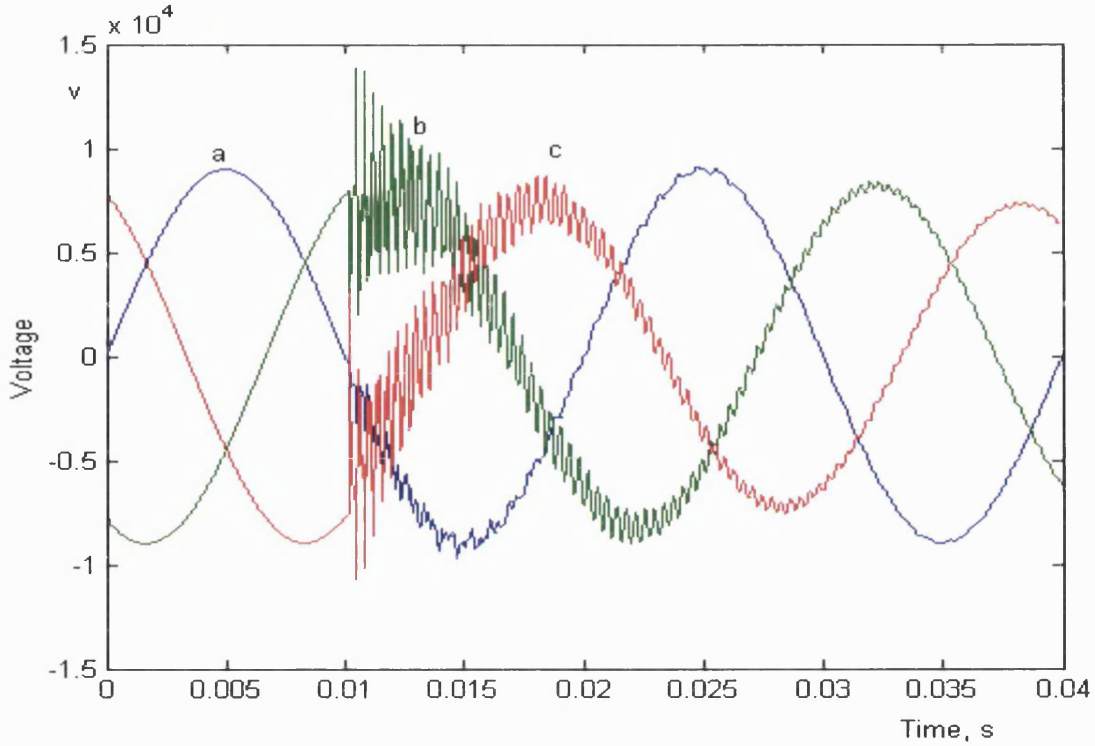

Fig.41- Three-phase Voltage waveforms, b-c fault, CM model

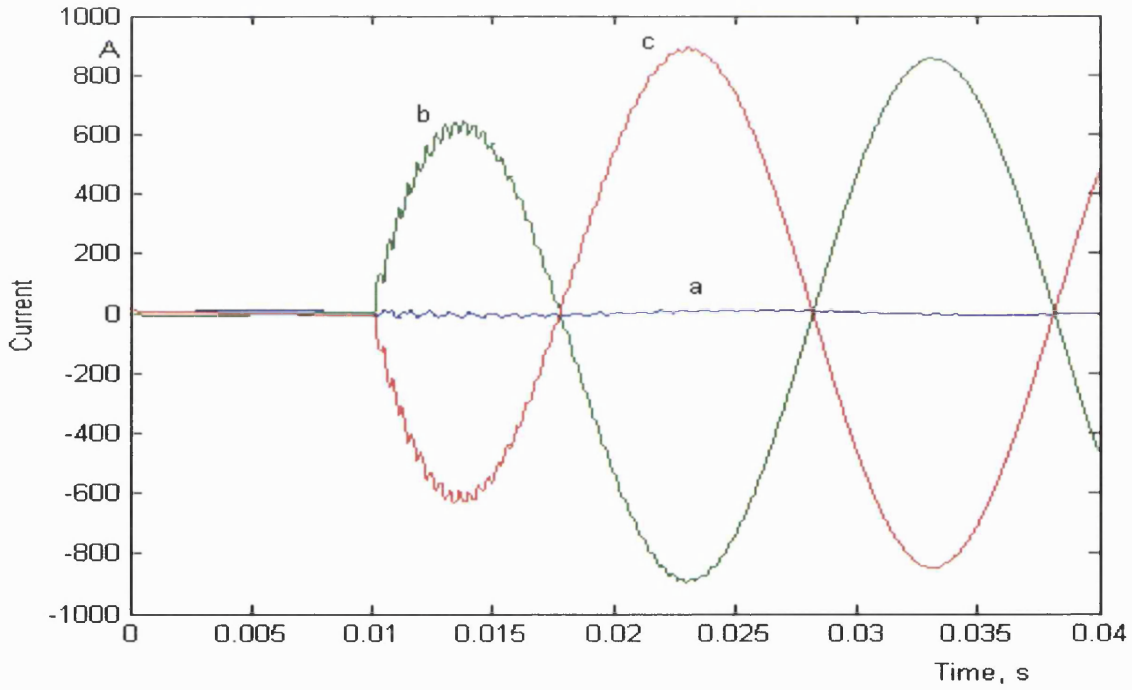

Fig.42- Three-phase Current waveforms, b-c fault, CM model

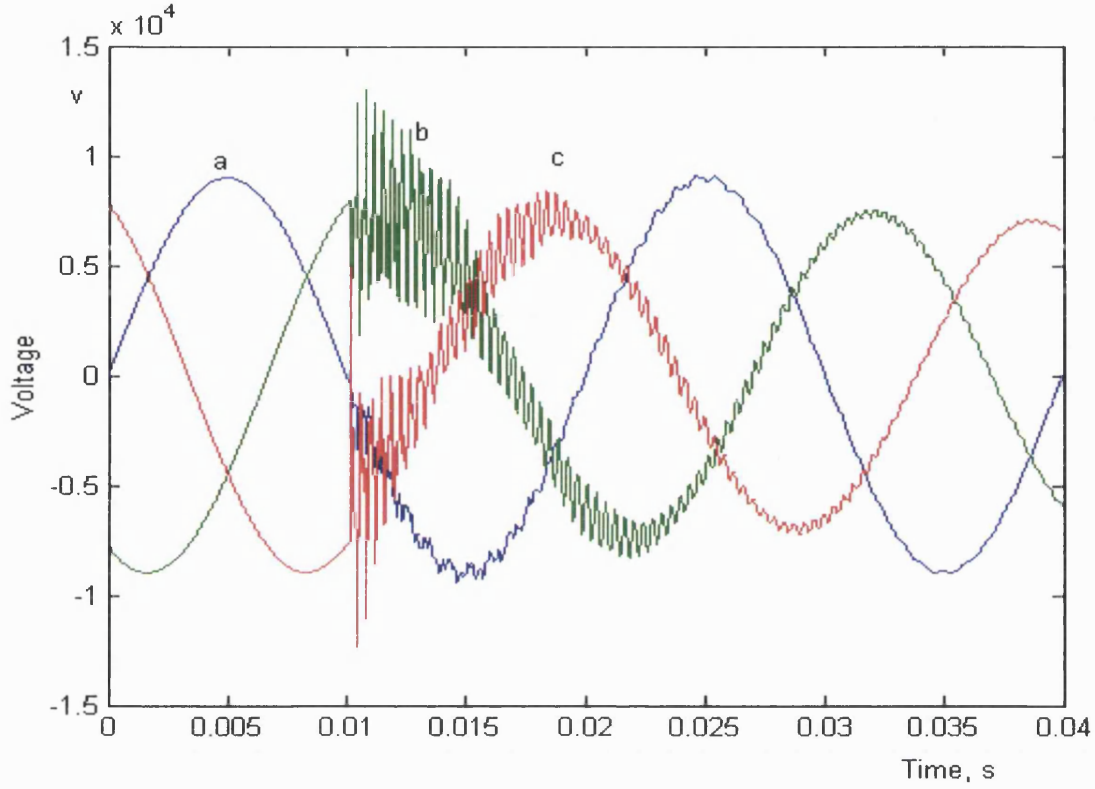

Fig.45- Three-phase Voltage waveforms, b-c-earth fault, CM model

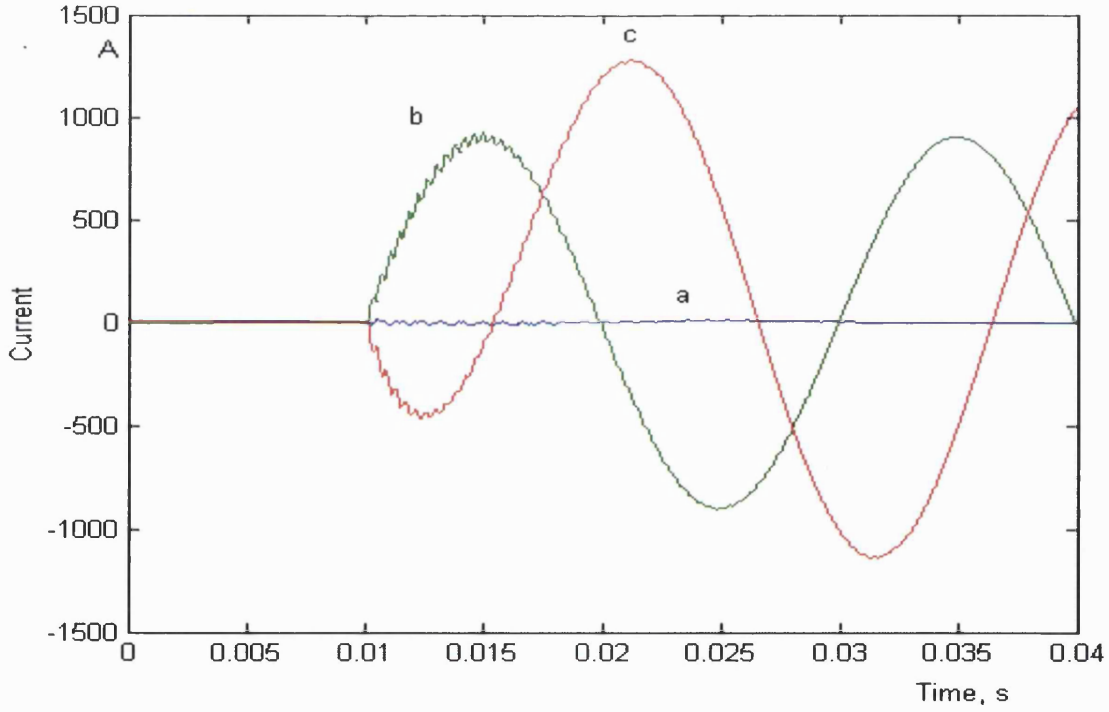

Fig.46- Three-phase Current waveforms, b-c-earth fault, CM model

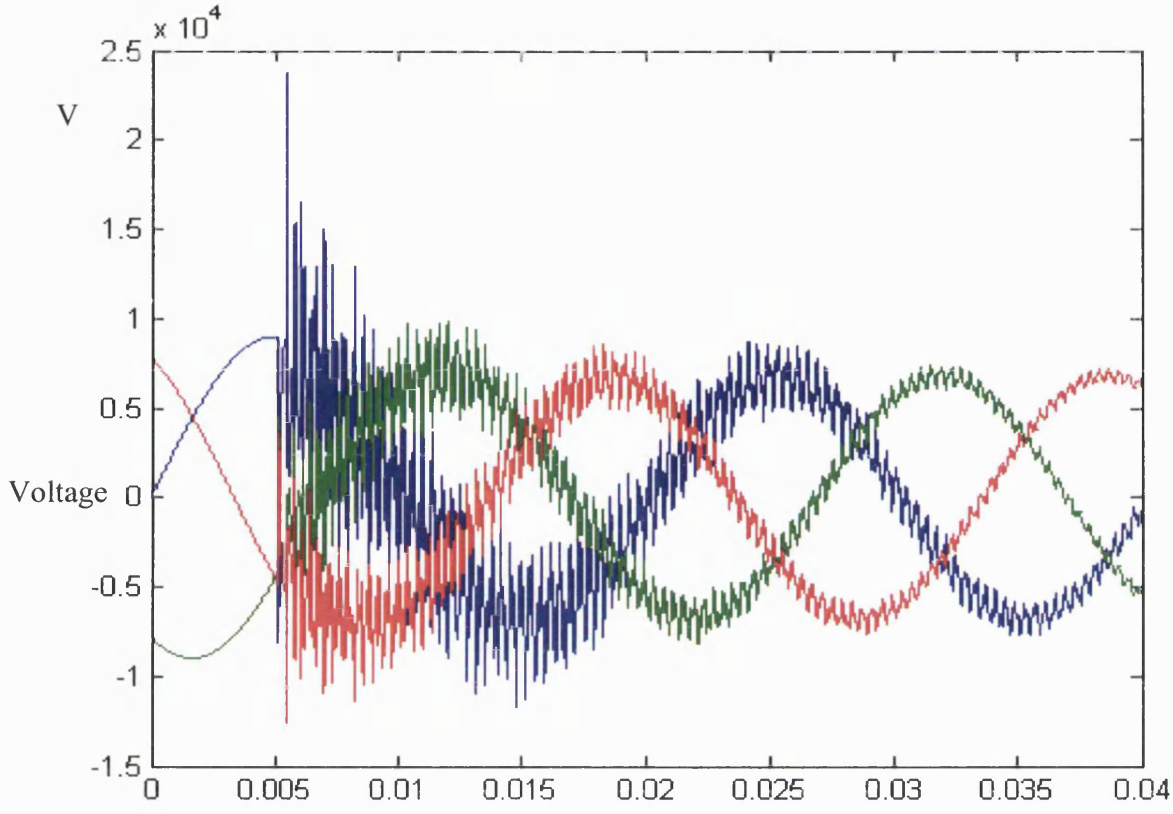

Fig.47- Three-phase Voltage waveforms, a-b-c fault, EMTP model

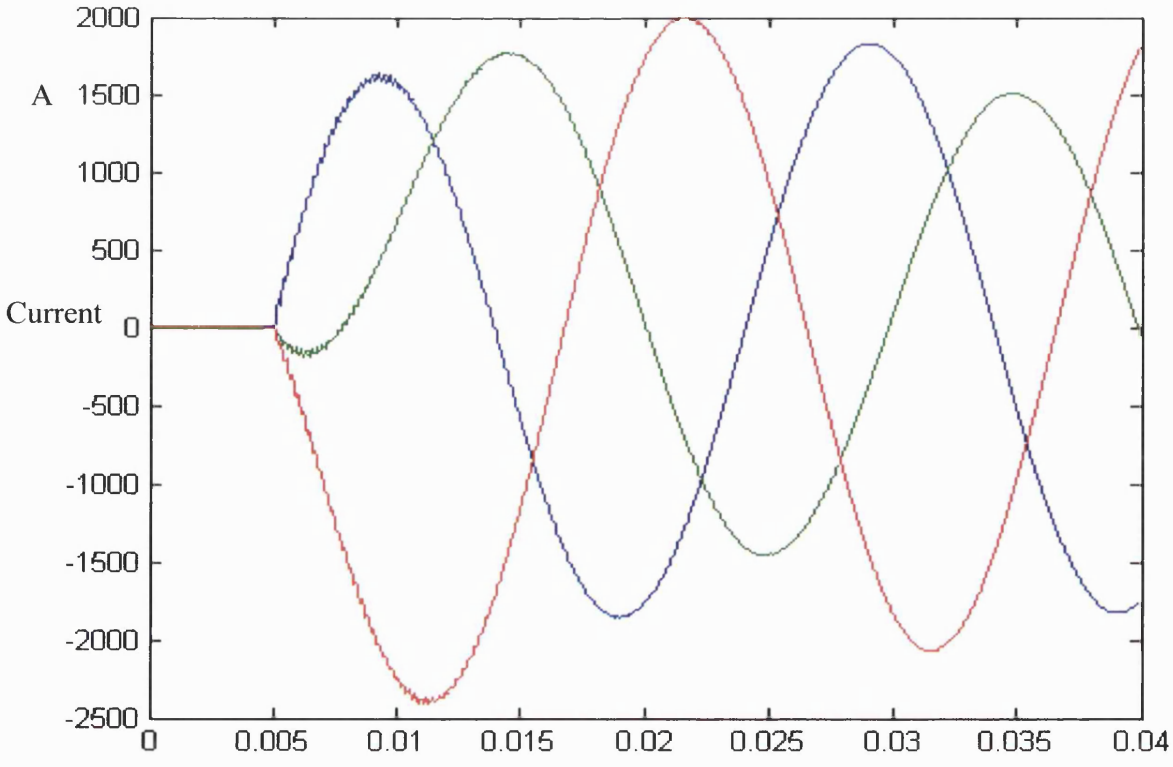

Fig.48- Three-phase Current waveforms, a-b-c fault, EMTP model

CHAPTER 4

TRANSIENT DATA SIMULATION UNDER FAULTS

4.1 Introduction

The EMTP software is a powerful tool for modelling the fault transients' phenomena in power system. This chapter gives a brief outline of the EMTP software and this is followed by a comprehensive study of the transient voltage and current signals simulated at one end of a typical 11kV underground cable system. As mentioned in previous chapter, for this part of the study, the EMTP software is used for modelling the distribution system into which is embedded the previously developed cable model based on CM. The voltage and current waveforms presented are under a variety of different systems and fault conditions including different types of tapped loads, remote source connection, different types of fault and fault position, both short circuit and open circuit faults, ect.

4.2 EMTP Program

The EMTP is a standard software widely used by the community for the simulation of electrical systems transient. It is a universally accepted program for the digital simulation of the Electromagnetic transient phenomena, as well as electromechanical behaviour of electrical power systems.

The EMTP basically, consist of six supporting programs, which are ATPDraw, PCplot, Programmer's File Editor (PEF), PlotXY, GTPPlot and ATP Control Centre. In this project, only the first two supporting programs are used thus only these two programs are explained herein.

4.2.1 ATPDraw

ATPDraw is a graphical, mouse-driven pre-processor to EMTP. It helps to create and edit the model of the electrical circuit that the user wants to simulate interactively. In ATPDraw, the user can create any electrical circuit by selecting the predefined components from an extensive library. After constructing the required circuit, it is

sorted by ATPDraw under .adp file. Next, ATPDraw generates the .atp file, which can be used for subsequent simulation as input to the EMTP.

In the case of the cable model with the EMTP, ATPDraw contains a module that reads punch files from Line/Cable constants and creates Lib files automatically. A punch file is a database relating to the model which specified by the user. Also the specified objects are included in the .atp file by $Include, <.lib filename>. In this respect, the new cable model can be added to the EMTP by creating a .lib file and has been shown in Table-1 in chapter 3.

4.2.2 PCPlot

When the EMTP program recognizes all the data and executes the case, it will create a .pl4 file. This is actually a plot file which contains the voltage and current signals of a particular simulation study. PCPlot is a plotting program originally designed for using with EMTP, but is now able to work satisfactorily also with ASCII data files. The user can read the outputs of the simulation, which are the .pl4 files by using PCPlot.

It should be mentioned that the .pl4 file cannot be read by the MATLAB program; this file thus needs to be converted into the .mat file by converter.exe program. In the data simulation process, the total voltage and current signal samples associated with all conditions are sorted into the data file in order to process the signals using some toolboxes in the MATLAB.

4.3 The Distribution System

The distribution system basically comprises of a network of feeders and distributors together with their associated sub-stations which contain switchgear and transformers. The feeder is a circuit carrying power from the main sub-station to a secondary substation. The Distributors supply power to individual customers and may therefore have service connections tapped off at intervals throughout its length. There are various types of network configurations, depending on the load density and system voltage level. Some typical types of network configuration are mesh network, interconnected network,

link arrangement, open loop and radial system. A radial system is the most commonly employed network in a low voltage distribution system because of its simplicity and also its ability to save cost. However, its major disadvantage is a lack of security of supply, as it does not have an inherent supply backup property. Any faults occurring at the upstream of the power supply will adversely affect all the downstream costumers. Also the open loop system in 11 kV underground systems is more common because of its simplicity and reliability; for this reason, in this research only such a system is considered and this is shown in fig(51).

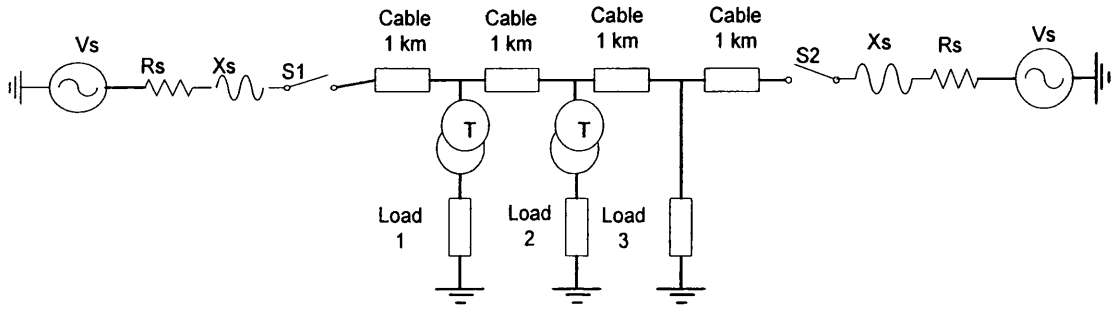

Fig.51- The 11 kV underground electrical power distribution network

Fig.(51) depicts a practical power distribution system with a remote source (the studies presented relate to either the latter connected or disconnected); comprises of a 4 km three-phase cable with three different loads (static and dynamic) tapped at 1 km, 2 km and 3 km from the main source. The first and second loads are low voltage loads and are supplied through a 11/0.4 kV transformer but the third load is connected to the 11 kV feeder directly. The specifications of various elements employed are as follows:

4.3.1 Source Configuration

The employed sources are star connected and the natural point is earthed with a solid conductor. The data relating to the sources is:

Short circuit level S_{sc} = 121 MVA

X/R =10

Xs $=2\Omega$

Rs $=0.2\ \Omega$

f =50Hz

The relationship between the source capacity and series impedance is given by:

$$Z_s = \frac{|V_L|^2}{S_{sc}} \quad , \quad Z_S = R_S + jX_S \quad , \quad R_s = \frac{Z_s}{\sqrt{1+(x_s/R_s)^2}}$$

V_L is the line voltage and equal to 11kV.

4.3.2 Loads

In the distribution system studied, different types of load including static, dynamic and a combination of them are considered. Herein, three loads are tapped into the system and the specifications of each of them are as follows:

-Load 1

This is a three-phase static load and is considered as a series R-L with a typical power factor assumed to be 0.8 lagging. The setting in the EMTP is: R_L = 1 Ω and L=2.38 mH $\Rightarrow$ X_L = 0.7477 Ω (at 50 Hz), V_L=380V (load voltage RMS). With regard to the following calculation, the active and reactive power of the load are P_L=92.62 kW and Q_L=69.252 kVAR:

$$S_L = \sqrt{3} * I_L * V_L \Rightarrow I_L = \frac{S_L}{\sqrt{3} * V_L} \tag{3-1}$$

$$P_L = 3 * R_L * I_L^2 \Rightarrow P_L = \frac{R_L * S_L^2}{V_L^2} \tag{3-2}$$

$$\frac{Q_L}{P_L} = \frac{X_L}{R_L} \Rightarrow Q_L = P_L * \frac{X_L}{R_L} \tag{3-3}$$

$$S_L^2 = P_L^2 + Q_L^2 = P_L^2 * (1 + \frac{Q_L^2}{P_L^2}) \tag{3-4}$$

From Eqs(3-2 ,3-3 & 3-4) active power becomes:

$$P_L = \frac{V_L^2}{R_L * (1 + X_L^2 / R_L^2)} \tag{3-5}$$

-Load 2

This type of load is a combination of the static and dynamic three-phase loads. In this work the dynamic load has been considered as a induction motor since the vast majority of the dynamic load taps are of this nature. The data relating to load 2 is:

Dynamic load: V_L=380V_{rms} , f=50Hz, P_L=200hp

Static load: V_L=380V_{rms} , R_L=1Ω, L=2.38mH, P_L=92.62kW, Q_L=69.252kVAR

-Load 3

This type of load is a three-phase static load with the nominal voltage 11kV. This load is represented as a series R-L with a typical power factor assumed to be 0.8 lagging. The specifications of the load are:

R_L = 616 Ω and L=1500 mH ⇒ X_L = 471.2 Ω, P_L=124kW, Q_L=95kVAR

4.3.3 Transformers

In order to simulate the data based on a practical network, the network considered has two transformers for supplying load-1 and load-2. The specifications of both transformers in the EMTP are as follows:

Name : General saturable transformer, 3 phase, 2 windings, Δ/Yg connection

R_m : 10^{12} Ω

Primary : V_{phase}=11kV, R_p=1 Ω, L_p=28.6mH

Secondary: V_{phase}=0.231kV, R_s=0.00044 Ω, L_s=0.01146mH

4.3.4 Cables

The network has 4 sections of cable and each section is 1km in length and all the cables are the same. The type of cable is XLPE, three-phase pipe type cable (core+grounded sheath) and the specifications of the cable are as follows:

Core : r_{in}=0, r_{out}=6.1mm, ρ=2.3*10^{-8} Ω.m, μ_r=100
Sheath : r_{in}=10mm, r_{out}=11mm, ρ=17*10^{-8} Ω.m, μ_r=100
Insulator between core and sheath: thickness=3.9mm, ε_r=3
Insulator between pipe and sheath: ε_r=8
Type of model : conformal mapping model

4.4 Practical Considerations

After scaling down the phase voltage and current waveforms to the appropriate operating levels, the discrete data is converted into a digital form as waveform samples through an emulation of a modern microprocessor-based digital fault recorder (DFR)

installed in a sub-station. The data via the transducers is recorded into the DFR, conditioned via the A/Dinterface, digitised through an ADC and then processed by the fault location algorithm implemented within the microprocessor.

Since the fault location technique is designed to work with recorded voltage and current signals via VTs and CTs which are subsequently digitised within the digital hardware associated with a pracical fault recorder, it is crucial to take into account any transducer/hardware errors so that the performance of the fault location technique affected is close to a practical situation. In this respect, the principal sources of errors are: (i) the frequency responses of the CTs and VTs, together with the analogue interface modules within the hadware, (ii) the response of the anti-aliasing filters, and (iii) the quantisation erors arsing as a result of converting analogue signals into sampled values through the ADC (analogue to digital converter).

The following outlines the various stages involved in the emulation of a practical DFR

4.4.1 Aliasing Effects

According to sampling theorem,if the highest frequency component in a signal is fmax, then the signal should be sampled at the rate of at least 2*fmax for the samples to describe the signal competely (and avoid any aiasing effects):

$$Fs \geq 2*fmax \qquad (3\text{-}6)$$

An important point to remember is that a signal often has significant energy outside of highest frequency of interest and/or contains noises, which invariably has a wide bandwidth. Thus the sanpling theorem will be violated if the signals or noises outside the band of interest are not removed. In practice, this is achieved by first passing the signal through an analogue anti-aliasing filter before the ADC.

The MATLAB program contains functions for designing four types of digital filters based on analogue filter design. Butterworth fiters have maximally flat passbands and stopbands. Chebyshev type I fiters have rippes in the passband, Chebyshev type II filters have ripples in the stopband and elliptic filters have ripples in both the passband

and stopband. In this research, Butterworth third order lowpass filter is employed to filter out any spurious noise and limit the frequency contents of the signals to < Fs/2. In this respect, fs=100kHz, fo=42kHz and fc=fo/fs, where fs=sampling frequency, fo=cut-off frequency, fc=normalised frequency.

To design a lowpass Butterworth filter, its coefficients are computed by using butter function as below:

[b,a]=butter(N,wn);

where N is the order of the filter and wn=2*fc. Thus, for a third-order lowpass Butterworth filter with 42kHz cut-off frequency, the coefficients can be determined as follows:

[b,a]=butter(3,42/50);

Now the signals can be filtered easily by using filter function as follows:

I_{phasef}=filter(b,a,I_{phase});
V_{hasef}=filter(b,a,V_{hase});

Where I_{phasef} and V_{phasef} are the filtered signals, I_{phase} and V_{phase} are the original signals, b and a are the filter's coefficients.

4.4.2 Quantization Error

The quantization error arises as a result of the analogue signals being digitised using an ADC. The error is very much a function of the resolution of the ADC employed that the most commonly employed ADC in power system protection is the 16-bit ADC with a voltage of ±10V. In this research, the simulation of quantization process is based on this type of ADC and is employed using the MATLAB program. The employed command in MATLAB is:

```
iphasefq=floor(iphasef*2^15/7000)*10/2^15+10/2^16;
vphasefq=floor(vphasef*2^15/22000)*10/2^15+10/2^16;
```

In order to keep the voltage and current signals within the range ±10V, these signals are divided by scaling factors based on the maximum values of the two signals.

In order to calculate the error due to quantization, the following points are considered. For a 16-bit converter: b=16bit, $N=2^{(b-1)}$, Xm=10V, $Q=Xm/N=3.0518*10^{-4}$, m=int(Xa/Q), Xd=m*Q, ε=| Xd-Xa |

Where b=number of bits, Xm=A/D supply voltage, Q=step value, m=digital value, Xd=quantized output signal, Xa=actual signal and ε=quantization error.

4.4.3 Frequency response and saturation of the CTs and VTs

The fault data recorder provides the voltage and current signals via the VTs and CTs which are connected to the distribution network. Both the CT and VT have limitations in terms of their frequency bandwidths and possible saturation (particularly in the CTs) and these can cause error in the recorded data. Bandwidth error is produced when the frequency of the transient signals exceed the frequency bandwidths of a CT or VT, these being a few MHz and approximately 50kHz respectively. However, by selecting a sample frequency 100kHz and choosing an anti-aliasing filter with a cut-off frequency of 42 kHz (as is the case herein), the bandwidth errors can be minimised. It should be noted that in order to obtain the LCC (line/cable constant) file in the EMTP, the sampling time must be less than twice the travel time (forward & backward) at the maximum modal velocity and the minimum cable length under a fault. With regard to a maximum cable velocity of propagation of $2.623*10^7$m/s (as discussed previously), the sampling rate within the EMTP has to be artificially set to 10MHz i.e. 100 times the normal sampling frequency of 100kHz; this allows faults to be put at a minimum cable length of 2.623m from the measuring end without introducing any computational errors within the EMTP software. However, since the data has been simulated within the EMTP, it is then decimated by a factor of 100 i.e. only every 100^{th} sample is taken as a new data file created, based on a sampling rate of 100kHz for subsequent processing.

Errors due to saturation are produced when the measuring transformer's core cannot support the flux generated by the transient signals, in particular when the waveforms have an offset. However, this problem is not so serious in low voltage underground

cables compared to high voltage transmission lines because of the relatively lower X:R ratio in the case of former and through a careful selection of the scaling factor (as is the case herein) this problem can be minimised.

4.5 Fault Conditions

Both the steady state and fault transient voltage and current waveforms can be influenced by such factors as type of fault, fault inception angle, fault distance, fault resistance, source configuration, type of load, etc. in order to research and investigate any fault location/protection technique, it is vitally important to employ data simulation under a whole variety of different systems and fault conditions, for the development of the new technique. The following gives a summary of all the different systems and fault conditions studies for generating the requisite data:

- Single phase to ground short-circuit fault (SPH-G-SC) for 3 cases: ag-sc, bg-sc and cg-sc
- Two phase to ground short-circuit fault (2PH-G-SC) for 3 cases: abg-sc, acg-sc and bcg-sc
- Phase to phase short-circuit fault (2PH-SC) for 3 cases: ab-sc, ac-sc and bc-sc
- Three-phase short-circuit fault (3PH-SC) for one case: abc-sc
- Single phase open-circuit fault (SPH-OC) for 3 cases: a-oc, b-oc and c-oc
- Two phase open-circuit fault (2PH-OC) for 3 cases: ab-oc, ac-oc and bc-oc
- Three-phase open-circuit fault (3PH-OC) for one case: abc-oc

In addition to the aforementioned types of fault, the following conditions are also considered.

- Three inception angles including 90°, 135° and 180°
- 13 fault distances from the recording point including 50m, 100m, 500m, 900m, 1100m, 1500m, 1900m, 2100m, 2500m, 2900m, 3100m, 3500m and 3900m
- 8 fault resistances in the case of single phase to ground fault including 0.1Ω, 0.2 Ω, 2 Ω, 6 Ω, 10 Ω, 14 Ω, 17 Ω and 20 Ω
- 4 fault resistances in the case of two-phase to ground fault including 0.1 Ω, 2 Ω, 10 Ω and 20 Ω
- The distribution network with and without the remote source

According to the aforementioned conditions, in this research, more than 3660 cases are processed.

Studies have shown that at the fault classification stage using an ANN, in addition to employing the phase components of voltage and current, the simulation of modal components of current waveforms make the results more accurate; these are particularly useful for recognising accurately the two phase faults whether are grounded or ungrounded. Modal components are obtained from appendix-2 Eq.(A2-13) as follows:

$$I_{modal} = T_i^{-1} . I_{ph}$$

Where T_i is the transformation matrix.

The following gives a selecting of some typical voltage and current waveforms simulated under different systems and fault conditions. Essentially, seven types of fault are considered.

4.5.1 Simulated waveforms for a single phase to ground fault

Because of limitation of space, the results presented herein are only a sample number of waveforms. Also as mentioned before such signals are directly obtained from the EMTP software and at this stage are raw signals. Fig(52) depicts the three phase voltage waveforms and includes the original, the filtered and quantized signal for 'a' phase to ground fault, Rf=10Ω, distance of fault=3500m, inception angle=135 degrees; the remote source is not connected.

The sample rate is 100 kHz and recording time is 40ms; this gives the dimensions of signal vectors as 4001 and the maximum frequency is 50kHz. As expected, the initial distortion of the faulted 'a' phase is much higher than the two healthy phases 'b' and 'c'. In all phases, the transients die down after a cycle (20ms). In order to discern the differences between the original, the filtered and quantized signals, fig.(52) is zoomed in on the higher distortion part of signals (i.e. between 5 and 10 ms) and fig.(53) shows the resulting signals. As it can be seen, the filtered signals and the original signals are almost identical and this is so because the cut-frequency of the filter is 42kHz and this is very close to the maximum frequency content of 50kHz in the original signal. Moreover, because the quantisation is done through a high resolution 16-bit ADC, there is little difference between the filtered and quantized signals. Fig.(54) depicts the corresponding three-phase current signals, again, the original, filtered and quantized signals. As would

be expected, the transients are significantly smaller than those on the voltage signals, and again, as would be expected, there is little difference between the original, filtered and quantised signals.

As mentioned before, in addition to the phase components of voltage and current signals, modal components of currents play an important role at the fault classification stage, particularly in the case of two-phase to ground and phase to phase faults. In this respect, fig.(55) depicts the modal components of the quantised current waveforms. It is important to know that both mode1 and mode 2 signals increase significantly when the fault occurs.

Since the waveforms of the original, filtered and quantised signals are the same and they are only different in terms of the range, only filtered signals will be considered for the other types of fault.

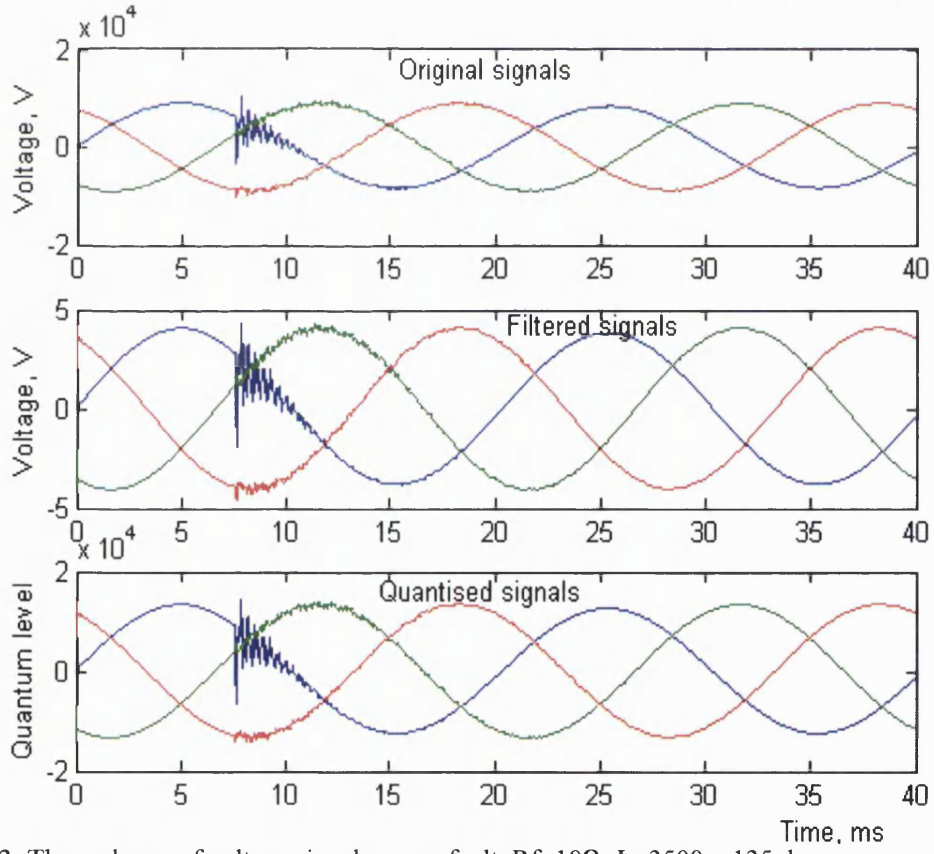

Fig.52- Three phases of voltage signals, ag-sc fault, Rf=10Ω, L=3500m,135 degrees one source

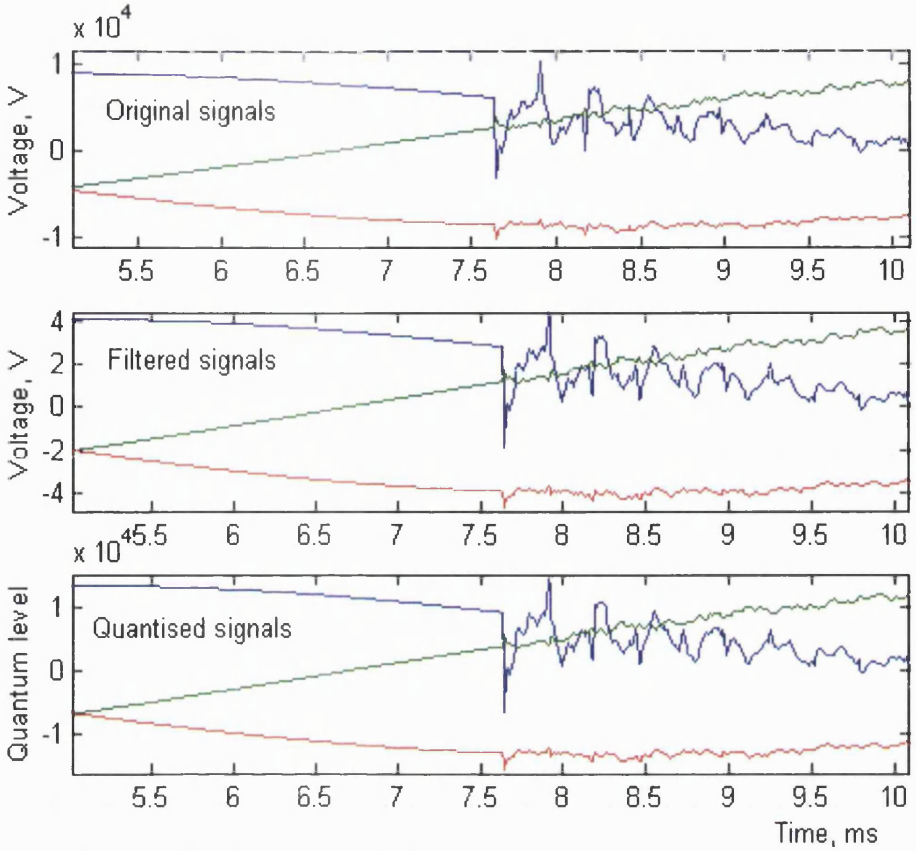

Fig.53- Three phases of voltage signals, zooming of fig.(52)

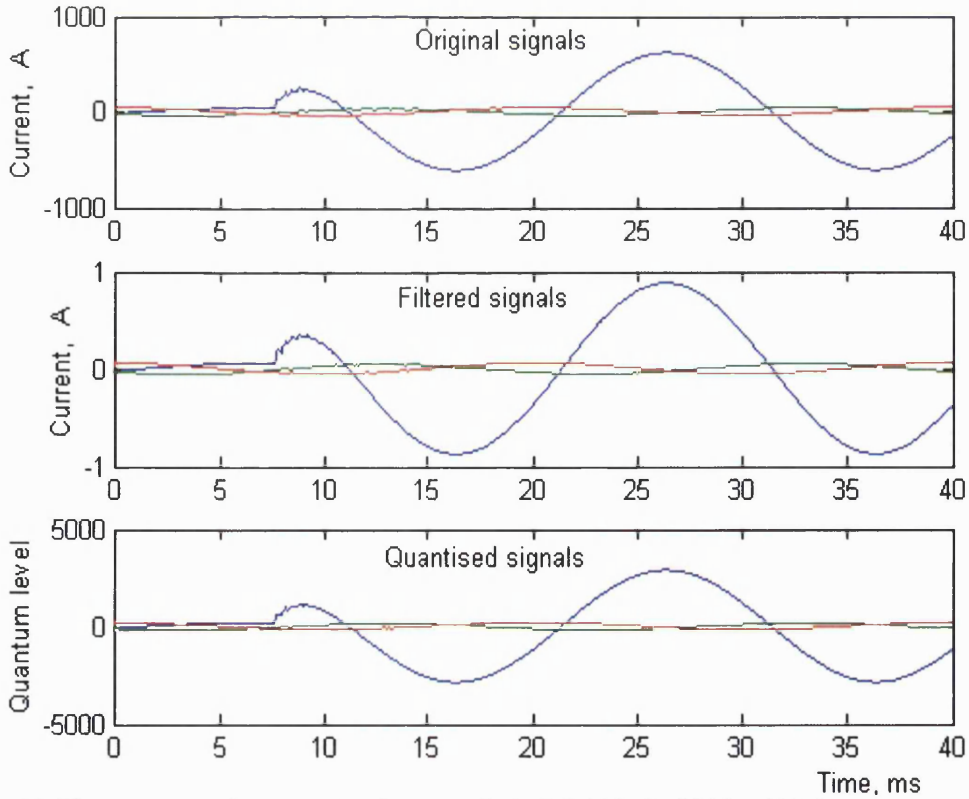

Fig.54- Three phases of current signals, ag-sc fault, Rf=10Ω, L=3500m,135 degrees one source

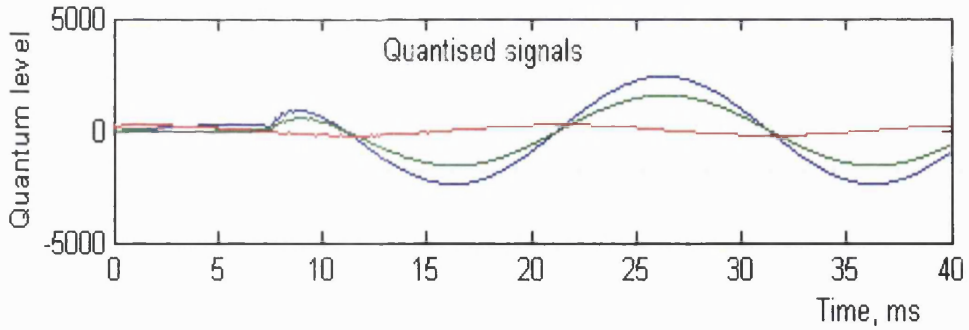

Fig.55- Three modes of current signals, ag-sc fault, Rf=10Ω, L=3500m,135 degrees one source

Figs.(56) shows the phase voltage and current waveforms at the measurement point for an 'a' phase to ground fault, Rf=0.1Ω, distance of fault=1100m, inception angle=90 degrees, with and without remote source connected. It is apparent that since the fault resistance is very small, thus the effect of remote source is very small, particularly in terms of the amplitude of current in faulted phase.

In order to observe the effect of remote source on the voltage and current signals, the fault resistance should be increased. The waveforms shown in Fig(57-59) relate to ag-sc fault; the distance of fault is 1100m, the fault resistance Rf=10Ω and inception angle=90 degrees, with and without remote source connected. It can be seen from fig.(57) that the initial transient of the voltage signals in faulted phase is higher in the case of one source but transient damping are the same for both cases. Also fig.(57) depicts that the initial transients for healthy phases 'b' and 'c' are higher in the case of connecting the remote source and the transients in healthy phases die down faster in the case of one source condition.

The influence of fault resistance on the voltage signals can be observed by comparing Figs.(56 and 57). These two figures show the voltage signals and as it can be seen, the initial distortion in all three phases (faulted and healthy phases) are much higher in comparison with fig.(57) because of being Rf much smaller in former. Also it is clearly evident that the transients die down much faster in the case of 10 Ω because of being higher the fault resistance.

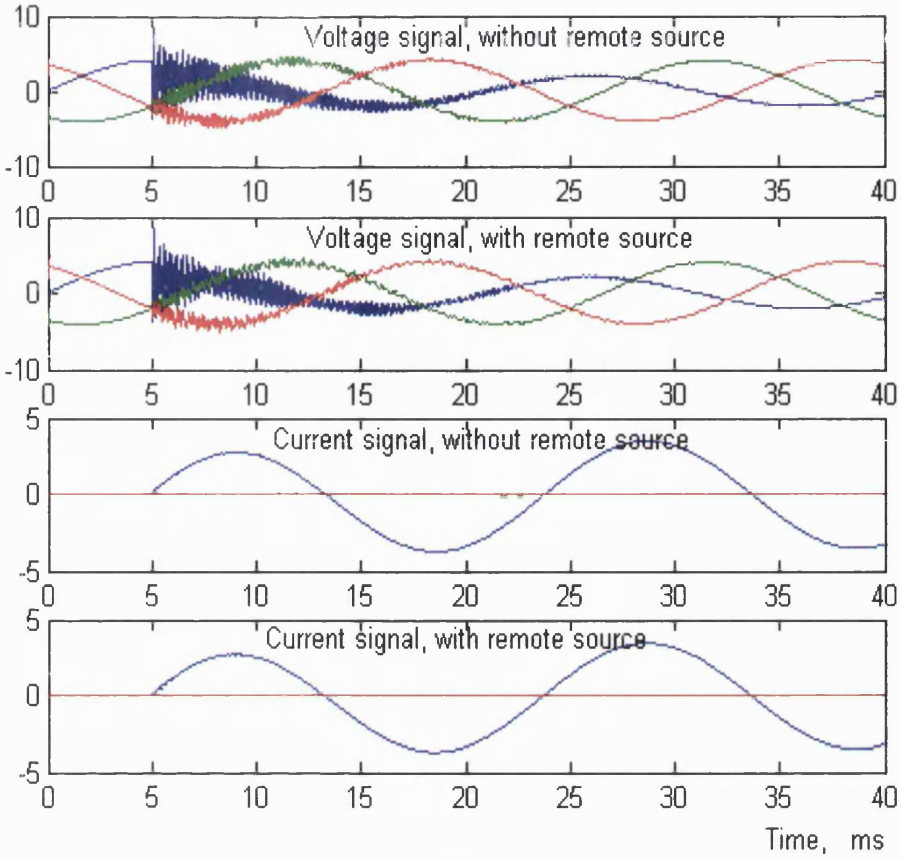

Fig.56- Three phases of voltage signals, ag-sc fault, Rf=0.1Ω, L=1100m, 90 degrees

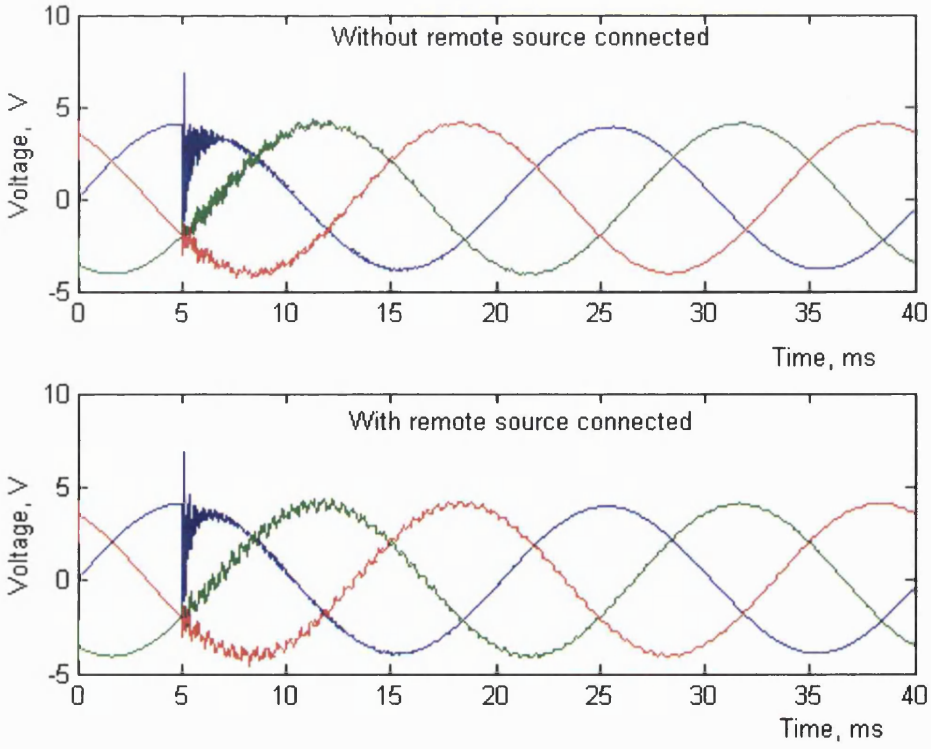

Fig.57- Three phases of voltage signals, ag-sc fault, Rf=10Ω, L=1100m, 90 degrees

Fig.(58) depicts the behaviour of the three-phase current signals both with and without the remote source connected. It can be seen (different scale) that the amplitude of current of the faulted 'a' phase is slightly larger in the case of the one source, in comparison to the case when the remote source is connected and this can be directly attributed to an increase in the voltage drop across the fault resistance Rf in the case of the latter. Also the transients in both healthy phases are higher in the case of the remote sources connected.

Fig.(59) shows three modes of current for both single and two sources connected. Here again, the behaviour of the signals is somewhat similar to that of the phase current i.e., the amplitude of the three modes are larger in the case of the one source but, the transients in three modes are higher in the case of two sources connected.

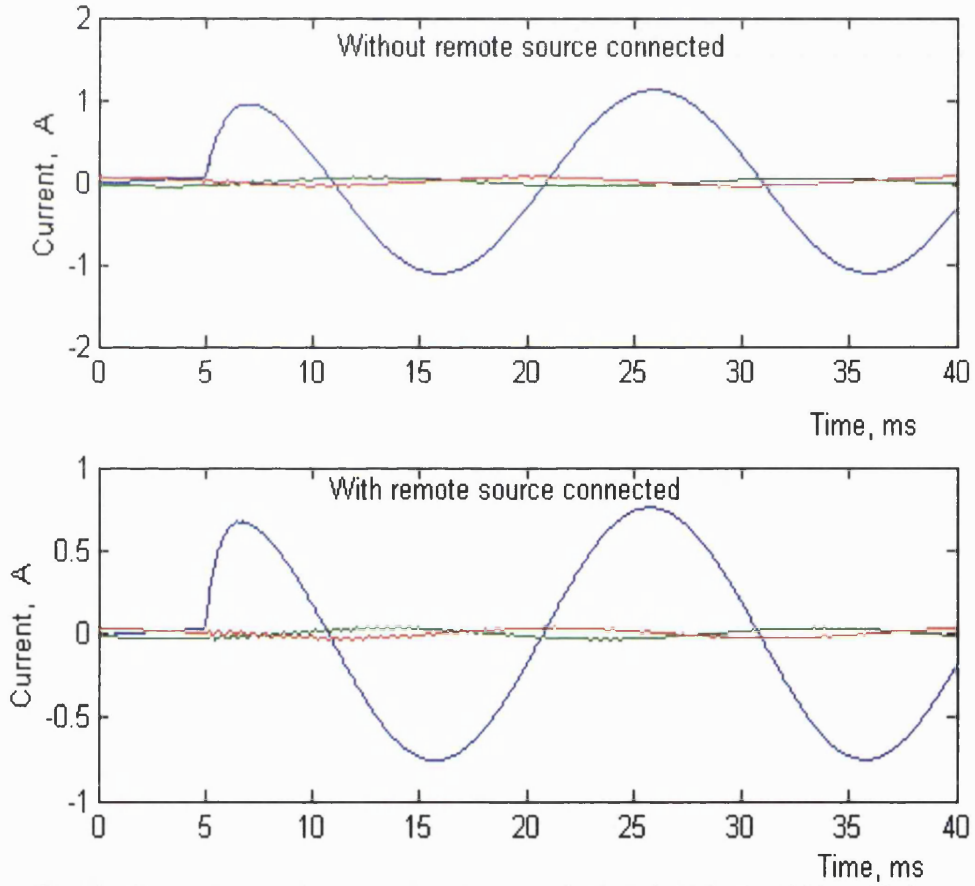

Fig.58- Three phases of current signals, ag-sc fault, Rf=10Ω, L=1100m, 90 degrees

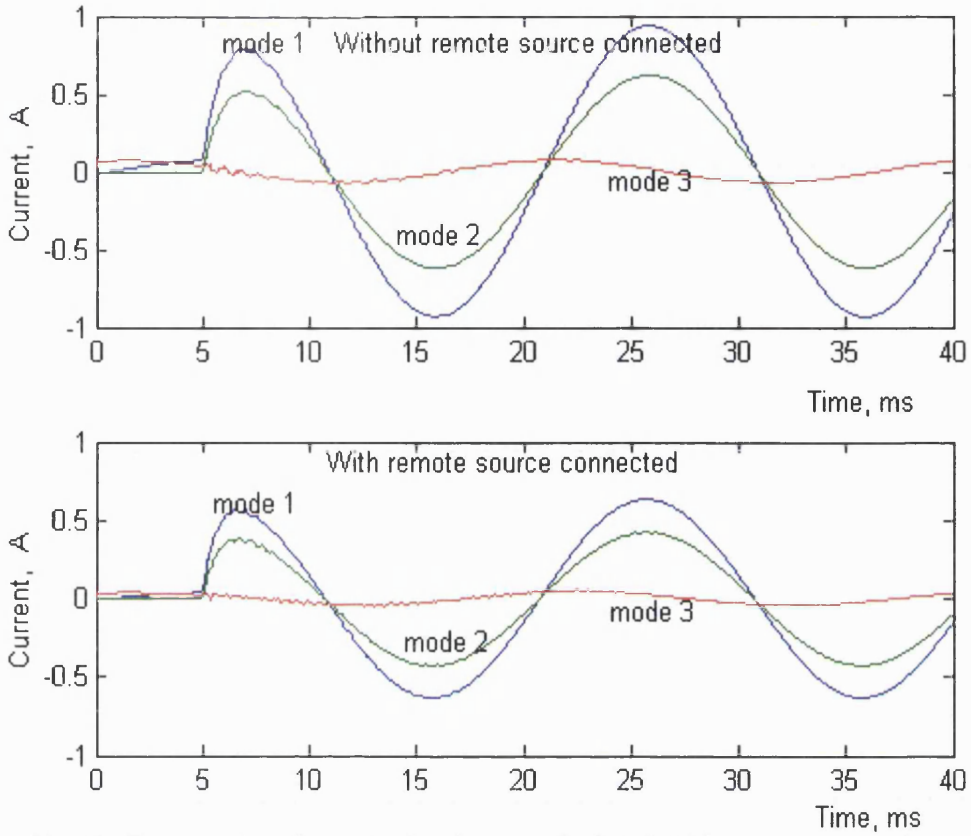

Fig.59- Three modes of current signals, ag-sc fault, Rf=10Ω, L=1100m, 90 degrees

4.5.2 Simulated waveforms for two-phase to ground faults

Because of the limitation in space, only a few sample fault conditions and related results are presented. However, an attempt is made to select such conditions that can bring out the salient features in the behaviour of the signals. In this respect, inception angles 90 degrees and 180 degrees are considered (based on 'a' phase signal) because they are related to the minimum and the maximum distortion respectively in the case of bcg-sc fault. Also typical fault resistances of 0.1Ω and 10 Ω signifying a small and a large Rf are selected in order to ascertain the effect of remote source and Rf on the voltage and current signals at the measurement point. It is apparent that the smaller Rf, the effect of the remote source is the less. The distance from the recording point is 1100m in all the cases presented. With regard to the aforementioned points, the following four conditions are presented and discussed.

Condition 1: inception angle=180 degrees, Rf=0.1 Ω, bcg-sc fault, with and without the remote source connected.

Condition 2: inception angle=180 degrees, Rf=10 Ω, bcg-sc fault, with and without the remote source connected.
Condition 3: inception angle=90 degrees, Rf=0.1 Ω, bcg-sc fault, with and without the remote source connected.
Condition 4: inception angle=90 degrees, Rf=10 Ω, bcg-sc fault, with and without the remote source connected.

Figs.(60 to 62) depict the three-phase voltage, three-phase current and the three modal current signals respectively, in the case of condition 1. Each figure contains two graphs associated with and without remote source connected. Fig.(60) shows that the initial distortion in the faulted phases 'b' and 'c' are much higher than the healthy phase 'a' for both with and without remote source. Also the transients die down quickly in all the three phases in both cases. Since the fault resistance is very small, the effect of remote source is very small. Fig.(61) shows that the initial distortion of current signals are much smaller than voltage signals and the amplitude of faulted phases increases significantly after the occurrence of the fault. Similar results are obtained when the remote source is connected and this is by virtue of the fact that the fault resistance Rf is very small.

Fig.(62) shows the corresponding modal components of the current signals which show an increase in the amplitude of the three modes; importantly there is little difference in both the cases, with or without a remote source connected.

Figs.(63 to 65) are based on Condition 2 and contain the three-phase voltages, the three-phase currents and the three-modal current signals respectively, with and without a remote source infeed. Although in this condition, the Rf is increased to ten Ohms, the effect of a remote source similar to the previous condition is fairly moderate, particularly in terms of low frequency components and the magnitude of the voltage and current signals. Therefore, in spite of a single phase to ground fault, this type of fault is not sensitive to the remote source, particularly in the magnitude of current signals in the faulted phases. Thus in the signal-processing stage, only a single source can be considered. A comparison between figs.(61 and 64) shows that the phase shifts of current signals between faulted phases are close to 120 degrees and 180 degrees in the cases of Rf = 0.1Ω and Rf = 10Ω, respectively. Also, the magnitude of current in faulted phases is much larger in the case of Rf = 0.1Ω.

The reason for the foregoing results in terms of the effect of Rf, are as follows: firstly, when Rf is increased, it is obvious that the amplitude of current in the faulted phases decreases; secondly, when Rf is very small, such as 0.1Ω, due to it being a symmetrical network, the phase shift between phases '*b*' and '*c*' will be close to 120 degrees. When Rf is increased, however, the type of fault will be closer to a phase-to-phase short-circuit fault where the current in the faulted phases is equal but in an opposite direction (this means phase shift is 180 degrees). Fig.(65) shows the modal components of current signals and it is apparent that the effect of the remote source is very small.

Figs.(66 to 71) are based on Conditions 3 and 4 i.e. the inception angle is 90 degrees and Rf is 0.1Ω and 10Ω, respectively. In these two cases, the voltages of the faulted phases '*b*' and '*c*' are equal when the fault occurs. Therefore, the initial distortions are as a minimum. When comparing figs.(60 and 66) and figs.(63 and 69) (same Rf and different inception angles), the aforementioned expectation can be reached. The other results are the same as with previous conditions in that there is only a very small effect of remote sources on the simulated signals. This also applies to the effect of Rf in relation to the amplitude of current signals and the level of phase shift between current signals in the faulted phases '*b*' and '*c*'.

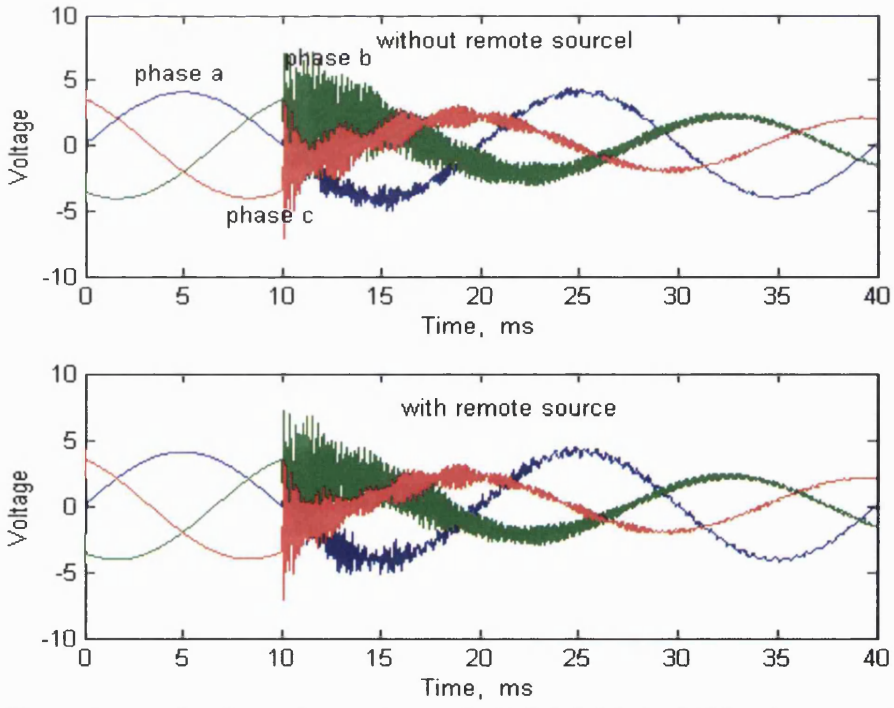

Fig.60- Three phases of voltage signals, *bcg-sc* fault, Rf=0.1Ω, L=1100m, inc. ang.=180

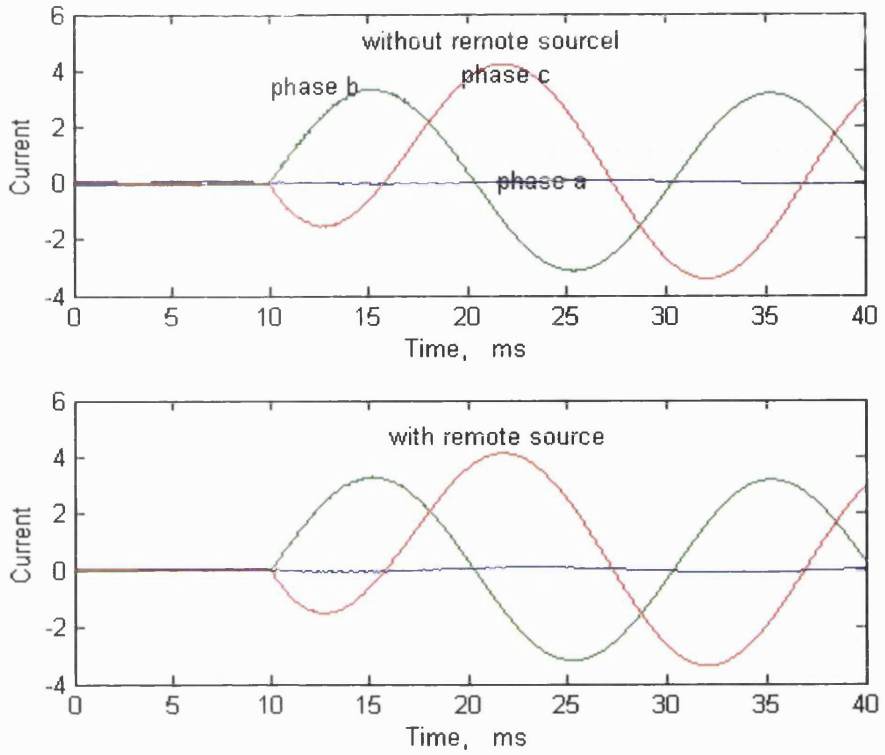

Fig.61- Three phases of current signals, *bcg-sc* fault, Rf=0.1Ω, L=1100m, inc. ang.=180

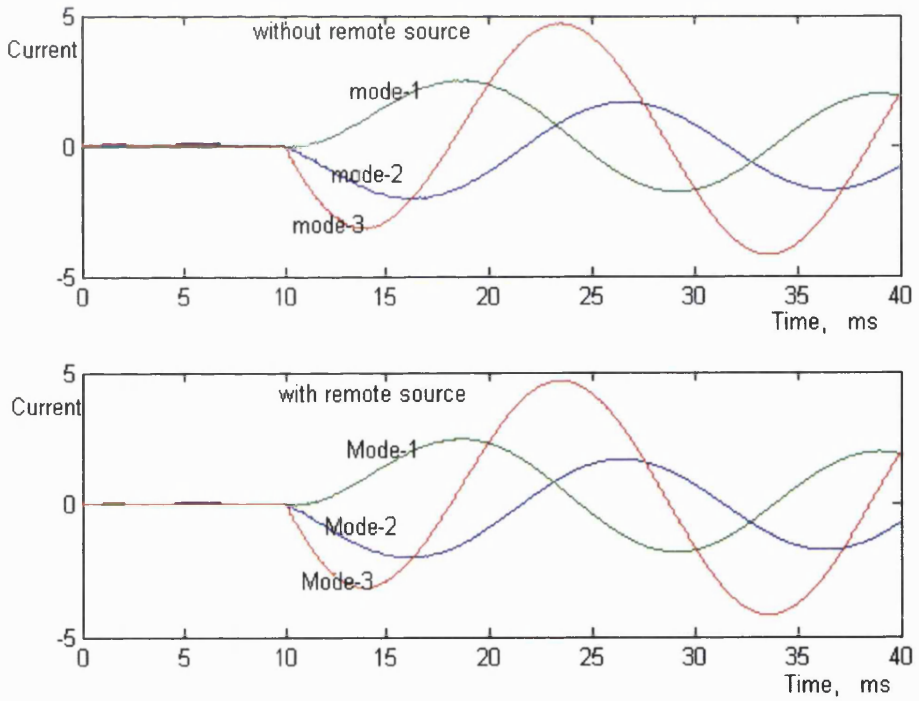

Fig.62- Three modes of current signals, *bcg-sc* fault, Rf=0.1Ω, L=1100m, inc. ang.=180

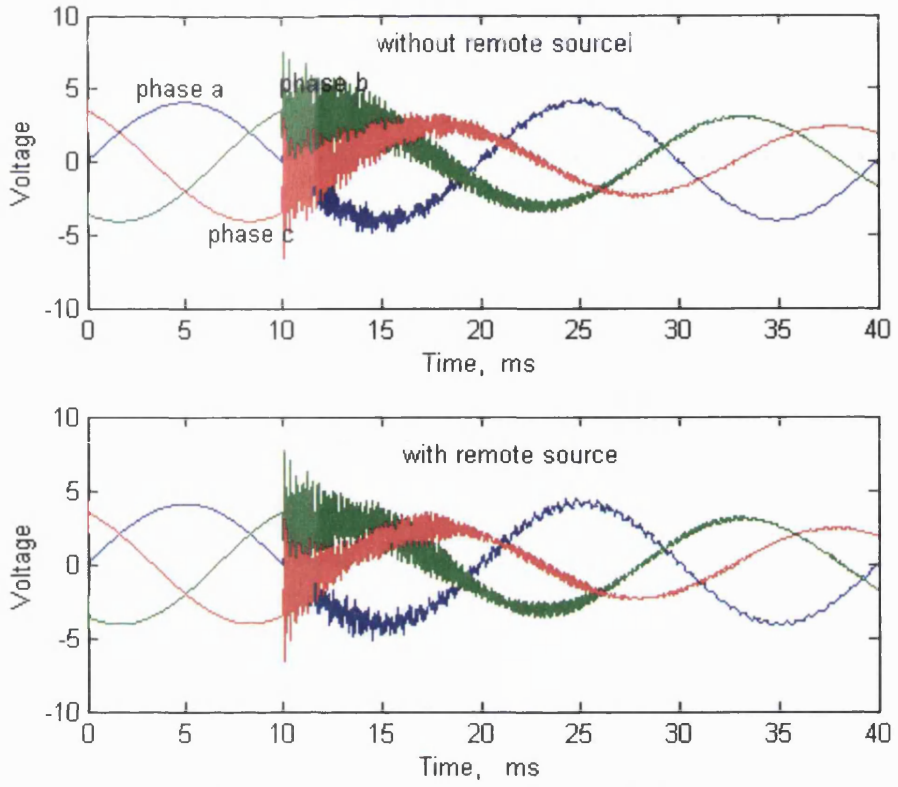

Fig.63- Three phases of voltage signals, bcg-sc fault, Rf=10Ω, L=1100m, inc. ang.=180

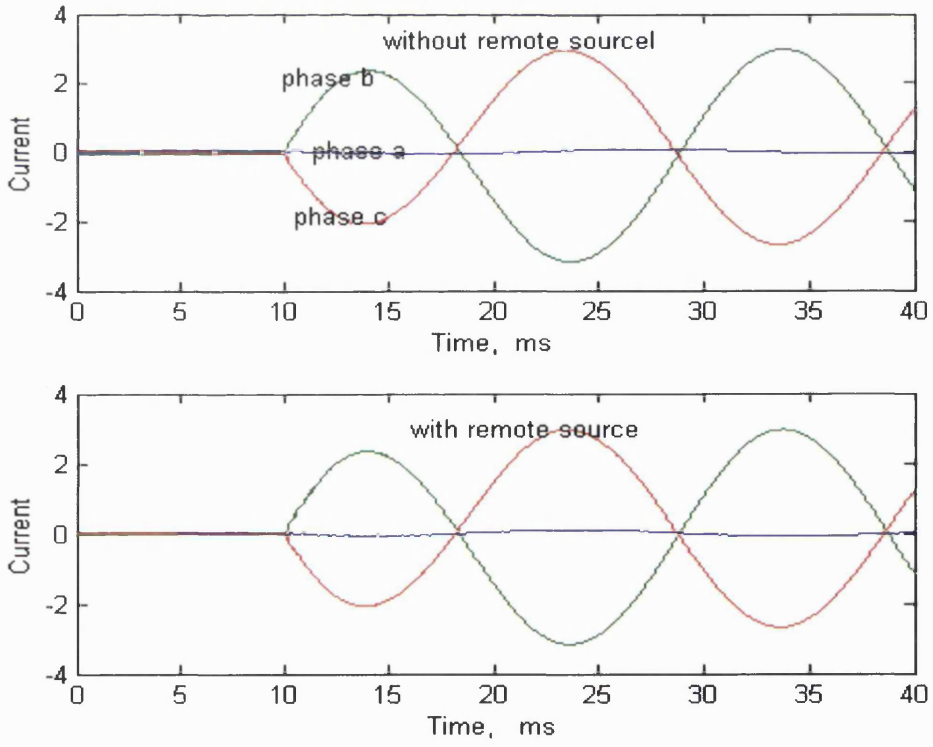

Fig.64- Three phases of current signals, *bcg-sc* fault, Rf=10Ω, L=1100m, inc. ang.=180

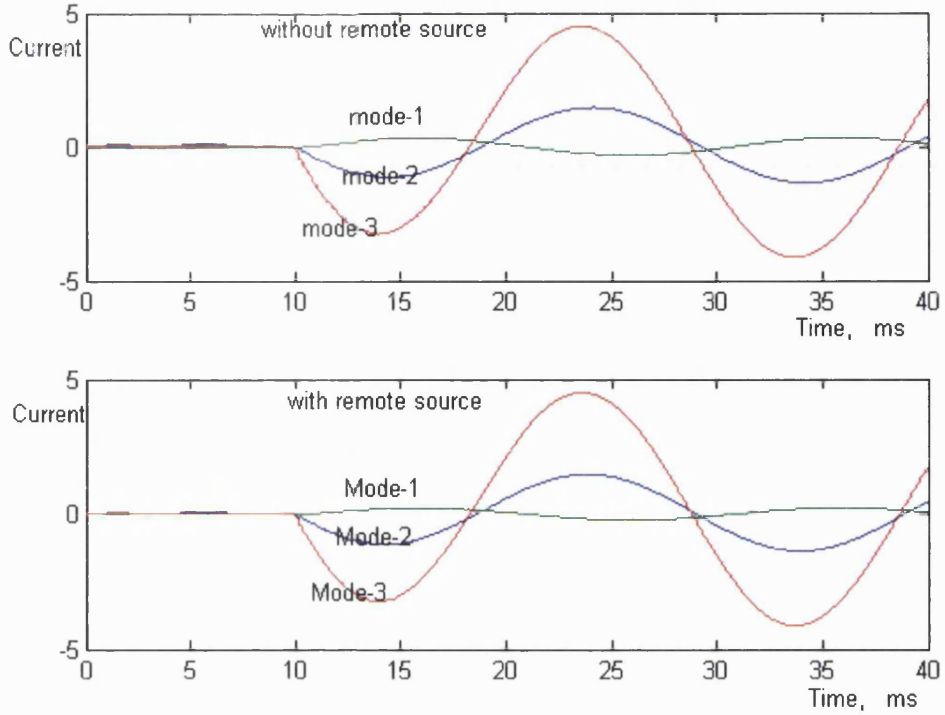

Fig.65- Three modes of current signals, *bcg-sc* fault, Rf=10Ω, L=1100m, inc. ang.=180

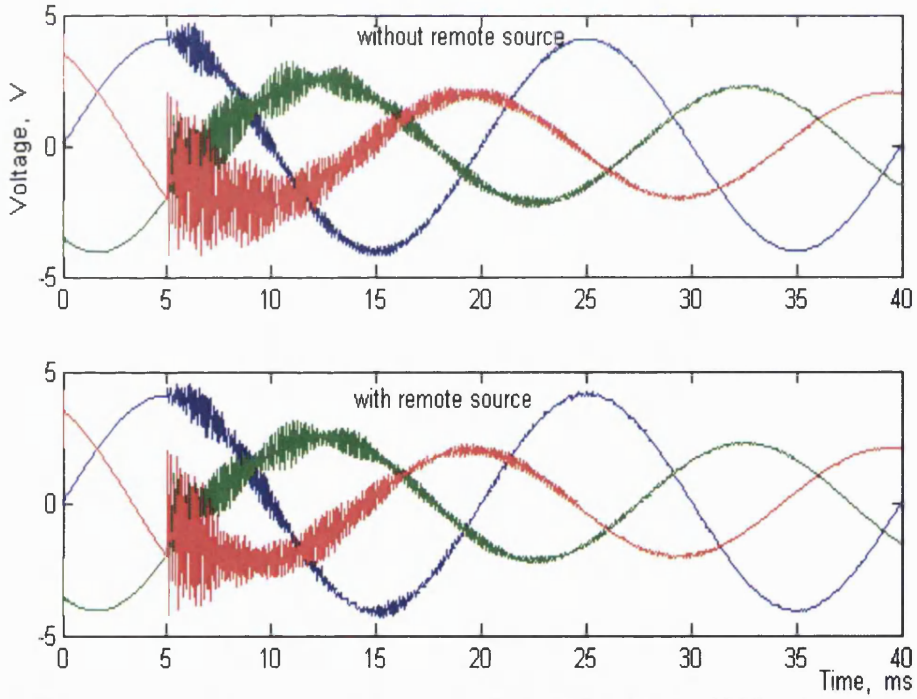

Fig.66- Three phases of voltage signals, *bcg-sc* fault, Rf=0.1Ω, L=1100m, inc. ang.=90

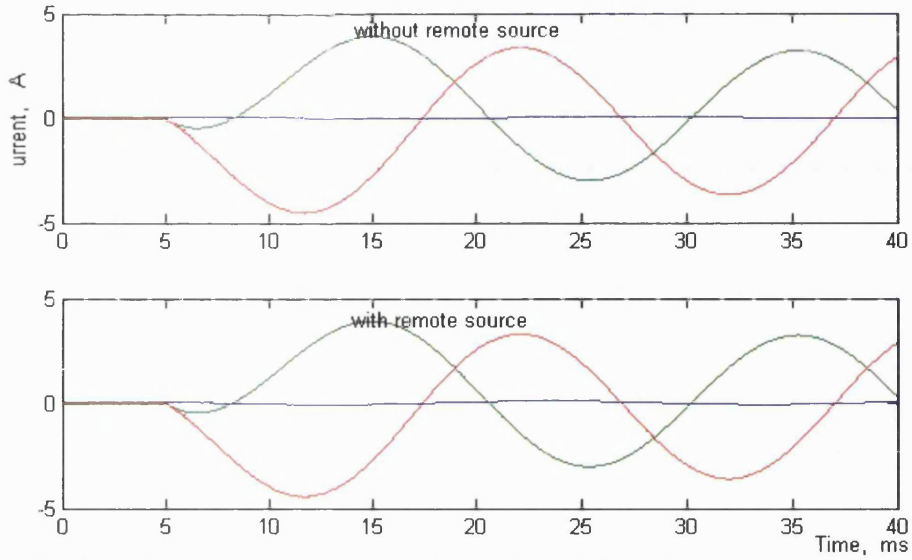

Fig.67- Three phases of current signals, *bcg-sc* fault, Rf=0.1Ω, L=1100m, inc. ang.=90

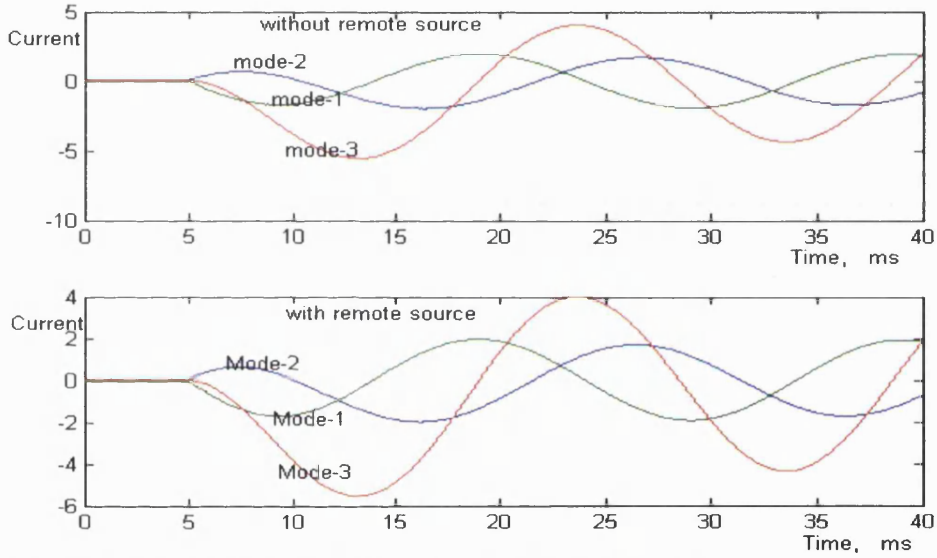

Fig.68- Three modes of current signals, *bcg-sc* fault, Rf=0.1Ω, L=1100m, inc. ang.=90

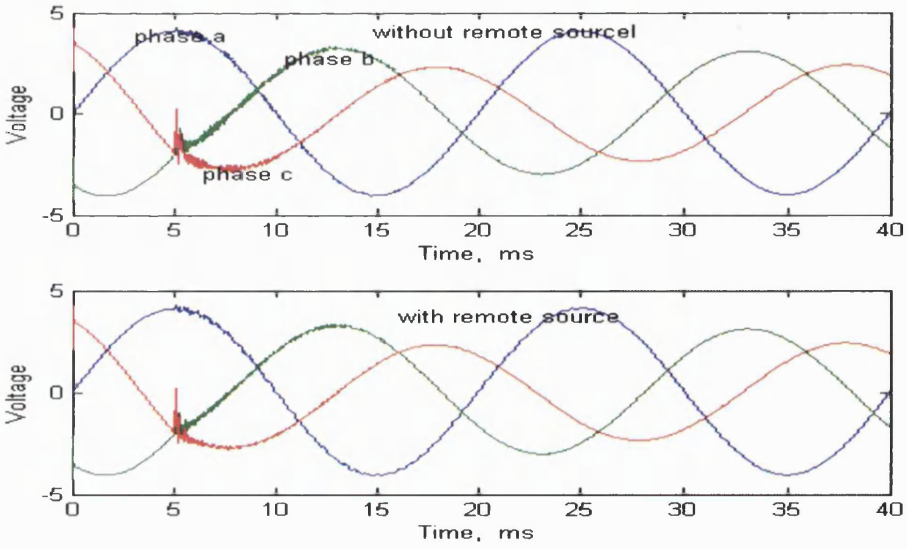

Fig.69- Three phases of voltage signals, *bcg-sc* fault, Rf=10Ω, L=1100m, inc. ang.=90

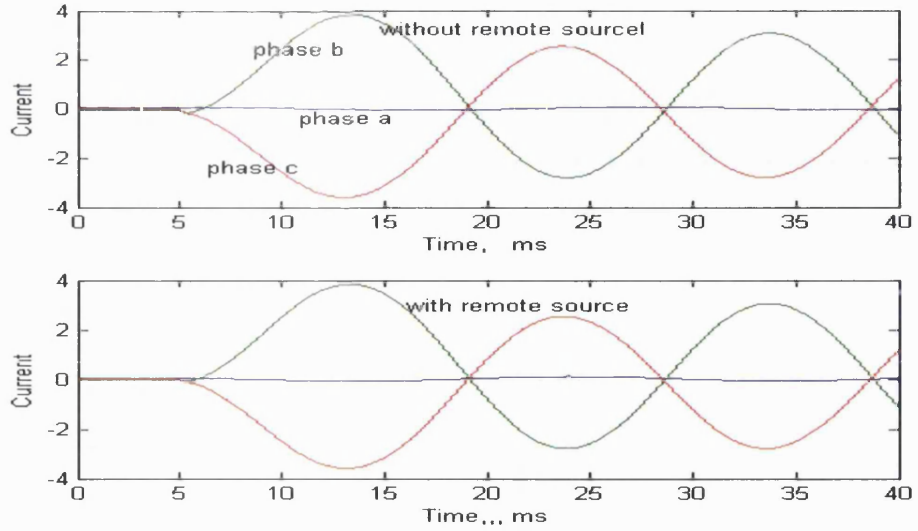

Fig.70- Three phases of current signals, *bcg-sc* fault, Rf=10Ω, L=1100m, inc. ang.=90

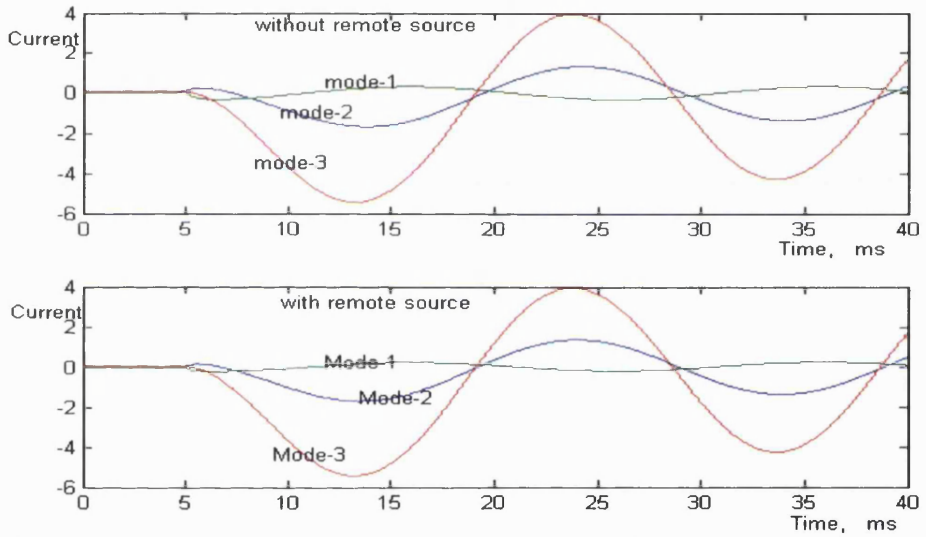

Fig.71- Three modes of current signals, *bcg-sc* fault, Rf=10Ω, L=1100m, inc. ang.=90

4.5.3 Simulated waveforms for phase-to-phase fault

Although a large number of conditions have been considered in the data simulation in order to use the results of the signal processing stage of the research, herein are presented only a few conditions and related results. Contrary to the two-phase to ground fault, the fault considered here is an ungrounded fault. Thus, neither fault resistance nor remote source, affect the obtained results at the measurement point; only inception angle and distance to fault are important parameters that need be considered. In this respect, inception angles of 90° and 180° are studied in order to present the minimum and the maximum distortion of signals. The conditions that are dealt with here are:

distance to fault = 1,100m, *bc-sc* fault, without remote source infeed, inception angles of 90° and 180°, respectively.

Figs.(72 to 74) show the three-phase voltages, the three-phase currents and the three-modal current signals. Each figure contains two graphs categorised by the two inception angles; the upper graph is based on the condition of an inception angle of 90°, while the lower shows the signals corresponding to 180°.

Fig.(72) shows the voltage signals and, as can be seen, initial distortions are much higher in the case of a 180° inception angle (i.e. V_{bc} maximum) because maximum difference in the voltage in the faulted phases occurs at this inception angle. Also, the amplitude of voltage in both faulted phases '*b*' and '*c*' falls considerably after the fault occurs.

Fig.(73) shows the current signals and it is clearly evident that the initial distortions are much smaller in comparison to the voltage signals. Also, the currents significantly increase in the faulted phases, and they are equal but of opposite polarities (180° phase shift). In the first cycle after the fault there is considerable difference between the current magnitudes in the case of a 90° inception angle (i.e. V_{bc} zero), whereas in the second cycle these levels are quite similar. This shows that the inception angle does not ultimately affect the current amplitude, and the larger difference in the first cycle is due to a larger DC offset in current signals (because at an inception angle of 90°, voltage in the two faulted phases is equal and the DC offset in currents will be at its maximum).
Fig.(74) depicts the modal current signals and, as shown, the amplitudes of mode-2 and mode-3 (aerial modes) crucially increase after the fault, but the earth-mode (mode-1) current remains at zero because the type of fault is an ungrounded one. What is interesting is that the important signature to classify and recognize the phase-to-phase fault from the two-phase to ground fault is the amount of earth-mode current, which in the latter is much higher than zero but in the former is zero all the time. A comparison between figs.(62 and 74) proves this.

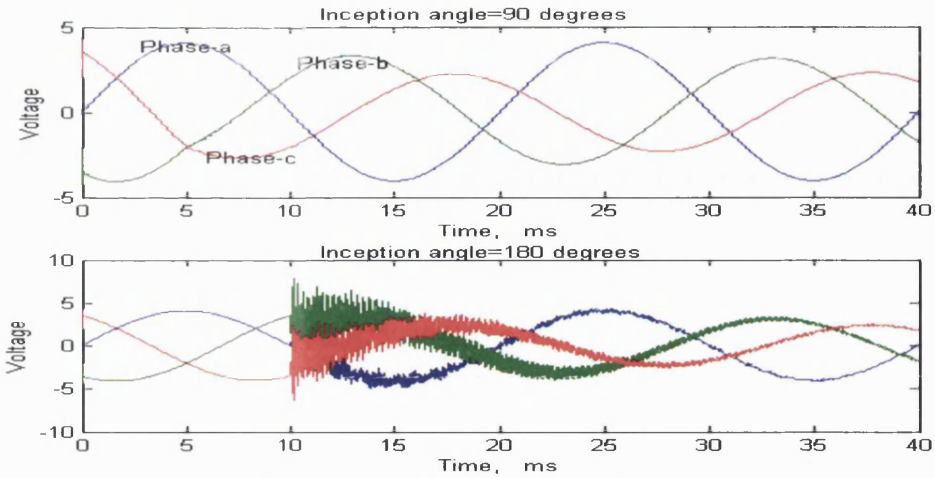

Fig.72- Three phases of voltage signals, *bc-sc* fault, L=1100m

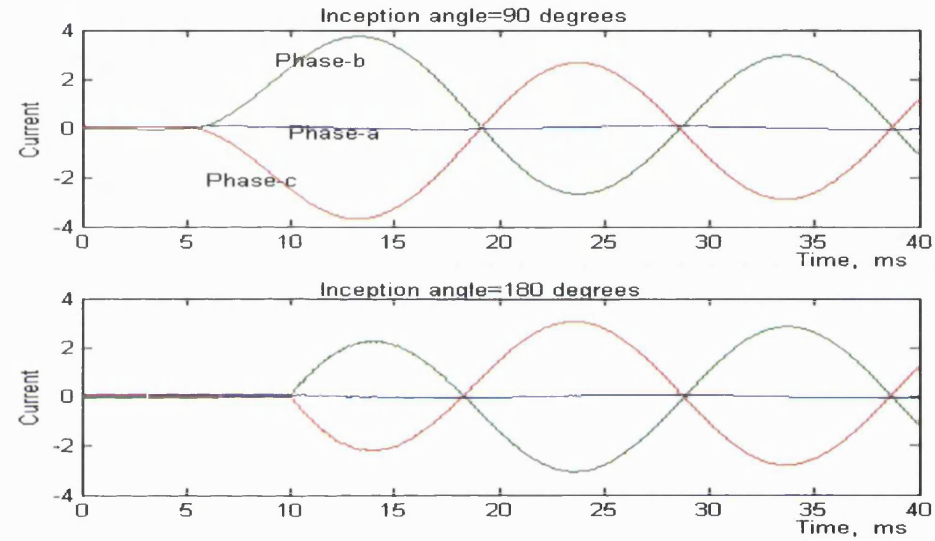

Fig.73- Three phases of current signals, *bc-sc* fault, L=1100m

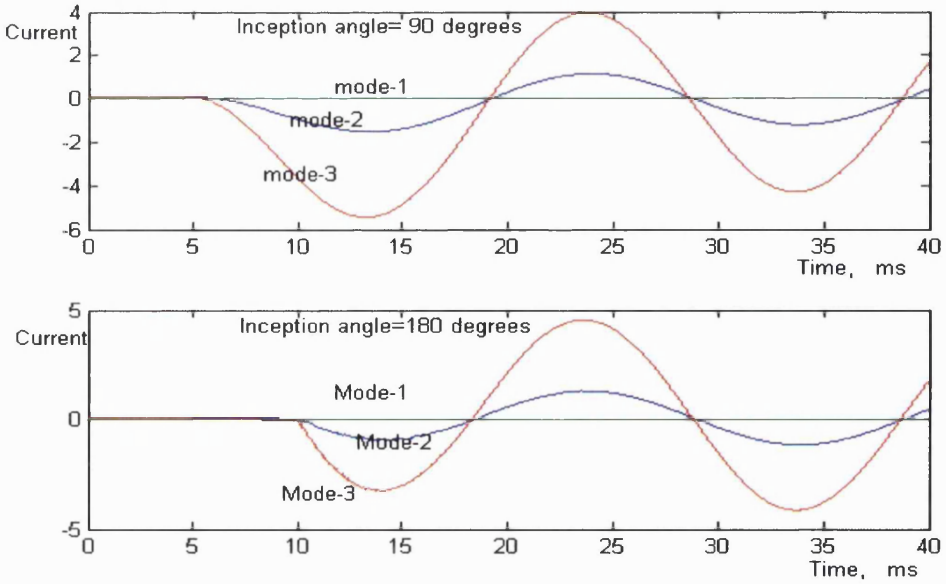

Fig.74- Three modes of current signals, *bc-sc* fault, L=1100m

4.5.4 Simulated waveforms for a three-phase short-circuit fault

A three-phase short-circuit fault is a symmetrical fault: the earth current is zero and neither fault resistance nor the remote source affect the recorded signals. Previous faults compared the results in the cases of different inception angles but here an attempt is made to present the effects of the distance of the fault from the measurement point. With this in mind, signals presented here are based on the following conditions: inception angle = 135°, *abc-sc* fault, without remote source connected, fault locations = 100m and 2,500m.

Figs.(75 to 77) depict the results themed by the three-phase voltage, the three-phase current and the three-modal current signals respectively, in both cases of fault location. Fig.(75) shows the voltage signals: the initial distortions are much higher and the transients die down much more slowly in the case of longer distance faults. This result at first appears strange (because one expects faults at shorter distances to cause higher distortion), but it should be noted that there are some factors that affect the transient part of signals. These include the inception angle, dynamic load and transition points (location of elements in the system, fault point and the location of branches). With regard to the maximum velocity of wave propagation 2.623e+7m/s, the minimum distance of fault at which useful features corresponding to the reflected wave from fault point can be captured is 624.5m (because of using lowpass filter with a cut-off frequency of 42kHz). Therefore, the transients due to reflected wave will not be captured in the case of a 100m fault and the transients are only due to the inception angle and dynamic load, tapped into the network as it is at 2,000m from the source. Also, contrary to expectations of long distance, the voltages after the transient fall significantly in the case of a distance of 100m fault. The reason for this is the shorter the distance and higher the current, the greater the voltage drop in internal impedance of source.

Fig.(76) shows the current signals and it can be observed that the initial distortions are much smaller compared to voltage signals. Importantly, the currents of the three faulted phases increase after the occurring of the fault but are much smaller in the case of a location of 2,500m compared to 100m fault.

Fig.(77) depicts the modal components of the current signals and, similar to previous types of fault, the earth-mode current is zero due to the symmetrical fault. The amplitude of mode-2 and mode-3, like the phase components, are much greater in the case of a closer fault. This figure also shows a small initial distortion in the case of a distance of 2,500m fault compared to smoother signals for the fault at 100m. This effect is due to dynamic load which is tapped into the network at 2,000m from the source.

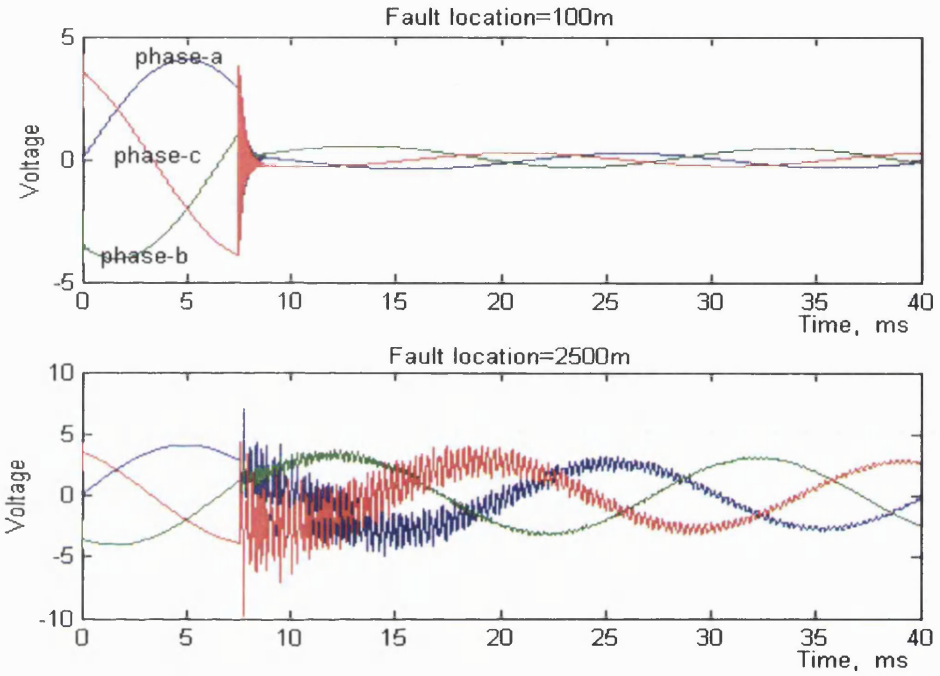

Fig.75- Three phases of voltage signals, *abc-sc* inc. ang.=135°

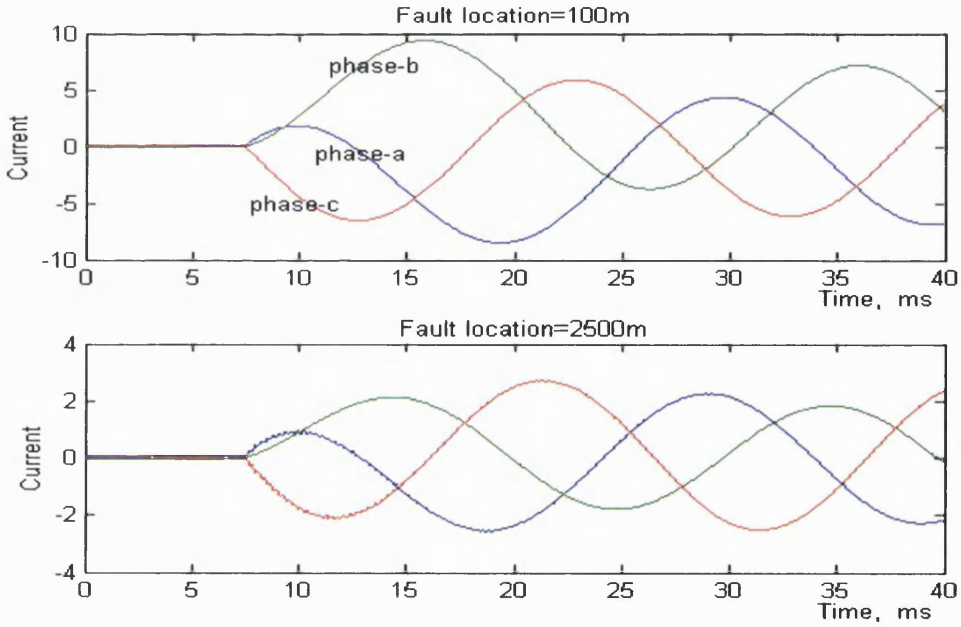

Fig.76- Three phases of current signals, *abc-sc* fault, inc. ang.=135°

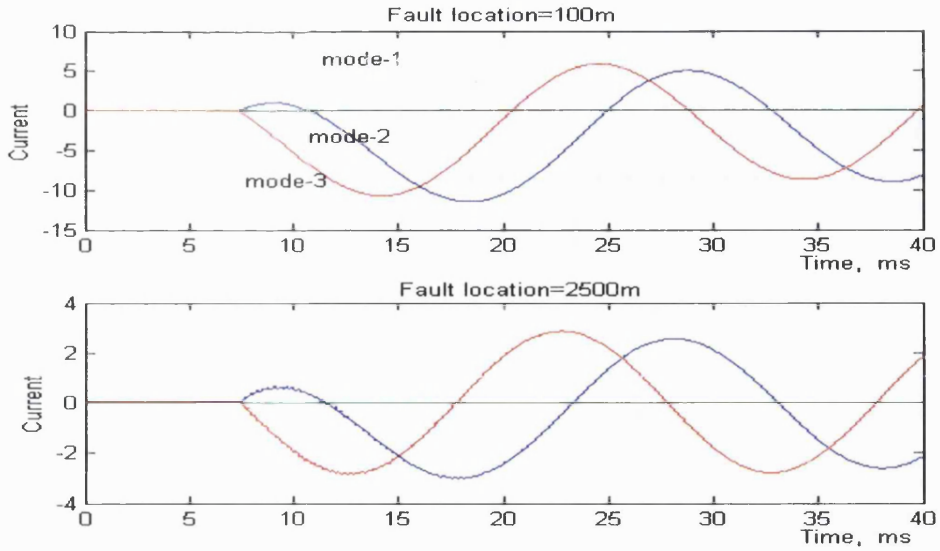

Fig.77- Three modes of current signals, *abc-sc* fault, inc. ang.=135°

4.5.5 Simulated waveforms for one-phase open circuit fault

Contrary to short-circuit faults, current signals are much smaller in the faulted phases in open-circuit faults. In order to study the behaviour of an open-circuit fault, phase '*a*' is disconnected at three locations, but using the same inception angle and without remote source infeed. Since maximum distortion occurs if the voltage of the phase is at its maximum at the instant of the fault, an inception angle of 90^{o} is considered. To present the effect of fault location on voltage and current signals, three fault distances of 900m, 1,900m and 2,900m are compared which are set before load-1, load-2 and load-3 (shown in figure 51), respectively.

Figs.(78 to 80) depict the three-phase voltage, the three-phase current and the three-mode current signals for the three conditions. Fig.(78) shows the voltage signals and it is clearly evident that the initial distortion in the faulted phase '*a*' is much higher than the healthy phases. In addition, the further away the fault, the lower the distortion and the faster the transients die down. In assessment with the previous section, the results obtained are exactly what can be expected because all three conditions have longer distances than the critical value 624.5m. Fig.(79) displays current signals and shows similar behaviour to voltage signals: higher distortion and slower damping the closer the fault. It should be noted that higher distortion translates into a larger magnitude and higher frequency of distortion. These effects occur in all phases, but more significantly in the faulted phases. Fig.(80) shows the three modes of current signals and depicts similar signatures to the phase voltage and current signals.

What is important to note here is that initial distortions of current signals are much higher in the case of open-circuit than short-circuit faults. The reason for this phenomenon is that the current signals in faulted phases are not sensitive to load taps with short-circuit faults, due to a much higher faulted current than load current. However, in an open-circuit case if a phase is disconnected, the network is still supplied by healthy phases, and a three-phase load, especially dynamic load, can affect the network significantly in the transient state.

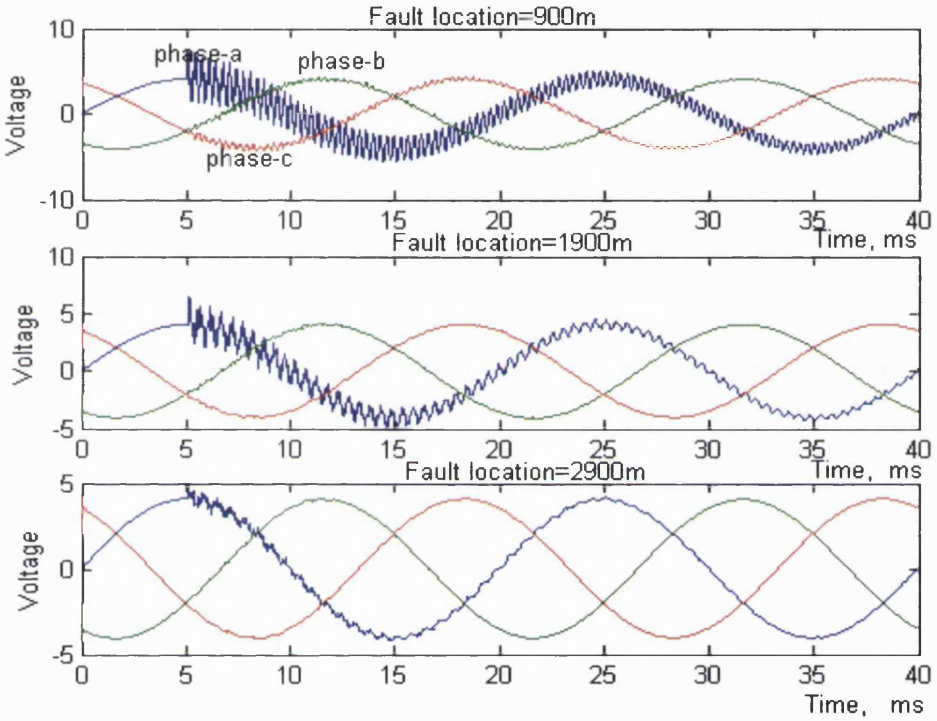

Fig.78- Three phases of voltage signals, *a-op* fault, inc. ang.=90°

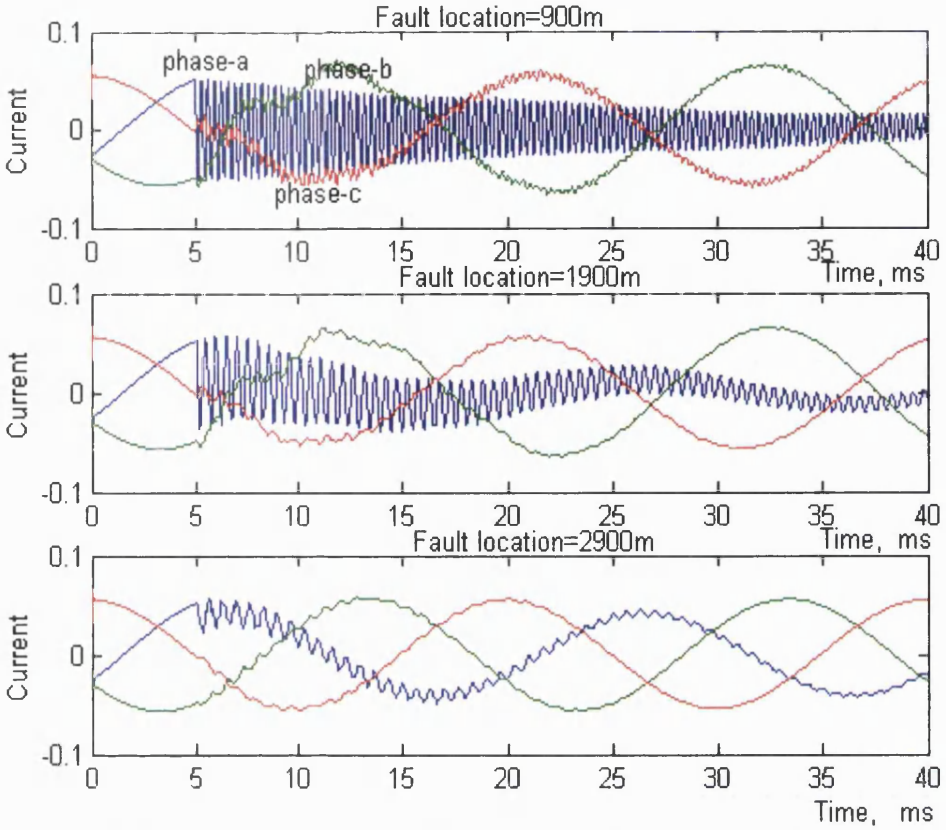

Fig.79- Three phases of current signals, *a-op* fault, inc. ang.=90°

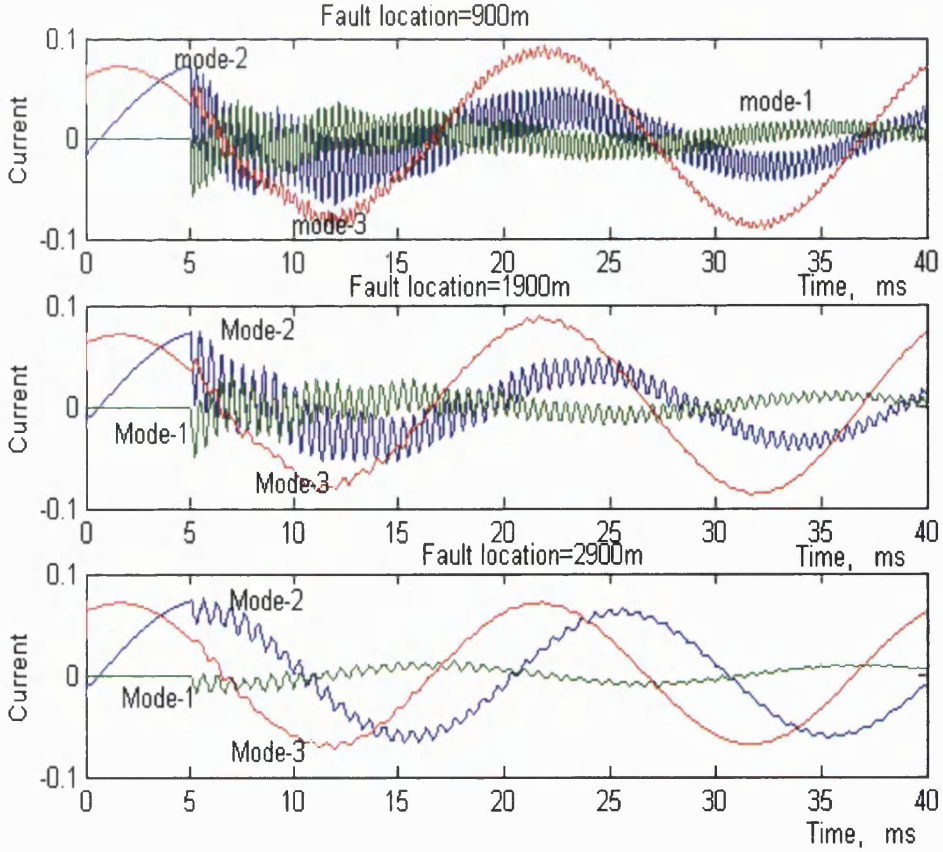

Fig.80- Three modes of current signals, *a-op* fault, inc. ang.=90°

4.5.6 Simulated waveforms for a two-phase open circuit fault

To present the behaviour of signals obtained in the two-phase open circuit fault, similar to the one above, distances of 900m, 1,900m and 2,900m, *ab-op* fault and an inception angle of 135 degrees are considered. Figs.(81 to 83) show the three-phase voltage, the three-phase current and the three-modal current signals in three different fault locations. As can be seen the same conclusions can be reached as with a one-phase open-circuit fault: (1) higher initial distortion and slower damping in faulted phases in the three signals including voltage, current and modal components of current; (2) higher distortion associated with amplitude and frequency in the case of shorter distance of fault from the measurement point; (3) higher distortion in the current signals in the case of open-circuit fault compared with short-circuit fault; and (4) distortion of current signals are depended on load taps in the case of open-circuit faults.

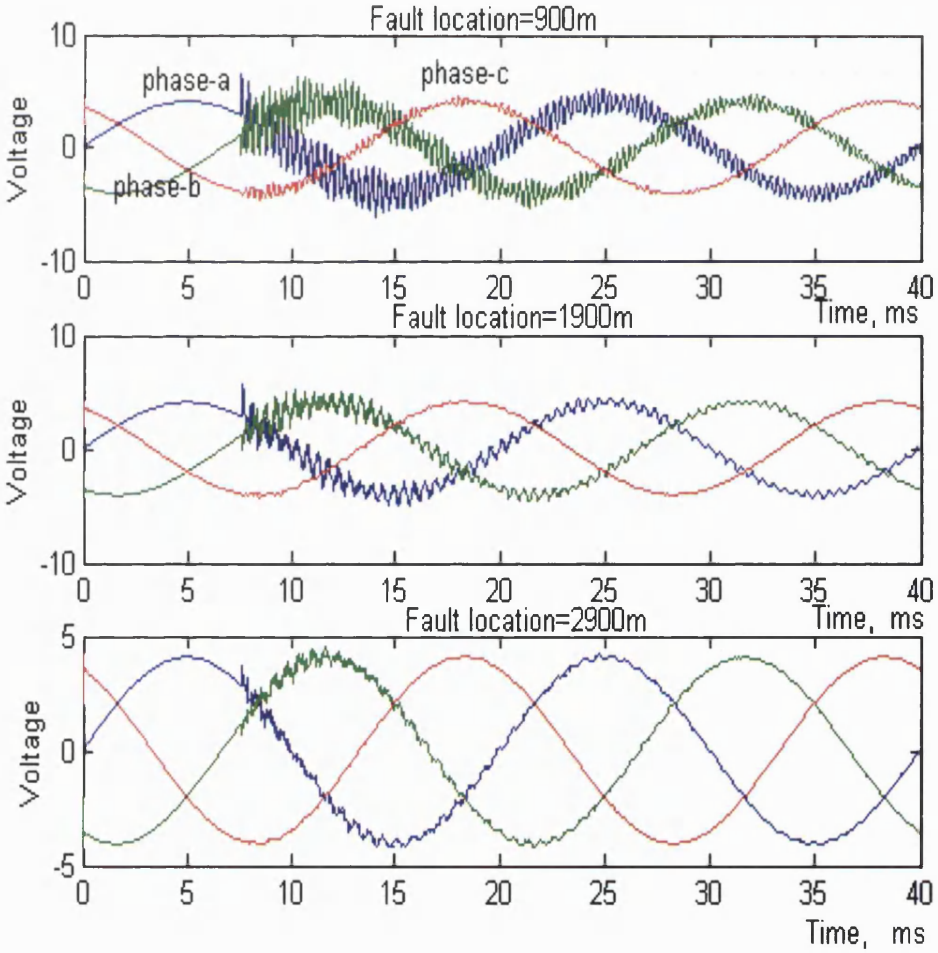

Fig.81- Three phases of voltage signals, *ab-op* fault, inc. ang.=135°

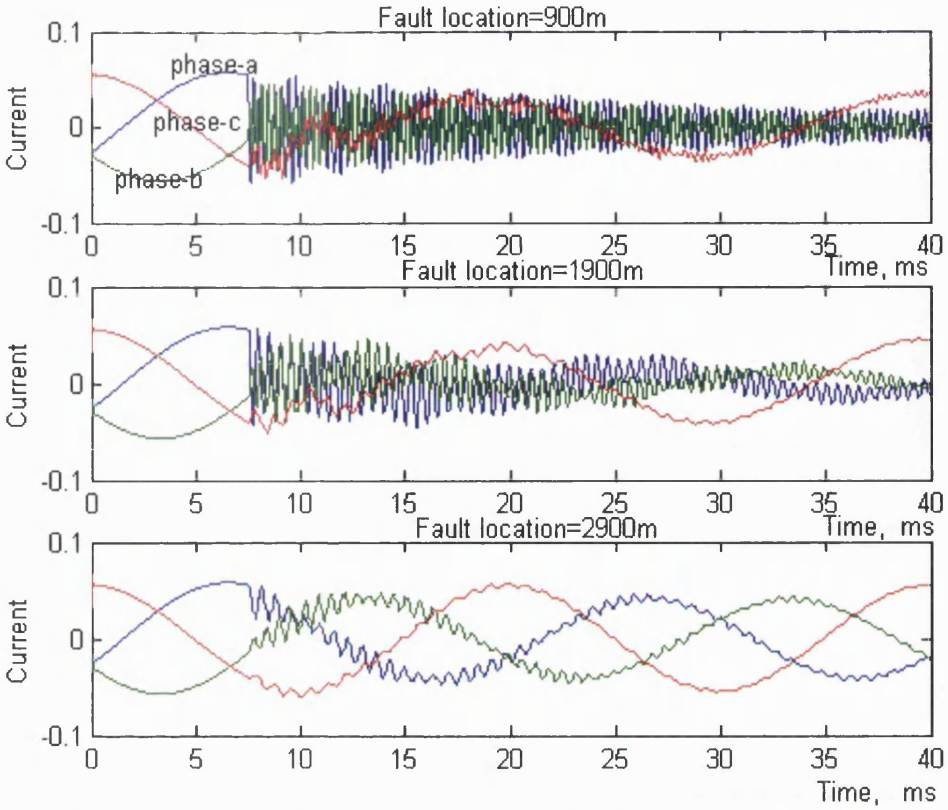

Fig.82- Three phases of current signals, *ab-op* fault, inc. ang.=135°

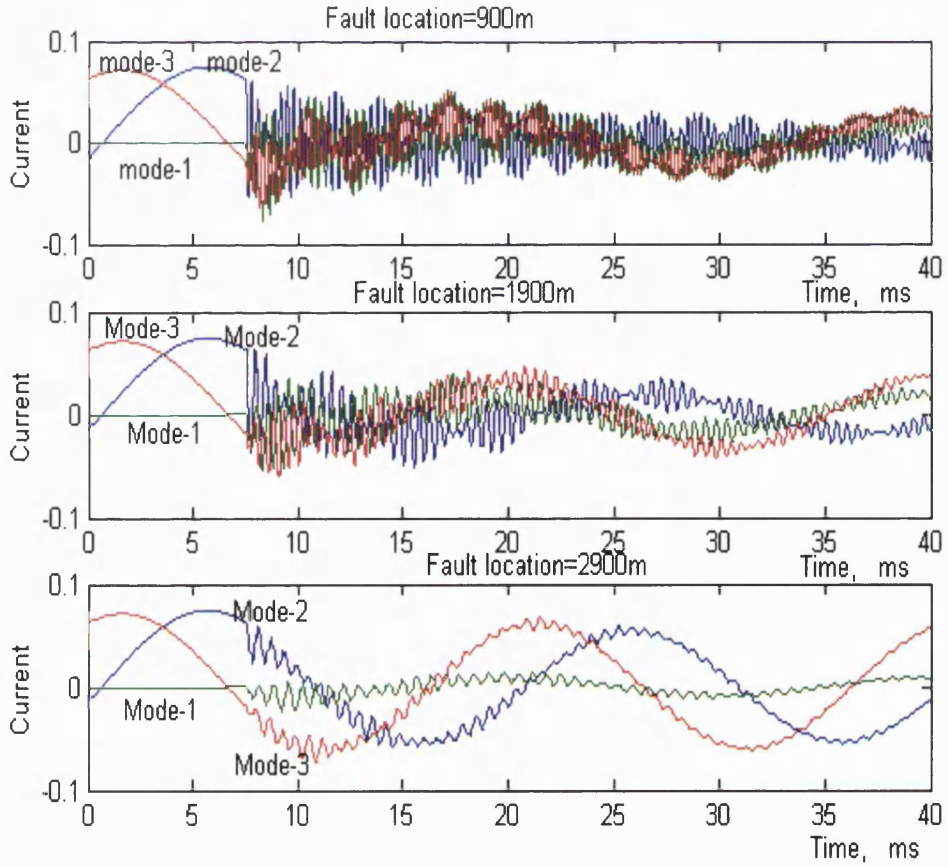

Fig.83- Three modes of current signals, *ab-op* fault, inc. ang.=135°

4.5.7 Simulated waveforms for a three-phase open circuit fault

Behaviour of this type of fault is presented based on previous conditions; inception angle of 135 degrees and distances of 900m, 1,900 and 2,900m. Figs.(84 to 86) show the results and it is evident that the four outcomes mentioned earlier also occur here (as in the cases of one- and two-phase open-circuit faults).

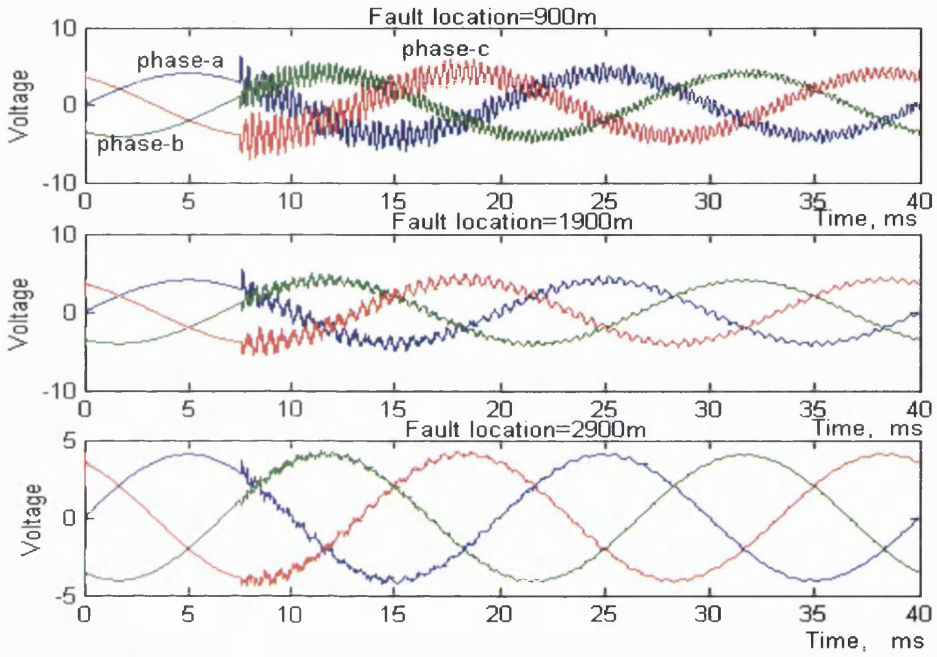

Fig.84- Three phases of voltage signals, *abc-op* fault, inc. ang.=135°

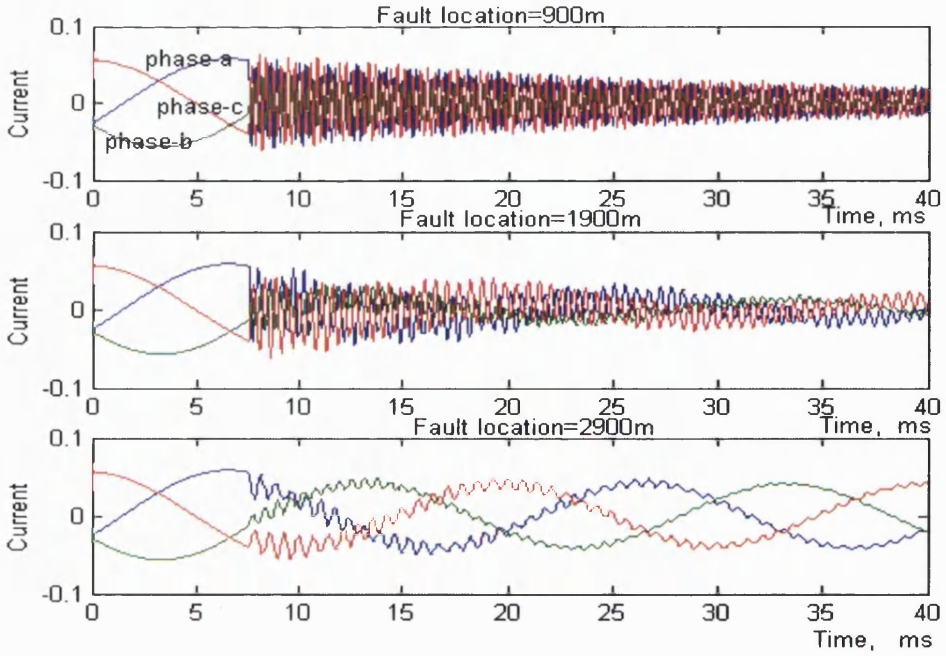

Fig.85- Three phases of current signals, *abc-op* fault, inc. ang.=135°

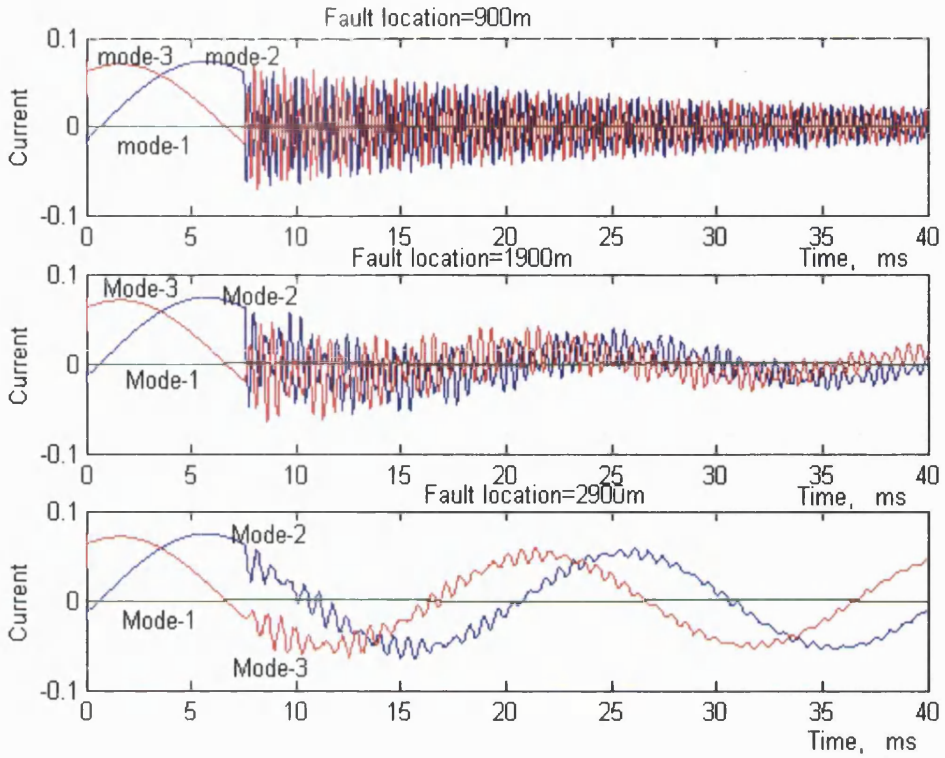

Fig.86- Three modes of current signals, *abc-op* fault, inc. ang.=135°

4.6 Summary

In this chapter, data simulation of the power DS has been carried out using the EMTP software based on a new cable model. In this respect, 17 types of fault, 13 locations, three inception angles, eight fault resistances (in the case of SPH-G short-circuit fault), and four Rf (in the case of 2PH-G short-circuit fault) have been employed. It is vitally important that the system simulation be as accurate as possible within the bounds of practically. Thus, all the practical considerations, such as the effect of transducers and hardware errors on the primary system fault data, are included in the simulation. The effects of Rf, distance of fault from measurement point, inception angle and remote source infeed have been studied. It can be clearly seen from the results that Rf influences the magnitude of current signals and attenuation of distortion of signals: as Rf increases, the magnitude of current signals decreases, the attenuation of distortion of signals increases and the effect of remote sources is amplified, particularly in the SPH-G-SC fault. Also it is apparent that the inception angle plays an important role in the transient state: if the difference between voltages of faulted phases is maximum at the fault instant, the distortion will be maximum in the voltage signal, while the DC off-set associated with the current signal is minimum.

Since capturing useful qualities from reflected signals requires a minimum fault distance of 624.5m (based on maximum velocity of wave propagation and cut-frequency of used filter), where it was beyond this critical distance there was less initial distortion and faster die-down in relation to voltage and current signals.

It is apparent that the initial distortion of current signals is significantly affected by load taps and the inception angle in the case of open-circuit faults as opposed to short-circuit faults. Since data simulation covers different system and fault conditions, this study apparently shows that there are some useful characteristics associated with voltage and current signals which can be extracted at the signal processing stage. They can also be used in training when employing ANNs, and this is dealt with in detail in the next chapters.

CHAPTER 5

SIGNAL PROCESSING

5.1 Introduction

Vibration signal analysis has been extensively used in fault location and condition monitoring of power system lines and cables. This often involves the use of signal processing algorithms on measured vibrations. Vibration signals are considered as non-stationary with transient components. The frequency characteristics of vibration signals are time-varying. Information about the fault condition in a distribution system can be extracted using methods such as amplitude or phase demodulation. The time and frequency information also can be calculated using techniques such as Fast Fourier Transform (FFT), Power Spectral Density (PSD), Short-Time Fourier Transform (STFT) and Wavelet Transform (WT). FFT, PSD and STFT techniques yield good information on the frequency content of the transients, but the time at which a particular disturbance in the signal occurred is lost [40]. Furthermore, since FFT and PSD map a given signal from the time domain into the frequency domain and since the frequency characteristics of transient signals are time-varying, some useful information in the original signals is lost when either FFT or PSD is employed. On the other hand, the STFT is computationally efficient, but has the drawback that the choice of the window length simultaneously affects both frequency and time resolution; for a good frequency resolution, a high window length has to be chosen, but this choice affects the time resolution significantly [41].

WT possesses some unique features that make it very suitable for particular application described herein. It maps a given function from the time domain into the time-scale domain. The wavelet (the basis function used in the WT), has band-pass characteristics which make this mapping similar to the mapping to the time-frequency plane. Unlike the basis function used in Fourier analysis, the wavelets are not only localized in frequency but also in time. This localisation allows detecting the time of abrupt disturbances, such as fault transients. Fault generated travelling waves appear as disturbances superposed on the power frequency signals. Processing these signals using

the WT reveals the positions of sudden changes and gives useful information to localise the fault point. In the case of WT, the analysing functions, which are called wavelets, will adjust their time-widths to their frequency in such a way that higher frequency wavelets will be very narrow and lower frequency ones will be broader. This property of multi-resolution is particularly useful for analysing fault transients which localise high frequency components superposed on power frequency signals; thus, WT is better suited for analysis of signals containing short lived high frequency disturbances superposed on lower frequency continuous waveforms by virtue of this zoom-in capability (Manago and Abur [31]).

In this chapter, the FFT, PSD, and STFT techniques are briefly overviewed and then it deals with the related commands and functions in the MATLAB software. The WT is then presented in detail as the most optimal technique. Finally, useful information and features which are subsequently used in an ANN to classify and locate the fault are introduced.

5.2 Overview of Existing Mathematical Transformations

Generally, the vast majority of signals obtained from any modern instrumental devices are in the time-domain. These, however, are not suitable for analysing since the most distinguished information is hidden in the frequency content of the signals. Thus mathematical transformations are applied to signals to obtain further information that is not readily available in the original signal. In this respect, some techniques for analysing the time-domain signals are presented herein.

5.2.1 Fourier Transform

One of the most popular transformations which is used to transform time-domain signals into frequency-domain signals is the Fourier transform (FT). Mathematically, the FT of a continuous-time signal x(t) is given by:

$$X(f) = \int_{-\infty}^{\infty} x(t) e^{-j2\pi . f . t} dt \qquad (5\text{-}1)$$

The continuous function X(f) is the frequency-domain representation of x(t) obtained by summation of an infinite number of complex exponentials. The result of the transform are the Fourier coefficients X(f), which then multiplied by a sinusoid of appropriate frequency f, yield the constituent sinusoidal components of the original signal.

In order to find X(f) in a digital computer with discrete (sampled) and finite-length (time-limited) signals, the Discrete Fourier Transform (DFT) is used. The DFT is defined as:

$$X[k] = \sum_{n=0}^{N-1} x[n] e^{-j\frac{2\pi.k.n}{N}} \tag{5-2}$$

$$x[n] = \frac{1}{N} \sum_{k=0}^{N-1} X[k] e^{j\frac{2\pi.k.n}{N}} \tag{5-3}$$

Where x[n] is a sequence obtained by sampling the continuous time signal x(t) every T_s s for N samples:

$$x[n]=x(nT_s) \qquad n=0, 1, 2, \quad , N-1 \tag{5-4}$$

The DFT produces a sequence of complex values X[k] whose magnitudes are those of discrete frequencies in x[n]. Because the derivation of the DFT strictly requires x[n] to be periodic, the representation of a signal by the DFT is best reserved for periodic signals. This and the Nyquist criteria (sampling at least twice as fast as the highest frequency in the signal) are two important factors that need to be considered when using the DFT.

Since the waveform associated with fast electromagnetic transients are typically non-periodic signals which contain both high-frequency oscillations and localised impulses superimposed on the power frequency and its harmonics, these characteristics thus present a problem for traditional Fourier analysis because its use assumes a periodic signal and also a wide-band signal requires more dense sampling and longer time periods to maintain good resolution in the low frequencies. In spite of this, Fourier analysis is still desirable to apply a frequency-based analysis method in an attempt to isolate the transient components of the signal which may help in identifying the particular phenomena producing the transient. Because of this, MATLAB provides the functions 'fft' and 'ifft' to compute the DFT and its inverse, respectively. The DFT is

the primary tool for digital signal processing. The foundation of the signal processing Toolbox is the FFT, a method for computing the DFT with reduced execution time. Many of the toolbox functions (including z-domain frequency response, spectrum and cepstrum analysis, and some filter design and implementation functions) incorporate the FFT. For the input sequence x and its transformed version X (the discrete-time Fourier transform at equally spaced frequencies around the unit circle), the Eqs. 5-2 and 5-3 become:

$$X[k+1] = \sum_{n=0}^{N-1} x[n+1] e^{-j\frac{2\pi.k.n}{N}} \tag{5-5}$$

$$x[n+1] = \frac{1}{N} \sum_{k=0}^{N-1} X[k+1] e^{j\frac{2\pi.k.n}{N}} \tag{5-6}$$

In these equations, the series subscripts begin with 1 instead of 0 because of MATLAB's vector indexing scheme and N=length(x).

X=fft(x,n) is the DFT of vector x and the n point FFT, computed with a FFT algorithm. If x is a matrix, X is the FFT of each column of the matrix. The fft function employs a radix-2 fast Fourier transform algorithm if the length of the sequence is a power of two, and a slower algorithm if it is not [42,43]. In order to normalize the output of fft so that a unit sinusoid in the time domain corresponds to unit amplitude in the frequency domain, a normalized discrete-time Fourier transform is produced by:

$$Pn = abs(fft(x))*2/length(x) \tag{5-7}$$

Also if the sequence x of N points is obtained at a sample frequency of fs, then for up to the Niquist frequency, or point n=N/2 + 1, the relationship between the actual frequency and the index k into x (out of N possible indices) is:

$$f = (k-1) * fs / N \tag{5-8}$$

5.2.2 Short-Time Fourier Transform

As mentioned above, the FFT technique has two important drawbacks; firstly, it assumes the signal as a periodic signal and secondly it transforms the signal from time domain into frequency domain and therefore, the information related to the time at

which a particular disturbance in the signal occurred is lost. With regard to these drawbacks, FFT is extremely suitable in analysing stationary signal (signal whose frequency content is constant in time). In order to analyse non-stationary waveforms and overcome aforementioned drawbacks, more sophisticated Fourier-based transforms have been developed. STFT is one of them. The STFT is similar to the FFT except that the input signal x(t) is multiplied by a window function w(t) whose position is translated in time by T:

$$STFT(f,T) = \int_{-\infty}^{\infty} x(t).w(t-T).e^{-j2\pi.f.t}dt \qquad (5\text{-}9)$$

For digital implementation of the STFT, the windowed Discrete Fourier Transform (WDFT) is used. The WDFT is defined as:

$$WDFT[k,m] = \sum_{n=0}^{N-1} x[n].w[n-m]e^{-j\frac{2\pi.k.n}{N}} \qquad (5\text{-}10)$$

Where the sequence w[n-m], in its simplest form, is the rectangular window function

$$w[n] = \begin{cases} 1 & if, 0 \le n-m \le N-1 \\ 0 & otherwise \end{cases} \qquad (5\text{-}11)$$

For each window $w_{mo}=w[n-m_o]$, the WDFT produces a sequence of complex value $WDFT[k,m_o]$, k=0, 1, ...N-1, whose magnitudes are those of the discrete frequencies of the input x[n].

The WDFT of a signal can be represented in a two-dimensional grid where the divisions in the horizontal direction represent the time extent of each window w[n-m]; the divisions in the vertical direction represent the frequencies k and the shade of each rectangle is proportional to the corresponding magnitude. With a comparison between STFT and FFT, in fact, FFT gives perfect frequency resolution but no time information due to its attribute of having infinite window.

The STFT is computationally efficient, as fine time resolution for short duration and high frequency signals, and fine frequency resolution for long duration and lower frequency signals are needed. However, the STFT has the limitation of a fixed window width, which means that the trade-off between frequency resolution and time resolution,

which depends on the signal to be analysed, must be fixed *a priori* in order to capture a particular phenomenon. A wide window, for example, gives good frequency resolution but poor time resolution, whereas a narrow window gives good time resolution but poor frequency resolution.

Because of the importance of STFT, the signal processing toolbox in the MATLAB software provides a function, specgram, which returns the STFT for a sequence, or displays this information as a spectrogram. Specgram computes the windowed discrete-time Fourier transform of a signal using a sliding window. The spectrogram is the magnitude of this function:

[B,f,t]=specgram(a,nfft,Fs,window,noverlap); calculates the spectrogram for the signal in vector 'a'.

nfft specifies the FFT length that specgram uses. This value determines the frequencies at which the DTFT is computed; Fs is a scalar that specifies the sampling of the frequency; window specifies a windowing function and the number of samples specgram uses in its sectioning of vector 'a'; noverlap is the number of samples by which the sections overlap. Any arguments that are omitted from the end of the input parameter list, function specgram uses the default values as follows:

- nfft = min(256,length(a))
- Fs = 2
- window = hanning(nfft)
- noverlap = length(window)/2

If 'a' is real, specgram computes the DTFT at positive frequencies only. If 'nfft' is even, specgram returns nfft/2 +1 rows (including the zero and Nyquist frequency terms). If n is odd, specgram returns (nfft+1)/2 rows. The number of columns in B is:

$$K=\text{fix}((n-\text{noverlap})/(\text{length}(\text{window})-\text{noverlap})) \qquad (5\text{-}12)$$

As n=length(a).

If 'a' is complex, specgram computes the DTFT at positive and negative frequencies. In this case, B is a complex matrix with nfft rows. Time increases linearly across the columns of B, starting with sample 1 in column 1. Frequency increases linearly down the rows, starting at 0.

Vector 'f' comprises such frequencies at which the function computes the DTFT. Fs has no effect on the output B and frequency step is Fs/nfft. Vector 't' is a column vector of scaled times, with length equal to the number of column of B. t(j) is the earliest time at which the j-th window intersects 'a'. t(1) is always equal to zero and the width of window is Δt * length(window) or length(window)/Fs.

5.2.3 Power Spectral Density Technique

The PSD is a measurement of the energy at various frequencies and one way of estimating the PSD of a process is to simply find the DFT of the samples of the process and take the magnitude squared of the result. In this respect, a crude estimate of the PSD of signal 'a' is:

$$Pxx=abs(fft(a,nfft)).^2/nfft \qquad (5\text{-}13)$$

This estimate is called the periodogram; as the number of samples increases, the expected value of the periodigram approaches the true PSD. The problem with the periodogram estimation is that its variance is large and does not decrease as the number of samples increases. The variance of the PSD can be reduced by breaking the signal into sections and averaging the periodogram of these sections. In order to improve the periodogram estimation, a nonrectangular data window is also applied to the sections prior to computing the periodogram, resulting is a modified periodogram. This reduces the effect of section dependence due to overlap, because the window is tapered to zero on the edges. Also, a nonrectangular window diminishes the side-lobe interference or spectral-leakage while increasing the width of spectral peaks. With a suitable window (such as Hamming, Hanning or Kaiser), overlap rates of about half the section length have been found to lower the variance of the estimate significantly. Eq. (5-14) shows the calculation of PSD base on modified periodogram.

Pxx= (abs(fft(w.*xn(1:256))).^2 + abs(fft(w.*xn(129:384))).^2 +.....
abs(fft(w.*xn(257:512))).^2 + abs(fft(w.*xn(385:640))).^2 +..... (5-14)
abs(fft(w.*xn(513:768))).^2 + abs(fft(w.*xn(641:896))).^2) / (norm(w)^2*6)

Where w=type of window with dimension 256 for instance hanning(256) and noverlap=128.

This method of averages is based on Welch's method of PSD estimation.
Because of the importance of PSD analysis, signal processing in the MATLAB software provides the function PSD to estimate the PSD of a signal using Welch's method, as:

[Pxx,f]=psd(a,nfft,Fs,window,noverlap)

The above function estimates the PSD of the sequence 'a'. All parameters have the same definition compared with the specgram function; the only difference is that in the specgram, the FFT is obtained for each section separately, but the PSD function obtains only one column by averaging the periodogram of the sections. Consequently, although PSD is widely accepted for analysing stationary signals since the frequency characteristics of transient signal on the fault condition are time-vary and its nature is non-stationary, thus, due to using PSD, some useful information are lost in original signal for example the time at particular disturbances. Therefore this technique can not process the signals perfectly and accurately in the different faults and conditions.

5.2.4 Wavelet Technique

Sinusoid waves which are smooth, periodic and have unlimited duration, are used in Fourier analysis which a signal is broken up into sine waves of various frequencies. Similarly, WT is the breaking up of a signal into shifted and scaled versions of the original (or mother) wavelet. However, a wavelet is a waveform of effectively limited duration and has an average value of zero. Thus, by definition, a wavelet is a transient signal and methods that make use of wavelet functions, would seemingly be suitable for transient analysis. That is, one would make use of a transient to analyse a transient, as opposed to using a stationary function (e.g., a sine or a cosine) for such analysis. Wavelets tend to be irregular, asymmetric, short and oscillatory waveforms. Wavelet analysis allows the use of both long time intervals and shorter regions in order to cover

both irregular low frequency and high frequency information. Therefore, WTs have multi-resolution properties and are well suited to wide-band transient signals that may not be periodic and may contain both sinusoidal and impulse components as is typical of fast power system transients. In particular, the ability of wavelets to focus on short time intervals for high-frequency components and long intervals for low-frequency components improves the analysis of the signals with localized impulses and oscillations, particularly in the presence of a fundamental and low-order harmonics.

5.2.4.1 Wavelet Analysis

The continuous wavelet transform (CWT) is defined as the sum over all time of the signal multiplied by scaled and shifted versions of the wavelet function, as given by:

$$WT(a,b) = \frac{1}{\sqrt{a}} \int_{-\infty}^{\infty} x(t).g(\frac{t-b}{a})dt \qquad (5\text{-}15)$$

Where x(t) is the signal which is analysed, 'a' and 'b' are the scaling (dilation) and time shifting (translation) factors respectively; g(t) is referred to as the mother wavelet and its dilates and translates are simply called wavelets. The results of CWT are many wavelet coefficients, which are the function of scale and position.

The CWT has a digitally implementable counterpart: the Discrete Wavelet Transform (DWT), which is defined as:

$$DWT[m,k] = \frac{1}{\sqrt{a_o^m}} \sum_n x[n].g[\frac{k - na_o^m}{a_o^m}] \qquad (5\text{-}16)$$

Where g[n] is the mother wavelet, and the scaling and translating parameters 'a' and 'b' of eq. (5-15) are functions of an integer parameter m, $a=a_o^m$ and $b=n\ a_o^m$. In a standard DWT, the coefficients are sampled from the CWT on a dyadic grid, $a_o=2$. The result is geometric scaling, i.e. 1, 1/2, 1/4,...., and translation by 0, n, 2n,....; this scaling gives the DWT logarithmic frequency coverage in contrast to the uniform frequency coverage of the STFT as compared in Fig.(87).

The DWT output can be represented in a two-dimensional grid in a similar manner as the STFT but with very different divisions in time and frequency are as shown in Fig.(88).

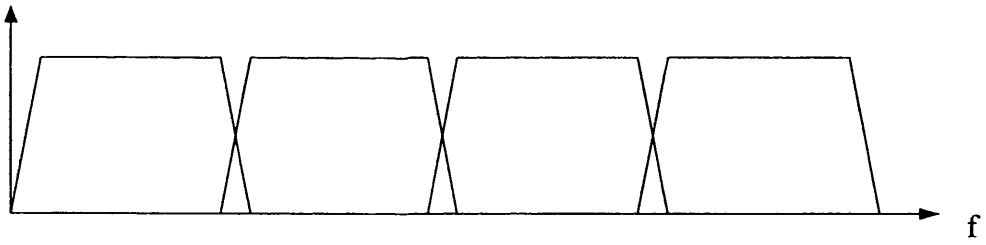

Fig.87.a- Windowed-DFT uniform frequency coverage

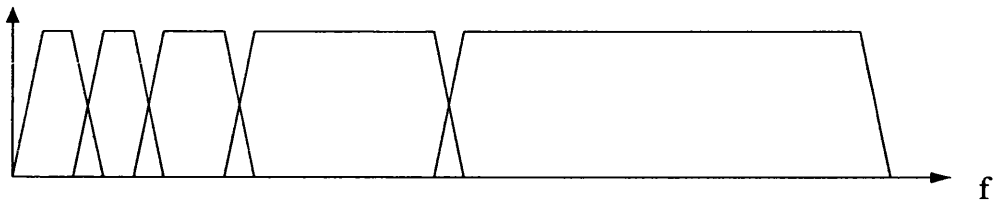

Fig.87.b- The logarithmic coverage of the DWT

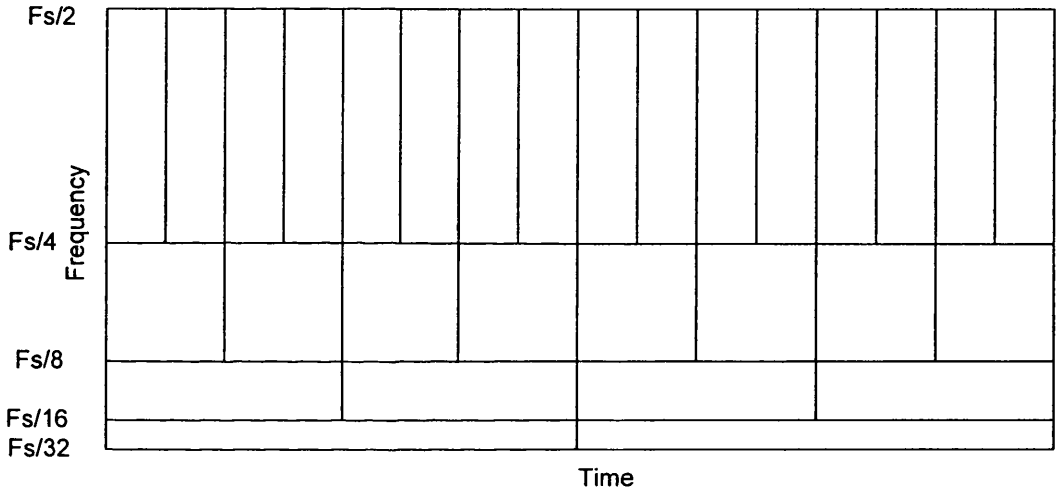

Fig.88- Discrete wavelets transform output

As it can be seen from fig. (88), if the original signal is being sampled at Fs Hz, the highest frequency that the signal could contain, from Nyquist's theorem, would be Fs/2 Hz. This frequency would be seen at the output of the high frequency filter, which is the first detail. Thus the band of frequencies between Fs/2 and Fs/4 would be captured in detail 1; similarly, the band of frequencies between Fs/4 and Fs/8 would be captured in detail 2, and so on. As an example, Table 5.1 gives the frequency band information for the different scale of the wavelet analysis, where the sampling frequency is F_s=100kHz. Thus it can be seen that the wavelet decomposition agrees with the Nyquist criteria and hence has a maximum measurable frequency of one half of the sampling frequency.

Table 5.1- Different scale of wavelet analysis

Detail	Frequency band	Approximation	Frequency band
D1	25-50 kHz	A1	0-25 kHz
D2	12.5-25 kHz	A2	0-12.5 kHz
D3	6.25-12.5 kHz	A3	0-6.25 kHz
D4	3.125-6.25 kHz	A4	0-3.125 kHz
D5	1.5625-3.125 kHz	A5	0-1.5625 kHz

Also the rectangles in Fig.(88) have equal area or constant time-bandwidth product such that they narrow at the lower scales (higher frequency) and widen at the higher scales (lower frequency).

The DWT can be implemented in the form of a filter bank, with the variable swap of 'k' for 'n', Eq. (5-16) can be written as:

$$DWT[m,n] = \frac{1}{\sqrt{a_0^m}} \sum_k x[k].g[a_0^{-m}n - k] \tag{5-17}$$

This has the similar form of Finite Impulse Response digital filters as follows:

$$y[n] = \frac{1}{c} \sum_k x[k].h[n-k] \tag{5-18}$$

This suggests that $g[a_0^{-m}n - k]$ is the impulse response of a low-pass digital filter with transfer function G(ω). Then by selecting a_0=2, or a_0^{-m} =1, ½, ¼, 1/8, ..., each dilation of g[n] effectively halves the bandwidth of G(ω).

The multi-stage filter bank implements the DWT using the low-pass mother wavelet g[n] and its high-pass dual h[n]. It should be mentioned that the coefficients of filter h[n] are the reverse of g[n] with every other coefficient negated. Here WT acts as a serial of Band-pass filters with variable central frequencies. It can be zoomed in by scaling and shifting the mother wavelet. This implies that the WT can be used to obtain the wanted non-stationary signals and to capture the transient components selectively and accurately. Hence the WT is an ideal technique to extract the different components from the wideband transient signal generated by a fault. It can be used to extract the wanted signals of different frequencies by applying down-sampling technique.

5.2.4.2 Decomposition of Wavelet Transform

Wavelet analysis leads to approximations and details. The approximations are the high-scale, low-frequency components of the signal. The details are the low-scale, high-frequency components. In the filtering process, the original signal, s, passes through two complementary filters and emerges as two signals, approximate and detail signals. In a real digital signal, it has to deal with twice as much data as it started with. In order to avoid this problem, downscaling concept is introduced in WT which simply means discarding every second data point.

The decomposition process can be iterated, with successive approximations by breaking down into many lower-resolution components. This is called the wavelet decomposition tree. It should be noted that the coefficient vectors cannot directly be combined to reproduce the signal and it is necessary to reconstruct the approximation and detail coefficients before combining them. Fig. (89) depicts the process for three levels of decomposition of signal S;

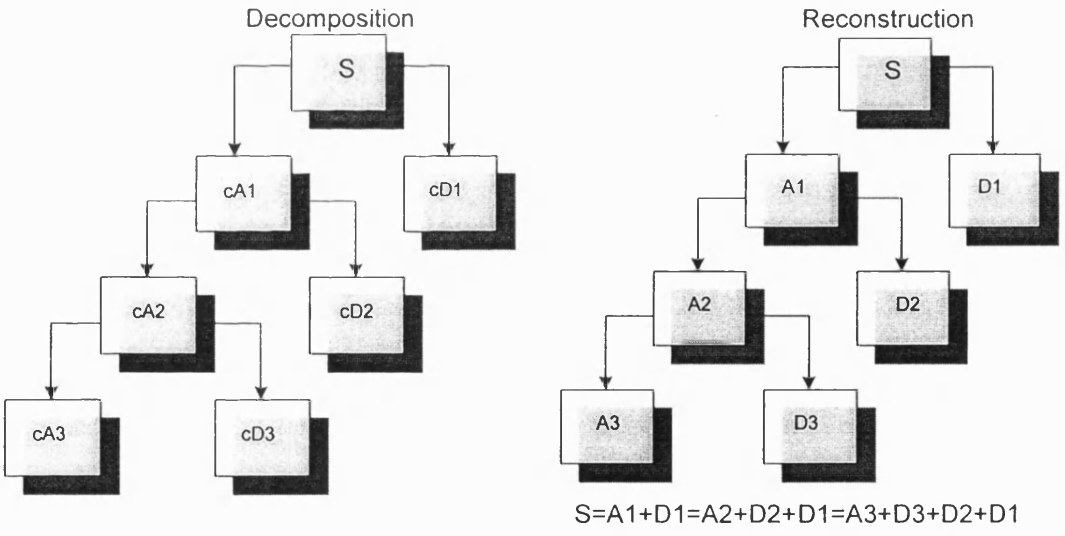

Fig.89- Decomposition and Reconstruction iterations

cAi and cDi are approximate and detail coefficients at level i respectively and also Ai and Di are approximate and detail signals at level i respectively. Since the analysis of process is iterative, in theory it can be continued indefinitely. In reality, the decomposition can proceed only until the individual details consist of a single sample. In practice, a suitable number of levels are selected based on the nature of the signal.

Since wavelet analysis involves filtering and downscaling, the wavelet reconstruction process consists of upsampling and filtering. Upsampling is the process of lengthening a signal component by inserting zeros between samples. Fig.(90) shows the reconstruction process including upsampling and filtering.

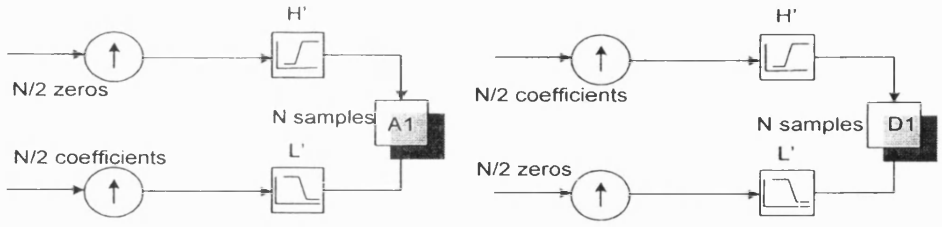

Fig.90- Reconstruction process

As can be seen, in order to reconstruct signals A1 (or D1) related to the approximate (or detail) signal, the coefficient vector cA1 (or cD1) is upsampled and passes through a lowpass (or highpass) filter then is fed by a vector of zeros. Appendix 3 illustrates in more detail the decomposition algorithm and break down of the original signal S into A_i and D_i.

The wavelet toolbox in the MATLAB software provides some functions to decompose and reconstruct the original signal. The command,

```
[C,L]=wavedec(S,N,'wavelet')
```

performs a multilevel wavelet decomposition of a signal *S*. *N* is the number of level and 'wavelet' is a mother wavelet selected from families of wavelets included in the toolbox. Vector *C* comprises the coefficients of all the components of the *N* level decomposition (that is the *Nth* level of approximate and the *N* levels of detail) and it is shown as $C=[cA_N\ cD_N\ cD_{N-1}\ \ldots.\ cD_1]$. Vector *L* gives the length of each component of Vector *C* and has *N*+1 dimension.

Command,

```
An=wrcoef('a',C,L,'wavelet',N)
```

performs a selective level (here level *N*) reconstruction of approximate signal and command.

```
Dn=wrcoef('d',C,L,'wavelet',N)
```

reconstructs the detail signal at level *N*.

5.2.4.3 Wavelet Families

There are different types of wavelet families whose qualities vary according to several criteria. The main criteria are as follows:

- The speed of convergence at infinity to zero of approximate and detail functions ($g(x)$ and $h(x)$) when the time or the frequency goes to infinity.
- The symmetry of vanishing moments for $h(x)$ or for $g(x)$ (if it exists), which is useful for compression purposes.
- The regularity, which is useful for recording notable features – for instance the smoothness of the reconstructed signal.

Definition: A signal x, defined on R, has a regularity of s. When s is an integer, the regularity in x_0 is defined as usual; s is the order of differentiability. When s is not an integer, such that $m < s < m+1$, then x has a regularity of s in x_0 if its derivative $x^{(m)}$ of order m resembles $| x-x_0 |^{s-m}$ locally around x_0.

Several families of wavelets that have proven to be especially useful are included in the wavelet toolbox in the MATLAB software. Appendix 4 explains in detail these families.

An overview of the aforementioned signal processing techniques shows that the wavelet technique is more efficient and more comprehensive; for this reason, in this research, the signals are processed based on wavelet technique. The next section presents the process in detail.

5.3 Wavelet Analysis for the Fault Location Technique

In the previous section, it was shown that WT provides greater resolution in time for high frequency components of a signal and greater resolution in frequency for the low frequency components of a signal. Therefore, the signal features extracted and represented by WT have a more distinct property than that extracted by FFT or STFT,

due to the good time and frequency localisation characteristics of WT. Based on the WT-based feature extraction method, this section describes a novel underground power distribution cable fault location approach. The approach is based on the analysis of signals described previously in the chapter 4 on data simulation.

At first, wavelet components are selected and employed as specific and significant features of fault classification and then implemented in fault location technique. In the developed approach, WT technique is first applied to decompose the voltage and current signals into a series of wavelet components. Then by processing selected wavelet components, the relationship between the specifications of wavelet components and the fault location and conditions are extracted.

5.3.1 Selection of Mother Wavelet

As mentioned earlier, there are many types of mother wavelets: Haar, Daubichies', Coiflet and Symlet, etc. The choice of the mother wavelet plays a significant role in classifying and localising different types of fault transients. In addition to this, the choice of wavelet also depends on the particular application. As it can be seen from the results of data simulation in Chapter 4 in the study of underground power distribution transients, there is particular interest in detecting and analysing short duration, fast decaying and oscillating types of high and low frequency voltage and current signals. The selected wavelet must be sufficiently regular, which implies a longer filter impulse response in order to detect the singularity. One of the most popular mother wavelets suitable for a wide range of applications is Daubechies' wavelet. Through a heuristic approach it has been found that Daubechies' family of wavelets of order 4 is very appropriate to the application. In this thesis, a *db*4 wavelet with a decomposing level of 5 has been considered. Thus, the number of vanishing moments of detail function $h(x)$ is four. The frequency band for approximate and detail signals is shown in Table 5.1 based on Fs=100kHz.

5.3.2 Wavelet Analysis in Different Faults and Conditions

In order to investigate the effectiveness of WT to detect and analyse underground power distribution cable transients, particularly fault voltage and current transients, various faults and conditions have been simulated in a practical system. These are presented in

detail in Chapter 4. As mentioned before, the *db*4 wavelet is used within the DWT and typical DWT detailed analysis is presented for different faults in the following section. The process comprises two stages: fault classification and fault location.

5.3.2.1 Fault Classification

In order to classify the fault type, both the voltage and current phase signals together with the modal components of current signals are employed. Firstly, the original signals are passed through a DWT, then five detailed and one approximate signals are extracted. Since the number of samples for the original signal is 4,001, thus the number of coefficients for the decomposed signals are 2,004, 1,005, 506, 256, 131 and 131 for details at levels 1-5 and approximate at level 5, respectively.

Fig.(91) illustrates the decomposed signal for the 'a' phase voltage at level 5 for the following conditions: Rf = 2Ω, inception-angle = 90 degrees, fault location = 1,100m, without the remote source connected for the *ag-sc* fault. It is apparent that there are high frequency distortions in the voltage signals. This is as a direct consequence of the effects of distributed inductance, resistance and capacitance of the cable considered in the system. Also it can be seen that the approximate signal shown in fig.(91-g) is much smoother than the original shown in fig.(91-a). The results show that there are very useful features in the signals, particularly in the approximate part of the signals, as its frequency band is DC to 1562.5Hz. Thus in this study, approximate-5 signal is considered for further feature analysis.

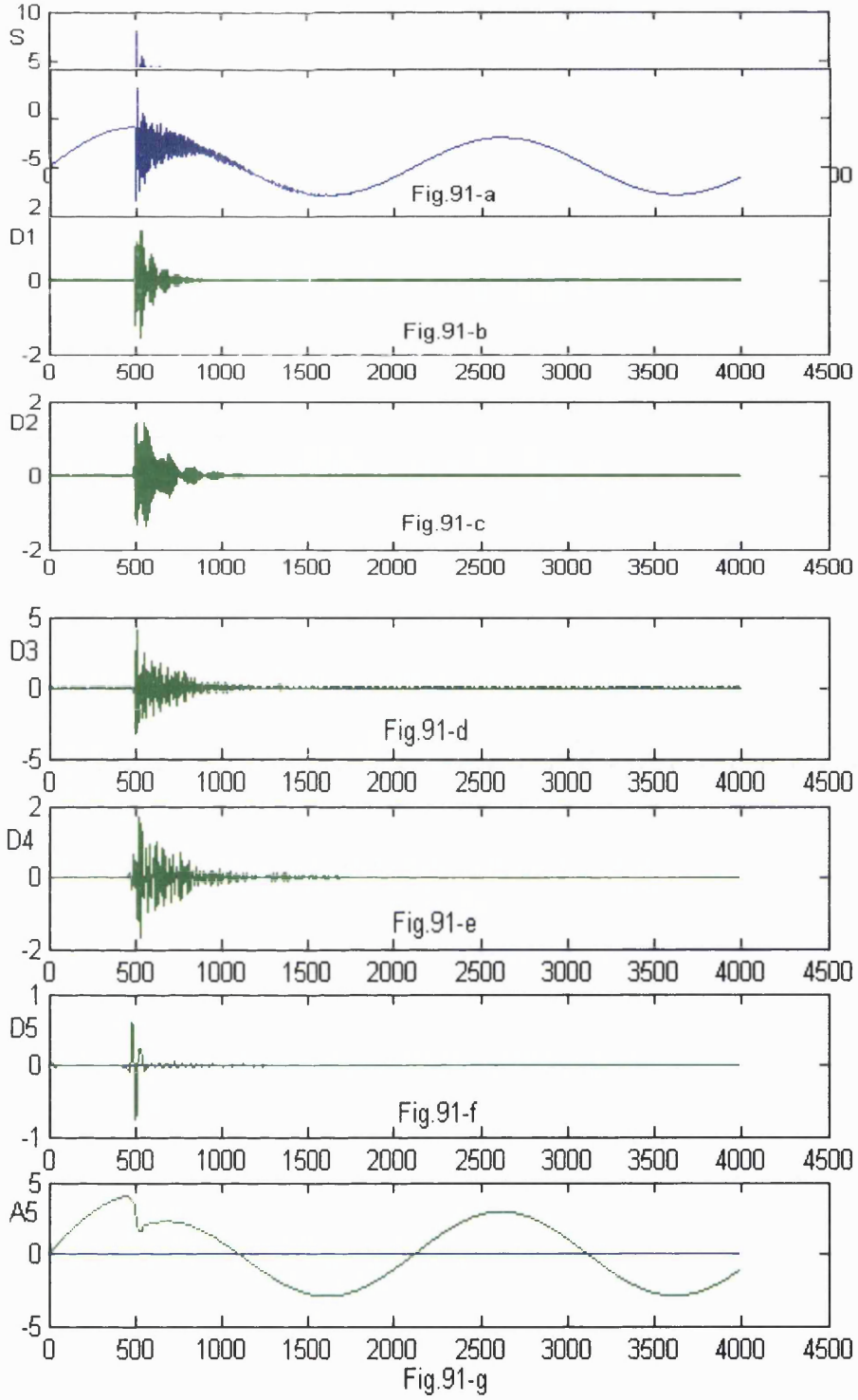

Fig.91- Details and approximate signals of an original signal *S* at level 5

Note that in implementing the DWT, the original signal has been sampled at 100 kHz and passed through a DWT. Thus according to fig.(88), the frequency bands for detailed signals are 25kHz to 50kHz at detail-1, 12.5kHz to 25kHz at detail-2, 6.25kHz to

12.5kHz at detail-3, 3.125kHz to 6.25kHz at detail-4, 1.5625kHz to 3.125kHz at detail-5.

The process of fault classification involves two stages: (i) type of fault i.e. short-circuit or open-circuit, and (ii) faulted phase(s) and whether the fault is grounded or ungrounded: For the statistics option within the wavelet toolbox and data processing on approximate signal of the voltage and current phases and modes of current signals, it was found that some useful information could be extracted from standard deviation (SD) of approximate-5 signals at the first stage of fault classification. SD equation is as follows:

$$SD(v) = \sqrt{\frac{1}{n-1}\sum_{i=1}^{n}(v_i - \bar{v})^2} \qquad (5\text{-}19)$$

Where v_i is the i_{th} sample of signal v , n is the number of samples and $\bar{v}$ is the average of the samples.

SD for every data input with dimension 9 (three-phase voltage, three-phase current and three modes) have a specific relationship with the type of fault. After recognising the type of fault, SD of voltage phases, current phases and modes are used for a short circuit fault to recognise the faulted phases and whether it is a grounded or ungrounded fault.

As mentioned before, the reason for using modal components of current signals in the case of short-circuit fault is that there is unique feature for recognising grounded or ungrounded faults. However, some features corresponding only to the detail of the voltage signals are employed in the open-circuit fault in order to obtain the opened phases. There are six useful features which are used to determine the faulted phase(s) in open-circuit faults at the second stage of classification: (i) since detailed signals consist of different frequency band and initial distortion in each band is depend on the distance of fault, thus first three features are based on the total SD of detailed voltage signal at all the 5 levels for three phases i.e. SDdva, SDdvb and SDdvc, (ii) in addition to the aforementioned features, some additional features are also necessary in the case of an open-circuit fault; this is so by the virtue of the fact that unlike short-circuit faults, for such faults, there is little current flowing in the circuit and heuristic approach based on an extensive series of studies have revealed that 3 additional features based on the

summation of the three aforementioned SD of signals divided by the SD of the detailed voltage signal for each phase provide the necessary information and hence an enhancement in the classification of open-circuit faults. The three additional features are as follows:

1- The sum of the three aforementioned features (associated with three phases) divided by the first feature corresponding to: 'a' phase i.e., *sum(SDdv)/SDdva*
2- The sum of the three aforementioned features (associated with three phases) divided by the first feature corresponding to: 'b' phase i.e., *sum(SDdv)/SDdvb*
3- The sum of the three aforementioned features (associated with three phases) divided by the first feature corresponding to: 'c' phase i.e., *sum(SDdv)/SDdvc*

Figs.(92 to 98) show the data used in the first stage of fault classification associated with the type of fault and also the data used in the second stage of fault classification in the case of short-circuit faults where the features are similar to the first stage. Each figure comprises three parts: voltage phase signals, current phase signals and modal currents. Each part of the figures shows three graphs related to three phases or three modes and each graph depicts the SD of approximate-5 of signal for the conditions dealt with in Chapter 4. Fig.(92) depicts SD of approximate-5 for the 156 conditions in the case of *ag-sc* fault and one source system. These conditions represent 13 fault locations (50m, 100m, 500m, 900m, 1,100m, 1,500m, 1,900m, 2,100m, 2,500m, 2,900m, 3,100m, 3,500m and 3,900m), three fault inception angles (90, 135 and 180 degrees) and four fault resistances (0.1, 2, 10 and 20 Ohms). As it can be seen, each graph comprises of 12 separate parts. The SD in each part is associated with 13 locations for a specific inception angle and Rf. Also, every three consecutive parts (1–3, 4–6, 7–9 and 10–12) are based on the same Rf but different inception angles (90, 135 and 180 degrees respectively). It should also be noted that the first three parts (1-3) correspond to Rf=0.1Ω, second three parts (4-6) to Rf=2Ω and so on. Fig.(92) (which is for ag-sc fault) shows a significant difference in the SD magnitudes between 'a' phase (faulted phase) and phases 'b' and '*c*' (healthy phases).

As can be seen, SD of voltage in the faulted phase '*a*' increases in each part as the fault distance increases from the measurement point, while it is more or less constant for both healthy phases. Although the difference between the maximum SD and minimum SD decreases, in particular the level of SD of the faulted phase approaches those in the

healthy phases as Rf increases, there is still a discernable difference in the SD levels between the faulted and healthy phases.

Also, the SD of current in the faulted phase *'a'* is a descending graph according to the fault distance in each part and the rate of descent of SD decreases as Rf increases. It should be noted that the difference in SD level is much clearer in the case of the current signals than that of the voltage signals. The SD of mode-1 and mode-2 are similar to the SD of faulted phase *'a'* and shows an apparent feature. The SD of mode-3 is however, near to zero; this would be expected by virtue of tact that the faulted 'a' phase does not play any part in this mode (as mode-3 of current is proportional to phase-b subtracted by phase-c of current).

Fig.(93) shows the SD of the voltage and current signals and like the previous case, it also comprises of 156 conditions, the difference being that it is related to the *bcg-sc* fault. The aforementioned features outlined in fig.(92) associated with faulted and healthy phases, can be seen from fig.(93). It is important to note that firstly, the differences in SD levels are more apparent in the case of the two-phase to ground faults than single-phase to ground faults. Secondly, in the latter case, the sensitivity to Rf is less and thirdly, in contrast to the former, the level of SD in mode-3 is much larger than the other modes for all conditions.

Fig.(94) depicts the SD of voltage and current signals and it comprises of 39 conditions, 13 locations and three inception angles, in the case of a *bc-sc* fault. The features shown in fig.(94) are similar to fig.(93) which correspond to the SD of voltage and current phase signals, but a significant difference between the two is in the graph relating to mode-1, which can be used to distinguish between a grounded or ungrounded fault. It is apparent from Fig. (94) that mode-1 is almost zero for all the conditions in the case of ungrounded faults.

Fig.(95) shows the SD of voltage and current signals for 3-phase fault and, like fig.(94), it comprises of the 39 different fault conditions. As can be seen, the features of the faulted phases are the same in comparison with the *bc-sc* fault for all the graphs corresponding to voltage and current phase and current modal signals. It also shows that

the difference in the level are more apparent than with the grounded faults shown in figs.(92 and 93) particularly in the case of modal signals.

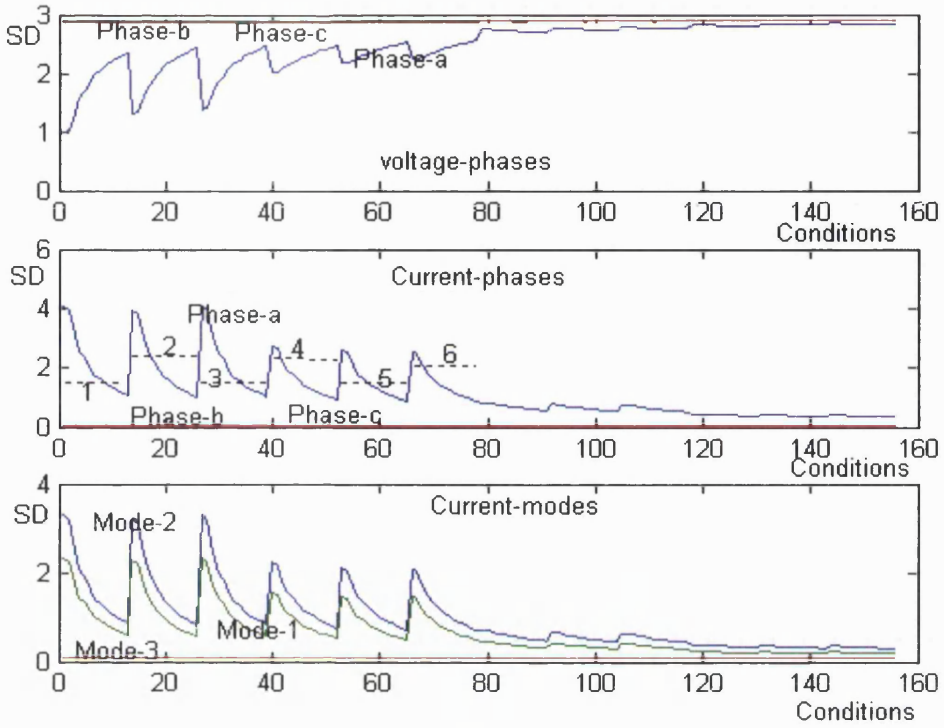

Fig.92- SD of approximate-5 signal in the case of *a-g-sc* fault

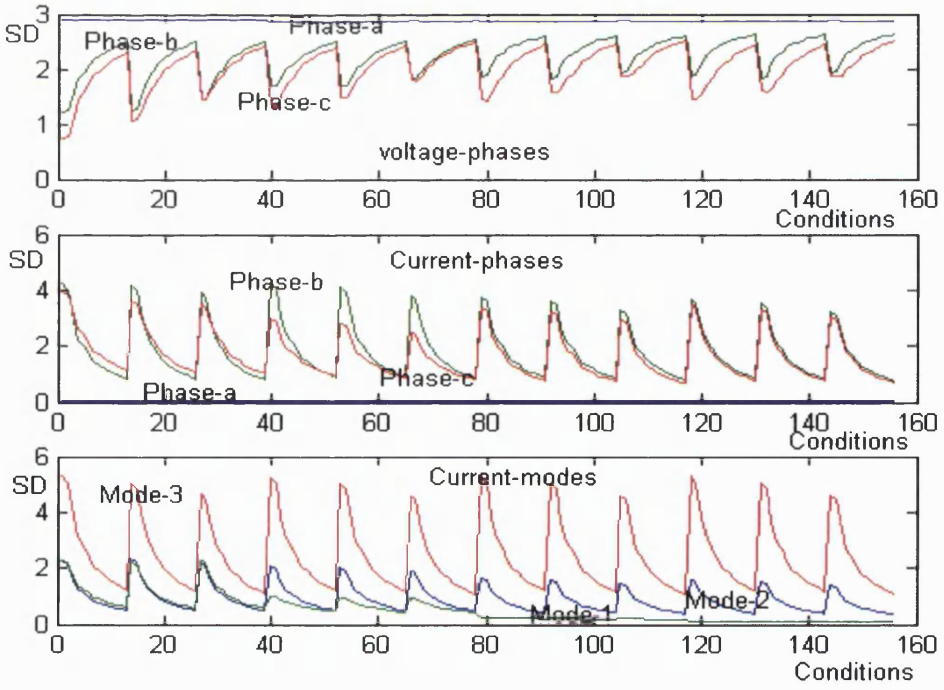

Fig.93- SD of approximate-5 signal in the case of *bc-g-sc* fault

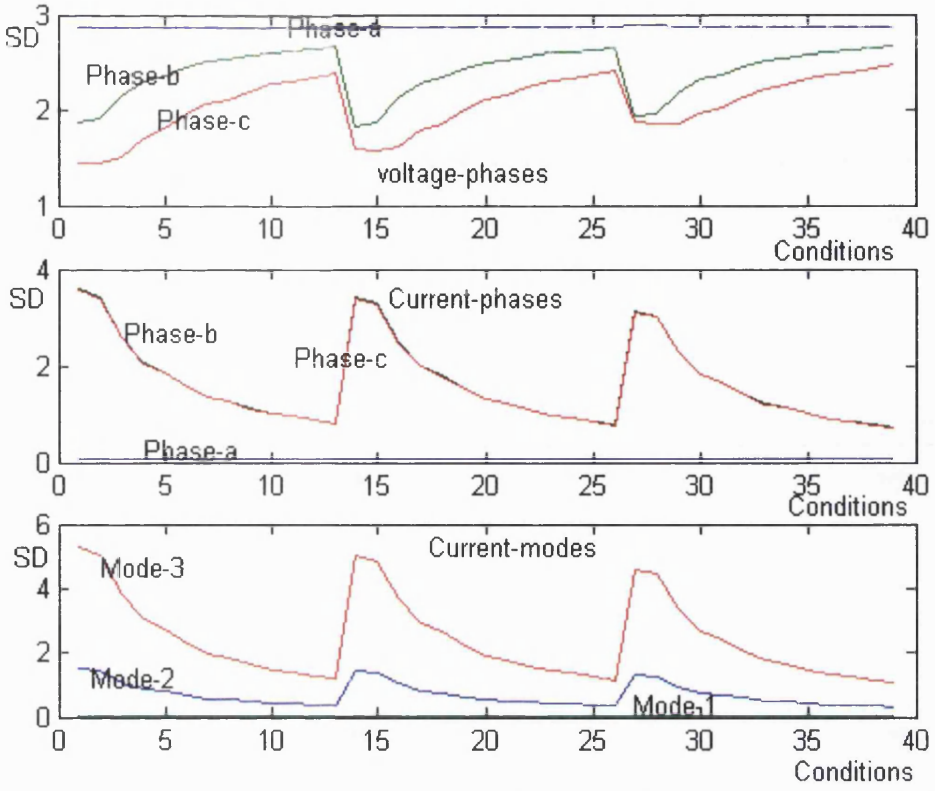

Fig.94- SD of approximate-5 signal in the case of *bc-sc* fault

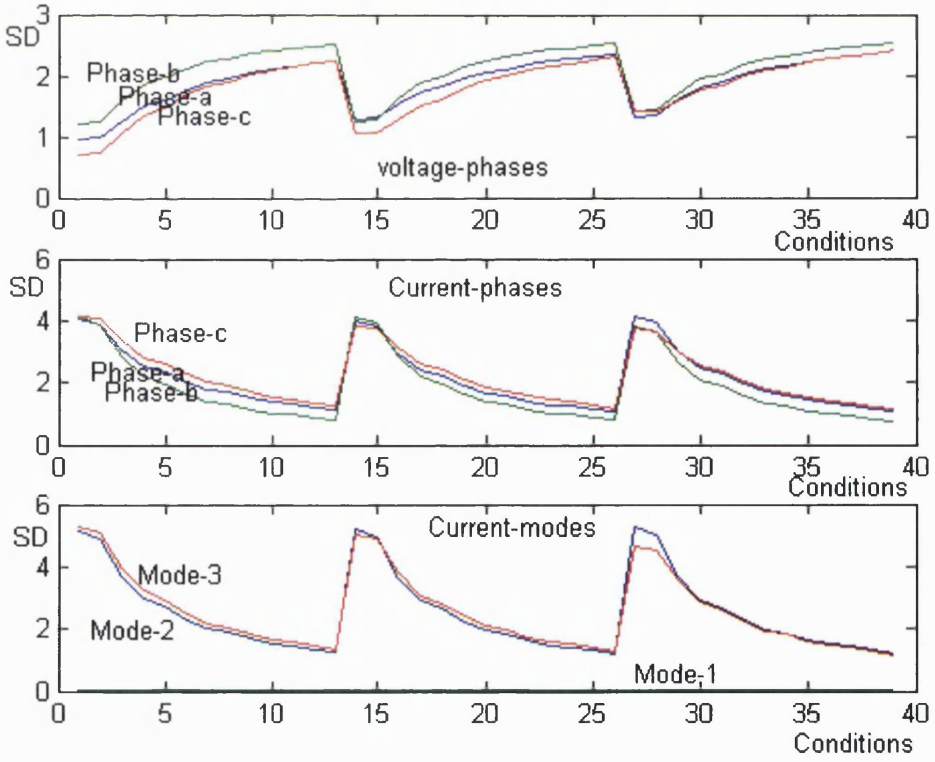

Fig.95- SD of approximate-5 signal in the case of *abc-sc* fault

Figs.(96 to 98) show the SD of voltage phase and current phase signals and modal components of current signals for the 39 conditions in the case of open-circuit faults. It can be seen that irrespective of being a faulted or a healthy phase, the SDs of the three voltages are much larger than those related to the faulted phases for all considered conditions under short-circuit faults. Also, the six graphs associated with the current phase and modal signals are much lower than the faulted phases in the case of short-circuit faults. It is apparent that this difference can be effectively used as the key feature in distinguishing short-circuit faults from open-circuit ones.

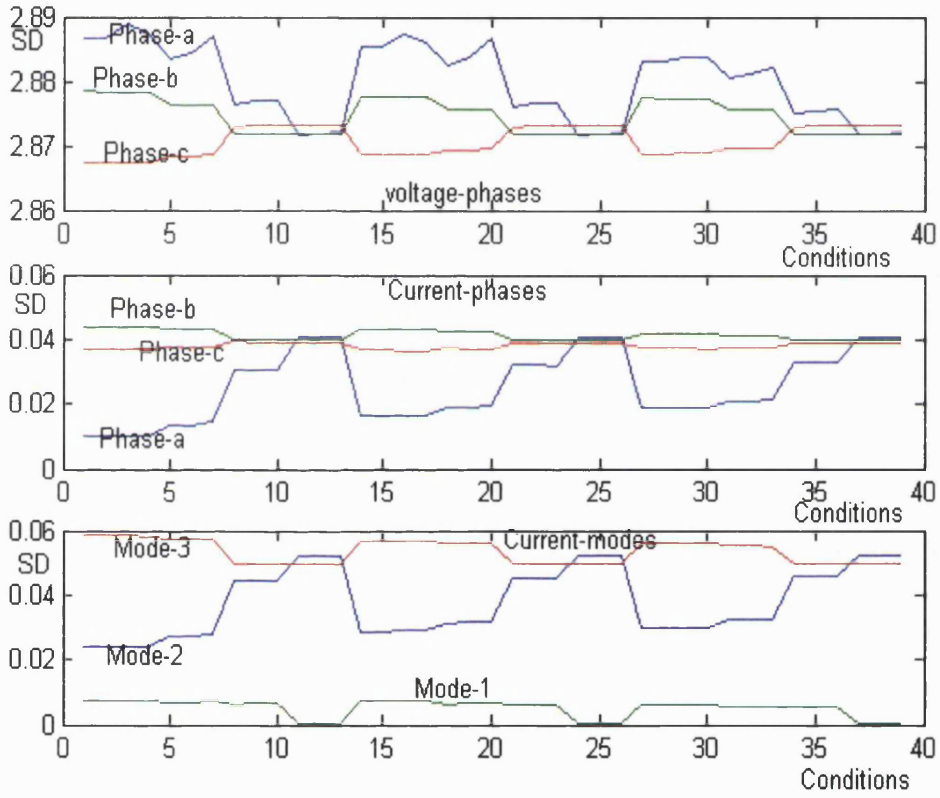

Fig.96- SD of approximate-5 signal in the case of *a-oc* fault

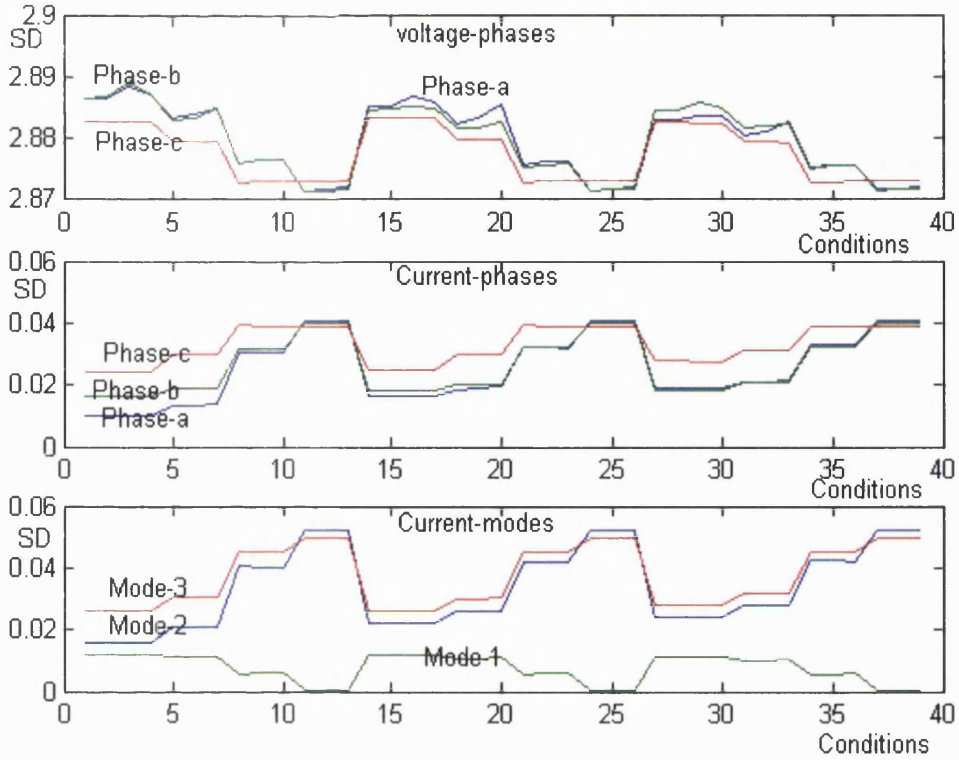

Fig.97- SD of approximate-5 signal in the case of *ab-oc* fault

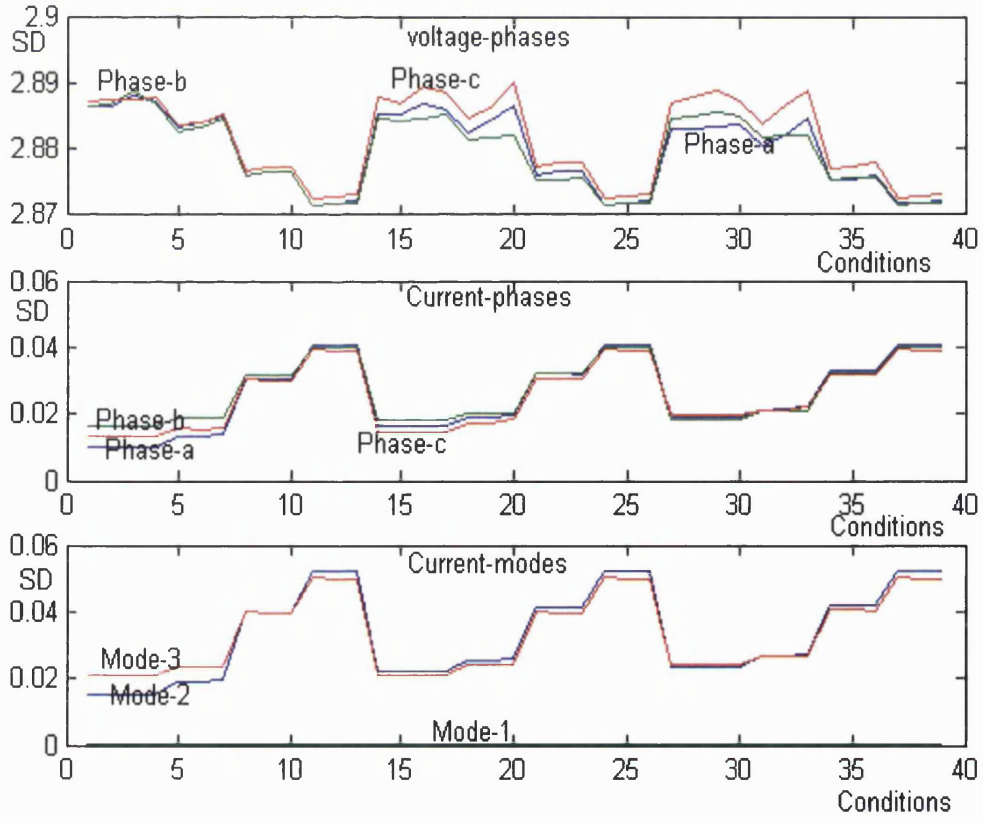

Fig.98- SD of approximate-5 signal in the case of *abc-oc* fault

As mentioned before, if an open-circuit fault is to be recognised, six important features must be used to detect the faulted phase(s). Figs.(99 to 101) show the results for three open-circuit faults namely, *a-oc*, *ab-oc* and *abc-oc*. Similar to previous faults, 39 fault conditions have been considered, comprised 13 locations and three inception angles. Each figure contains two graphs; the upper graph shows the total SD of detailed 'a', 'b' and 'c' voltage signals at all the 5 levels while the lower graph depicts the three features associated with the sum of the three aforementioned features divided by the detailed voltage signal shown in the upper graph.

Fig.(99) shows the six aforementioned features in the case of *a-oc* fault. It shows that there is an obvious discernable difference in magnitude between faulted and healthy phases only for the first ten conditions of 13 locations. The reason for this is that locations 11, 12 and 13 are in the last section of the cable and it is apparent that open-circuit in this section has little effect on the voltage and current signals, as the system is supplied by only one source. Figs.(100 and 101) show that there are similar features in SD results associated with the difference in signal levels between faulted and healthy phases as those presented in fig.(99).

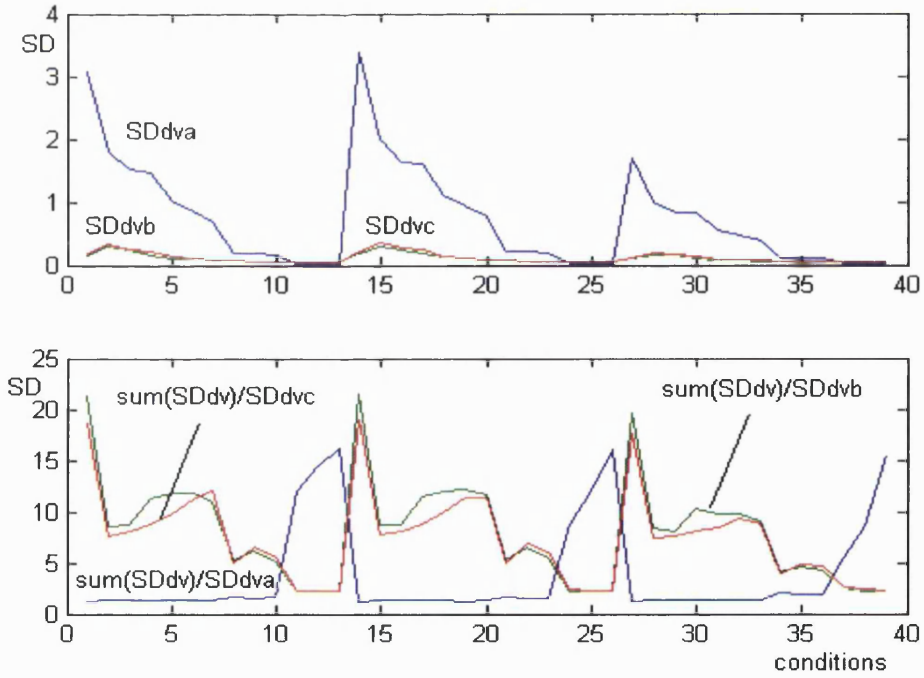

Fig.99- SD of detailed voltage signals (at level 1 to 5) in the case of *a-oc* fault

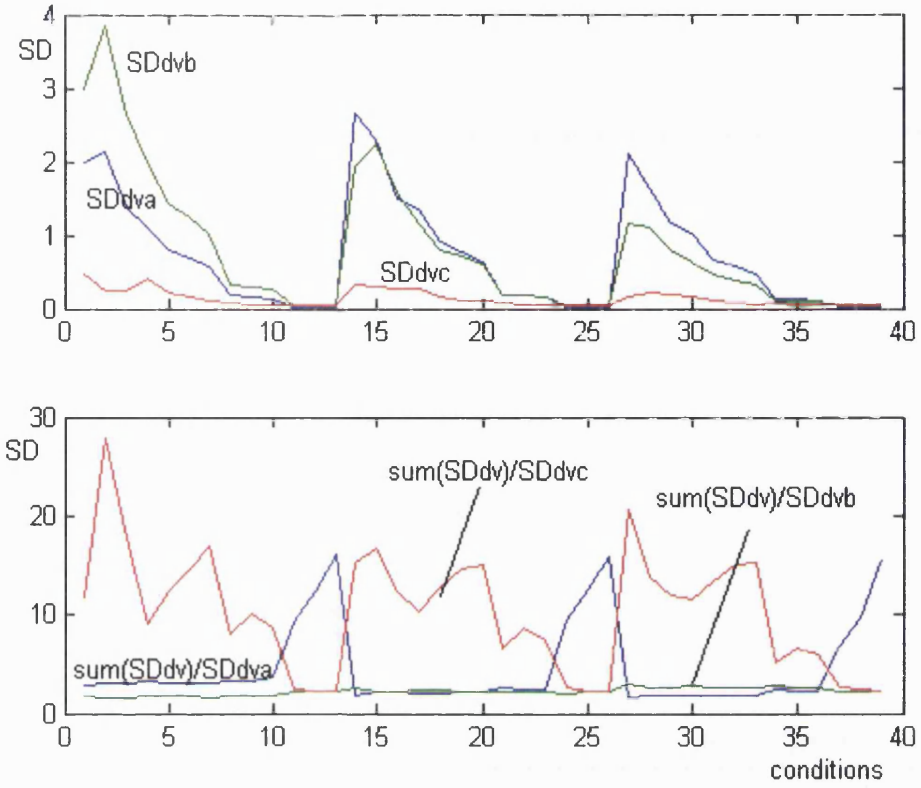

Fig.100- SD of detailed voltage signals (at level 1 to 5) in the case of *ab-oc* fault

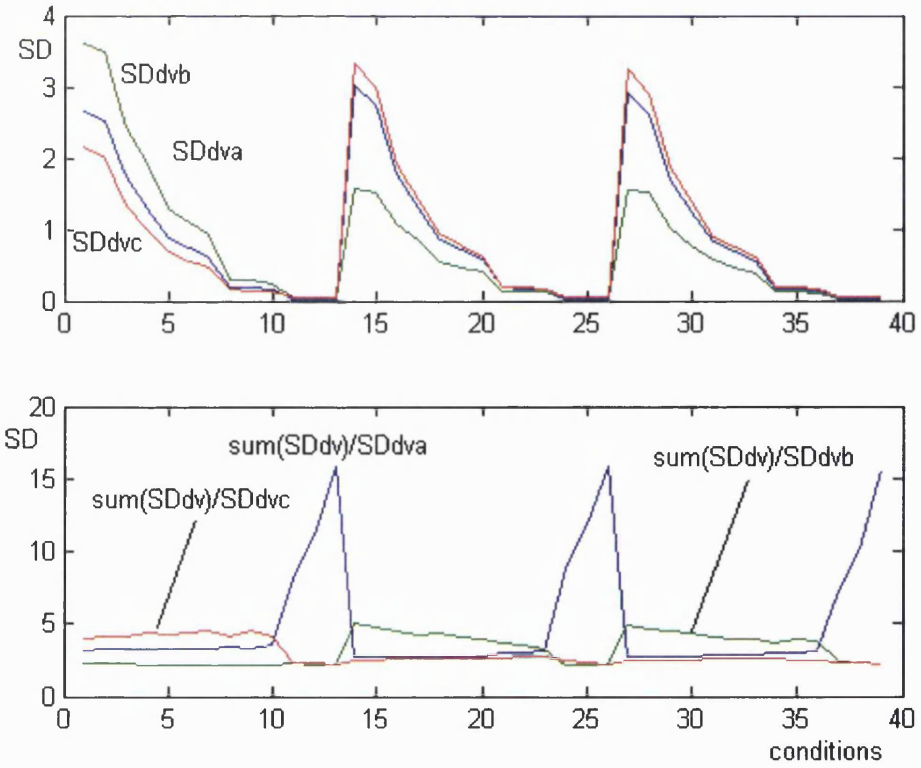

Fig.101- SD of detailed voltage signals (at level 1 to 5) in the case of *abc-oc* fault

5.3.2.2 Fault Location

As mentioned before, the fault location technique presented herein comprises of two stages. In the previous section the fault classification stage was studied and some important parameters were presented whose features play a significant role in classifying faults. In this section other parameters and features in different types of fault are presented.

I- Single phase to ground short-circuit fault:

Similar to previous studies, it can be seen that there are very useful features in the decomposed voltage and current signals using the DWT . In certain cases, high frequency component can be located better in time than a low frequency component and vice versa and this effectively means that all of the features for a particular signal should be obtained. In this study, the components employed are located in low frequency range. Therefore, approximate-5 is considered for further feature analysis. In order to obtain useful features, first, 14 voltage and current approximate-5 signals as an example are presented which are related to 'a' phase, and seven conditions. These conditions are associated with seven locations; 100m, 500m, 900m, 1,500m, 2,100m, 2,900m and 3,500m; an inception angle of 90 degrees and an Rf value of 2 Ohms in the case of *ag-sc* fault.

Fig.(102) shows the signals, consisting of two parts relating to voltage and current signals. The magnitude of the second peak of the current signals decreases significantly as the fault distance increases, while the location of the peaks is almost constant (waveform 1 shown in Fig.(102) is related to 100m fault distance and waveform number 7 is associated with fault distance 3500m). The reason for decreasing the magnitude of current by virtue of increasing the fault distance is that the more distance causes the more total impedance from the source. In contrast, the second peak of voltage signals increases due to decreasing of voltage drop on the source internal impedance (because the current decreases), also the sample number corresponds to the second peak decreases considerably. In fact, the nature of Rf is resistance, while the impedance of cable comprises inductance, capacitance and resistance, therefore, the phase-shift between voltage and current is changed by virtue of the fault distance for the same Rf. It

is apparent that these differences can be effectively used as significant features in locating faults.

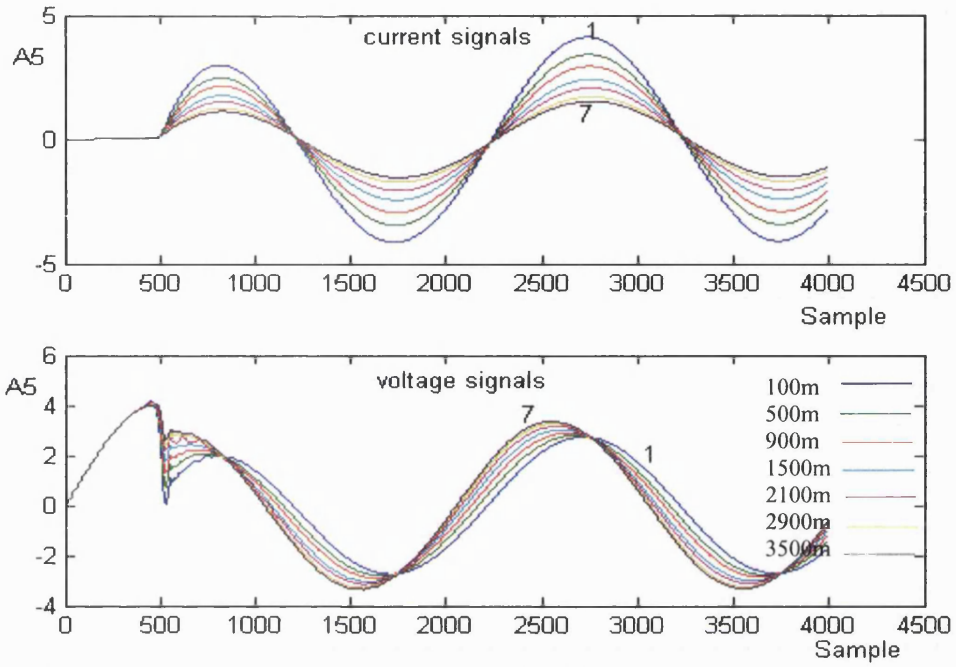

Fig.102- Voltage and current approximate signals at level 5 in 7 conditions, *ag-sc* fault, phase *a*

Based on the behaviour of the voltage and current signals shown in Fig. (102), three important parameters are employed to locate the faults: 1- ratio of peak-peak voltage approximate to peak-peak current approximate at level five (a_ppv/a_ppi), 2- sine of phase-shift between current and voltage approximate at level 5 multiplied by a_ppv/a_ppi, (sin(ϕi-ϕv).v/i), 3- ratio of SD of voltage approximate to SD of current approximate at level 5 (SDv/SDi). It should be noted that these three factors are employed for localise all short-circuit faults and are obtained only for the faulted phase(s).

However, because of the high sensitivity of single-phase to ground (SPH-G-SC) faults to the fault resistance in the case of two sources being connected, particularly in the case of high value of Rf and in order to cover this condition only by recorded data at one end, an additional four parameters are considered. These parameters are: 1- *cosine* of phase angle of the voltage approximate signal at level 5 correspond to second peak (*cos*(ϕv)); 2- *cosine* of phase of current approximate signal at level 5 correspond to second peak (*cos*(ϕi)); 3- the mean of absolute of coefficients 102 to 125 for voltage approximate

signal at level 5 (Mabs_coev); 4- the mean of absolute of coefficients 102 to 125 for current approximate signal at level 5 (Mabs_coei). Furthermore, data processing is based on eight fault resistance values (0.1, 0.5, 2, 6, 10 14, 17, 20 Ohms) instead of the four Rf used in fault classification. The number of conditions is therefore 312, with 13 locations, three inception angles and eight values of Rf for each fault. It should be noted that the sample number of coefficient for approximate-5 is 131 and considered samples 102 to 125 are related to second half of the second cycle of signal where DC off-set has been died down and also the first two parameters indicate the effect of fault resistance that play as an important role in the case of remote source infeed.

Fig.(103) shows seven graphs associated with the SPH-G-SC fault with one source and indicates the results of signal processing using wavelet technique and the parameters used in the fault location stage. In order to obtain more accurate results based-ANNs, the signals are normalized according to *Eq.* (5-20). Normalisation refers to desired range of values required at the input and output of the NNs and is dealt with in next chapter in detail.

$$I_{normed} = \frac{I - I_{\min}}{I_{\max} - I_{\min}} \qquad (5\text{-}20)$$

All seven graphs consist of 24 parts related to three inception angles and eight values of Rf. Each part involves 13 conditions related to 13 locations of fault and each three continual parts correspond to the same Rf but different inception angles. Graph a_ppv/a_ppi illustrates that all parts are ascending due to the location of the fault increasing and hence an increase in impedance. For the same reason, each of the three consecutive parts of the curve increases according to the value of Rf. Changes to the inception angle, however, do not affect results. Graphs *cos*(φv) and *cos*(φi) show the phase shift of voltage and current signals at the measurement point compared with the voltage source.

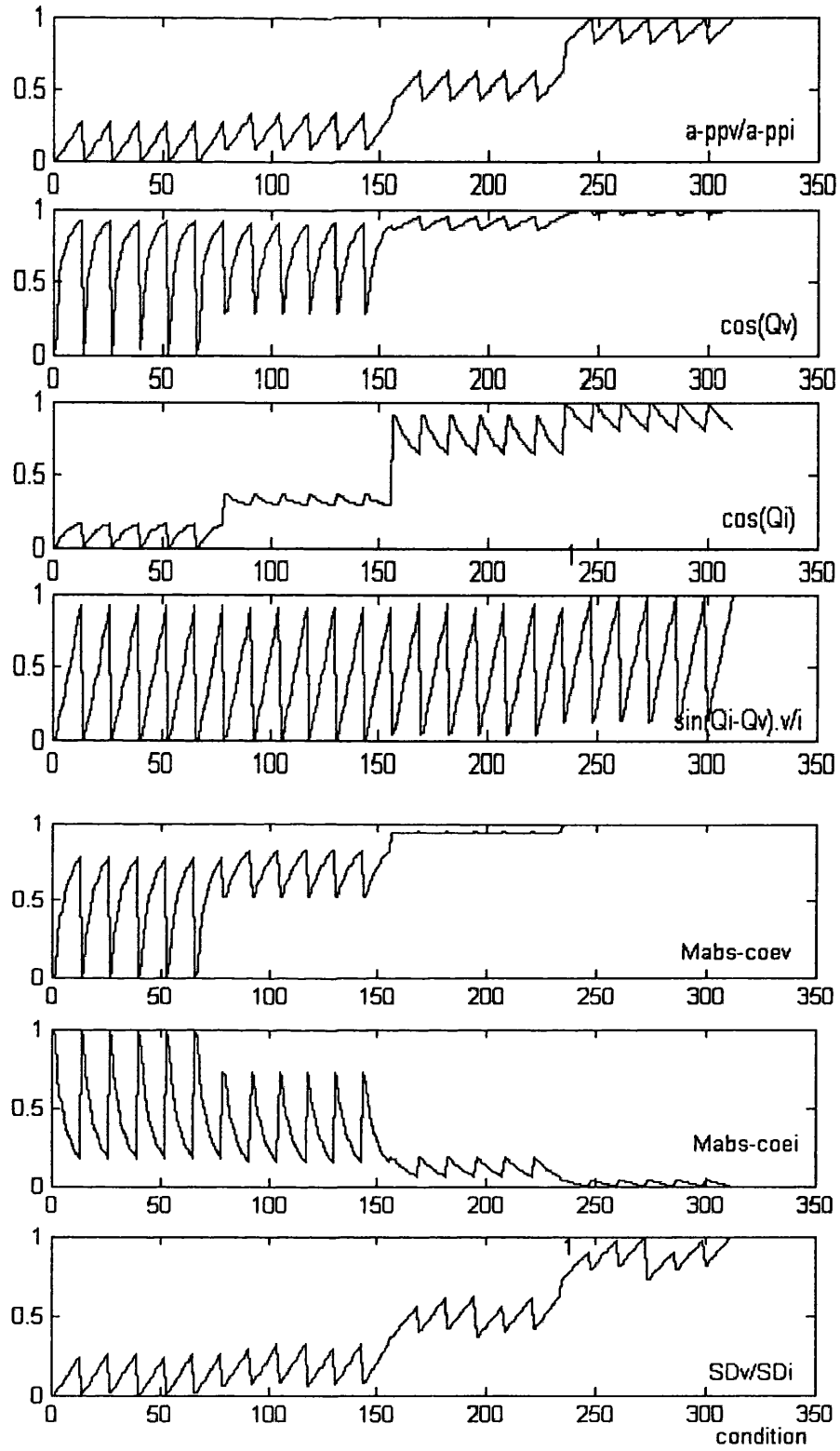

Fig.103- Seven parameters used in the fault location stage in the case of *ag-sc* fault (one source)

An explanation of the reasons for the changes in these graphs is shown in fig.(104). This shows a single line diagram after the fault (eliminating the loads) in the case of a steady state condition, where the results v_r and i_r (shown in fig.(104)) are very close to

approximate-5 signals in wavelet analysis, because in approximate signal, high distortion component related to the transient state is eliminated. X_s is ten times that of R_s (i.e. X_s:R_s ratio of the source), while V_s is the voltage source. Point *a* is the measuring point, v_r and i_r are the measured signals, *Lx* and *Lr* represent cable series impedance (*L* is the distance of fault and *x* and *r* are inductance and resistance per unit length of cable) and Rf is fault resistance The phase shift between current i_r and voltage source V_s is:

$$\Phi_1 = \tan^{-1}\left(\frac{Lx + X_s}{Lr + R_s + Rf}\right) \tag{5-20}$$

And the phase shift between current i_r and voltage v_r is:

$$\Phi_2 = \tan^{-1}\left(\frac{Lx}{Lr + Rf}\right) \tag{5-21}$$

It is apparent that *r* is more prominent than *x* in the cable model (typical x:r ratio is less than 2). With regard to X_s compared with R_s (X_s»R_s), and taking into consideration the nature of the fault impedance (this is purely resistance), it is clear that when Rf is very small – for instance 0.1 or 0.5 Ohms – φ_1 decreases by virtue of increasing the distance of *L*, while φ_2 remains constant. However, when Rf becomes larger, both φ_1 and φ_2 increase according to an increase in *L*. Therefore, with regard to $\varphi_v = \varphi_2 - \varphi_1$ and $\varphi_i = -\varphi_1$, all parts of graph $cos(\varphi_v)$ are ascending but the first six parts of $cos(\varphi_i)$ associated with Rf 0.1 and 0.5 Ohms are ascending while the other parts of the graph are descending.

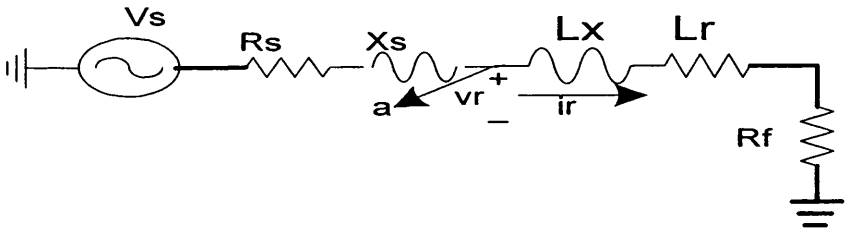

Fig.104- Single line diagram for SPH-G-SC fault

With regard to fig.(104), the following calculation can be implemented:

$$|V_r| = \sqrt{(Lr + Rf)^2 + (Lx)^2} \times |I_r| \tag{5-22}$$

$$\sin(\varphi_2) = \frac{Lx}{\sqrt{(Lr + Rf)^2 + (Lx)^2}} \tag{5-23}$$

Therefore $$\sin(\varphi_2) \times |V_r| / |I_r| = Lx \tag{5-24}$$

As a result, the graph with function $sin(\varphi_i - \varphi_v).V/I$ is independent of Rf and the inception angle, but all parts of the graph are proportional to distance L, as can be seen in fig.(103). The other graphs here are associated with parameters Mabs-coev, Mabs-coei and SDv/SDi. It can be observed that all parts are independent of inception angle, but in relation to fault distance are ascending, descending and ascending, respectively. Parameter SDv/SDi is very close to parameter a_ppv/a_ppi. Furthermore, with increase or decrease in Rf, parameter Mabs-coev increases or decreases accordingly, but the changes of parameter Mabs-coei is vice versa.

Fig.(105) is similar to figure (103), but is for a DS with two sources. It is apparent that the remote source infeed affects the voltage and the current signals at the measuring end and this effect depends largely on the value of Rf. In theory, if Rf is zero, then the results for the two conditions (one and two sources) should be the same; this is verified by comparing figs (103 and 105) from which it can be seen that the parts of the graphs relating to low levels of Rf (0.1 & 0.5 Ω) are little different from each other. If, however, the value of Rf increases, the infeed from the remote source has a significant influence on the measured signals and hence on the various aforementioned parameters and hence the mathematical relationships as described previously for a single-end fed DS are no longer valid.

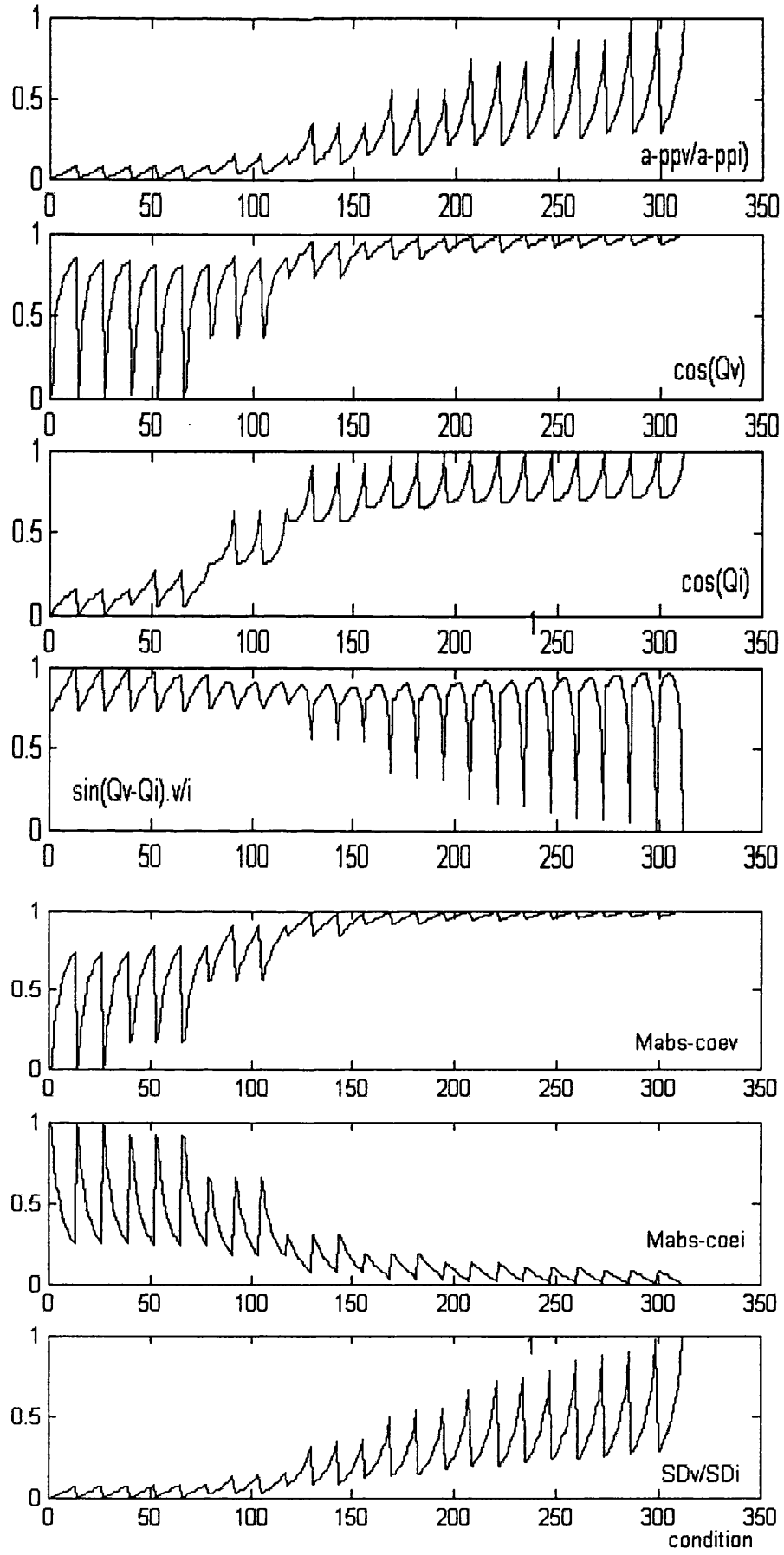

Fig.105- Seven parameters used in the fault location stage in the case of the *ag-sc* fault (two sources)

II- Two-phase to ground short-circuit fault

Similar to the SPH-G-SC fault, voltage and current approximate-5 signals are again taken into account when obtaining useful information at the fault location stage for two-phase to ground (2PH-G-SC) faults. In order to obtain useful features, 14 voltage and current approximate-5 signals are first presented relating to bcg-sc fault. They correspond to 'b' phase and seven conditions; these conditions represent seven locations of 100m, 500m, 900m, 1,500m, 2,100m, 2,900m and 3,500m, an inception angle of 90 degrees and an Rf value of 2 Ohms in the case of single-source infeed.

Fig.(106) shows the results which shows the voltage and current signals. Firstly, with regard to the current signals, it can be seen that the second peak of the current signals is significantly lower than the first peak and the magnitude varies with the distance to fault. Importantly, the location of the peaks is almost constant. The second peak in the voltage signals graph, however, shows an increase with fault distance and also in contrast to the current signals, the instants at which the peaks occur are different. It can be observed that the results are similar to those for the SPH-G-SC fault analysed in the previous section.

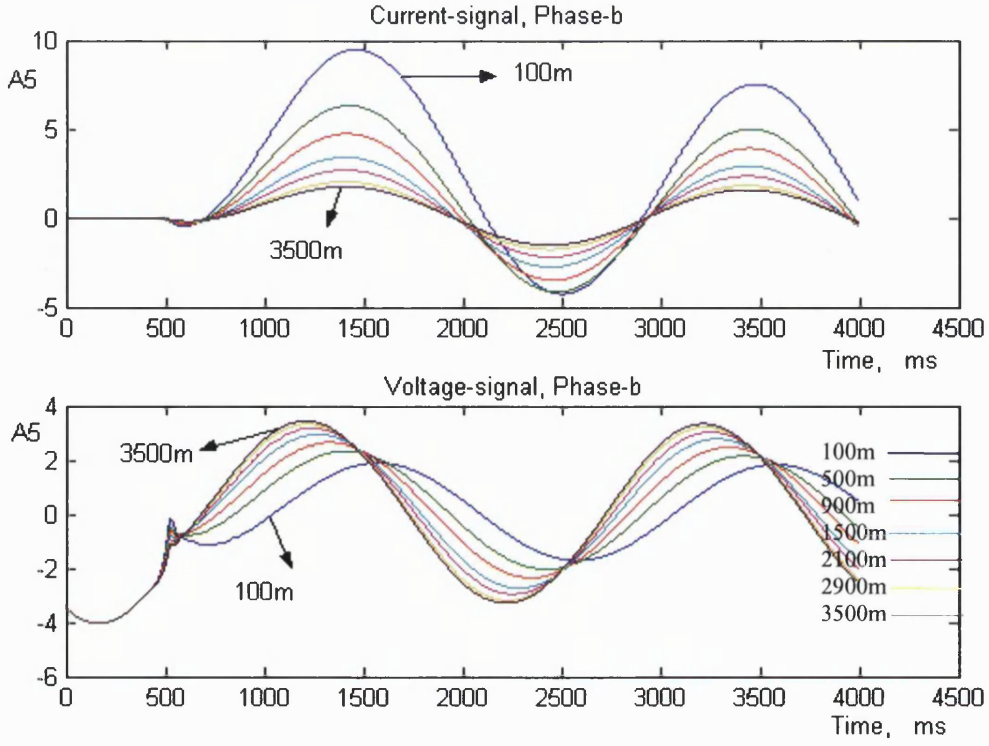

Fig.106- Voltage and current approximate signals at level 5 in 7 conditions, *bcg-sc* fault, phase '*b*'

For this type of fault and with regard to obtained results from Fig. (106) associated with magnitude of voltage and current signals and also phase-shift in voltage signal, three important parameters are employed when locating the faults: 1- ratio of peak-peak voltage approximate to peak-peak current approximate at level five (a_ppv/a_ppi), 2- sine of phase-shift between current and voltage approximate at level 5 multiple by a_ppv/a_ppi, (sin(φi-φv).v/i), 3- ratio of SD of voltage approximate to SD of current approximate at level 5 (SDv/SDi). It should be mentioned that these three parameters are employed only for the faulted phases and the time period for recorded signal is 40ms (two cycles) and the technique to find parameters a_ppv and a_ppi is based on the last maximum and last minimum of voltage and current approximate signals. Here, the data processing is based on four fault resistances (0.1, 2, 10, 20 Ohms) and hence the number of fault condition is 156 with 13 locations, three inception angles and four values of Rf.

Fig.(107) shows the behaviour of parameters a-ppv/a-ppi, $sin(\varphi_i - \varphi_v).V/I$ and SDv/SDi for both the faulted phases '*b*' and '*c*' according to the aforementioned 156 fault conditions. All graphs comprise 12 parts related to three inception angles and four values of Rf and each part depicts their behaviour depending on the 13 fault locations. Each three consecutive parts correspond to the same Rf but a different inception angle. All parts of the graphs are ascending by virtue of the increasing distance *L*. It can be observed that the inception angles cause a change in the magnitudes of the parameters for the same values of Rf and fault distance. The inception angle should not in essence affect the results but this change is actually a direct consequence of there being a DC component in both the voltage and current approximate signals; DC component is a maximum when the inception angle is zero. Also, the phase shift between phases '*b*' and '*c*' is 120 degrees and the DC components are different for different inception angles. Thus the changes in different parts of the graphs do not follow a specific pattern but what is important is that all parts of the graphs are ascending according to the increasing distance *L* and all data training and testing is extracted based on the same technique.

From fig.(107) it can be seen that the six parameters (three parameters for each faulted phase) have a distinct relationship with the location of the fault. Also it is apparent that these features are clearer than the SPH-G-SC fault and the sensitivity of 2PH-G-SC to fault resistance is lower than in the case of SPH-G-SC. This low sensitivity to Rf causes

a small change in the results in the case of remote source connected, thus only one source network is used herein.

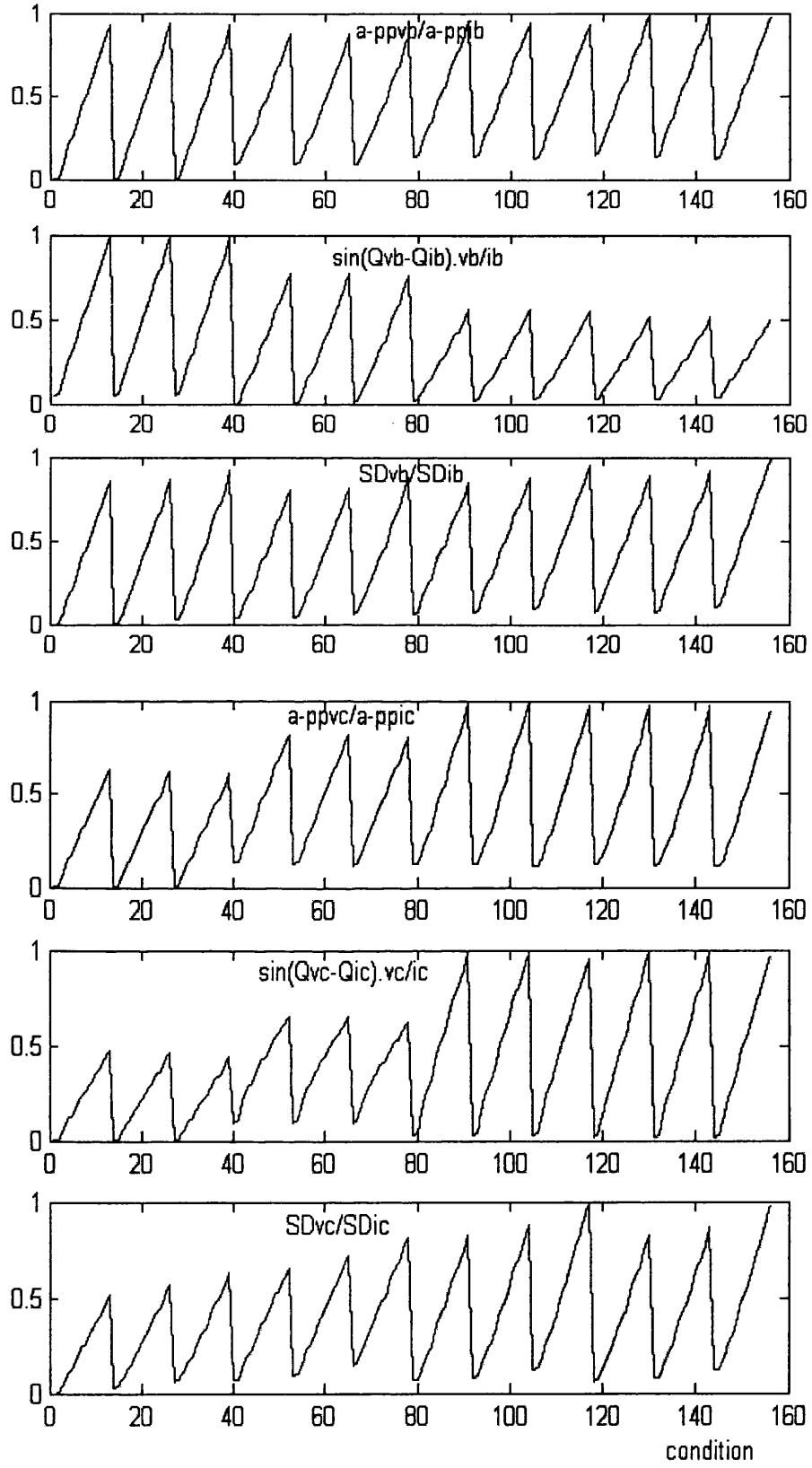

Fig.107- Six parameters used in the fault location stage, *bcg-sc* fault (one source)

III- Two-phase short-circuit fault

Similar to the 2PH-G-SC fault, the voltage and current approximate-5 signals are again considered as important in obtaining useful information at the fault location stage in a two-phase short-circuit (2PH-SC) fault. In this respect, similar to the 2PH-G-SC fault here, three important parameters are employed to locate the faults: 1- ratio of peak-peak voltage approximate to peak-peak current approximate at level five (a_ppv/a_ppi), 2- sine of phase-shift between current and voltage approximate at level 5 multiple by a_ppv/a_ppi, (sin(φi-φv).v/i), 3- ratio of SD of voltage approximate to SD of current approximate at level 5 (SDv/SDi). It should be noted that these three parameters are employed only for the faulted phases. In contrast to the 2PH_G-SC fault, data processing is based on ungrounded fault signals and therefore the number of conditions is 39 including 13 locations and three inception angles.

Fig.(108) comprises of six graphs (similar to figure 107), but these are in relation to 39 fault conditions in the case of phase '*b*' to phase '*c*' fault. Each graph consists of three parts: all of them ascend by virtue of distance *L* increasing. In theory, 2PH-G-SC and 2PH-SC faults should be the same when Rf is infinite. Fig.(108) exhibits a clear relationship between considered parameters and fault location and since in this case Rf does not affect the signals as an unknown parameter, the analysis of features for locating faults is simpler and more accurate than in the case of grounded fault location.

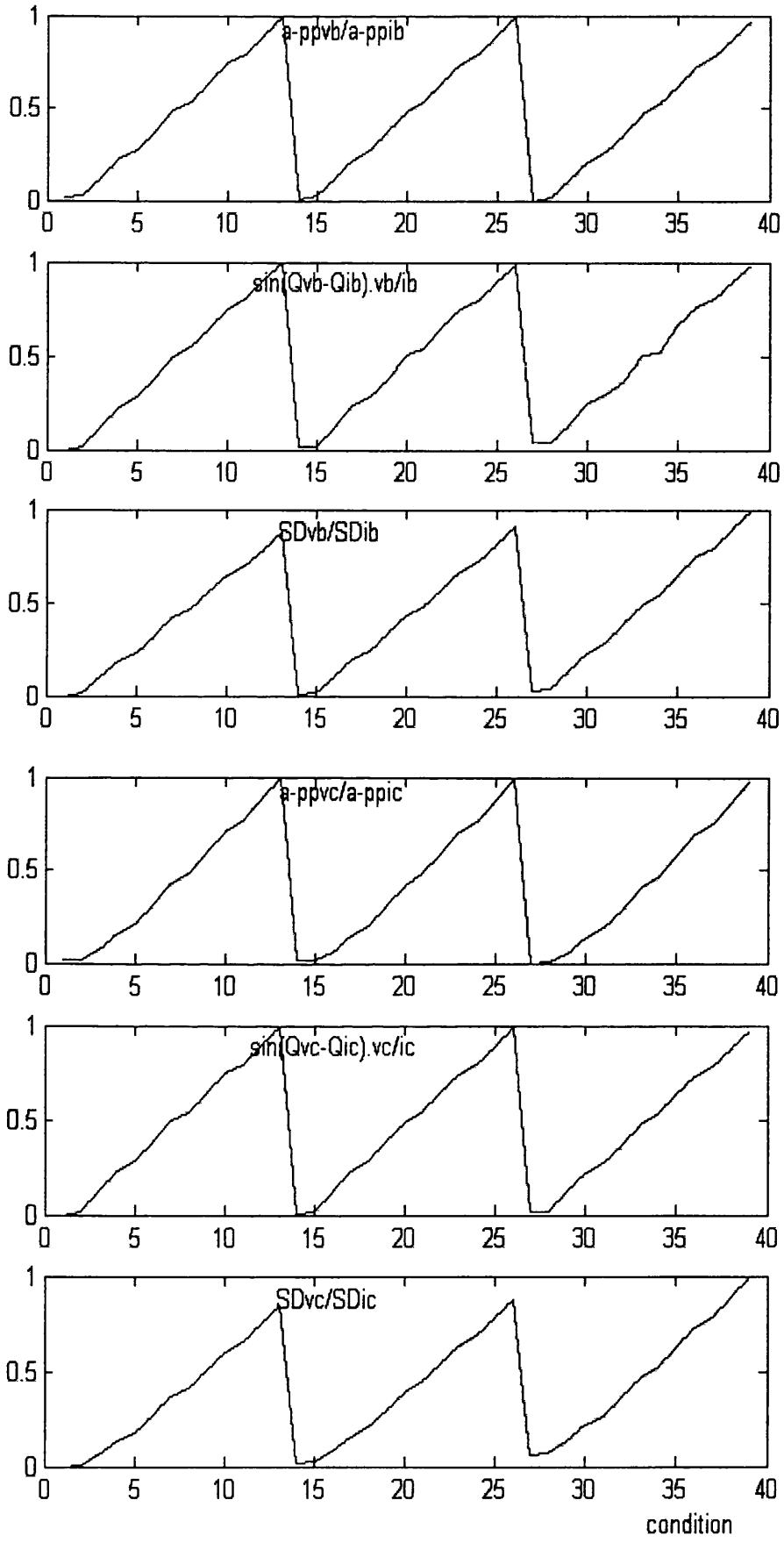

Fig.108- Six parameters used in fault location stage, *bc-sc* fault (one source)

IV- Three-phase short-circuit fault

Since this case is a case of symmetrical fault, the nature of the fault is ungrounded, and the obtained results are similar to those of a 2PH-SC fault in respect of independing of Rf. Fig.(109) depicts three graphs according to 39 fault conditions associated with 13 locations and three inception angles, solely for 'a' phase in the case of the 3PH-SC fault. These three parameters are similar to those in the case of 2PH-SC. The reason for only selecting phase *'a'* is the similarity between the three phases in terms of the considered parameters. It can be seen that the results are similar to those in fig.(108) with regard to the changes in parameters as a function of the fault distance and there is a distinct relationship between the parameters and the fault distance. This relationship can thus be effectively used for key features to locate the fault in a 3PH-SC case. It should be remembered that remote source connection does not affect the voltage and current signals at the measurement point in ungrounded faults. These three parameters can give accurate results for both one and two sources connection.

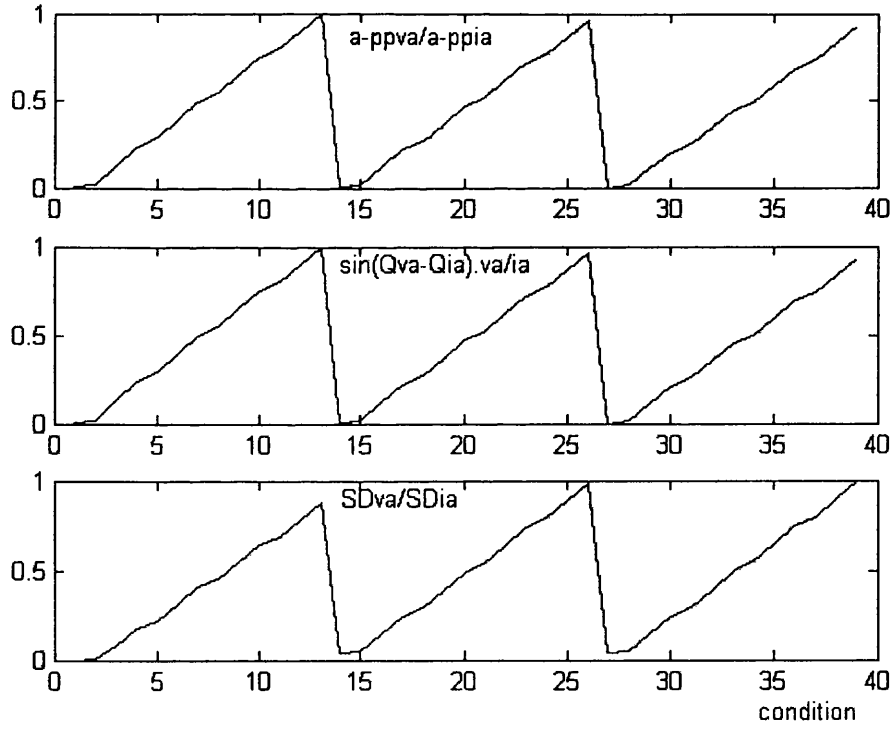

Fig.109- Three parameters used in fault location stage – *abc-sc* fault

V- Open-circuit fault

In contrast to short-circuit faults, current signals are much smaller in the case of an open-circuit fault. Furthermore, approximate current signals significantly depend on the

loads. As figs.(84 to 86) showed earlier, the closer the fault is to the measurement point, the higher the distortion (including magnitude and frequency) corresponds to the voltage. Therefore, instead of approximate-5 of current and voltage signals, more useful information from detail-1 to detail-5 of the voltage signal can be extracted to locate the fault accurately. In this respect, it is necessary that the fault-time be also detected. For this purpose, detail-1 of voltage signal is used for the faulted phase(s) as its frequency band is 25kHz to 50kHz. It should be noted that if the faulted phases are more than one, only one of them is employed. Fig.(110) displays detail-1 of the 'a' phase voltage signal for the conditions L = 500m and inception angles are 90, 135 and 180 degrees for an *ab-oc* fault. The figure comprises three graphs corresponding to the three inception angles. Since the sample frequency is 100kHz and two cycles of signal (40 ms) is processed, thus each graph contains 4,001 samples. As it can be seen from the figure there is a clear and sudden change in detail-1 signal when the fault occurs, and the particular sample related to the sudden change can be detected accurately. It is apparent that the sample number determines the inception angle: for instance, the number 500 specifies an inception angle of 90 degrees (inception angle= sample number * 720° /4001).

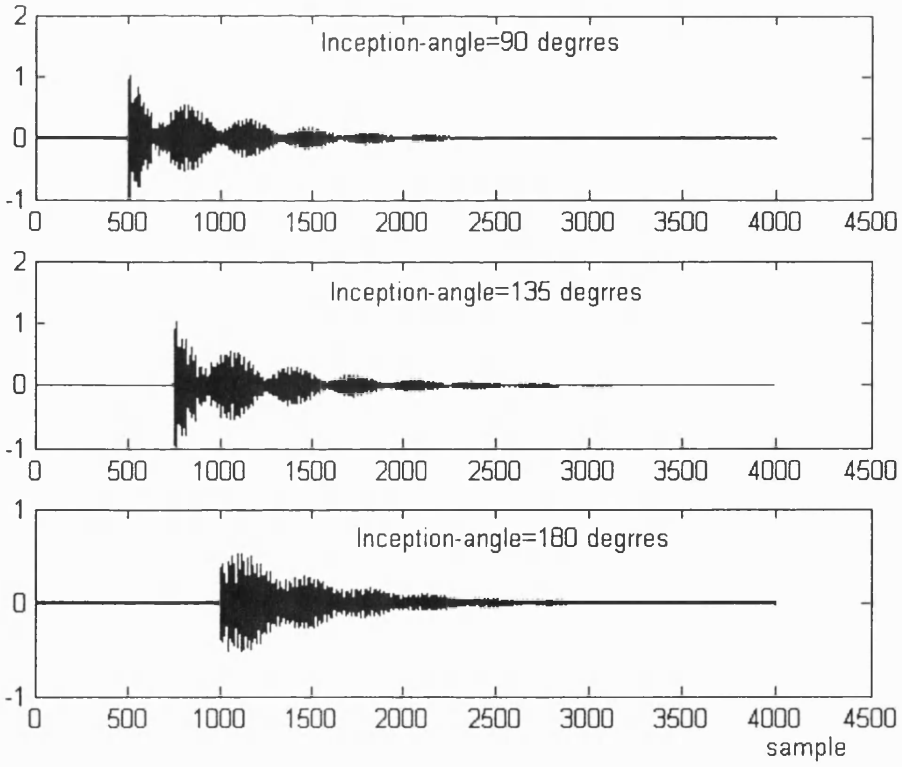

Fig.110- Detail-1 of 'a' phase voltage signal for the three conditions in the case of *ab-oc* fault

Since for all three cases of the open-circuit fault – one-phase, two-phase and three-phase – similar parameters are used to locate the fault, all the cases are dealt with collectively in this section. There are three parameters employed to locate the open-circuit fault as follows:

1- The *sine* of inception angle, which is determined by,

$sin(\varphi)= \sin(sd1/1000*\pi)$

where *sd1* is the number of the sample the fault occurs in .

2- The total of the complete SD of details for the voltage phase signals, determined by,

SD-dv=SD(d1vpha)+SD(d2vpha)+ SD(d3vpha)+ SD(d4vpha)+ SD(d5vpha)+
SD(d1vphb)+SD(d2vphb)+ SD(d3vphb)+ SD(d4vphb)+ SD(d5vphb)+
SD(d1vphc)+ SD(d2vphc)+ SD(d3vphc)+ SD(d4vphc)+ SD(d5vphc)

where *d1vpha* is detail-1 of 'a' phase voltage signal, and so on.

3- The total of the wavelet coefficients of all the details and phases for only one cycle after the fault are determined by:

Coe-dv=coe1va+coe2va+coe3va+coe4va+coe5va+coe1vb+coe2vb+coe3vb+
coe4vb+ coe5vb+ coe1vc+ coe2vc+coe3vc+coe4vc+coe5vc

where *coe1va* is the coefficients of detail-1 of 'a' phase voltage signal, and so on.

To extract significant features from the parameters given above, 39 conditions are considered. Similar to previous types of fault, these conditions correspond to 13 locations and three inception angles. Figs.(111 to 113) show the results in the three cases: *a-oc*, *ab-oc* and *abc-oc*. Each figure shows three graphs themed by the three aforementioned parameters. As before, each 13 consecutive conditions are based on the same inception angle but different locations. Since the DS is energised by only one source and the remote end of the system is open, an open-circuit fault in the last section of cable causes only very minor change in the voltage and current signals. Thus distinct characteristics cannot be ascertained from the graphs for fault conditions related to the

last section of the cable. It can be seen that in contrast to the short-circuit fault, here inception angle can affect the results. Because of this, the first parameters are used as important features in determining the inception angle. The second and third graphs are descending graphs and demonstrate the sensitivity of Parameters 2 and 3 to the distance of fault. Taking this into account, these features can be effectively used as significant features in locating open-circuit faults. It should be mentioned that in order to achieve more accurate fault location, all parameters are normalized, based on *Eq.* (5-20).

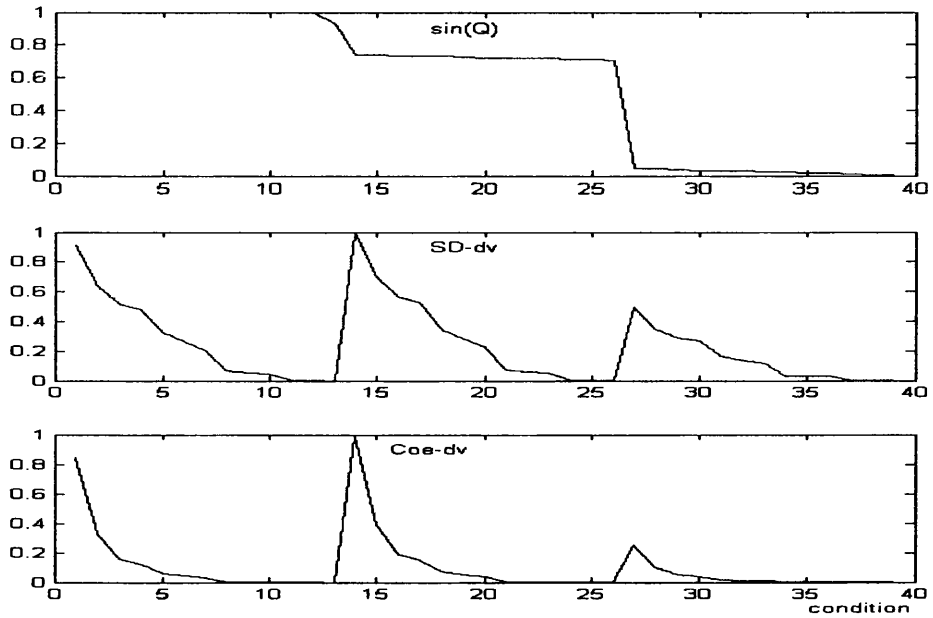

Fig.111- Three parameters used in the fault location stage, *a-oc* fault

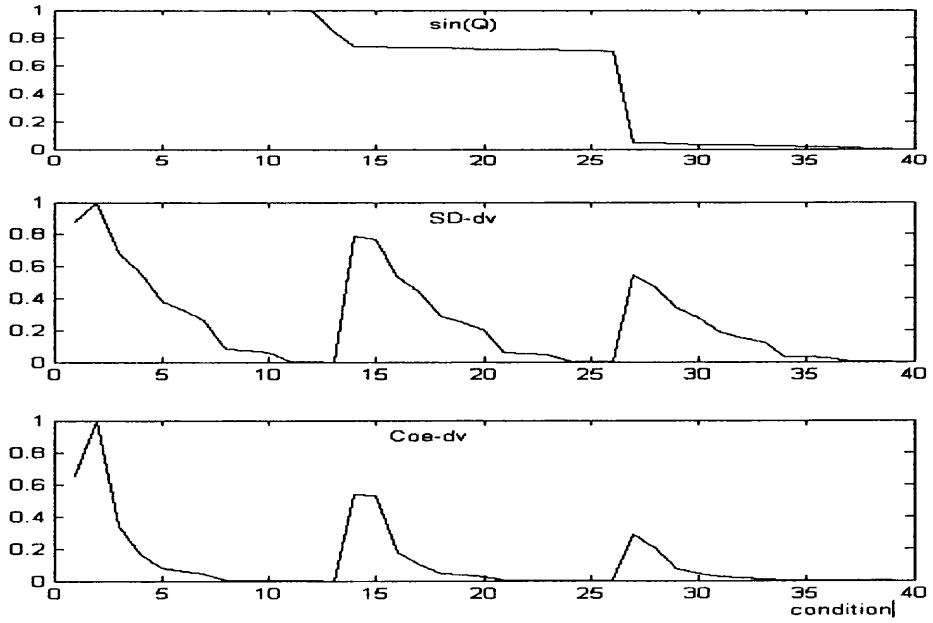

Fig.112- Three parameters used in the fault location stage, *ab-oc* fault

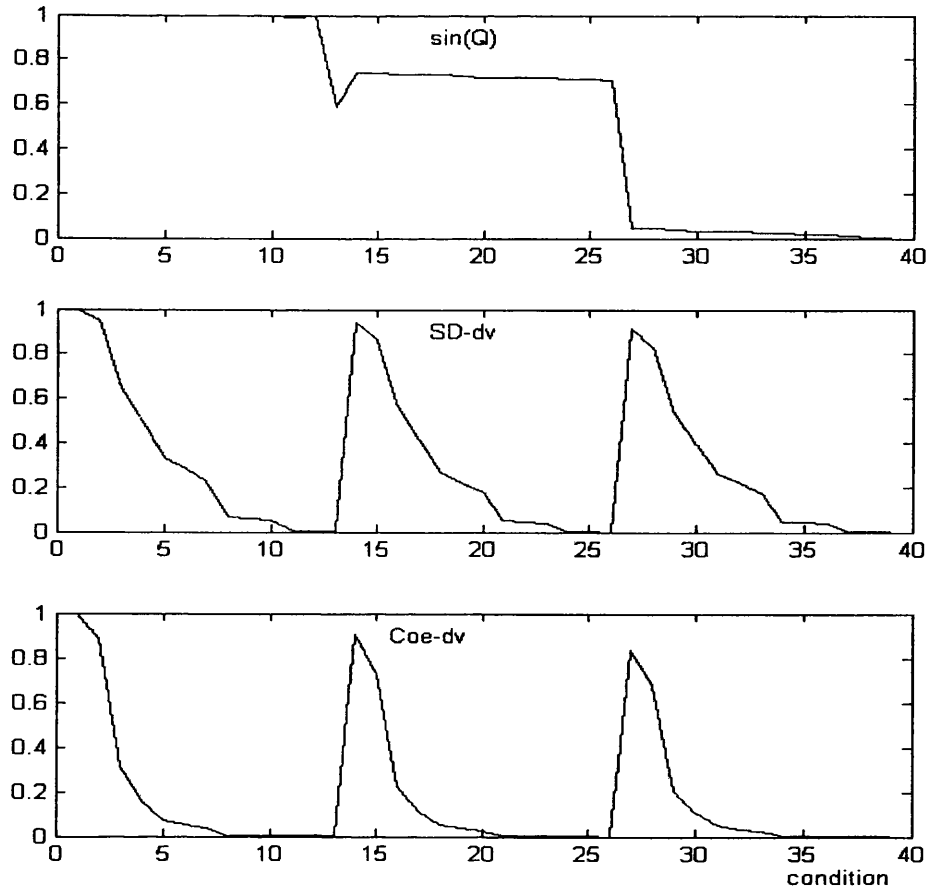

Fig.113- Three parameters used in the fault location stage, *abc-oc* fault

5.4 Summary

In this chapter, a new method of analysing power DS transient phenomena is proposed using WT technique. This method offers important advantages over other methods (such as FFT, PSD and STFT) due to good time and frequency localisation characteristics. Analysis results presented clearly show that particular wavelet components can be used to set up specific function to locate faults in underground DS. This attribute is now used in the design of neural networks to locate the fault in DS, as outlined in the next chapter.

CHAPTER 6

Fault Location Technique Based on Artificial Neural Network

6.1 Introduction

Artificial Neural Networks (ANNs) have emerged as a powerful pattern recognition technique. Since the need for pattern recognition arises whenever computers interact with the real world, ANNs are useful in a range of applications. Like other pattern recognition techniques, ANNs act on data by detecting some form of underlying organisation not explicitly given or even known by human experts and it possesses certain features which are not attainable by the conventional methods. The networks can recognise spatial, temporal or other relationships and are able to perform such task as classification, prediction and function estimation. This can bridge the gap between individual examples and general relationships. This characteristic has encouraged various researchers to apply ANNs to solve various power system problems such as fault diagnosis, fault location, load forecasting, etc. This chapter describes a new method for accurate fault location based on the application of ANN techniques. At first, the characteristics of ANNs are presented including architecture, processing algorithm and learning algorithm, it then deals with training/test data and finally the sensitivity of the technique is tested to the some important parameters such as variation in load taps, location of the loads, length of the cable and remote source. It is shown that the trained ANNs are able to make correct decisions under a wide variety of system and fault conditions. It should be noted that the main simulation for data preparation and training process of the networks is done off-line and the fault location technique is based on an off-line application. Since the fault location is performed off-line, computation time is not a major issue. However, the accuracy in the location of the fault is of fundamental importance. Since the done work is based on MATLAB programming, MATLAB commands which have been used in the programs have also been presented herein.

6.2 Motivation for Using ANNs for Power System Engineers

An ANN is an intelligent system motivated by research into the human brain. The human brain is the most complex computing device, and its powerful thinking,

remembering and problem-solving capabilities have motivated scientists to investigate how a machine can implement the thoughts and actions of human beings.

The computer programs developed are based on mathematical models and are implemented using languages suitable for numeric computation only. Although methods based on mathematical models have been successful for solving a number of problems in the power system area, there remain a number problems where methods based on mathematical model lead to less than satisfactory solutions. In this respect, an ANN provides an attractive alternative computational concept to the conventional approach, the latter being based on a programmed instruction sequence and prescribed rules. The main advantages of the ANN are [44-49]:

- ANNs are adaptive in nature, as they can take data and learn from it. Thus ANNs bridge the gap between individual examples and general relationships. This ability differs from standard software techniques because it does not depend on the programmer's prior knowledge of rules. ANNs can reduce development time by learning underlying relationships even if they are difficult to find and describe. They can also solve problems that lack existing solutions.

- ANNs can generalise; they can handle incomplete data and provide an ability to fault tolerance. Generalisation is useful in practical applications because real world data is noisy and incomplete.

- ANNs are non-linear: they can capture complex interaction amongst the input variables in a system.

- ANNs are highly parallel: their numerous identical, independent operations can be executed simultaneously.

It should be mentioned that in spite of several advantages, motivating the application of ANNs in solving the field of power system problems, there are still some drawback in their application. The inability for extrapolation beyond the area which is trained for, is inherent characteristic to ANNs application in any field. Also as the network size increases, the training time is longer. This appears as a critical constrain on the way of

ANNs application. Other disadvantages of ANNs can be outlined as: there is no definite way of choosing the optimum architecture, there is no definite way of finding the best solution and the solution depends upon the accuracy of the training set.

6.3 Biological Basis for ANNs

The human brain consists of approximately 10 billion individual nerve cells called neurons. All human activities and behaviour can ultimately be traced to the activity of these tiny cells. Each neuron is interconnected to many other neurons, forming a densely connected network call a neural network. These massive interconnections provide an exceptionally large computing power and memory. From an information-processing point of view, the signal flow goes from dendrites through the cell body and out through the axon. The junction point of an axon with a dendrite of another neuron is called synapse. Synapse provide memory to the past accumulated experience or knowledge [50]. The basic building block of the nervous system is the neuron. A schematic diagram of the biological neuron is shown in fig.(114) which comprises of a cell body, dendrites and an axon.

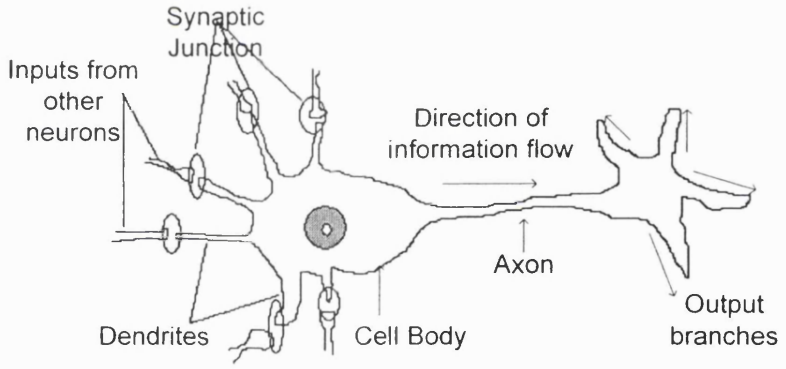

Fig. 114- A schematic view of the biological neuron

Each neuron is activated by the flow of bio-chemicals across the synapses. The transmission of these bio-chemicals across the synaptic junction causes a change in the ionic concentration within the neuron, which, in turn, produces a change in its electrochemical potential. These inputs may be excitatory (positive) and increasing the electrochemical potential of the post-synaptic neuron, or conversely, they may be inhibitory (negative) and reduce the electrochemical potential. If the net potential is above a certain threshold level then the neuron will fire a sequence of pulses along an

axon leading to the synaptic junction of another neuron. The electrochemical activities at these synaptic junctions exhibit complex behaviour because each neuron makes several hundred interconnections with other neurons. Each neuron acts as a parallel processor because it receives pulses in parallel from neighbouring neurons and then transmits pulses in parallel to all neighbouring synapses [50].

The explanation of the biological operation is greatly simplified when seen from a neuro-biological point of view, although it explains the basic principles involved. ANNs are grossly simplified than their biological counterparts. They are described in the following section.

6.4 Artificial Neural Networks Models

Due to the complexity and diversity of the properties of biological neurons, it is extremely difficult to compress their characteristics into a model. Toward this goal, a model of the biological neuron, also called a neural unit, or simply a neuron has been developed in the neural network paradigm. The neuron receives inputs from a number of other neurons or from the external world. Fig.(115) depicts a model of an artificial neural unit. Mathematically, the function of a neuron can be modelled as:

$$Z = \sum_{i=1}^{n} W_i X_i - \Theta_0 \tag{6-1}$$

$$y = f(Z) = f[\sum_{i=1}^{n} W_i X_i - \Theta_0] \tag{6-2}$$

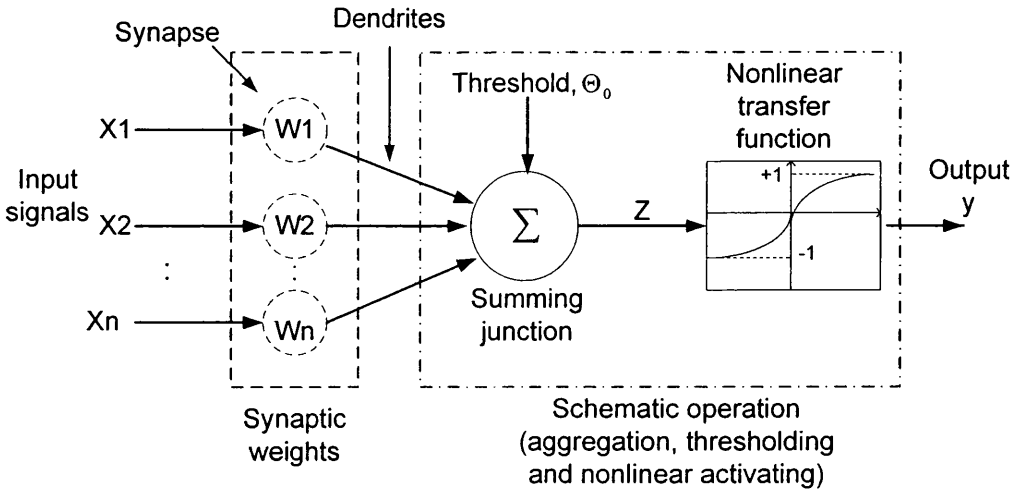

Fig. 115- Model of an artificial neuron (unit)

Where, [X1, X2,..., Xn] represents the input signals, [W1, W2,..., Wn] is the connection weights from input signals to neuron, Z is weighted summation of input signals, y is the neuron output and f(Z) is the nonlinear transfer (or activation) function with threshold Θ_0 (bias).

6.4.1 Non-Linear Transfer Function

The transfer function is one of the important elements in the neuron model. It defines the output of a neuron in terms of the activity level of its input. There are four basic types of transfer functions: Step function, Linear function, Sigmoid function and Hyperbolic tangent function; the commonly used Sigmoid function is defined by:

$$y = f(Z) = \frac{1}{1+e^{z}} \tag{6-3}$$

And the Hyperbolic tangent function is defined by:

$$y = f(Z) = \frac{e^{z} - e^{-z}}{e^{z} + e^{-z}} \tag{6-4}$$

Hyperbolic tangent function is just a bipolar version of the sigmoid function. Fig.(116) shows the characteristics of the Sigmoid and the Hyperbolic tangent transfer functions.

There are four commands to use these transfer functions in the MATLAB software as follows; y=hardlim(Z), y=purelin(Z), y=logsig(Z) and y=tansig(Z) associated with Step, Linear, Sigmoid and Hyperbolic tangent functions, respectively.

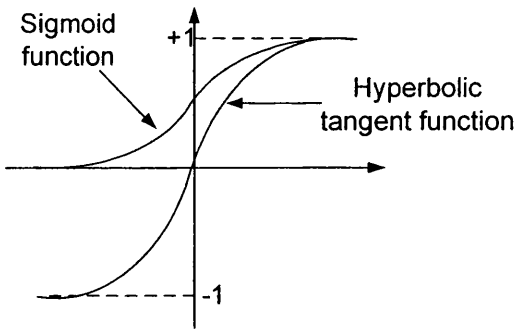

Fig. 116- Characteristic of Sigmoid and Hyperbolic tangent functions

6.4.2 Neural Network Architecture

The neurons are normally connected to each other in a specified fashion to form the neural network. These arrangements of interconnections could form a single layer or several layers. In a large number of neural network models, such as the Perceptron, Linear Association and Multi-layer feed-forward network (MFN), the output from the units from one layer is only allowed to activate neurons in the next adjacent layer. However, in some models such as Kohonen networks, the signal is allowed to activate neurons in the same layer [51,52]. Some important networks are as follows:

6.4.2.1 Perceptron Network

This network has the same basic structure shown in fig.(115) and employs Step transfer function. This transfer function gives a Perceptron the ability to classify input vectors by dividing the input space into two regions. Perceptron networks have several limitations. Firstly, the output values of a Perceptron can take on only one of two values (0 or 1) due to the Step transfer function. Secondly, Perceptrons can only classify linearly separable sets of vectors. If a straight line or a plane can be drawn to separate the input vectors into their correct categories, the input vectors are linearly separable. If the vectors are not linearly separable, learning will never reach a point where all vectors are classified properly. It is only fair, however, to point out networks with more than one Perceptron that can be used to solve more difficult problems. For instance, there is a set of four vectors to classify into distinct groups, and in fact, two lines can be drawn to separate them. A two neuron network can be found such that its two decision boundaries classify the inputs into four categories.

6.4.2.2 Adaptive Linear Neuron (ADALINE) Networks

The ADALINE networks are similar to the Perceptron, but their transfer function is Linear rather than Step function. Also, this network can use the Least Mean Squares (LMS) learning rule which is much more powerful than the Perceptron learning rule. However, both the ADALINE and the Perceptron networks can only solve linearly separable problems.

6.4.2.3 Multilayer Feed-forward Networks

The most commonly used ANNs is the Multilayer Feed-forward networks (MFNs) [53-55]. MFNs often have one or more hidden layers of sigmoid neurons followed by an output layer of linear neurons. Multiple layers of neurons with nonlinear transfer functions allow the network to learn nonlinear and linear relationship between input and output vectors. The linear output layer lets the network produce values outside the range -1 to +1. In theory, a three-layer network can form arbitrarily complex shapes, and is capable of separating any classes. In view of the fact, this research is based on MFNs, such networks are dealt with in more detail herein.

MFNs can overcome the problems associated with the perceptron and ADALINE networks. This network is also sensitive to the number of neurons in its hidden layers. Too few neurons can lead to underfitting. Too many neurons can contribute to overfitting, in which all training points are well fitted, but the fitting curve undergoes wild oscillations between these points [56]. A neural network is characterized by its architecture, its processing algorithm and its learning algorithm.

I- The Architecture:

The architecture specifies the way the neurons are connected. The appropriate notation is used in the two-layer (hidden+output layer) hyperbolic-tangent/linear network shown in fig.(117).

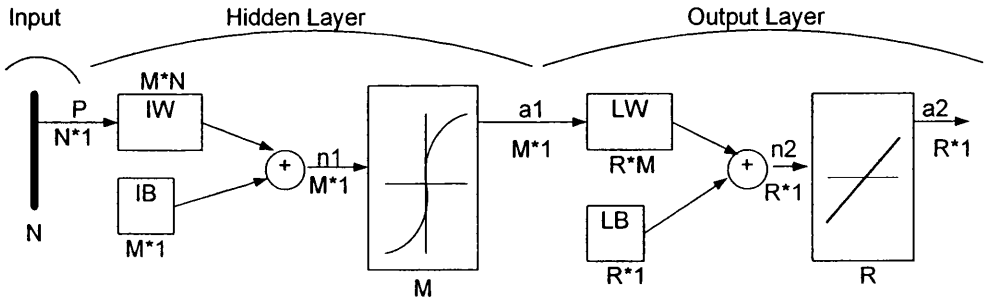

Fig. 117- Two-layer feed-forward network

The figure depicts a two-layer feedforward network. P is input vector in dimension N*1. IW and IB are weights matrices in dimension M*N and biases vector in

dimension M*1, respectively, between input and hidden layer. LW and LB are similar to IW and IB but for the next layer. It is assumed that there are N inputs, M neurons in hidden layer and R neurons in the output layer.

This network can be used as a general approximator. It can approximate any function with a finite number of discontinuities, given sufficient neurons in the hidden layer.

II- The Processing Algorithm

The processing algorithm specifies how the neural network with a given set of weights calculates the output vector (a2 shown in fig.(117)) from any input vector (P shown in fig.(117)). As it can be seen from fig.(117), the process algorithm is based on eqs.(6-5 & 6-6).

. a1=tansig(IW*P+IB) (6-5)

. a2=purelin(LW*a1+LB) (6-6)

III- The Learning Algorithm

The learning algorithm specifies how the neural network adapts its weights for all given training vectors P. There are several different training algorithm for MFNs. All of these algorithm use the gradient of the error to determine how the weights to minimize error. The gradient is determined using a technique called backpropagation, which involves performing computations backwards through the network. The basic backpropagation learning algorithm is based on updating the network weights and biases in the direction which the error decreases most rapidly (the negative of the gradient). One iteration of this algorithm can be written as:

$$X_{k+1}=X_k-\alpha_k.g_k \quad (6\text{-}7)$$

Where X_k is a vector of current weights and biases, g_k is the current gradient, and α_k is the learning rate.

There are two different ways in which this gradient algorithm can be implemented: incremental mode and batch mode. In the incremental mode, the gradient is

computed and the weights and biases are updated after each input is applied to the network. In the batch mode all of the inputs are applied to the network before the weights and biases are updated. Appendix 5 describes in details, these two types of training.

6.5 Practical Consideration of ANNs

The successful development of ANN approaches for solving power system problems depends on the successful learning of the correct relationship or mapping between the input and output patterns by the ANN. In order to achieve this, practical issues surrounding the design, training and testing of a ANN need to be addressed and examined.

6.5.1 Determining the Best Network Size

The degree of freedom of an ANN is equal to the number of inter connections/size, and therefore is proportional to the number of hidden neurons and it must be matched, in some sense, to the complexity of the classification boundary. Currently, in the absence of parameter/theoretical guidance, the only proposed method of determining the best number of hidden neurons is by comparative cross validation among performance of several ANNs. Moving from a small number of hidden neurons to a large number should decrease the overall probability of error while maintaining an equivalent error performance for the test and training data. For a small number of hidden layer neurons, the ANN will be unable to learn the training data. As this number is increased, the training error will reduce until a very large number of neurons are used, when the error will start to increase again.

6.5.2 Generalization versus Memorisation

One of the major features of ANNs is their ability to generalise. There is a difference between training and memorisation. The generalization is the ability to successfully classify patterns that have not been previously presented. Memorisation, on the other hand, guarantees that when the ANN is presented with a specific element in the training

data set, the classifier will respond in exactly the same manner that it was trained. In the case of memorisation, the response to data other than training data is not satisfactory.

The ability to interpolate among the training data does not necessarily imply good generalization. A properly trained classifier should respond with the same error to the training data as to test data. This is necessary but not sufficient condition. If the error from the test data is much higher than that from the training data, then the ANN is over determined; in other words, the degree of freedom in the classification is too high.

6.5.3 Feature Extraction

One of the classical problems in pattern recognition is how to extract the discriminatory features from a given set of measurements. The mathematical approach to feature selection is to identify certain invariant properties of the pattern classes. These properties are then used to reduce the dimensionality of the pattern vectors either through a linear transformation or through the preferential choice of subset of attributes. However, it is important to recognize that the superiority of any one procedure is ultimately determined by the problem at hand. In this respect, as mentioned in the signal processing chapter, considerable effort has been expanded to obtain a number of significant features of voltage and current signals using the WT that can be employed as a data set for the training and testing of ANNs.

6.5.4 Convergence of Training Process

To ensure that the convergence of the training process is achievable, firstly an efficient learning algorithm should be selected, and then such parameters which are related to the algorithm should be determined satisfactorily. However, it is very difficult to know which training algorithm will be the fastest for a given problem. It will depend on many factors, including the complexity of the problem, the number of data points in the training set, the number of weights and biases in the network and the error goal. In general, in MFNs which contain up to a few hundred weights, the Levenberg-Marquardt algorithm will have the fastest convergence. This advantage is especially noticeable if very accurate training is required [56]. This is the reason as to why in this research such an algorithm is employed.

6.5.5 Scaling of Input/Output

For effective training of the ANNs, scaling both the input and output values are required. Scaling refers to the desired range of values required at the input and output of the network. The range into which the values must be scaled are primarily defined by the transfer functions in the nodes. If the input value to a node is large then the output of the node defined by the transfer function will be in an area of the function where the output is almost saturated. This means that the network is unable to learn. Similarly, the network may perform better when output values are within a certain range. For example, in training a backpropagation network whose output layer has a sigmoid transform, it will be better if desired output values are between 0 and 1.

The same scaling method must be used for both training and testing data. A linear scaling which for a variable I in the range of [I_{min}, I_{max}] will assign the value A in the range of [A_{min}, A_{max}] is adopted to linearly scale the inputs to the network. This scaling is suitable for the transfer function. Thus the general equation to scale the inputs is:

$$A = \left[\frac{A_{max} - A_{min}}{I_{max} - I_{min}}\right](I - I_{min}) + A_{min} \qquad (6\text{-}8)$$

In this research, the input and output are normalised, therefore A_{max}=1 and A_{min}=0. Thus eq.(6-8) becomes eq.(5-19); as mentioned in the previous section. It should be mentioned that this normalisation is only employed at the fault location stage, but the fault classification stage is based on the original inputs; this is so because in this stage, there are no saturation problems.

6.6 ANN Based Scheme

ANNs have the ability to learn the desired inputs/outputs mapping based on training examples, without looking for an exact mathematical model. Once an appropriate ANN has been trained, the interconnections or links of the ANN will contain a representation of the non-linearity of desired mapping between inputs and outputs. The basic configuration of the ANN-based fault location technique is shown in fig.(118).

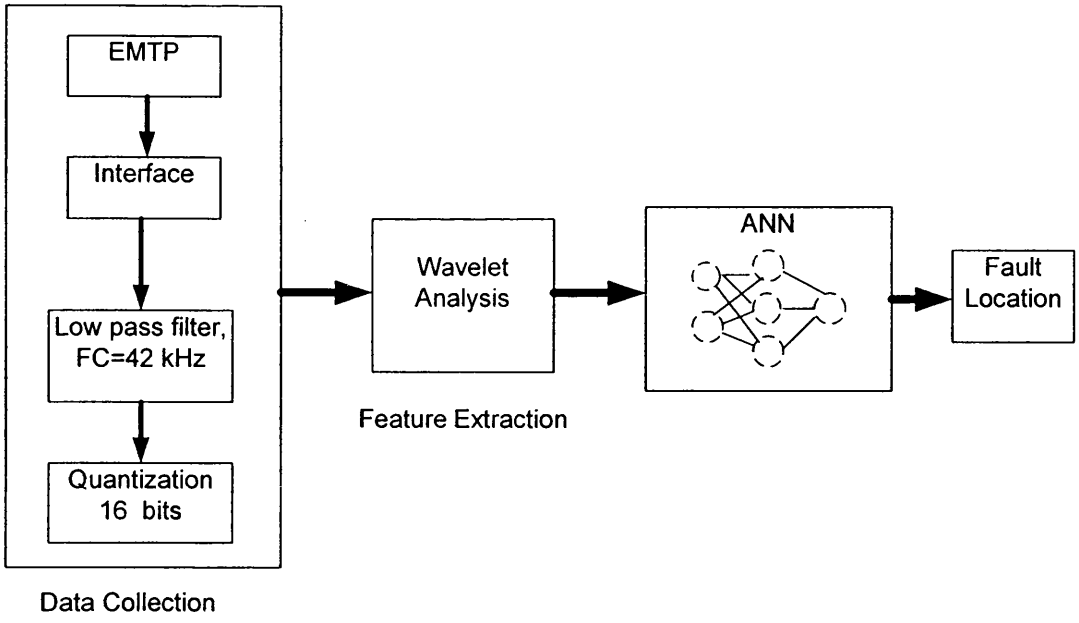

Fig. 118- Basic Configuration of the ANN-based fault location technique

The problem of developing a fault location technique based on identifying the characteristics of the faulted waveforms, is essentially one of pattern recognition. The application of ANN to fault location scheme consists of four basic tasks as follows:

1- Data Collection

Collecting or producing sets of sample of fault voltage and current waveforms is the first basic step to locate the faults using ANNs. Fig.(118) depicts that this step is based on data simulation using the EMTP discussed in chapter 4 and the signals employed are based on phase values. The effect of transducers- current transformers (CTs) and voltage transformers (VTs), and hardware errors such as anti-aliasing filters and quantisation are taken into account; therefore, the information processed throughout the fault location algorithm is very close to real-life situation.

2- Feature Extraction

Feature extraction is an integral part of the signal processing represented in chapter 5 since it conditions the raw data into a form suitable for input into the ANN. As a second step in any pattern recognition technique, feature extraction is used to reduce the dimension of the raw data and extract useful information in a concise form. For the ANNs considered in this thesis, this process leads to a considerable reduction in

the size of the networks, thereby significantly improving the performance and speed of the training process.

3- Selecting and building the most appropriate ANN

As mentioned before, A neural network is characterized by its architecture, its processing algorithm and its learning algorithm. These characteristics were generally explained in the previous section, but the ANN topology for accurate fault location is presented in the next section.

4- Training and testing the ANN

Training is based on using the process sample data and testing the network is based on separate sets of processed data.

The first two aforementioned tasks were presented in the previous chapters and the following sections deal with the other tasks.

6.7 ANN Topology for Accurate Fault Location

In order to find the best topology for accurate fault location under all practically encountered different system and fault conditions, an extensive series of studies have revealed that it is not satisfactory to merely employ a single ANN and attempt to train it with a large amount of data. A much better approach is to separate the problem into two parts: firstly to employ and train some ANNs to classify the faults, as they indicate on which type of fault (open or short circuit) and which phase(s) the fault is and whether there is ground involved in a particular fault, irrespective of the actual fault location at this stage; secondly, in order to achieve a good generalization, to use separately trained ANNs (one for each type of fault and faulty phase(s)) to accurately locate the actual fault position on the underground distribution system; these are of course all driven from the ANNs designed at the first stage and the input for the ANNs at the second stage is generated the same way as mentioned in chapter 5. Although this modular approach requires many networks, they are nonetheless quite simple in architecture, much easier to train and require significantly less training data than would otherwise be the case if simply on single ANN be employed also the method only needs a few second to test new input data if a Pentium 4 PC be employed. Fig.(119) illustrates the accurate fault location scheme based on ANNs.

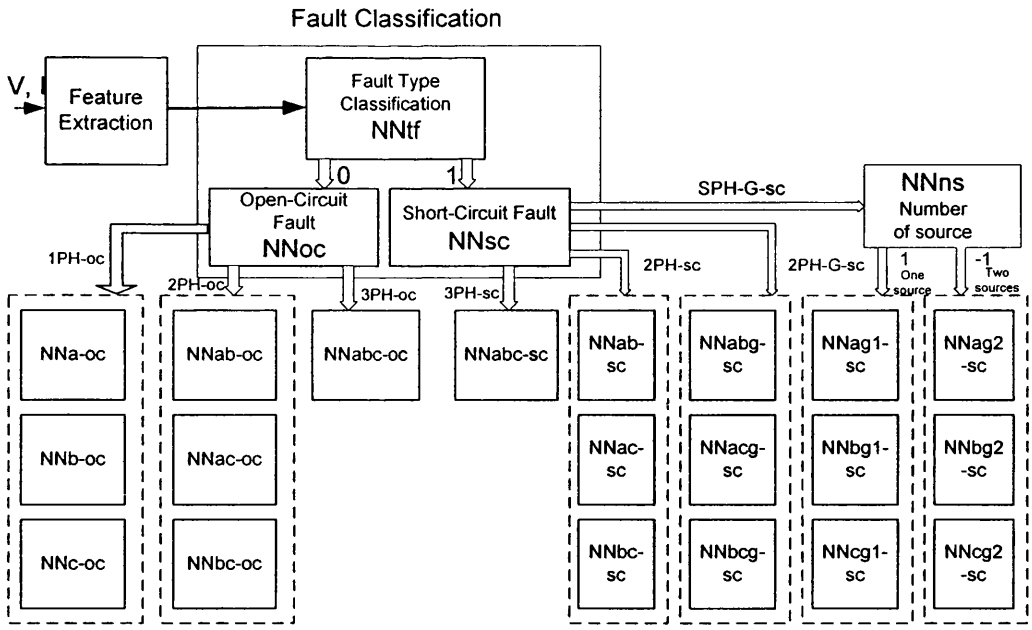

Fig. 119- Schematic diagram of fault location technique based on ANNs

With regard to the feature extraction in the case of SPH-G short-circuit fault presented in the previous chapter and having the high sensitivity to the remote source particularly for high value of fault resistance Rf, it is necessary to use another NN (NNns shown in fig.(119)) to recognise whether there is a remote source present.

6.7.1 Network Architecture

There are many types of ANNs but the most commonly used are the previously discussed MFNs. As mentioned before, a three-layer network (input, one hidden and output layers) can form arbitrary complex shapes, and is capable of separating any classes, and is therefore the most commonly used architecture for solving power system problems. Because of this, a fully connected three-layer feed-forward ANN with Levenberg-Marquardt (LM) learning algorithm has been used in all the fault classification and fault location networks.

It should be noted that the number of inputs to the networks are determined by the number of elements or features in the input vector. The number of nodes required in the hidden layer depends on the complexity of the relationship between the inputs and outputs. If there are too many nodes in the hidden layer, the network will simply learn all of the input/output relationships individually without learning to generalise relationships for the previously encountered data. If, however, there are not enough

nodes in the hidden layer, then the network will not be able to learn correctly. This applies similarly to the number of adjustable weights; too many weights will allow the network to learn all of the training set explicitly, and too few will not allow it to obtain the relationship between input and output correctly. Considering the complexity of the accurate fault location problem and the amount of data available, in order to determine the most appropriate structure for each NN, the following network training methods were tested.

- Different number of hidden neurons in the hidden layer.
- Different transfer functions (sigmoid, linear and hyperbolic tangent).
- Different learning algorithm

After an extensive series of studies, the topology of each of the ANNs shown in Fig. (119) is given in Table 6.1; this is based on the appropriate number of training data discussed in data simulation chapter.

Table 6.1 – specifications of employed NNs

NN name	No. of training data	No. of neuron in input layer	No. of neuron in hidden layer	No. of neuron in output layer	Transfer function in hidden layer	Transfer function in output layer
NNtf	1833	9	4	1	Tan-Sig	Linear
NNoc	273	6	10	5	Tan-Sig	Linear
NNsc	1560	9	7	5	Tan-Sig	Linear
NNns	936	9	3	1	Tan-Sig	Tan-Sig
NNag1-sc	312	7	4	1	Tan-Sig	Tan-Sig
NNbg1-sc	312	7	4	1	Tan-Sig	Tan-Sig
NNcg1-sc	312	7	4	1	Tan-Sig	Tan-Sig
NNag2-sc	312	7	7	1	Tan-Sig	Tan-Sig
NNbg2-sc	312	7	7	1	Tan-Sig	Tan-Sig
NNcg2-sc	312	7	7	1	Tan-Sig	Tan-Sig
NNabg-sc	156	6	5	1	Tan-Sig	Tan-Sig
NNacg-sc	156	6	5	1	Tan-Sig	Tan-Sig
NNbcg-sc	156	6	5	1	Tan-Sig	Tan-Sig
NNab-sc	39	6	4	1	Tan-Sig	Tan-Sig
NNac-sc	39	6	4	1	Tan-Sig	Tan-Sig
NNbc-sc	39	6	4	1	Tan-Sig	Tan-Sig
NNabc-sc	39	3	7	1	Tan-Sig	Tan-Sig
NNa-oc	39	3	6	1	Tan-Sig	Linear
NNb-oc	39	3	6	1	Tan-Sig	Linear
NNc-oc	39	3	6	1	Tan-Sig	Linear
NNab-oc	39	3	6	1	Tan-Sig	Linear
NNac-oc	39	3	6	1	Tan-Sig	Linear
NNbc-oc	39	3	6	1	Tan-Sig	Linear
NNabc-oc	39	3	7	1	Tan-Sig	Linear

As it can be seen, the numbers of training data for such ANNs correspond to the classification are much larger than such ANNs which have been employed in fault location. The reason for this is that NNs in classification stage need to be trained by all the training data including different type of fault, but the NNs in fault location stage are only trained by a set of training data which are related to the specific type of fault.

6.7.2 Fault Type Classification

The fault type classification technique is based on training three-layer MFNs by the LM learning algorithm and also after an extensive series of studies, Hyperbolic tangent and linear transfer functions were selected as the hidden and the output layer neurons, respectively. The fault classification block comprises three NN including NNtf (type of fault), NNsc (faulted phase(s) for short-circuit faults) and NNoc (faulted phase(s) for open-circuit faults). As it can be seen from table 6.1, the number of data training for NNtf, NNsc and NNoc are 1833, 1560 and 273 respectively and are much more than such NNs which are employed in fault location stage because they deal with all the related type of faults. The LM learning algorithm used here is based on batch mode in which all of the inputs are applied to the network before updating the weights and biases. Thus the numbers of iterations are much less than the incremental mode in which after each input, updating is implemented.

The learning performance is shown in fig.(120) for these three NNs. It can be seen that the NNtf and NNsc reach the requisite RMS in 75 and 16 iterations and the NNoc reached the 0.00365 RMS after 500 iterations.

The NNtf architecture is based on 9 inputs, one output and 4 neurons in the hidden layer and recognizes the type of fault (short or open circuit fault). As mentioned in chapter 5, nine inputs are associated with the SD of approximate at level-5 of the WT realisation for three phase voltages, three phase currents and three modal current signals. A value close to unity for output correspond to the short-circuit fault and close to zero indicates the open-circuit fault. The NNsc architecture is based on 9 inputs, 5 outputs and 7 neurons in the hidden layer and recognizes the faulted phase(s) in the case of short-circuit fault. The outputs of the NNsc comprise of five variables T, A, B, C and G; of these, T is associated with the type of fault (a value close to unity indicates a short-circuit faults and near to zero shows open-circuit faults), a value close to unity for any

of the A, B and C corresponds to the appropriate a, b or c phases being faulty, respectively. A near unity of G signifies that ground is involved in a fault. The NNoc is similar to NNsc but is for the open-circuit fault and is based on 6 inputs as mentioned in the previous chapter. It consists of 5 outputs and 10 neurons in the hidden layer. The NNsc and NNoc logic for output representation is depicted in table 6.2.

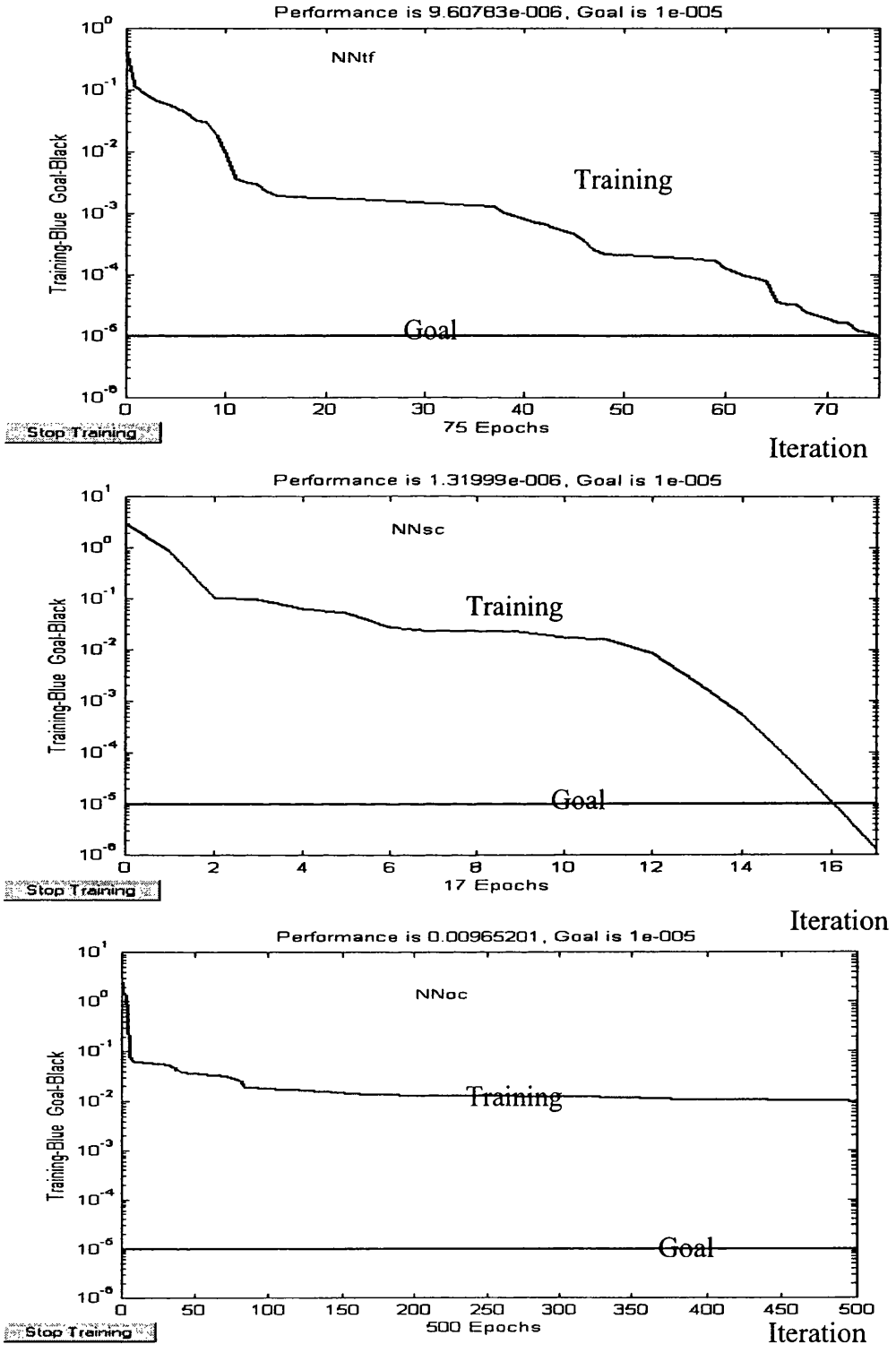

Fig. 120 – Performance of NNtf, NNsc and NNoc training

Table 6.2 – NNsc and NNoc logic for output representation

Fault Type	T	A	B	C	G
ag-sc	1	1	0	0	1
bg-sc	1	0	1	0	1
cg-sc	1	0	0	1	1
abg-sc	1	1	1	0	1
acg-sc	1	1	0	1	1
bcg-sc	1	0	1	1	1
ab-sc	1	1	1	0	0
ac-sc	1	1	0	1	0
bc-sc	1	0	1	1	0
abc-sc	1	1	1	1	0
a-oc	0	1	0	0	0
b-oc	0	0	1	0	0
c-oc	0	0	0	1	0
ab-oc	0	1	1	0	0
ac-oc	0	1	0	1	0
bc-oc	0	0	1	1	0
abc-oc	0	1	1	1	0

6.7.3 Fault Location ANNs

As mentioned before, separate ANNs are designed to accurately locate fault position for each type of fault under all practically encountered different fault conditions. They are all driven from the ANNs designed to classify the fault type and the input data is generated the same way as mentioned in chapter 5 in detail. ANNs are trained with different training data to cater for all types of commonly encountered faults.

Except for the SPH-G fault, other faults are not sensitive to the presence of the remote source and hence in the case of the latter, data training set for the condition of one source can cover both cases (with & without remote source) satisfactorily. However, in the case of a SPH-G fault, each condition (with and without remote source) significantly influences the signal waveforms and hence all data training set associated with the two

cases must be used in the ANNs training. In this respect, the following two states were implemented; the first state had one ANN for each SPH-G fault and data training set involved both cases (with and without remote source), but in the second state, two serial NNs were employed, firstly to recognise the number of source(s) connected (i.e. one or two) (NNs shown in Fig. (118)) and in the second stage, 6 ANNs were used to locate the fault based on the faulted phase (3 cases) and the number of source(s) (2 cases). The studies verified the latter approach as a more accurate algorithm for fault location of such types of fault. Thus in order to locate the SPH-G fault, the second state is presented and it should be mentioned that this two stage process is required only for the SPH-G-SC faults.

After classifying the fault, 20 ANNs shown in fig (118), are trained for different fault types. These 20 ANNs which are activated based on the result of NNtf and NNns, are as follows; three SPH-G faults in the case of one source connected (NNag1-sc, NNbg1-sc, NNcg1-sc), three SPH-G faults in the case of remote source being connected (NNag2-sc, NNbg2-sc, NNcg2-sc), three 2PH-G faults (NNabg-sc, NNacg-sc, NNbcg-sc), three 2PH-sc faults (NNab-sc, NNac-sc, NNbc-sc), a 3PH-sc fault (NNabc-sc), three SPH-oc faults (NNa-oc, NNb-oc, NNc-oc), three 2PH-oc faults (NNab-oc, NNac-oc, NNbc-oc) and a 3PH-oc fault (NNabc-oc). It is vitally important to have the lowest number of neurons but without jeopardising the accuracy of the classification. Through a series of tests and modifications, the number of neurons in the hidden layer shown in table 6.1 produced a satisfactory performance. Moreover, it was found that the ANN converged in a shorter time with a simpler structure when the hyperbolic tangent transfer function rather than the commonly used sigmoid function, was employed for both hidden and output layers in the case of short-circuit faults and hyperbolic tangent and linear transfer functions were employed for hidden and output layers respectively in the case of open-circuit faults.

The specifications of all the employed ANNs in the fault location stage have been depicted in table 6.1. As can be seen, the dimension of output for all ANNs in the fault location stage is one and determines the distance of fault from measurement point. The output of NNns comprises of one variable corresponding to the presence or no presence of remote source and a near unity value signifies the system without remote source and a near to -1 indicates the presence of the remote source in the system.

In order to investigate the training process used for the NNs at the fault location stage, herein, learning performances are presented for NNag1-sc, NNbcg-sc, NNbc-sc, NNabc-sc, NNa-oc, NNab-oc and NNabcc-oc. Figs (121-127) show the results. These figures indicate a very good performance of the ANNs learning phase, significantly by the fast convergence of the training process. As can be seen from figs (121-124), the number of iterations in which the requisite RMS is reached are 37, 12, 14 and 9 epochs for NNag-sc, NNbcg-sc, NNbc-sc and NNabc-sc respectively. For the open-circuit faults, the convergence process takes much longer and the minimum errors attained are 0.00096, 0.00122 and 0.00119 for NNa-oc, NNab-oc and NNabcc-oc, respectively. it should be mentioned that for open-circuit faults the accuracy of the NNs is less than for other types of fault and this is reflected in the overall accuracy in fault location with respect to former, as discussed later.

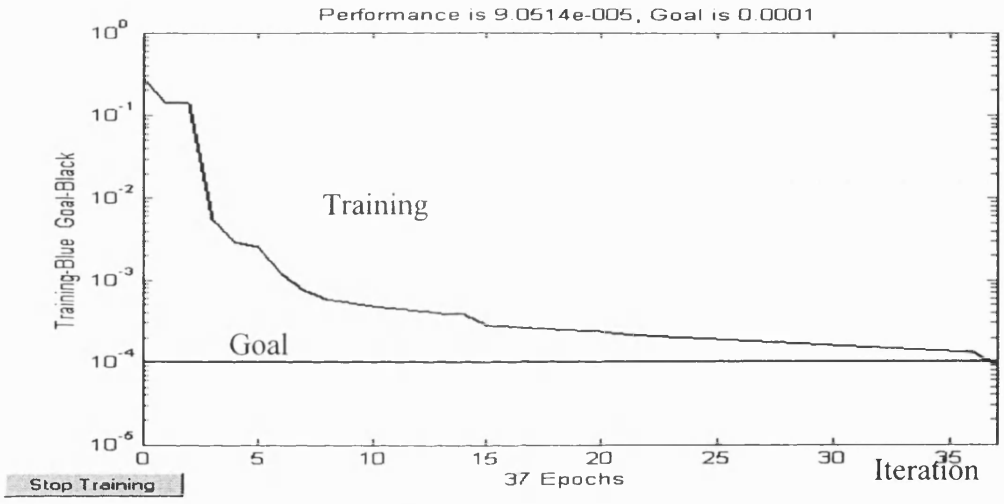

Fig. 121 – Performance of NNag-sc network training

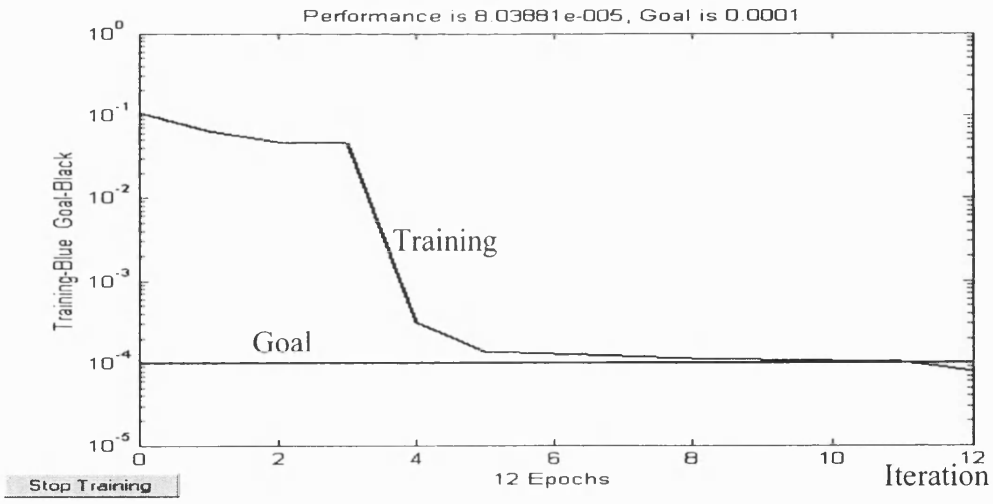

Fig. 122 – Performance of NNbcg-sc network training

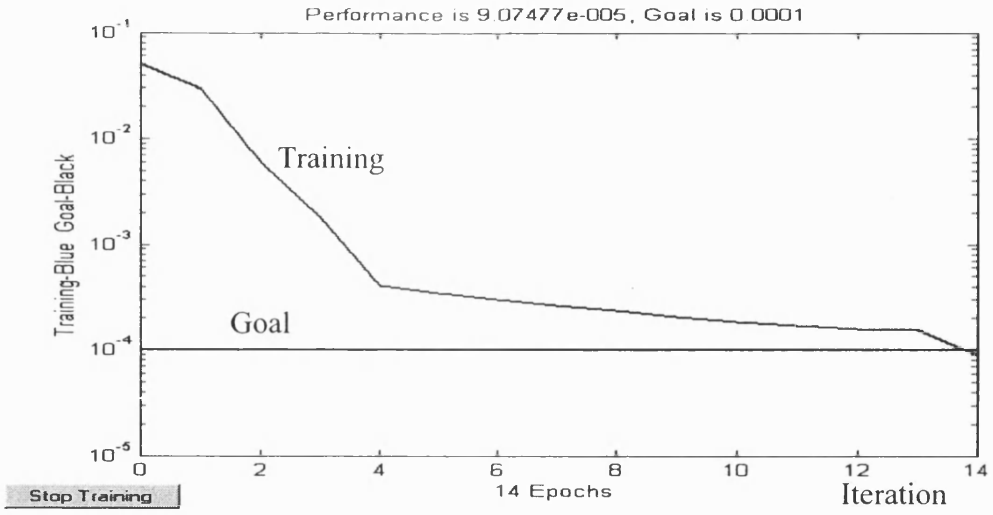

Fig. 123 – Performance of NNbc-sc network training

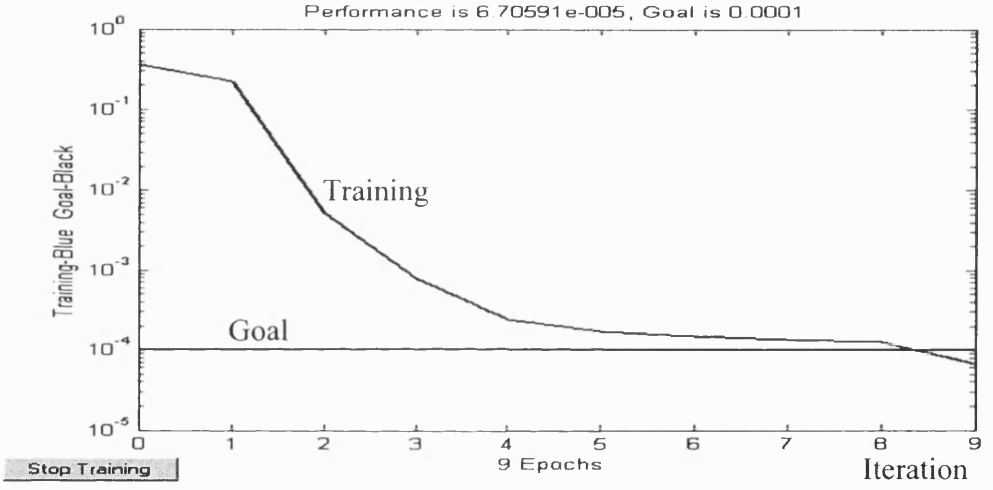

Fig. 124 – Performance of NNabc-sc network training

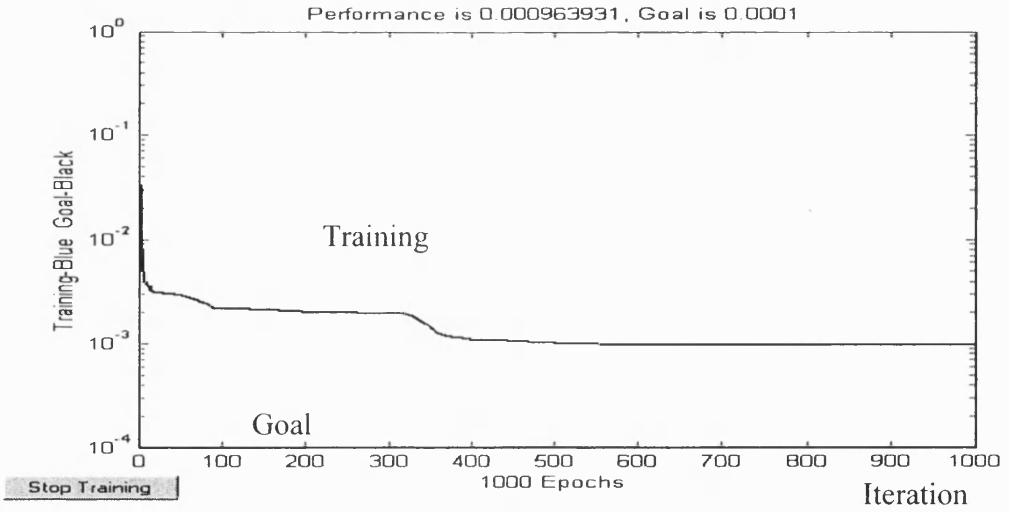

Fig. 125 – Performance of NNa-oc network training

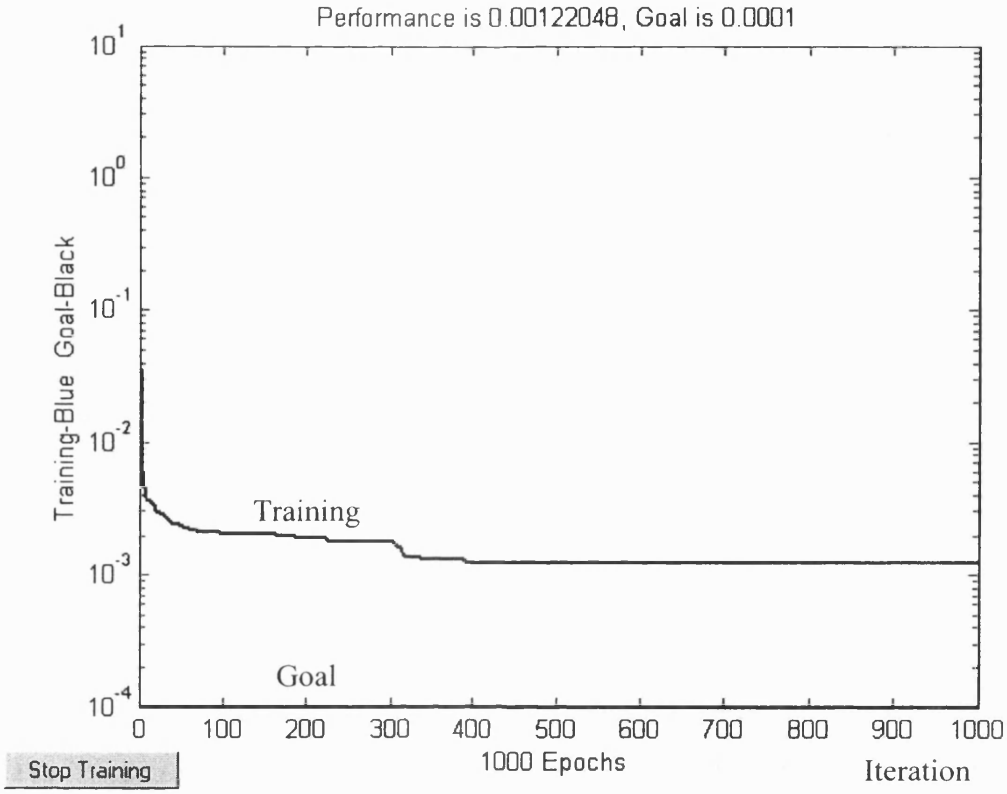

Fig. 126 – Performance of NNab-oc network training

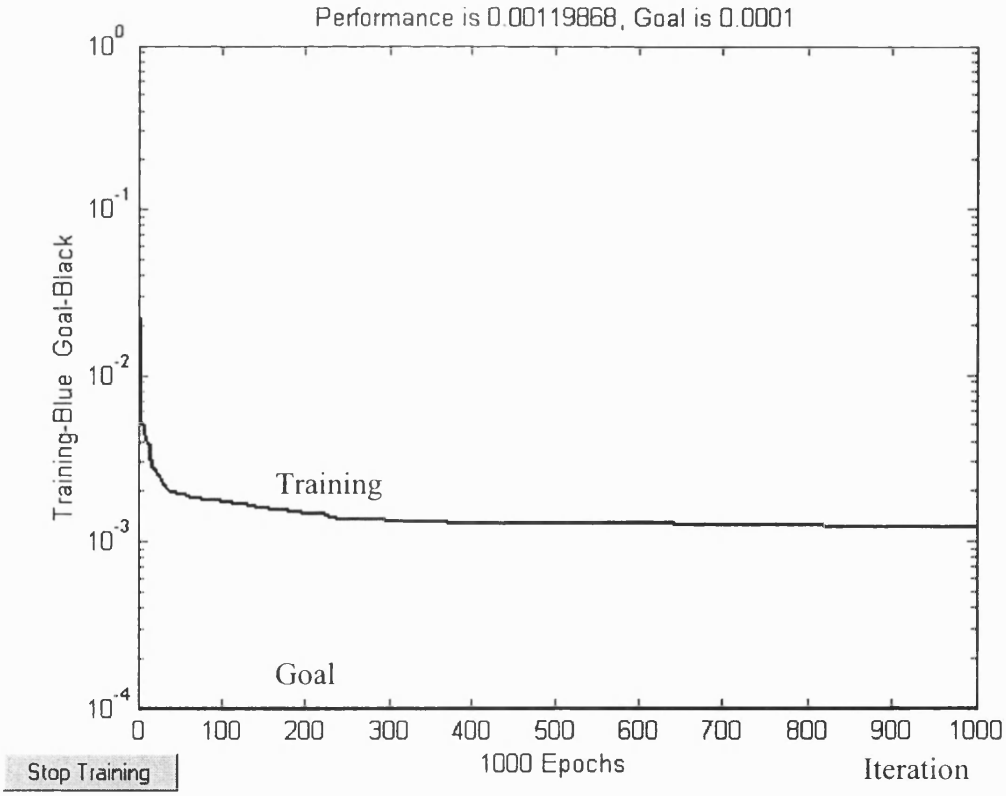

Fig. 127 – Performance of NNabc-oc network training

6.8 Analysis of Test Results

In order to analyse the accuracy of the proposed method, the data used for testing is different and unseen from that used for training; details of the training data including the different systems and fault conditions are outlined in chapters 4 and 5. In this respect, seven groups of test data have been selected to investigate the accuracy and sensitivity of the method to the system parameters such as fault resistance and inception angle and system elements such as the capacity, type and location of load taps, the length of cable, presence of remote source and external faults. These seven groups of test data are as follows:

-Group 1:

This group contains test data which is obtained from the typical DS shown in fig (51) in chapter 4. There are 63 data sets based on seven types of fault (ag-sc, bc-sc, bc-sc, abc-sc, a-oc, ab-oc and abc-oc faults) and 9 conditions for each fault, there being different from those employed during the training process. Table 6.3 shows the various fault conditions employed during the test procedure.

Table 6.3- Group-1 of data test

location	Inception angle	Rf
80 m	117 degree	1 Ω
350 m	117 degree	5 Ω
750 m	117 degree	15 Ω
1250 m	162 degree	12 Ω
1750 m	162 degree	5 Ω
2250 m	162 degree	1 Ω
2750 m	162 degree	5 Ω
3250 m	117 degree	1 Ω
3800 m	117 degree	12 Ω

-Group 2:

This group contains such data which is similar to group 1 but the only difference is that the system is supplied by two sources i.e. the remote source is also connected.

-Group 3:

This group of data is associated with changing the location of the second load (shown in fig (51)) from 2000m to 1500m. This data set tests the sensitivity of the proposed method to the location of load taps. 49 data sets are used based on the seven aforementioned faults and 7 conditions for each fault. Table 6.4 shows seven locations with different inception angles and Rf.

-Group 4:

In this group, data is obtained from the DS shown in fig (51) based on doubling the capacities of the three loads employed at the tap points. The sensitivity of the proposed method to such load changes is then tested. This group also contains 49 data sets similar to group 3.

Table 6.4- Testing data for group 2

location	Inception angle	Rf
80 m	117 degree	1 Ω
350 m	117 degree	5 Ω
1100 m	90 degree	2 Ω
1750 m	162 degree	5 Ω
2500 m	135 degree	10 Ω
3250 m	117 degree	1 Ω
3800 m	117 degree	12 Ω

-Group 5:

This group contains data which is based on swapping the positions of loads 1 and 2 (as shown in Fig. (51)) and also doubling all the three loads. This data is to ascertain the sensitivity of proposed method to the changes in capacity and type of load taps (static and dynamic). Also 49 data are obtained based on the same condition in group 3 & 4.

-Group 6:

This group comprises of 49 data sets based on the same conditions shown in table 6.4 and the same DS shown in fig (51), but the length of cable in each section is

changed from 1000m to 1500m thereby testing the sensitivity of the proposed algorithm to non-algorithmic errors such as changes in cable length and also a change in the locations of the load taps.

-Group 7:

This group contains 4 data sets based on four aforementioned short-circuit faults for external faults (i.e. faults that occur behind the measurement point).

6.8.1 Performance of the Fault Classifier

Since the output of three networks NNtf, NNsc and NNoc only indicate unity and zero, also in practice there are small fluctuations in the actual NNs outputs around '1' and '0', therefore a threshold level has to be built into the NN algorithms in order to minimise the degree of uncertainty. In this application, this threshold was set at 0.2, that is, if the output fell within the range less than 0.2 then it would be classed as '0' ie, a healthy phase indication, and if it fell within the range more than 0.8 then it was classed as unity ie, a faulty phase indication. Tables 6.5 to 6.11 give some examples for the test results of the faulted system. As can be seen, the ANNs can correctly classify a large number of test patterns, but in some cases particularly in the case of open-circuit at last section of cable, the outputs of ANNs fall into the uncertain category i.e., 0.2<output<0.8 and it means that in such cases, ANNs can not deliver the desired classification information.

Table 6.5- classification test results for ag-sc fault for different positions, inception angles and fault resistance

Out put	Fault Position								
	80m 117° 1Ω	350 m 117° 5Ω	750 m 117° 15Ω	1250 m 162° 12Ω	1750 m 162° 5Ω	22500 m 162° 1Ω	2750 m 162° 5Ω	3250 m 117° 1Ω	3750 m 117° 12Ω
T	1.0000	1.0000	1.0000	1.0000	1.0000	1.0000	1.0000	1.0000	1.0000
A	1.0002	1.0001	1.0001	1.0001	1.0001	1.0002	1.0001	1.0002	1.0001
B	-0.0008	0.0484	-.0007	0.000	0.0161	0.0109	0.0046	-0.0007	-0.0018
C	-0.0001	-.0002	-.0003	-.0003	-.0003	-.0002	-.0003	-.0002	0.0000
G	1.0006	1.0005	1.0005	1.0005	1.0004	1.0006	1.0004	1.0006	1.0005

Table 6.6- classification test results for bcg-sc fault for different positions, inception angles and fault resistance

Output	Fault Position								
	80m 117° 1Ω	350m 117° 5Ω	750m 117° 15Ω	1250m 162° 12Ω	1750m 162° 5Ω	22500m 162° 1Ω	2750m 162° 5Ω	3250m 117° 1Ω	3750m 117° 12Ω
T	1.00	1.00	1.00	1.00	1.00	1.00	1.00	1.00	1.00
A	-.0001	-.0001	-.0001	-.0001	-.0001	-.0001	-.0001	-.0001	-.0001
B	1.0014	1.0014	1.0014	1.0013	1.0011	1.0012	1.0008	1.0011	1.0007
C	1.0001	1.0001	1.0001	1.0001	1.0001	1.0001	1.0001	1.0001	1.0001
G	0.9998	0.9998	0.9998	0.9998	0.9997	0.9998	0.9997	0.9997	0.9997

Table 6.7- classification test results for bc-sc fault for different positions, inception angles and fault resistance

Output	Fault Position								
	80m 117° 1Ω	350m 117° 5Ω	750m 117° 15Ω	1250m 162° 12Ω	1750m 162° 5Ω	22500m 162° 1Ω	2750m 162° 5Ω	3250m 117° 1Ω	3750m 117° 12Ω
T	1.00	1.00	1.00	1.00	1.00	1.00	1.00	1.00	1.00
A	-.0002	-.0002	-.0002	-.0002	-.0002	-.0002	-.0002	-.0002	-.0002
B	1.0011	1.0011	1.0011	1.0012	1.0013	1.0014	1.0014	1.0014	1.0013
C	1.0001	1.0001	1.0001	1.0001	1.0001	1.0001	1.0001	1.0001	1.0001
G	-.0007	-.0007	-.0006	-.0001	.0008	.0021	.0037	.0047	.0068

Table 6.8- classification test results for abc-sc fault for different positions, inception angles and fault resistance

Output	Fault Position								
	80m 117° 1Ω	350m 117° 5Ω	750m 117° 15Ω	1250m 162° 12Ω	1750m 162° 5Ω	22500m 162° 1Ω	2750m 162° 5Ω	3250m 117° 1Ω	3750m 117° 12Ω
T	1.00	1.00	1.00	1.00	1.00	1.00	1.00	1.00	1.00
A	0.9998	0.9998	0.9998	0.9998	0.9998	0.9998	0.9998	0.9998	0.9998
B	1.0039	1.0038	1.0036	0.9972	0.9965	0.9962	0.9962	1.0008	1.0004
C	1.00	1.00	1.00	1.00	1.00	1.00	1.00	1.00	1.00
G	-.0006	-.0006	-.0006	-.0006	-.0006	-.0006	-.0006	-.0006	-.0006

Table 6.9- classification test results for a-oc fault for different positions, inception angles and fault resistance

Out put	Fault Position								
	80m 117° 1Ω	350m 117° 5Ω	750m 117° 15Ω	1250m 162° 12Ω	1750m 162° 5Ω	22500m 162° 1Ω	2750m 162° 5Ω	3250m 117° 1Ω	3750m 117° 12Ω
T	0.0078	0.0081	0.0096	-.0042	0.0031	0.0114	0.0138	-.0035	-.0043
A	1.0009	1.0009	0.9987	1.0009	1.0009	1.0018	1.0019	1.0075	1.0300
B	-.0069	-.0069	0.0236	-.0069	-.0069	-.0008	0.0054	0.5928	0.6011
C	0.0018	0.0018	0.0532	0.0018	0.0018	0.0044	0.0076	0.3278	0.2541
G	0.00	0.00	0.00	0.00	0.00	0.00	0.00	0.00	0.00

Table 6.10- classification test results for ab-oc fault for different positions, inception angles and fault resistance

Out put	Fault Position								
	80m 117° 1Ω	350m 117° 5Ω	750m 117° 15Ω	1250m 162° 12Ω	1750m 162° 5Ω	22500m 162° 1Ω	2750m 162° 5Ω	3250m 117° 1Ω	3750m 117° 12Ω
T	-.0018	-.0002	-.0002	-.0042	0.0022	-.0008	0.0028	-.0037	-.0044
A	1.0026	1.0026	0.9968	1.0027	1.0033	0.9931	0.9807	1.0167	1.0270
B	1.0069	1.0069	1.0103	1.0077	1.0145	0.9115	0.8863	0.9474	0.6389
C	0.0117	0.0117	0.0091	0.0123	0.0170	-.0166	-.0533	0.2446	0.2687
G	0.00	0.00	0.00	0.00	0.00	0.00	0.00	0.00	0.00

Table 6.11- classification test results for abc-oc fault for different positions, inception angles and fault resistance

Out put	Fault Position								
	80m 117° 1Ω	350m 117° 5Ω	750m 117° 15Ω	1250m 162° 12Ω	1750m 162° 5Ω	22500m 162° 1Ω	2750m 162° 5Ω	3250m 117° 1Ω	3750m 117° 12Ω
T	0.0020	0.0075	0.0076	0.0023	0.0148	-.0097	-.0080	-.0055	-.0046
A	0.9967	0.9967	0.9967	0.9951	0.9951	1.0032	1.0199	1.0084	1.0206
B	1.0097	1.0097	1.0097	1.0004	1.0004	1.0699	1.0702	0.9552	0.6407
C	1.0074	1.0074	1.0074	0.9975	0.9975	0.9263	0.9226	0.4389	0.3008
G	0.00	0.00	0.00	0.00	0.00	0.00	0.00	0.00	0.00

The indices used to quantitatively ascertain the performance of the fault classification ANN are as follows:

Misclassification Rate Index (MRI) = (No. of misclassification) / (No. of total tests)* 100 Eq. (6.9)

Single Confidence Index (SCI) = (1-|Desired – Simulated|) * 100 Eq. (6.10)

Average Confidence Index (ACI) = (Sum of SCI) / (No. of tests) Eq. (6.11)

Tables 6.12 to 6.14 tabulate the ANN performance indices for the tests carried out on a system in the case of short-circuit, open-circuit at first three sections of cable and open-circuit faults at last section of cable, respectively. Out of 138 test cases carried out for short-circuit fault and an excellent MRI of 0.0% is achieved. For the open-circuit fault, the number of misclassification is 6 while the number of test cases is 27 and what it should be noted is that all the misclassification are related to such open-circuit faults which they occur at the last section of cable. The reason for this is that any open-circuit fault in the last section of the system without remote source does not have a significant effect on the voltage and current signals.

Table 6.12- Performance evaluation of fault classification for short-circuit fault

	T	A	B	C	G
SCI (min)	100%	99.98%	92.98%	99.99%	99.32%
SCI (Max)	100%	100%	100%	100%	100%
ACI	100%	99.99%	99.12%	99.99%	99.75%
No. of misclassification	0				
Misclassification Rate	0.0%				

Table 6.13- Performance evaluation of fault classification for open-circuit fault (first three section of cable)

	T	A	B	C	G
SCI (min)	98.52%	98.01%	95.16%	99.99%	92.26%
SCI (Max)	100%	100%	100%	100%	100%
ACI	99.35%	99.24%	98.34%	99.99%	96.75%
No. of misclassification	0				
Misclassification Rate	0.0%				

Table 6.14- Performance evaluation of fault classification for open-circuit fault (last section of cable)

	T	A	B	C	G
SCI (min)	99.45%	97.0%	59.24%	56.11%	100%
SCI (Max)	100%	100%	100%	100%	100%
ACI	99.78%	98.84%	88.34%	86.34%	100%
No. of misclassification	6				
Misclassification Rate	100%				

6.8.2 Performance of the Fault Locator

This section presents the performance evaluation of the fault location technique under different system and fault conditions. The trained ANNs involved in the second stage of the fault location technique were tested with the seven aforementioned groups of data test. As mentioned before, this stage comprises of a number of ANNs (each corresponding to a different type of fault), the appropriate ANN being activated by the outputs from the ANNs in the first stage.

The error for fault location is expressed as a percentage of the length of the cable, and is given as:

$$\%error = \left| \frac{(actual\_location) - (obtained\_location)}{(cable\_length)} \right| \times 100 \qquad (6\text{-}12)$$

6.8.2.1 Effect of Different Fault Conditions

Separate sets of test data (unseen by the ANNs before) in group 1 was supplied as input to each ANN involved in the fault location stage in order to evaluate their performance under different fault locations and conditions for a typical DS shown in Fig. (51).

As discussed in the data simulation chapter (4), the fault conditions, particularly fault location, inception angle and Rf for grounded faults, significantly affect the fault transient voltage and current signals. Therefore, it is vitally important to verify the effect of these conditions on the performance of the proposed fault location technique. Table 6.15 shows the accuracies attained for group-1 of the test results and Fig.(128) is a visual performance of Table 6.15. L in the table is defined as obtained location.

Table 6.15 Performance of the fault locator based on group-1 of test data

Fault Location		80 m	350 m	750 m	1250 m	1750 m	2250 m	2750 m	3250 m	3800 m
ag-sc	L	57.9	308.3	709.1	1218	1740	2260	2724	3248	3821
	%e	0.55	1.04	1.02	0.8	0.25	0.25	0.65	0.05	0.525
		The Mean of Error = % 0.6								
bcg-sc	L	75.4	353.7	749.1	1248	1752	2225	2763	3225	3813
	%e	0.115	0.092	0.022	0.05	0.05	0.625	0.325	0.625	0.325
		The Mean of Error = % 0.247								
bc-sc	L	79.7	349.9	749	1253	1751	2252	2753	3246	3811
	%e	0.007	0.002	0.025	0.075	0.025	0.05	0.075	0.1	0.275
		The Mean of Error = % 0.07								
abc-sc	L	72.4	350.1	759.3	1263	1764	2261	2766	3284	3827
	%e	0.195	0.002	0.232	0.325	0.35	0.275	0.4	0.85	0.675
		The Mean of Error = % 0.367								
a-oc	L	82.9	305.7	1039	1291	1729	2525	2480	3506	3512
	%e	0.072	1.09	7.22	1.025	0.525	6.875	6.75	6.4	7.2
		The Mean of Error = % 4.128								
ab-oc	L	66.5	445.5	925.5	1322	1679	2531	2543	3483	3509
	%e	0.337	2.387	4.375	1.8	1.775	7.025	5.175	5.825	7.275
		The Mean of Error = % 3.997								
abc-oc	L	80	441	749.9	633	1087	2278	2336	3469	3507
	%e	0.0	2.275	0.002	15.42	14.07	0.7	10.35	5.475	7.325
		The Mean of Error = % 6.18								

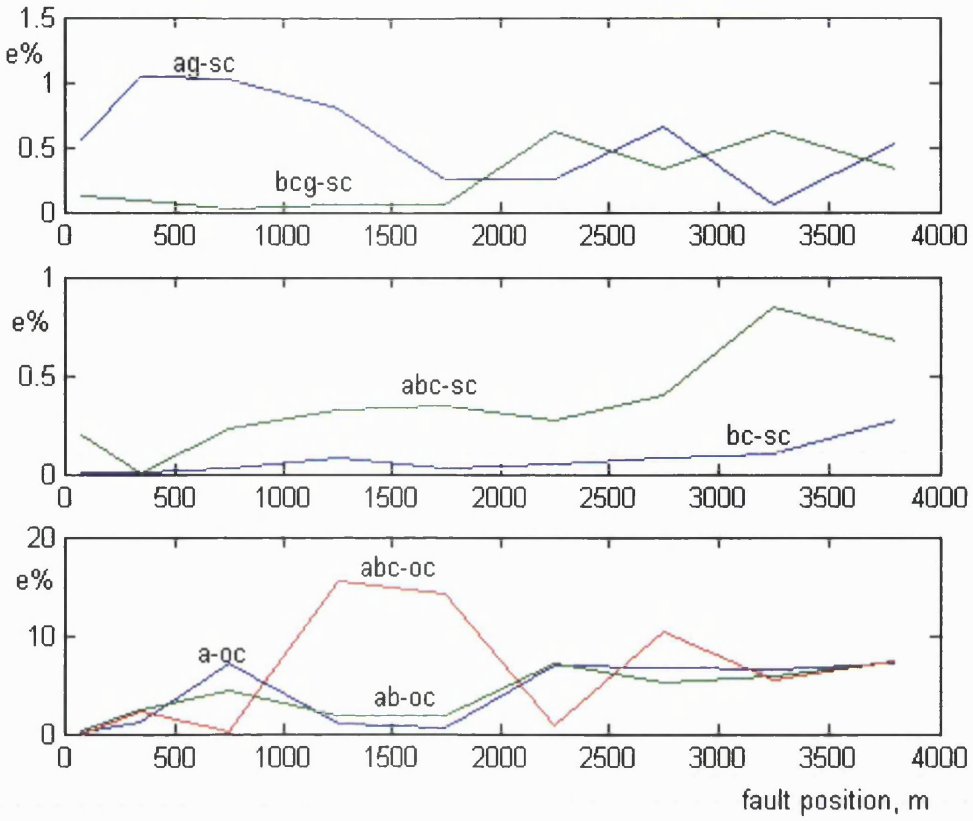

Fig. 128- Measuring accuracy for group-1 of test data for seven types of faults

It is clearly evident from the results that the ANNs give very accurate evaluation of fault position in the case of short-circuit faults, particularly ungrounded faults as there is no fault resistance and they are largely independent of inception angle. As can be seen from the table and figure, the maximum and mean errors corresponding to ag-sc, bcg-sc, bc-sc and abc-sc faults (short-circuit faults) are (1.04 & 0.6), (0.625 & 0.247), (0.275 & 0.07) and (0.85 & 0.367) percent respectively. An extensive series of tests have shown that the method is independent of fault resistance in the case of grounded fault. This is a very significant advantage over conventional techniques, particularly those based on impedance to fault measurements, which tend to produce excessive errors when dealing with resistive faults. Also since the results associated with short-circuit faults are significantly independent of the inception angle, therefore this study clearly demonstrates that the fault location algorithm is virtually immune to any errors caused by either the higher frequency transients, which are associated with faults near voltage maximum or DC offset caused by faults near voltage zero. This feature is important since in practice, faults can occur at any point on the wave i.e. the fault inception angle cannot be defined in advance. It should be mentioned that the NNns network which

classifies the system with and without the remote source connected gives the correct classification (1 for one source and -1 for two sources) for all types of system and fault conditions.

However, it can be seen from table 6.15 and Fig. (128) that the errors are much higher in the case of open-circuit faults in comparison to short-circuit faults; the maximum and mean of the error related to a-oc, ab-oc and abc-oc faults are (7.22 & 4.128), (7.275 & 3.997) and (15.42 & 6.18) percent respectively. The main reasons for these errors are because:

- The reason for using approximate level for short-circuit faults is that fault current is much higher than load currents, however in the case of open-circuit faults the levels of the two currents are small and comparable to each other. Hence in order to have some discernability between different fault positions in the case of open-circuit faults, detail levels have been utilised i.e. high frequency signals, as discussed in chapter 4.

- The high frequency signals associated with detailed levels are attenuated by the anti-aliasing filter. A direct consequence of this is that some of the travelling wave components, in particular those associated with faults less than 624.5 meters are more or less eliminated as shown by following equation (cut-off frequency for the filter is 42kHz and maximum velocity of the wave propagation is 2.623e+7):

$$L=v*T=v/f=2.623e+7/42000=624.5 \qquad (6.13)$$

This inevitably adds to the inaccuracy. From the foregoing, it is apparent that in order to obtain high accuracy in the case of open-circuit faults, much larger training data e.g. more inception angles are needed. This will be the basis for future works. With regard to the aforementioned aspects, open-circuit faults are significantly sensitive to the remote source and load taps, therefore next sections only deal with evaluating the performance of proposed technique in different systems for short-circuit faults.

6.8.2.2 Effect of Remote Source

Although hitherto the majority of distribution systems comprise of feeder with remote end open, with the deregulation of the Electricity Supply Industry, coupled with renewable-energy based generation, it is highly likely that there will be an increasing of amount of penetration of small-scale distributed generation into the distribution network, changing its status from being passive to active. A direct consequence of this is an increase in the complexity of DSs and more importantly for such systems, any fault will also have remote infeed. It is well known that a remote infeed can adversely affect the accuracy of conventional fault locators. In this respect, the accuracy of the proposed fault location technique was tested based on group-2 of test data based on the system shown in fig. (51) but with a remote source connected at the end of the system. Table 6.6 and Fig.(129) depict the results.

Table 6.16 - Performance of the fault locator based on group-2 of test data

Fault	ag-sc Fault		bcg-sc fault		bc-sc fault		abc-sc fault	
Location	L	%e	L	%e	L	%e	L	%e
80m	64	0.4	79.4	0.015	72.5	0.187	72.7	0.182
350m	343.3	0.167	349.8	0.005	339.1	0.272	349.9	0.002
750m	810.5	1.512	744.1	0.147	737.6	0.31	758.6	0.215
1250m	1172	1.95	1244.7	0.132	1245.3	0.117	1266.1	0.402
1750m	1826	1.9	1746.4	0.09	1754.6	0.115	1768.8	0.47
2250m	2280	0.75	2252.5	0.062	2273.2	0.58	2268.2	0.455
2750	2781	0.775	2734.9	0.377	2805.2	1.38	2772.9	0.572
3250	3267	0.425	3238.6	0.285	3328.3	1.957	3279.4	0.735
3800	3772	0.7	3859.8	1.495	3814.4	0.36	3825.7	0.642
The Mean of Error %	0.952		0.29		0.586		0.408	

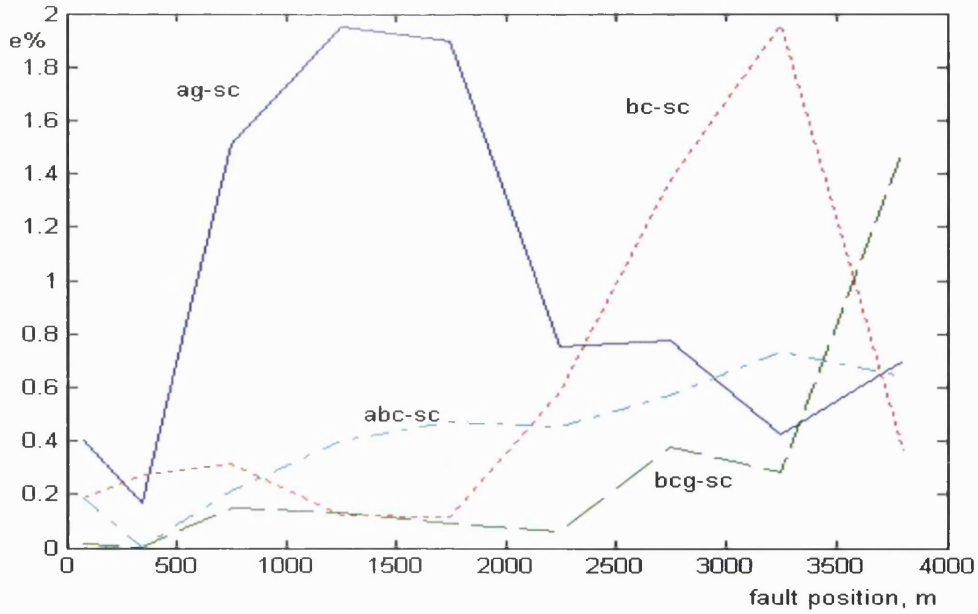

Fig. 129- Measuring accuracy for group-2 of test data for short-circuit faults

In comparison to the results attained for the radial feeder system discussed in the previous section, it is evident that the presence of a remote source has only a slight effect on the accuracy particularly in the case of SPH-G fault. As can be seen, the maximum and the mean of errors associated with the four aforementioned short-circuit faults increases very slightly to (1.95 & 0.952), (1.495 & 0.29), (1.957 & 0.586) and (0.735 & 0.408), respectively. These small changes can be directly attributed to the fact that with a remote source, the current increases in the fault resistance path and changes in the healthy phase(s) in terms of magnitude and distortion. It is clearly evident from the results that the accuracy achieved in fault location is still very high, being less than 2 percent in all the test cases.

6.8.2.3 Effect of Load Taps

There are many different loads in terms of type (dynamic & static) and the capacity in the DS. In this respect, the system employed as presented in chapter 4, has three different types of load and the training set is based on these loads. It is apparent that load parameters (type, location and capacity) significantly affect the fault transient waveforms. Therefore, it is vitally important to examine the effect of the load taps using a test data set different from the training set. In this respect three conditions are considered; firstly, group-3 of test data in which the location of second load shown in

fig. (51) has been changed from 2000m to 1500m; secondly, group-4 of the test data in which the capacity for all the three loads (shown in fig.(151)) has been changed to double; thirdly, group-5 of the test data in which the types of load 1 & 2 and the capacity of all the three loads are changed. It should be mentioned that in groups-3,4 & 5 of test data, in addition to the load taps, fault conditions (inception angle and Rf) are also varied. The following results can be obtained correspond to the three aforementioned conditions:

1- Table 6.17 and Fig.(130) depict the results based on group-3 of test data associated with four types of fault ag-sc, bcg-sc, bc-sc and abc-sc. It is clearly evident from the results that the accuracy achieved in fault location is again very high in the case of bcg-sc and bc-sc faults, being less than 0.2% error and for the other faults the accuracy is still high and is less than 1.05% error in all the test cases. Thus it can be concluded that the ANNs give accurate evaluation of fault location that is largely independent of the location of load taps. This is a very significant advantage in view of the fact that in practice, the location of the load can change.

2- Table 6.18 and Fig.(131) illustrate the results associated with group-4 of the test data for the four aforementioned types of short-circuit faults. Again for this group, it is clearly evident that the accuracy of the fault location is very high in the last three faults. However, it should be noted that for such conditions after load-2 which is dynamic in nature, the accuracy of fault location decreases to 94% in the case of the SPH-G-SC fault. It is then apparent the capacity of the dynamic load can affect the accuracy of the proposed technique only for such conditions that a SPH-G fault occurs after the dynamic load. However, since the proposed method is flexible to retrain the ANNs by new training data set based on the new conditions, thus, this technique can be largely independent of the load capacity even dynamic load particularly for the last three faults, being less than 1% error in all the test data and less than 0.2% of the mean of error.

3- Table 6.19 and Fig.(132) show the results related to group-5 of the test data in which the type and the capacity of loads are changed. It is evident that the same results can be achieved in comparison with the group-4 of the test data. If the

load-2 at point 2000m changes from dynamic load to static load, the transients waveform are significantly affected in the case of SPH-G-SC fault and the accuracy of method decreases slightly, but as mentioned the accuracy can be achieved to very high value by retraining the ANNs using new training data set. It should be mentioned that even without retraining the accuracy of method for the last three cases correspond to the 2PH-G, 2Ph and 3PH short circuit faults are still very high, being less than 1% in all the cases of test data.

With regard to three aforementioned points associated with the effect of load taps, it can be concluded that the capacity of dynamic load can only decrease the accuracy in the case of SPH-G faults; however, since the method is flexible in retraining the ANNs, it is apparent that in order to obtain high accuracy in this case much larger training data e.g. more load taps with different capacity are needed. This will be the basis for future work.

Table 6.17 - Performance of the fault locator based on group-3 of test data

Fault	ag-sc Fault		bcg-sc fault		bc-sc fault		abc-sc fault	
Location	L	%e	L	%e	L	%e	L	%e
80m	57	0.575	75.4	0.115	79.8	0.005	72.4	0.185
350m	308.3	1.042	353.7	0.092	350	0.0	350.1	0.002
1100m	1067	0.825	1098	0.05	1100	0.0	1103	0.075
1750m	1737	0.325	1753	0.075	1752	0.05	1765	0.375
2500	2459	1.025	2498	0.05	2499	0.025	2505	0.125
3250	3236	0.35	3219	0.025	3242	0.2	3289	0.975
3800	3811	0.275	3801	0.025	3808	0.2	3825	0.625
The Mean of Error %	0.631		0.061		0.068		0.337	

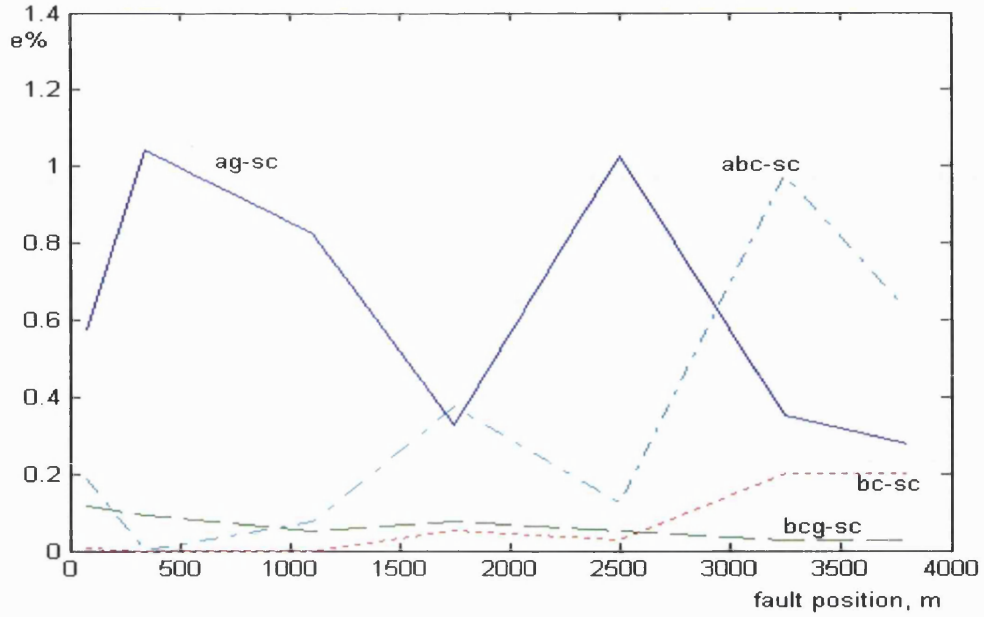

Fig. 130- Measuring accuracy for group-3 of test data for short-circuit faults

Table 6.18 - Performance of the fault locator based on group-4 of test data

Fault Location	ag-sc Fault		bcg-sc fault		bc-sc fault		abc-sc fault	
	L	%e	L	%e	L	%e	L	%e
80m	66.2	0.455	75.6	0.085	75.6	0.085	72.0	0.2
350m	308.3	1.042	356.9	0.172	356.4	0.16	350.3	0.007
1100m	1097	0.075	1100	0.0	1098	0.05	1097	0.075
1750m	1866	2.9	1752	0.05	1750	0.0	1757	0.175
2500	2749	6.225	2503	0.075	2502	0.05	2496	0.1
3250	3289	0.975	3213	0.925	3243	0.175	3273	0.575
3800	4000	5.0	3800	0.0	3772	0.7	3815	0.375
The Mean of Error %	2.381		0.186		0.174		0.19	

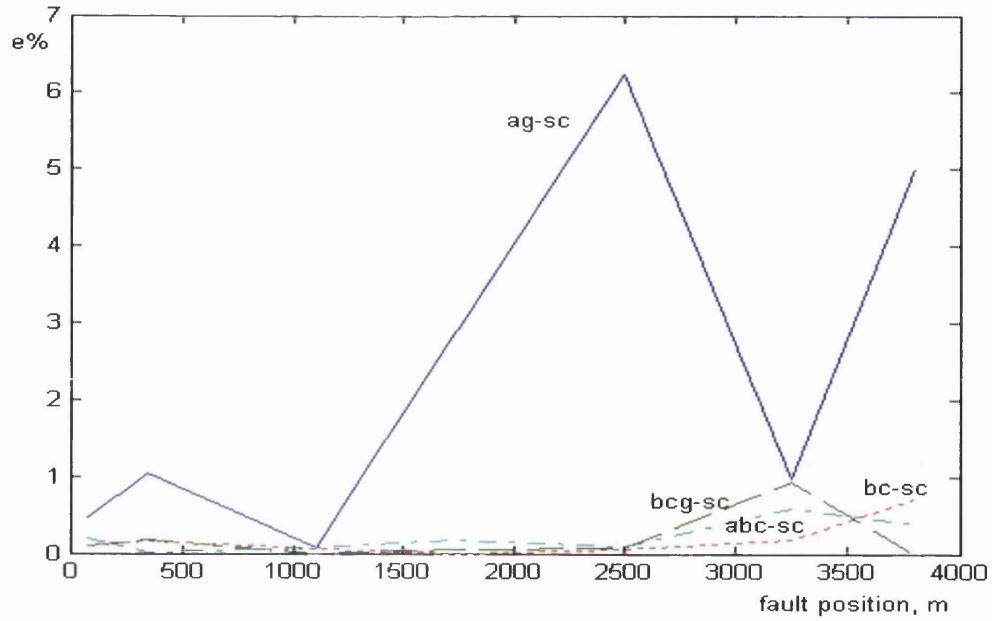

Fig. 131- Measuring accuracy for group-4 of test data for short-circuit faults

Table 6.19 - Performance of the fault locator based on group-5 of test data

Fault Location	ag-sc Fault		bcg-sc fault		bc-sc fault		abc-sc fault	
	L	%e	L	%e	L	%e	L	%e
80m	66.3	0.417	75.6	0.11	75.6	0.11	72.0	0.2
350m	408.9	1.472	356.8	0.17	346.3	0.092	350.3	0.007
1100m	1099	0.025	1101	0.025	1099	0.025	1100	0.0
1750m	1888	3.325	1761	0.275	1757	0.175	1760	0.25
2500	2808	7.7	2512	0.3	2507	0.175	2492	0.2
3250	3301	1.275	3213	0.925	3246	0.1	3263	0.325
3800	4000	5.0	3802	0.05	3770	0.75	3809	0.225
The Mean of Error %	2.274		0.265		0.204		0.172	

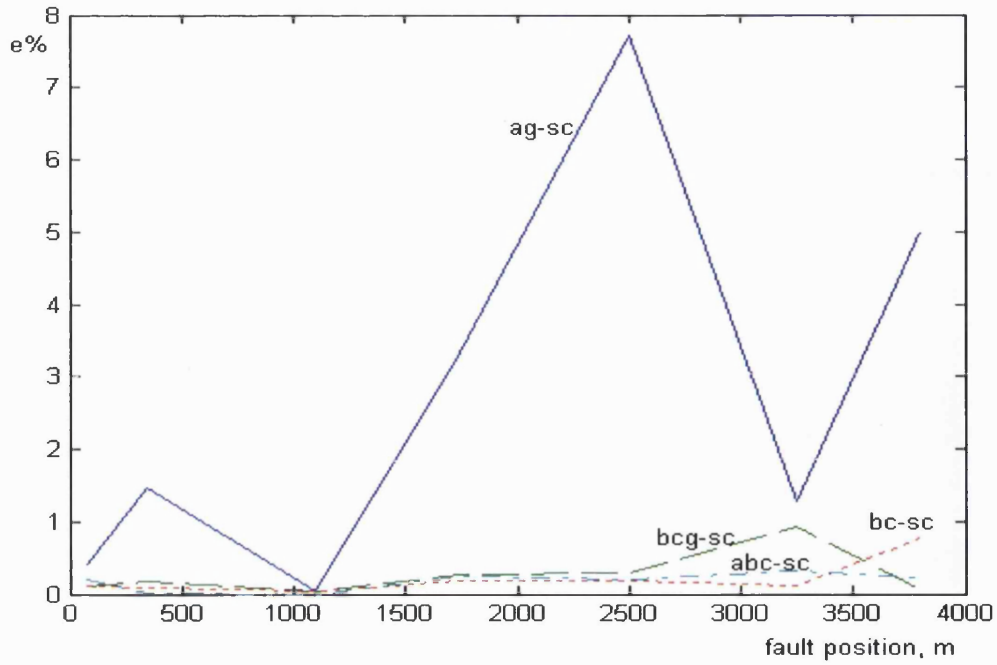

Fig. 132- Measuring accuracy for group-5 of test data for short-circuit faults

6.8.2.4 Effect of Cable Length

The cable length can vary considerably in the DS, it is vitally important to ascertain as to what extent the fault location accuracy is affected as a result of a change in the cable length. Table 6.20 and Fig.(133) illustrate the performance of the ANN-based technique for the four aforementioned short-circuit faults when subjected to the cable length 1500m instead of 1000m for each section of such system in which the configuration has been shown in fig.(51) (group-6 of the test data). The results clearly demonstrate that the accuracy achieved in fault location is very high; being less than 1.15% error in all the types of fault and all the test cases and shows that the ANNs give accurate evaluation of fault position that is robust to changes in cable length i.e.; the non-algorithmic errors are quite small.

6.8.2.5 Effect of External Fault

In any fault location technique, although a high accuracy for internal faults is of primary concern, nonetheless, it should also be stable under external faults. For the fault location technique described herein, an external fault (before switch-1 shown in Fig.(51)) produces an estimation which is consistently gives a negative distance and results

shown in table 6.21 being a typical example. It is evident from the results that when the ANNs give such abnormally high and negative values, then it can be safely assumed that the fault is external. Studies have shown that the aforementioned result is true for all practically encountered external faults.

Table 6.20 - Performance of the fault locator based on group-6 of test data

Fault	ag-sc Fault		bcg-sc fault		bc-sc fault		abc-sc fault	
Location	L	%e	L	%e	L	%e	L	%e
80m	57.4	0.315	75.5	0.112	80.2	0.005	72.4	0.19
350m	304.3	1.142	354	0.05	350.5	0.012	350.1	0.002
1100m	1066	0.85	1099	0.025	1100	0.0	1103	0.075
1750m	1738	0.3	1754	0.1	1754	0.1	1766	0.4
2500	2472	0.7	2503	0.075	2503	0.075	2501	0.025
3250	3265	0.375	3230	0.5	3253	0.075	3281	0.775
3800	3814	0.35	3823	0.575	3823	0.575	3834	0.85
The Mean of Error %	0.576		0.205		0.12		0.331	

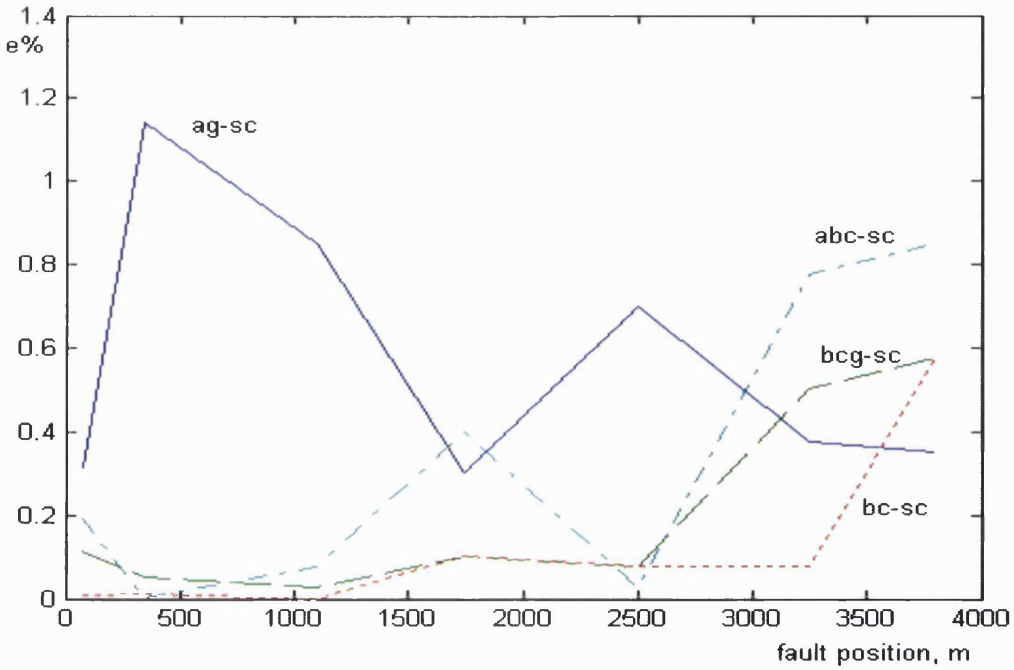

Fig. 133- Measuring accuracy for group-6 of test data for short-circuit faults

Table 6.21 - Performance of the fault locator based on external fault

Fault Location	ag-sc Fault	bcg-sc fault	bc-sc fault	abc-sc fault
External Fault	-2708	-2006	-2728	-2438

6.9 Summary

In this chapter, firstly, the applications of neural network in power system is reviewed briefly and ANNs are discussed with practical emphasis on multi-layer feed-forward ANNs and the back-propagation algorithm that is used to adapt the weights and biases to achieve the desired non-linear mapping from inputs to outputs. Then an accurate fault location technique based on ANN is developed. Three ANNs are trained to classify the fault type and separate ANNs are designed to accurately locate the actual fault position associated with all the commonly encountered types of fault on a practical underground DS. In this respect, some practical issues surrounding the design, training and testing of ANNs have also been covered. Also the performance evaluation of the fault location technique is discussed. Through a series of tests, it is shown that the ANNs can very accurately classify the type of fault on the underground DS under all practically encountered system and fault conditions. In order to illustrate the effectiveness of the ANN fault location technique, each ANN is tested with a separate set of unseen data and its performance on the accuracy of the results are presented. The results presented herein clearly show that the proposed method gives a high accuracy in fault location under a whole variety of different system and fault conditions particularly in the case of short-circuit faults.

Thus it can be concluded that the proposed approach based on the combined WT and ANN is robust to different case studies; this is a significant advantage and can be directly attributed to the fact that the WT technique effectively extracts the very crucial time-frequency features from the DS transient signals which are then transformed into unique parameters using novel mathematical functions for inputting into ANNs; it is clearly demonstrated that this approach gives a very high accuracy in both, fault classification and fault location.

CHAPTER 7

Conclusions and Future Work

7.1 Introduction

This thesis presents a new approach to cable model using conformal mapping compared to the conventional approach based on EMTP cable models (time and frequency dependent model). The simulated results attained via the improved cable model are then employed to research and effect a novel fault location technique for low voltage UG distribution systems with or without remote source infeed. The technique based on combined WT and ANNs, shows a vastly improved performance over conventional techniques. The robustness of the fault location technique in terms of retaining its high accuracy is clearly demonstrated for DSs with multiple load taps and variable capacities and a whole variety of different systems and fault conditions. Equally important, it is also demonstrated that the technique is tolerant to non-algorithmic errors arising due to small changes in cable length, changes in the position of load tap locations etc.

7.2 Summary of Work

A general literature review of cable model and fault locator techniques for underground DS have been outlined in chapter 2. The cable model is divided into two main groups; 1-time domain model including lumped-parameters and distributed-parameters; 2-frequency domain model. Because of the heavy frequency dependency of modal transformation matrices in a cable model, some optimization method for these matrices is presented. Also, with regard to the effect of some important factors in achieving an accurate cable model such as skin effect, proximity effect, semi- conducting screens and nonlinear B-H curve, some improved modelling techniques are reviewed. Moreover, in chapter 2 four basic principles in fault location techniques are outlined including: 1-on-line or off-line methods 2-high or low frequency techniques 3-voltage class 4-terminal and tracer methods. This is followed by an explanation of some existing methods and their abilities and drawbacks. Currently employed methods such as Bridge techniques,

Time Domain Reflectometry methods, impedance techniques and shock methods are reviewed and finally a number of other techniques based on theoretical studies are also reviewed.

Chapter 3 is concerned with an outline of the mathematical analysis associated with the calculation of the per unit length series impedance Z and shunt admittance Y using the EMTP software which is widely employed for modelling the transient phenomena in power systems. Then a new cable model based on conformal mapping is introduced as a more accurate model. Also, a comparison is made between the EMTP and CM model for a typical DS consisting of UG cables.

In chapter 4, the system simulation of the DS has been implemented using the EMTP software based on the new cable model. It is vitally important that the system simulation be as accurate as possible within the bounds of practicality. In this respect, all the practical considerations, such as the effect of transducers and hardware errors, on the primary system fault data are included in the simulation. In order to ascertain the effects of Rf, distance of fault from recording point, inception angel and remote source infeed on the extracted signals, a practical underground DS is simulated under different system and fault conditions. The results clearly show that there are unique and distinct features in both the voltage and current signals that can be employed in the design of the fault locator.

The digitised voltage and current signals are processed using advanced signal processing techniques for extracting the significant features from the signals in chapter 5. In this respect, some signal processing methods such as FFT, STFT and WT are reviewed, particularly their advantages and disadvantages. Decomposition of voltage and current signals using WT is adopted in the feature extraction process and a set of important variables are then simulated to set up data set vectors for training ANNs, as detailed in the next chapter.

In chapter 6 firstly, the applications of neural network in power system is reviewed briefly and ANNs are discussed with practical emphasis on multi-layer feed-forward ANNs and the back-propagation algorithm that is used to adapt the weights and biases to achieve the desired non-linear mapping from inputs to outputs. Then an accurate fault

location technique based on ANNs is developed; three ANNs are trained to classify the fault type and separate ANNs are designed to accurately locate the actual fault position associated with all the commonly encountered types of fault on a practical underground DS. In this respect, some practical issues surrounding the design, training and testing of ANNs have also been covered. In order to evaluate the performance of the fault classification and fault location technique and determine the sensitivity of the proposed method to the fault parameters (such as Rf and inception angle), load taps, remote source infeed and the length of cable, the presented method is tested using 'unseen' data test based on different systems and fault conditions.

7.3 Conclusions

This thesis presents a new approach to the calculation of the crucially important parameters Z and Y (series impedance and shunt admittance) of a commonly employed 3-phase pipe-type cable in a low voltage distribution system. It is clearly demonstrated that the conformal mapping (CM) approach adopted herein overcomes a number of approximations associated with the EMTP based cable model which makes certain approximations in the configuration of the cable when the conductors are eccentric. The CM method overcomes this assumption by mathematically transforming the eccentric circles into concentric circles. The results presented clearly demonstrate the differences observed in the cable parameters via the two cable models. The greatest impact is on the attenuation constant (this is a function of both Z and Y), that for the more accurate CM model being higher than that for the EMTP model. The next effect of the latter is that the high frequency transients superimposed upon the power frequency voltage and current waveforms are attenuated much faster in the case of the more accurate CM model compared to the EMTP model and this is the case for all types of faults. Equally important, some distortion is also observed on the healthy phase(s) in the case of the CM model and this is distinctly absent in the EMTP model largely due also to the approximations and their impact on the mutual coupling amongst conductors in the case of latter.

The choice of feature extraction methodology is critical to the time taken for the ANN to train and more importantly, to the results emanating from the actual testing. In this

respect, although there are many methods available for extracting the features, an extensive series of studies have shown that the WT, which is based on time-frequency domain decomposition, is best suited for the application discussed herein and this is the one adopted here. Moreover, a series of tests have revealed that there are some useful features according to the type of fault that contain the major part of the information in a signal and are the most significant in that they are representative of the vast majority of different system and fault conditions and there are the ones employed as input features into the ANNs; this feature extraction methodology is near optimal in both correctly classifying the type of fault and in defining the fault position on underground DS with a high degree of accuracy.

The overall performance of the ANNs for fault type classification under a vast majority of different system and fault conditions has indicated 100% accuracy to find the type of fault and 97% accuracy to determine the faulted phase(s). This clearly shows that the ANN is very effective in classifying all types of fault (short and open circuit faults) on underground distribution systems.

It is clearly shown that the proposed fault location technique gives an inherently accurate evaluation of fault position for all types of short-circuit fault and is not significantly influenced by changes in fault resistance and fault inception angle. The former is a very important advantage over conventional techniques, particularly those based on impedance to fault measurements, which tend to produce excessive errors when dealing with resistive faults. However, the results show that the error are higher in the case of open-circuit faults in comparison with short-circuit faults. As an example, the maximum and mean of the error related to a-oc, ab-oc and abc-oc faults are (7.22 & 4.128), (7.275 & 3.997) and (15.42 & 6.18) percent respectively compared to the corresponding errors for ag-sc, bcg-sc, bc-sc and abc-sc faults which are (1.04 & 0.6), (0.625 & 0.247), (0.275 & 0.07) and (0.85 & 0.367) percent respectively.

Since the approximate voltage and current signals at level 5 are associated with the power frequency, these signals are thus strongly dependent on the capacity and location of the load taps in the case of open-circuit faults. Thus contrary to the short-circuit faults, only detailed signals corresponding to the high frequency voltage signals have been selected to extract useful features using WT in the case of open-circuit faults. Since the

inception angle and the capacity and location of dynamic loads influence the transient components of the voltage and current signals, thus this makes the proposed fault location method sensitive to the aforementioned factors in the case of open-circuit faults. It is apparent that in order to obtain high accuracy in this case, much larger training data e.g. more inception angles and more dynamic loads (different capacities and locations) are needed as this will be the basis for the future works.

In comparison to the results attained for the radial feeder system discussed in this research, it is evident that the presence of a remote source has only a slight effect on accuracy particularly in the case of SPH-G fault, but the accuracy achieved in fault location is still high, being less than 2 percent in all the test cases. These small changes can be directly attributed to the fact that with a remote source, the current increases in the fault resistance path and it changes in the healthy phase(s) in terms of magnitude and distortion.

It is clearly depicted from the evaluation of the performance of the technique in relation to the location of the load taps that the accuracy achieved in fault location is very high in the case of bcg-sc and bc-sc faults, being less than 0.2% error and for the other faults the accuracy is still high but being less than 1.05% error in all the test cases. Thus it can be concluded that the ANNs give accurate evaluation of fault location that is largely independent of the location of load taps. This is a very significant advantage since the location of load taps can somewhat vary from one DS to another.

Results show that the capacities of dynamic loads in a particular system can affect the accuracy of the proposed technique only for such conditions that a SPH-G fault occurs after the dynamic load. However, since this method is flexible to retrain the ANNs based on new data correspond to the new conditions, thus, this technique can be largely independent of load capacity (even dynamic load), being less than 1% error in the entire data test and being less than 0.2% for the mean of error.

Since in practice, the cable length can vary in the DS, therefore it is vitally important to ascertain as to what extent the fault location accuracy is affected as a result of a change in the cable length. The results clearly demonstrate that the accuracy achieved in proposed fault location technique is very high; being less than 1.15% error in all the test

cases that the cable length increases from 4 km (training data-based) to 6 km. The result apparently shows that the ANNs give accurate evaluation of fault position that is robust to changes in cable length i.e., the non-algorithmic errors are quite small.

For the fault location technique described herein, an external fault produces an estimation which is consistently shows a high negative distance. It is evident from the results that when the ANNs give such abnormally high negative values, then it can be safely assumed that the fault is external. Studies have shown that the aforementioned result is the case for all practically encountered external faults. This very important feature of the algorithm makes it totally immune to any mal-operation for external faults.

7.4 Future Work

As emphasised in the thesis, an extensive series of tests have been conducted to ascertain the accuracy of the proposed cable model and the fault location ANN-based technique under different system and fault conditions, using the EMTP software and a data pre-processing technique; every effort has been made to develop the fault location technique using extensive training and test data covering the vast majority of different system and fault conditions. Equally important, a vast majority of practical considerations associated with the current transducers, anti-aliasing filters and quantisation have been taken into account, however, in practice there is always some unexpected events and a level of spurious noise present in the measured signals. As a logical step, both approaches associated with the cable model and fault location technique should be tested with real input data captured from practical systems and the necessary refinements should be carried out to the algorithm.

As emphasised before, the proposed technique is based on an off-line application and makes use of information from one end only for the fault distance estimation and consequently a communication link is not necessary. In this respect, the data for the aforementioned validation/algorithm refinement can be captured from a digital fault recorder which can be subsequently processed in the fault location algorithm (described in this thesis) on a standard PC in an off-line mode.

Three or more load spurs are commonly used in the DS and it is apparent that additional problems can be encountered by the presence of such spurs with different types of cable in fault location technique. The process thus requires special attention i.e. there is a need to be able to localise the fault on the tap line itself when a fault occurs.

The algorithm described in this thesis is only developed for cable-based DS; however, there are many DSs with a mixture of cables and overhead lines. Thus, the performance of the proposed fault location method for such a mixed DS should be further investigated and validated.

The presented method only covers DSs with and without remote source connected. However, there are some DSs with several types of generators e.g. distributed generators including those based on solar and windy sources; thus as a part of future work, a logical step would be to develop the proposed method further in order to implement it for more complex DSs, including those with renewal-energy-based generation connected.

As mentioned before, the proposed method is sensitive to the inception angles and dynamic load taps in the case of open-circuit faults; thus the method needs to be further researched and developed to cater for such types of faults.

Bibliography

[1] L.Marti, "Simulation of transients in underground cables with frequency-dependent modal transformation matrices", IEEE transaction on power Delivery, Vol. 3, Page(s): 1099-1110, July 1988.

[2] T.Nguyen & H.Y.Chan "Evaluation of modal transformation matrices for overhead transmission lines and underground cables by optimization method", IEEE transaction on power Delivery, Vol. 17, Page(s): 200-209, Jan. 2002.

[3] EMTP Theory book, Chapter 5: Underground Cable.

[4] J.A.Tegopoulos & E.E.Kriezis, "Eddy current distribution in cylindrical shells of infinite length due to axial current", Part I: shells of one boundary, IEEE, PAS, Vol. 90, page(s): 1278-1286, May-June 1971.

[5] J.A.Tegopoulos & E.E.Kriezis, "Eddy current distribution in cylindrical shells of infinite length due to axial current", Part II: shells of finite thickness, IEEE, PAP, Vol. 90, page(s): 1287-1294, May-June 1971.

[6] X.B.Xu & G.Liu & P.Chow, "A finite-element method solution of the zero-sequence impedance of underground pipe-type cable", IEEE transaction on power Delivery, Vol. 17, Page(s): 13-17, Jan. 2002.

[7] D.L.Paul, C.J.Railton & I.J.Craddock, "Full-wave modelling of coaxial cables by FDTD technique", electronics letters, Vol. 38, No. 21, Sep./Oct. 2002.

[8] E C Bascom, D W V Dollen & H W Ng, "Computerized Underground Cable Fault Location Expertise", IEEE Transmission and Distribution Conference, Page(s): 376-382, April 1994.

[9] B. Clegg, "Underground cable fault location", McGraw-Hill, 1993.

[10] No. 1 Kim Keat Lane, Singapore 328858, Website: www.westasia.com.sg.

[11] Bradford, West Yorkshire, England, BD7 1hr, Website: www.calibrationuk.org/otc.

[12] S Navaneethan, J Soraghan, W H Siew, F Mcpherson & P F Gale, "Automatic Fault Location for Underground Low Voltage Distribution Networks", IEEE Transactions on Power Delivery, Vol. 16, No. 2, Page(s): 346-351, April 2001.

[13] T Dalstein, T Friedrich, B Kulicke & D Sobajic, " Multi Neural Network Based Fault Area Estimation for High Speed Protective Relaying", IEEE Transactions on Power Delivery, Vol. 11, No. 2, Page(s): 740-747, April 1996.

[14] A. Kynaston & L.M.Sloman "Cross linked polyethylene (XLPE) for distribution cables up to 11 kV",IEE, 1977.

[15] J. M. Marti, "Accurate modelling of frequency-dependent transmission lines in electromagnetic transient simulations", IEEE Transactions on Power Apparatus and systems, Vol. Pas-101, No. 1, Page(s): 147-157, Jan. 1982.

[16] A. Semlyen & A. Dabuleanu, "Fast and accurate switching transient calculations on transmission lines with ground return using recursive convolution", IEEE Trans. PAS, Vol. PAS-94, Page(s): 561-571, Mar./Apr. 1975.

[17] A. Ametani, "A highly efficient method for calculating transmission line transients", IEEE Trans. PAS, Vol. PAS-95(2), Page(s): 1545-1551, 1976.

[18] B. Gustavsen, A. Semlyen, "Simulation of transmission line transients using vector fitting and modal decomposition", IEE, Vol. 13, Issue 2, Page(s): 605-614, April 1998.

[19] A.Moched & B.Gustavsen & M.Tartibi "A universal model for accurate calculation of electromagnetic transients on overhead lines and underground cables",IEEE transaction on power Delivery, Vol. 14, Page(s): 1032-1038, July 1999.

[20] Ting-Chung Yu, J. R. Marti, "A robust phase-coordinates frequency-dependent underground cable model (zcable) for the EMTP", IEEE Trans. Power Delivery, Vol. 18, Issue 1, Page(s): 189-194, Jan. 2003.

[21] G.Liu, "Improved modelling of the nonlinear B-H curve and its application in power cable analysis", IEEE Transaction on magnetic, Vol. 38, Part 2, Page(s): 1759-1763, July 2002.

[22] M.Feliziani, F.Maradei, "Full-wave analysis of shielded cable configurations by the FDTD method", IEEE Transaction on magnetic, Vol. 38, Part 1, Page(s): 761-764, March 2002.

[23] A.F.Moreira. T.A.Lipo, G.Venkataramanan & S.Bernet, "High-frequency modelling for cable and induction motor over voltage studies in long cable drives", IEEE Transaction on industry applications, Vol. 38, Page(s): 1297-1306, Sep./Oct. 2002.

[24] A Ametani, Y Miyamoto, N Nagaoka, "Semiconducting layer impedance and its effect on cable wave-propagation and transient characteristics", IEEE Transaction on Power Delivery, Vol. 19, Page(s): 1523-1531, Oct. 2004.

[25] B.Gustavsen, "Panel session on data modelling system transients insulted cables", 0-7803-6674-IEEE 2000.

[26] C M Ho, W K Lee & Y S Hung," Signature Representation of Underground Cables and its Applications to Cable Fault Diagnosis", IEE 2th International Conference on Advances in Power System Control, Operation and Management, Dec. 1993, Hong Kong

[27] G D Atkinson & G F L Dixon, "Dealing with Faults and Supply Interruptions on Low-Voltage Cable Networks", Yorkshire Electricity Board, UK

[28] N. Inoue, T Tsunekage & S Sakai, "On-Line Fault Location System For 66kV Underground Cables With Fast O/E and Fast A/d Technique", IEEE Transactions on Power Delivery, Vol. 9, No. 1, Page(s): 577-584, January 1994.

[29] J zhu, D L Lubkeman & A Girgis, "Automated Fault Location and Diagnosis on Electric Power Distribution Feeders", IEEE Transactions on Power Delivery, Vol. 12, No. 2, Page(s): 801-809, April 1997.

[30] M Komoda, T kawashima, M Arakane, M Aihara, Y Fujiwara & J Shinagawa, "Development of a Current Detection Type Cable Fault Location", IEEE Transactions on Power Delivery Vol. 6, No. 2, Page(s): 541-545, April 1991.

[31] F H Magnago & A Abur, "Fault Location Using Wavelet", IEEE Transactions on Power Delivery, Vol. 13, No. 4, Page(s): 1475-1480, October 1998.

[32] F H Magnago & Ali Abur, "A New Fault Location Technique for Radial Distribution Systems Based on High Frequency Signal", IEEE Power Engineering Society Summer Meeting, Vol. 1, Page(s): 426-431, July 1999.

[33] P Bastard, L G Santander, X Le Pivert, I Gal & E L Parra, "A Voltage-Based Fault Location Method For Radial Distribution Networks", IEE, 5th International Conference on Power System and Management, Page(s): 216-221, April 2002.

[34] P M V Oirsouw & F Provoost, "Fault Localisation in an MV Distribution Network", CIRED 17th International Conference on Electricity Distribution, Barcelona May 2003.

[35] M M Saha, F Provoost & E Rosolowski, "Fault Location Method For MV Cable Network", IEE Development in Power System Protection Conference, No. 479, Page(s): 323-326, April 2001.

[36] R.K.Aggarwal, Y.Aslan & A.T.Johns, "New Concept in Fault Location for Overhead Distribution Systems using Superimposed Components", IEE Journal, Vol. 144, Page(s): 309-316, May 1997

[37] M T Glinkowski & N C Wang, "ANNs pinpoint underground distribution faults",IEEE on Computer Applications in Power, Vol. 8, Page(s): 31-34, Oct. 1995.

[38] G.W.Brown & R.G.Rocamora, "Surge propagation in Three-phase cables", Part I –unsaturated pipe, IEEE, PAS, Vol. 95, Page(s): 89-95, Jun./Feb. 1976.

[39] R Schinziger & A Ametani, "Surge propagation characteristics of pipe enclosed under ground cables". IEEE, PAS, Vol. 97, Page(s): 1680-1688, Sept. 1978.

[40] V Perrier, T Philipovitch, and C Basdevant, "Wavelet spectra compared to fourier spectra", J. Math. Phys, Vol. 36, No. 3, 1995.

[41] S Conforto and T Dalessio, "Spectral analysis for non-stationary signals from mechanical measurements", Mechanical System and Signal Processing 13(3), Page(s): 395-411, 1999.

[42] User's Guide, "Signal Processing Toolbox for Use with MATLAB", Revised for MATLAB 5.2 Second Printing, Jan. 1998.

[43] A Wayne Galli & O M Nielsen, "Wavelet Analysis for Power System Transients", IEEE Computer Applications in Power, Vol. 12, Page(s): 16-25, Jan. 1999.

[44] R K Aggarwal, Y H Song, "Tutorial: Artificial Neural Networks in Power System", Power Engineering Journal, June 1997.

[45] Stamatios V Kartalopoulos, "Understanding Neural Network and Fuzzy Logic: Basic Concepts and Applications", The Institute of Electrical and Electronics Engineers, Inc., New York, 1996.

[46] Kevin Warwick, Arthur Ekwue, Raj Aggarwal, "Artificial Intelligence Techniques in Power System", The Institute of Electrical Engineers, London, UK, 1997.

[47] Carl G Looney, "Pattern Recognition Using Neural Networks: Theory and Algorithms for Engineers and Scientists", New York, Oxford University Press, 1997.

[48] Shigeo Abe, "Neural Networks and Fuzzy Systems: Theory and Applications", Kluwer Academic Publishers, Boston/London/Dordrecht, 1997.

[49] Richard P Lippman, "An Introduction to Computing with Neural Nets", IEEE ASSP Magazine, Page(s): 4-22, April 1987.

[50] Churchland, Patricia Smith & T. J. Sejnowski,, "*The computational brain*", MIT press, 1992.

[51] Hertz J, Krogh A and Palmer R G, "Introduction to the Theory of Neural Computing", Addison Wesley, Reading, May 1991.

[52] Pao Y H, "Adaptive Pattern Recognition and Neural Networks", Addison Wesley, Reading, May 1989.

[53] Thomas Dalstein, Bernd Kulicke, "Neural Network Approach to Fault Classification for High Speed Protective Relaying", IEEE Trans. On Power Delivery, Vol. 10, No. 2, Page(s): 1002-1011, April 1995.

[54] Atish K Ghosh, David L Lubkeman, "The Classification of Power System Disturbance Waveforms Using a Neural Network Approach", IEEE Trans. On Power Delivery, Vol. 10, No. 1, Page(s): 109-115, Jan. 1995.

[55] Mladen Kezunovic, Igor Rikalo, "Detect and Classify Faults Using Neural Nets", IEEE Computer Applications in Power, Page(s): 42-47, Oct. 1996.

[56] Howard Demuth & Mark Beale, "Neural Network Toolbox for Use with MATLAB", Version 3, July 1998.

APPENDIX 1

The cable shown in Fig.(13) consists of tubular conductors inside a metallic sheath and armour with insulation between them. In this model, series impedances and shunt admittances per unit length are represented by the following equations and appendix-1 deals with these equations in detail.

$$-\begin{bmatrix} \frac{dv_{core}}{dx} \\ \frac{dv_{sheath}}{dx} \\ \frac{dv_{armour}}{dx} \end{bmatrix} = \begin{bmatrix} z_{cc} & z_{cs} & z_{ca} \\ z_{sc} & z_{ss} & z_{sa} \\ z_{ac} & z_{as} & z_{aa} \end{bmatrix} \times \begin{bmatrix} I_{core} \\ I_{sheath} \\ I_{armour} \end{bmatrix} \qquad \text{(A1-1)}$$

Where v_{core} = voltage from core to ground

v_{sheath} = voltage from sheath to ground

v_{armour} = voltage from Armour to ground

$I_{core} = I_1$

$I_{sheath} = I_2 - I_1$

$I_{armour} = I_3 - I_2$

with $z_{cc} = z_{11} + 2z_{12} + z_{22} + 2z_{23} + z_{33}$

$z_{ss} = z_{22} + 2z_{23} + z_{33}$

$z_{aa} = z_{33}$ (A1-2)

$z_{cs} = z_{sc} = z_{12} + z_{22} + 2z_{23} + z_{33}$

$z_{ca} = z_{ac} = z_{as} = z_{sa} = z_{23} + z_{33}$

Where $z_{11} = z_{core-out} + z_{core-sheath-insulation} + z_{sheath-in}$ (A1-3)

$z_{22} = z_{sheath-out} + z_{sheath-armour-insulation} + z_{armour-in}$ (A1-4)

$z_{33} = z_{armour-out} + z_{armour-earth-insulation} + z_{earth}$ (A1-5)

$z_{12} = z_{21} = -z_{sheath-mutual}$ (A1-6)

$z_{23} = z_{32} = -z_{armour-mutual}$ (A1-7)

Also:

$$z_{insulation} = \frac{1}{2\pi} j\omega\mu_o\mu_r \ln\left(\frac{r}{q}\right) \quad \text{(A1-8)}$$

$\mu_{r=}$ permeability of insulation

$\mu_o = 2*10^{-4}$ H/Km

r=outside radius of insulation (or tube)

q=inside radius of insulation (or tube)

$$z_{tube-in} = \frac{\rho m}{2\pi qD}[I_O(mq)*k_1(mr)+k_o(mq)*I_1(mr)] \quad \text{(A1-9)}$$

$$z_{tube-out} = \frac{\rho m}{2\pi rD}[I_O(mr)*k_1(mq)+k_o(mr)*I_1(mq)] \quad \text{(A1-10)}$$

$$z_{tube-mutual} = \frac{\rho}{2\pi rqD} \quad \text{(A1-11)}$$

With $D=I_1(mr)*k_1(mq)-I_1(mq)*k_1(mr)$ (A1-12)

$$m = \sqrt{j\omega\mu/\rho} \quad \text{(A1-13)}$$

Where the I_O,I_1,K_0 and K_1 are Bessel function.

These can be simplified to the following:

$$\begin{aligned} b_{er}(x)+jb_{ei}(x) &= I_0(x\sqrt{j}) \\ b_{er}(x)+jb_{ei}(x) &= \sqrt{j}I_1(x\sqrt{j}) \\ k_{er}(x)+jk_{ei}(x) &= k_0(x\sqrt{j}) \\ k_{er}(x)+jk_{ei}(x) &= -\sqrt{j}k_1(x\sqrt{j}) \end{aligned} \quad \text{(A1-14)}$$

For the current changes along the cable:

$$-\begin{bmatrix} \frac{-dI_{core}}{dx} \\ \frac{dI_{sheath}}{dx} \\ \frac{dI_{armour}}{dx} \end{bmatrix} = \begin{bmatrix} Y_1 & -Y_1 & 0 \\ -Y_1 & Y_1+Y_2 & -Y_2 \\ 0 & -Y_2 & Y_2+Y_3 \end{bmatrix} * \begin{bmatrix} v_{core} \\ v_{sheath} \\ v_{armour} \end{bmatrix} \quad \text{(A1-15)}$$

With $Y_i=G_i+j\omega C_i = j\,2\pi\omega\varepsilon_0\varepsilon_r/\ln(r/q)$ (A1-16)

$$\varepsilon_r = 2.5+\frac{0.94}{\left(1+j\omega 6*10^{-9}\right)^{315}} = \varepsilon' - j\varepsilon'' \quad \text{(A1-17)}$$

The support routine cable constants now assume $\varepsilon''=0$, ε' being constant. The dielectric losses are of little importance for the attenuation [3], and using a constant ε' with $\varepsilon''=0$ should therefore give acceptable results in most cases.

APPENDIX 2

It is apparent that the solution of M-phase cable equations becomes simpler if the M coupled equations can be transformed into M decoupled equations. These decoupled equations can then be solved as if they were single-phase equations. For balanced cables, this transformation is achieved with Eq(A2-1).

$$[T]=\begin{bmatrix} \frac{1}{\sqrt{M}} & \frac{1}{\sqrt{2}} & \cdots & \frac{1}{\sqrt{M(M-1)}} \\ \vdots & \vdots & \vdots & \vdots \\ \frac{1}{\sqrt{M}} & 0 & -\frac{(J-1)}{\sqrt{J(J-1)}} & \cdots \\ \frac{1}{\sqrt{M}} & 0 & 0 & -\frac{(M-1)}{\sqrt{M(M-1)}} \end{bmatrix} \qquad \text{(A2-1)}$$

However, many cables are with ungrounded sheath or armour and thus they are unbalanced cables. Fortunately, the matrices of an unbalanced cable can be diagonalized as well, with transformations to modal parameters derived from eigenvalue/eigenvector theory.

To explain the theory, the two system of equations (3-1) & (3-8) can be used as a starting point:

$$-[\frac{dV_{phase}}{dx}]=[Z_{phase}].[I_{phase}] \qquad \text{(A2-2)}$$

$$-[\frac{dI_{phase}}{dx}]=[Y_{phase}].[V_{phase}] \qquad \text{(A2-3)}$$

Where $[Y_{phase}]=j\omega[C_{phase}]$ if shunt conductances are ignored, as is normally done. By differentiating the first equation with respect to x and replacing the current derivative

with the second equation, a second-order differential equation for voltage only is obtained:

$$-[\frac{d^2V_{phase}}{dx^2}] = [Z_{phase}].[Y_{phase}].[V_{phase}] \qquad \text{(A2-4)}$$

Similarly, a second-order differential equation for currents only can be obtained:

$$-[\frac{d^2I_{phase}}{dx^2}] = [Y_{phase}].[Z_{phase}].[I_{phase}] \qquad \text{(A2-5)}$$

Where the matrix products are now in reverse order from that in Eq.(A2-4) and therefore different. Only for balanced matrices and for lossless high-frequency approximations, would the matrix products in Eqs (A2-4) & (A2-5) be identical.

With eigenvalue theory, it becomes possible to transform the two coupled Eqs (A2-4) & (A2-5) from phase quantities to modal quantities in such a manner that the equations become decoupled, or in terms of matrix algebra, that the associated matrices become diagonal e.g., for the voltage:

$$[\frac{d^2V_{mode}}{dx^2}] = [\Lambda][V_{mode}] \qquad \text{(A2-6)}$$

Where [Λ] is a diagonal matrix. To get from Eq.(A2-4) to (A2-6), the phase voltages must be transformed to modal voltages as:

$$[V_{phase}]=[T_V].[V_{mode}] \qquad \text{(A2-7)}$$

hence

$$[V_{mode}]=[T_v]^{-1}.[V_{phase}] \qquad \text{(A2-8)}$$

Then Eq.(A2-4) becomes:

$$[\frac{d^2V_{mode}}{dx^2}] = [T_v]^{-1}[Z_{phase}][Y_{phase}][T_v][V_{mode}] \qquad \text{(A2-9)}$$

Which, when compared with Eq.(A2-6), shows us that

$$[\Lambda] = [T_v]^{-1}[Z_{phase}][Y_{phase}][T_v] \qquad \text{(A2-10)}$$

To find the matrix $[T_v]$ which diagonalizes $[Z_{phase}]*[Y_{phase}]$ is an eigenvalue/eigenvector problem. The diagonal elements of $[\Lambda]$ are the matrix of eigenvectors or modal matrix of that matrix product. There are many methods for finding eigenvalues and eigenvectors. As in the supporting routines LINE CONSTANTS and CABLE CONSTANTS, the "EISPACK"-subroutines (ref. [67], in the EMTP theory book) are used, in which the eigenvalues and eigenvectors of a complex upper Hessenberg matrix are found by the modified LR-method due to Rutishauser. For a given eigenvalue λ_k, the corresponding eigenvector $[t_{vk}]$ (=k-th column of $[T_v]$) is found by solving the system of linear equations:

$$\{[Z_{phase}][Y_{phase}] - \lambda_k[U]\}[t_{vk}] = 0 \ , \qquad \text{(A2-11)}$$

Where [U] = unit or identity matrix. Eq. (A2-11) shows that the eigenvectors are not uniquely defined in the sense that they can be multiplied with any nonzero (complex) constant and still remain as eigenvectors, in contrast to the eigenvalues which are always uniquely defined. In general, a different transformation must be used for the currents:

$$[I_{phase}]=[T_i].[I_{mode}] \qquad \text{(A2-12)}$$

and

$$[I_{mode}]=[T_i]^{-1}.[I_{phase}] \qquad \text{(A2-13)}$$

Because the matrix products in Eqs. (A2-4) & (A2-5) have different eigenvectors, though their eigenvalues are identical. Eq. (A2-6) is thus transformed to:

$$[\frac{d^2 I_{mode}}{dx^2}] = [\Lambda][I_{mode}] \qquad \text{(A2-14)}$$

With the same diagonal matrix as in Eq. (A2-6).

APPENDIX 3

In order to clarify the decomposition algorithm and break down of the original signal *S* into Ai and Di, a simple digital signal consisting of nine numbers [32 38 26 23 43 52 17 15 20] is considered. The method used here is known as the Haar WT. This WT is perhaps the simplest; however, it illustrates all the important aspects that are also present in more general and more powerful wavelet transforms. The coefficients of low-pass and high-pass filters in the Haar wavelet are [1/2, 1/2] and [1/2, -1/2]. Therefore it is carried out by forming averages and differences (divided by two) of adjacent pairs in the original signal. The averages are placed in the left half of the resulting vector and the differences placed in the right half. The transform splits the signal into a low-pass signal and a high-pass signal, with each new signal being half the length of the original signal. This process can be inverted by recombining elements from the two halves as sums and differences. The results are as follows:

S = [32 38 26 23 43 52 17 15 20]

cA1 = [35 24.5 47.5 16 20] cD1 = [-3 1.5 -4.5 1 0]

cA2 = [29.75 31.75 20] cD2 = [5.25 15.75 0]

cA3 = [30.75 20] cD3 = [-1 0]

cA4 = [25.375] cD4 = [5.375]

Approximation function $g(x)$ and detail function $h(x)$ are defined as follows:

$$g(x)=\begin{cases}1 & if, x\in[0,1]\\ 0 & if, x\notin[0,1]\end{cases} \quad \text{and} \quad h(x)=\begin{cases}1 & if, \quad x\in[0,1/2)\\ -1 & if, \quad x\in[1/2,1]\\ 0 & if, \quad x\notin[0,1]\end{cases}$$

Ai and Di are obtained:

A1 = [35 35 24.5 24.5 47.5 47.5 16 16 20]

D1 = [-3 3 1.5 -1.5 -4.5 4.5 1 -1 0]

A2 = [29.75 29.75 29.75 29.75 31.75 31.75 31.75 31.75 20]

D2 = [5.25 5.25 -5.25 -5.25 15.75 15.75 -15.75 -15.75 0]

A3 = [30.75 30.75 30.75 30.75 30.75 30.75 30.75 30.75 20]

D3 = [-1 -1 -1 -1 -1 1 1 1 1 0]

A4 = [25.375 25.375 25.375 25.375 25.375 25.375 25.375 25.375 25.375]

D4 = [5.375 5.375 5.375 5.375 5.375 5.375 5.375 5.375 -5.375]

APPENDIX 4

Several families of wavelets that have proven to be especially useful are included in the wavelet toolbox in the MATLAB software. These families are as follows:

- **Daubechies:** Supports orthogonal and biorthogonal wavelets and makes discrete wavelet analysis practicable. It is written *dbN*, where N is the order of Daubechies' wavelet. The support length of $g(x)$ and $h(x)$ (approximate and detail functions) is $2N$-1 and the number of vanishing moments of $h(x)$ is N. Most *dbN* are not symmetrical and the regularity increases with the order; it is $0.2N$ for large N.

- **Symlets:** The symlets are a near symmetrical wavelet proposed by Daubechies as modification to the *db* family. The properties of the two wavelet families are similar.

- **Coiflets:** Written *coifN*, where N is the order of family. $g(x)$ and $h(x)$ are much more symmetrical than *dbNs*. With respect to the support length, *coifN* has to be compared to *db3N* and is also compared to *db2N* in terms of vanishing moments.

- **Biorthogonal:** Supports both orthogonal and biorthogonal wavelets. This family of wavelets exhibits the property of linear phase, which is needed for signal reconstruction. By using two wavelets, one for decomposition and the other for reconstruction, instead of the same single one, interesting properties are derived. It is written $bioN_r.N_d$, where $_r$ is for reconstruction and $_d$ is for decomposition. Support lengths are $2N_r+1$ and $2N_d+1$. The vanishing point for h_d is N_d-1 and the regularity for h_r is N_r-1 and N_r-2 at the knots. It supports only biorthogonal wavelets.

- **Meyer:** Supports both orthogonal and biorthogonal wavelets and its support length is infinite, while its regularity is driveable indefinitely. It is written *meyr* in MATLAB.

There are another two wavelets, Morlet and Mexican Hat. They do not support either orthogonal or biorthogonal wavelets. Their application is much reduced compared to the families listed above.

APPENDIX 5

This appendix describes the incremental and batch training and also in order to be able to use these algorithms in MATLAB software, the related commands are presented.

- **Incremental training:**

There are two important training algorithms which are based on incremental mode and are used in MATLAB software.

1- *Gradient Descent:*

For the basic gradient descent algorithm, the weights and biases are moved in the direction of the negative gradient of the error function. In order to use this algorithm in the MATLAB software, the individual learning function parameters for the weights and biases are set to "*learngd*" function. The function *learngd* has one learning parameter as learning rate *lr*. The changes to the weights and biases of the network are obtained by multiplying the learning rate times the negative of the gradient. The large the learning rate, the step is the bigger. If the learning rate is made too large the algorithm will become unstable. If learning rate is set too small, the algorithm will take a long time to converge. The other parameter which should be set for sequential training is the number of the iteration that passes through the training set during training.

2- *Gradient Descent with Momentum*

This algorithm provides faster convergence in compared with the previous algorithm. In the MATLAB, the performance of this algorithm is *learngdm*. Momentum allows a network to respond not only to the local gradient, but also to recent trends in the error surface. Also, momentum allows the network to ignore small features in the error surface. Without momentum a network may get stuck in a shallow local minimum. With momentum a network can slide through such a minimum. Momentum can be added to backpropagation learning by making weight changes equal to the sum of a fraction of the last weight change and the new change suggested by the backpropagation rule. The

magnitude of the effect that the last weight change is allowed to have is mediated by a momentum constant is 0 a weight change is based solely on the gradient. When the momentum constant is 1, the new weight change is set to equal the last weight change and the gradient is simply ignored.

- **The Batch Training**

The alternative to incremental training is batch training which is invoked using the function train in the MATLAB software. There are several training algorithm which are based on bacht mode as follows:

1- Gradient Descent

In the MATLAB the bachting equivalent of the incremental function *learngd* is *traingd*, which implements the bachting form of the standard gradient descent training function. The weights and biases are updated in the direction of the negative gradient of the error function.

2- Gradient Descent with Momentum

The bacht form of gradient descent with momentum is invoked using the training function *traingdm.* This algorithm is equivalent to *learngdm*, with two exeptions. Firstly, the gradient is computed by summing the gradients calculated at each training example, and the weights and biases are only updated after all training examples have been presented. Secondly, if the new error function on a given iteration exceeds the error function on a previous iteration by more than a predefined ratio, the new weights and biases are discarded, and the momentum coefficient *mc* is set to zero.

These two aforementioned methods are often too slow for practical problems. In addition to these, there are several high performance algorithms which can converge from ten to hundred times faster. These faster algorithms fall into two main categories. The first category uses heuristic techniques, which were developed from an analysis of the performance of the standard gradient descent algorithm. For instance, one heuristic modification is the momentum technique, which was presented in the previous section. Another two more heuristic techniques are: variable learning rate backpropagation, *traingda,* and resilient backpropagation *trainrp.* The second category of fast algorithms uses standard numerical optimization techniques which three of them are: conjugate gradient, quasi-Newton and Levenberg-Marquardt techniques [56].

3- Conjugate Gradient Algorithms

The basic backpropagation algorithm adjusts the weights and biases in the gradient descent direction (negative of the gradient). This is the direction in which the error function is decreasing most rapidly. It turns out that, although the error decreases most rapidly along the negative of the gradient, this does not necessarily produce the fastest convergence. In the conjugate gradient algorithms a search is performed along conjugate directions, which produces generally faster convergence than gradient descent directions. Ref.[56] presents four different variations of conjugate gradient algorithms in detail, as the related functions in MATLAB are *traincgf, traincgp, traincgb* and *trainscg.*

4- Quasi-Newton Algorithms

Newton's method is an alternative to the conjugate gradient methods for fast optimization. The basic step of Newton's method is:

$$X_{k+1}=X_k-A^{-1}{}_k.g_k \qquad \text{(A5-1)}$$

Where A_k is the Hessian matrix (second derivatives) of the performance index at the current values of the weights and biases. Newton's method often converges faster than conjugate gradient methods. However, it is complex and expensive to compute the Hessian matrix for MFNs. There is a class of algorithms that are based on Newton's method but which do not require calculation of second derivatives of Hessian matrix. These are called quasi-Newton methods. They update an approximate Hessian matrix at each iteration of the algorithm. The update is computed as a function of the gradient. The quasi-Newton method which has been most successful in published studies is the Broyden, Fletcher, Goladfarb and Shanno update. This algorithm has been implemented in the *trainbfg* routine in the MATLAB software [56].

5- Levenberg-Marquardt Algorithm

Like the quasi-Newton algorithm, this method was designed to approach second-order training speed without having to compute the Hessian matrix. When the error function has the form of a sum of squares (as is typical in training MFNs), then the Hessian matrix can be approximated as:

$$H = J^T.J \qquad \text{(A5-2)}$$

And the gradient can be computed as:

$$g = J^T.e \qquad \text{(A5-3)}$$

Where J is the Jacobian matrix, which contains first derivatives of the network errors with respect to the weights and biases, and e is a vector of network errors. The Jacobian matrix can be computed through a standard backpropagation technique that is much less complex than computing the Hessian matrix.

The Levenberg-Marquardt algorithm uses this approximation to the Hessian matrix in the following Newton- like update:

$$X_{k+1}=X_k-[J^T.J+\mu I]^{-1}.J^T.e \qquad \text{(A5-4)}$$

When the scalar μ is zero, this is just Newton's method, using the approximate Hessian matrix. When μ is large, this becomes gradient descent with a small step size. Newton's method is faster and more accurate near an error minimum, therefore the aim is to shift towards Newton's method as quickly as possible. Thus, μ is decreased after each successful step (reduction in error function) and is increased only when a tentative step would increase the error function. In this respect, the error function will always be reduced at each iteration of the algorithm.

The main drawback of the Levenberg-Marquardt algorithm is that it requires the storage of some matrices which can be quite large for certain problems. The size of the Jacobian matrix is Q*n, where Q is the number of training sets and n is the number of weights and biases in the network. It turns out that this matrix does not have to be computed and stored as a whole. For example, if the Jacobian matrix be divided into two equal submatrices, the approximate Hessian matrix can be computed as follows:

$$H = J^T.J = \left[J_1^T, J_2^T\right]\begin{bmatrix} J_1 \\ J_2 \end{bmatrix} = J_1^T.J_1 + J_2^T.J_2 \qquad \text{(A5-5)}$$

Therefore the full Jacobian does not have to exist at one time. The approximate Hessian can be computed by summing a series of subterms. Once one subterm has been computed, the corresponding submatrix of the Jacobian can be cleared. The function *trainlm* has been provided to use this algorithm in the MATLAB software.

Related Publications

[1] J Moshtagh, R.K Aggarwal, "A new approach to fault location in a single core underground cable system using combined fuzzy logic and wavelet analysis", Developments in Power System Protection, Eighth IEE International Conference, Volume 1, 5-8 April 2004.

[2] J Moshtagh, R.K Aggarwal, "A new approach to single-phase pipe type cable modelling using conformal mapping", Universities Power Engineering Conference (UPEC), 39th International Conference, Volume 1, Sept. 2004.

[3] J Moshtagh, R.K Aggarwal, "A new approach to modelling high voltage three-phase cable using conformal mapping", IEEE Bulgarian Conference, ELMA2005, Sofia, Bulgaria, Sept. 2005.

[4] J Moshtagh, R.K Aggarwal, "A new approach to modelling high voltage three-phase pipe type cable using conformal mapping", The Eighth IASTED International Conference on Power and Energy Systems, Marina del Rey, LA USA, Oct. 2005.

[5] J Moshtagh, R.K Aggarwal, "A new approach to ungrounded fault location in a three-phase underground distribution system using combined neural networks & wavelet analysis", IEEE Canadian Conference on Electrical and Computer Engineering (CCECE), Ottawa, Canada, May 2006

A NEW APPROACH TO FAULT LOCATION IN A SINGLE CORE UNDERGROUND CABLE SYSTEM USING COMBINED FUZZY LOGIC & WAVELET ANALYSIS

J Moshtagh , R K Aggarwal

University of Bath, U.K

ABSTRACT:

Electric utilities often face the problem of finding the exact location of a fault in a distribution cable. These faults often occur at the worst possible time and cause the maximum amount of inconvenience to the utility's customers. Most fault location techniques in use today require the judgment of skilled operators can also produce less than desired results for rapid fault location and thus may inflict additional damage to the cable. When a fault occurs in a cable, there are specific relationships between fault voltage, fault current, the resulting fault impedance and location. Thus, with regard to fuzzy logic which is an effective way to map an input space to an output space, it can be employed in fault location as an efficient, economic and adaptable method (compared with other artificial intelligence systems) by simply representing the aforementioned specific relationships as "if-then" rules combined with a set of common-sense rules.
This paper presents the results of investigations into a new fault location technique using advanced signal processing technique based on wavelet technology to extract useful information and this is then applied to fuzzy logic in order to identify and locate the disturbances in a distribution system comprising of single core underground cables, through pattern recognition.

Keywords: fault location, wavelet, fuzzy logic, ATP software.

INTRODUCTION

With an increased environmental concern, there is an upsurge in demand for underground cables. It is thus very likely that more and more overhead lines comprising underground cables will be built. This inevitably leads to a demand for accurate cable fault detection and location technique. In recent years, there have been many activities in using fault generated travelling wave method for fault location (FLL) and protection. The travelling wave current-based FLL scheme in which the distance to fault is determined by the time differences measured at the sending end between an incident wave and the corresponding wave reflected from the fault have been developed for a transmission line by Gale [1]. With the advent of new technology , the ' Transient Based Protection ', a more accurate on-line FLL scheme together with a protection function, has been developed by Bo et al [2]. A new concept in cable FLL based on the fault generated high frequency travelling wave voltage signals has also been developed by Bo et al [3]. However, due to the limitation of the bandwidth of the conventional CT (up to 80 kHz), the accuracy of FLL provided by such a scheme is not satisfactory for a power cable. This paper presents a new off-line method in cable FLL based on signal processing using wavelet and intelligent system using fuzzy logic. An 11 kV pipe type single core cable including core and sheath of radial network is modelled using the ATP software; the faulted current and voltage responses are then extracted from the sending end for different faults and fault conditions. Finally, the simulated data is processed in order to locate the fault point. This paper can be divided into three basic parts as follows:
I- simulating the faulted current and voltage data under different faults and conditions using ATP
II-Extracting useful information from fault data using the wavelet transform (WT)
III-Designing a fuzzy logic system (FLS) for accurate FLL based on extracted information.

SIMULATION DATA

ATP program is a powerful tool for modelling power system transients and is used herein to calculate the voltage and current transient signals at the sending end of a cable.system Fig.(1) shows the system configuration used in the simulation; this is a practical 11 kV radial power distribution network. The cable model presented here is based on the Bergeron model. The technique is based on recognising a sudden change in voltage and current signals due to the reflection of a wave from the fault point; thus it is related to fault distance and velocity of wave propagation.

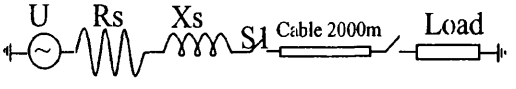

Fig. (1) The radial distribution system

The specifications of the various elements in Fig. (1) are as follows:

Source: $V_{Max\text{-}ph\text{-}G} = 8981.5$ V, $f = 50$ Hz, $X_s{:}R_s = 10$, $X_s = 2\Omega$, $R_s = .2\Omega$

Cable: pipe type single core (core+sheath), Bergeron's model, $r_{total} = 17.5$mm, length=2000m

core: $r_{in} = 0$, $r_{out} = 6.9$mm, $\mu_r = 1$, $\varepsilon_r = 2.3$ (between

core & sheath), ρ=2.3*10e-8Ω.m
sheath: r_{in}=12.5mm, r_{out}=14.5mm, μ_r=1, ε_r=8
(on the sheath), ungrounded ρ=1.2*10e-7Ω.m
pipe: r_{in} = 50mm, r_{out} = 70mm, μ_r=1, $\varepsilon_{r\text{-}in}$ = 1
ρ=5*10e-8Ω.m

With regard to the off-line method in this paper, by using switch1, inception angle is adaptable; thus it can be assumed as an arbitrary constant value during processing. In this paper, four types of fault have been considered as follows; Core open circuit (CROC), core and sheath open circuit (CRSHOC), core with sheath short circuit (CRSHSC) and core and sheath through ground short circuit (CRSHGSC).

FLL is determined by setting the length of cable in Fig(1). In order to obtain LCC (line/cable constant) file in ATP, the sampling time must be less than twice the travel time (forward & backward) for maximum modal velocity and minimum cable length under consideration. With regard to a velocity of $2.145*10^8$m/s and $\Delta t=10^{-7}$s, minimum acceptable cable length becomes 10.725m, but in order to increase Δt to 10μs in order to record voltage and current signals, print frequency option in ATP is set to 100; thus the sample frequency becomes 100KHz. In order to extract useful information of data through signal processing, the four aforementioned faults and five fault points including 200m, 700m, 1000m, 1300m and 1900m have been considered. Studies have shown that the most effective way of extracting useful information from signals is by decomposing data into modal components. Modal components are obtained from Eqs.(1,2) as follows:

$$V_{modal} = T_v^{-1}.V_{ph} \quad (1)\,,\; I_{modal} = T_i^{-1}.I_{ph} \quad (2)$$

where T_v and T_i are transformation matrices. In order to compare modal and phase components, Figs.(2,3) show voltages for CRSHGSC fault at 1.3km.

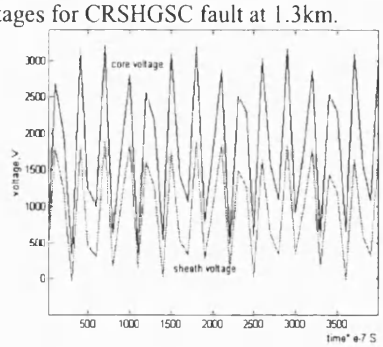

Fig.(2) phase voltage (core and sheath)

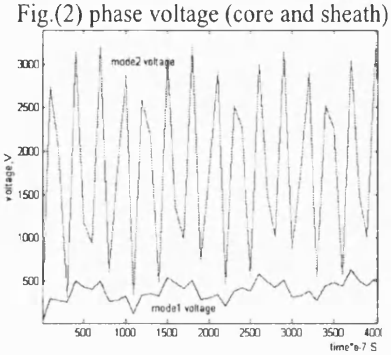

Fig(3) modal voltage (mode1 and mode2)

SIGNAL PROCESSING USING WAVELET

Methods of FLL can be broadly classified into two categories: one based on the power frequency components, and the other utilizing the higher frequency components of the transient fault signals. The latter is also referred to as travelling wave FLL method, due to its usage of travelling wave theory and shorter sampling windows. An overview of travelling wave based FLL methods can be found in Ancell and Pahalawaththa [4]. Amongst the limitations of the travelling wave methods, the requirement of high sampling rate is frequently stated. Recent developments in optical current transducers technology enable high sampling rate recording of transient signals during faults (Blake et al [5]). Availability of such broad bandwidth sampling capability facilitates better and more efficient use of travelling wave based methods for fault analysis. The correlation based FLL method introduced in Rajendra and McLaren [6], is very effective as long as the width of the time window to capture the forward moving wave is properly selected.

In this paper a new approach, based on the wavelet transform (WT) of the fault transients, is presented. WT possesses some unique features that make it very suitable for this particular application. It maps a given function from the time domain into time-scale domain. The wavelet (the basis function used in the WT), has bandpass characteristics which make this mapping similar to a mapping to the time-frequency plane. Unlike the basis function used in Fourier analysis, the wavelets are not only localized in frequency but also in time. This localization allows the detection of the time of occurrence of abrupt disturbances, such as fault transients.

Wavelet transform

In the case of WT, the analysing function, which is called wavelets, will adjust their time-widths to their frequency in such a way that higher frequency wavelets will be very narrow and lower frequency ones will be broader. This property of multi-resolution is particularly useful for analysing fault transients which localize high frequency components superposed on power frequency signals; thus, WT is better suited for analysis of signals containing short lived high frequency disturbances superposed on lower frequency continuous waveforms by virtue of this zoom-in capability (Manago and Abur [7]).

WT of sampled waveforms can be obtained by implementing the discrete WT which is given by:

$$DWT(f,m,n) = \frac{1}{\sqrt{a_0^m}} \sum_k f(k) h^*\left(\frac{n - k a_0^m}{a_0^m}\right) \quad (3)$$

where, the parameters a_0^m and $k a_0^m$ are the scaling (dilation) and translation (time shift) constant respectively, k and m being integer variables and h is the wavelet function which may not be real, as assumed in the above

equation for simplicity. In a standard discrete WT, the coefficients are sampled from the continuous WT on a dyadic grid, a_0=2, yielding $a_0^0 = 1, .a_0^{-1} = 1/2$, etc. Actual implementation of the discrete WT involves successive pairs of high-pass and low-pass filters at each scaling stage of the WT. At each detail, there is a signal appearing at the filter output at the same sample rate as the input; thus, by using a sample rate F and scaling by two (a_0=2), Eq.(4) shows the association of each scale 2^m with a frequency band containing distinct components of power signals.

$$\text{Frequency band of scale } 2^m = F/2^{m+2} \rightarrow F/2^{m+1} \quad (4)$$

Therefore, with regard to a sample rate 100kHz, as used in this paper, frequency bands for scale 1 and scale 2 are 25 kHz to 50 kHz and 12.5 kHz to 25 kHz respectively.
The choice of analysing wavelets plays a significant role in detecting and localizing types of disturbances. This is especially true when considering one or two scale signal decompositions. The next section deals with the choice of an effective mother wavelet.

Choice of mother wavelet

As mentioned earlier, choosing of mother wavelets plays an important role in localizing disturbances. The more the mother wavelet is similar to the disturbance, the higher is the localisation accuracy. With regard to the nature of faulted signals which are similar to pulses and with regard to Gaouda et al [8], the squared wavelet coefficients (WTC1) of the first resolution level have been used to detect the number of notches per cycle; the Haar wavelet is chosen as the mother wavelet in this paper with two-scale signal decomposition. The reason for choosing two scale signal decomposition is that the faulted signals are fast and short transient disturbances and scales 1 & 2 are sufficient to localize any disturbance in signals.

Extracting useful information using wavelet

As mentioned earlier, four types of fault, five different fault points, two signals (current and voltage) and two modal components are processed. Also with regard to two details, in totality, 160 different waveforms have been processed in this paper. By usage of statistics option in wavelet and data processing on details reconstructed for two scales, it has been observed that from standard deviation (SD), some useful information can be extracted, as the amount of SD for every waveform has an obvious relationship with the type and distance to fault. As an example some results are outlined in table 1.

Type of fault	Voltage-scale1-	Current-scale1-
	mode2	mode2
CROC	798-1314 AS	4.9—9 W
CRSHOC	1390-4060 AN	3.4—9.3 AS
CRSHSC	690-900 W	5.3—8.6 P
CRSHGSC	45-900 AS	10.97--15 AN

Table 1: The range of standard deviation

where, AS=ascending, AN=anticlimactic, W=wobbly, and P=parabola
The Next part of paper deals with using the results of Table 1 to design the structure of a fuzzy logic system.

FUZZY LOGIC TECHNIQUE

Fuzzy logic system (FLS) is a convenient way to map an input space to an output space with a set of common-sense rules. In almost every case, FLS can be replaced by other options, such as linear, non-linear, Neural-Network, expert system and genetic algorithm, but FLS is faster and more adaptable. Furthermore, it is conceptually easy to understand as well as is flexible, tolerant to imprecise data and is based on natural language. Also it can be built on the experience of experts and can be blended with conventional control techniques. Because of previously mentioned points, in this paper, FLS has been selected to localize and identify different types of fault. Different steps are needed in the practical design of FLS in power engineering applications. There are essentially eight major steps needed typically to perform an iterative development cycle as follows (Song and Johns [9]):
I-Define the problem and classify the existing data
II-Define input and output fuzzy sets
III-Define the linguistic variables for each fuzzy set
IV-Define behaviour of fuzzy sets (fuzzy rules)
V-Define membership function (MF) for each variable
VI-Build the system
VII-Test the system
VIII-Tune and validate the system

Step1: Table 1 (results of signal processing) shows the problem definition and classification of data.

Step2: As can be observed from Table 1, six input fuzzy sets are extracted including;IS1M2 (current-scale1-mode2), VS1M2 (voltage-scale1-mode2), VS2M2 (voltage-scale2-mode2), VS1M1 (voltage-scale1-mode1), VS2M1 (voltage-scale2-mode1) and VL2M1 (voltage-scale2-mode10. Also five output fuzzy sets can be obtained including, four types of fault (CROC, CRSHOC, CRSHGSC, CRSHSC) and DIS (fault distance), but with regard to the relationship between input fuzzy sets and type of fault, the first four of the output fuzzy sets can be eliminated.

Step3: for each mentioned fuzzy set, some linguistic variables are defined as follows:
-"SD" is defined as low (LW) and high (HI) for IS1M2 fuzzy set.
-"SD" is defined as small (S) and big (B) for VS2M1

-"SD" is defined as small (S), medium (M) and big (B) for VS1M1 fuzzy set
-"SD" is defined as short (SH) and large (LG) for VS1M2 & VS2M2 fuzzy sets.
-"SD" is defined as little (LI) and much (MU) for VL1M2 fuzzy set.
-"Distance of fault" is defined as close (C), medium (M) and far (F) for DIS fuzzy set

step4: behaviour of fuzzy sets and relationship between input fuzzy set can be defined by fuzzy rules. With regard to accurate processing of data in Table 1, following results were obtained.

If (VS1M2=LG) Then (DIS=M)
If (IS1M2=HI) Then (DIS=M)
If (VS2M1=B & VS1M2=SH & VL2M1=MU) Then (DIS=M)
If (VS2M1=S & IS1M2=LW & VS1M1=S & VS2M2=SH) Then (DIS=C)
If (VS2M1=S & IS1M2=LW & VS1M1=M & VS2M2=LG) Then (DIS=F)

Step5: MF of input/output linguistic variables are based on designer's knowledge and experience. MF for all variables in VS2M1 and VS1M1 are step functions, but for other input variables, Custom-built MF have been considered by interpolating of existing data. Finally chosen MF for output variables is a triangle function.

Step6: in order to build a FLS, there is a need to determine the techniques of fuzzification, fuzzy logic operators, implementation, aggregation and defuzzification. Fuzzification was explained in step5. Chosen fuzzy logic operators are as follows:
AND→min, OR→Max and NOT (A) →1-A
In the implementation of the technique, the input set is truncated according to the value obtained. Also in aggregation, Max and in defuzzification SOM (small of Maximum) have been chosen.

Step7: According to the existing data, the accuracy of the system was tested and suitable Custom-built MFs were allocated.

Step8: The system was tested by a random fault apart from that previously mentioned five locations and Table2 shows the results. As can be seen, the results are quite satisfactory. It should be mentioned if another MF for output variables is chosen then the values of error are changed (increased or decreased). In fact the most important part of FLS is the choice of MF. For example increasing the number of initial data and interpolating existing data in custom MF plays a significant role in reducing the error.

Type of fault	Real DIS 120 m	Real DIS 470 m	Real DIS 830 m	Real DIS 1120 m	Real DIS 1680 m
CROC	147	462	882	1130	1620
CRSHOC	105	530	860	1160	1760
CRSHSC	84	441	861	1160	1720
CRSHGSC	147	483	860	1130	1680

Table2 results of test

CONCLUSIONS

This paper presents a new approach to fault location for a radial cable power distribution network. In the first instance, a pipe type single core cable including core and ungrounded sheath is modelled in LCC support routine of the ATP software, and voltage and current signals are obtained at the sending end. The transient signals are then decomposed into their modal components. At the second stage, useful information is extracted by signal processing using the wavelet transform and finally the fault position is localized through a fuzzy logic system. The results presented show a satisfactory performance in term of accuracy, more so in view of the fact that the overall cable length involved is relatively short (2000m). Results show a good approach and it can be confirmed as an accurate and acceptable method in fault location in cable systems.

REFERENCE

1-P F Gale, IEE, Fault location based on travelling wave, Vol.388, 55-59
2-Z Q Bo, A T Johns, R K Aggarwal, 1995, A new non unit protection scheme based on fault generated high frequency current signals, APSCOM-95, Hong Kong
3- Z Q Bo, A T Johns, R K Aggarwal, P J Moore, 1996 IEEE, Accurate fault location and protection scheme for power cable using fault generated high frequency voltage transients, 777-780
4-G B Ancell, N C Pahalawaththa, 1992 IEE, Effects of frequency dependence and line parameters on single ended travelling waved based fault location schemes, Vol.139, No.4, 332-342
5- J Blake, P Tantaswadi, and R T de Carvalho, 1996 IEEE, In-line sagnac interferometer current sensor, Vol.11, No.1, 116-121
6- S Rajendra, and P G Mclaren, 1985 IEEE, Travelling wave techniques applied to the protection of Teed circuit; principle of travelling wave techniques, Vol.PAS-104, No.12, 3544-3550
7- F H Magnago, and A Abur, 1998 IEEE, Fault location using wavelets, Vol.13, No.4, 1475-1480
8- A M Gaouda, S H Kanoun, M M A Salama, and A Y Chikhani, 2002 IEE, Wavelet-based signal processing for disturbance classification and measurement, Vol.149, No.3, 310-318
9- Song, Johns, 1999 Power Engineering Journal, Application of Fuzzy Logic in power systems-part3 Example applications, 97-103

A NEW APPROACH TO SINGLE-PHASE PIPE TYPE CABLE MODELLING USING CONFORMAL MAPPING

J Moshtagh , R K Aggarwal
Bath University, U.K

R.K.Aggarwal@bath.ac.uk

ABSTRACT

The increasing use of cable systems and the growing levels of capacity make the analysis of wave propagation and determining an accurate model for cables an important branch in Electrical Power Engineering. In particular, dealing with accurate determination of the per unit length cable series impedance Z and it's per unit length shunt admittance Y can play an important role. For example, the results of this analysis can lead to finding an accurate method for the transient state, such as fault location. The EMTP as a powerful software tool in the transient state obtains Z and Y on the basis of certain assumptions and approximations being made. This paper presents a new method using conformal mapping (CM) in order to modify impedance and admittance per unit length in a single-phase pipe type cable in EMTP. With this approach, both the constant-frequency and frequency-dependent parameters have been studied. In order to have a comparison between Z and Y in EMTP and CM methods, a practical radial single-phase pipe type cable is analysed. The results confirm the validity and higher accuracy of the new proposed method.
Keyword: conformal mapping, cable modelling, EMTP, pipe type cable.

1- Introduction:

The use of underground systems has increased extensively in recent years. Nowadays, increased competition due to the deregulation of the power industry and the desire to provide better services to the customers having more and more sensitive loads, makes the development of faster, reliable and accurate fault location methods for distribution systems an important issue. One of the most important factors in accurate fault location is to develop an accurate model of a cable which then needs to be integrated into an overall distribution system model; this is essentially to determine accurately, the per unit length impedance and admittance of a network which determine the relationships between current, voltage, attenuation and velocity of travelling wave in the transient state.

A number of models have been proposed to date. These models can be classified into the following two main groups; time domain and frequency domain model. With regard to the advantages and disadvantages of mentioned groups, in [1] the presented model belongs to the class of time-domain, frequency-dependent models. It overcomes the main limitations of existing time-domain cable models, that is, it takes into account the frequency dependence of the modal transformation matrices. A general method based on constrained optimization for evaluating the modal transformation matrices for overhead transmission lines and underground cables have been developed and tested in [2]. The method guarantees in the calculation, the smoothness of all of the eigenvectors and modal characteristic impedances over a wide range of frequencies. In many analyses of line parameters, approximations ignoring eddy currents in conductors can be used. But in close conductors, the AC parameters vary significantly with frequency and conductor spacing. In [3] and [4], the distributions of current density due to proximity effect and skin effect are determined analytically by solving the differential equation for penetration of currents in the conducting material and appropriately applying boundary conditions. In the majority of methods such as [3], and [4], μ has been considered constant. But an improved modelling of the nonlinear B-H curve of ferromagnetic material is introduced in [5], as the B-H curve is represented by a Fourier series, based on a set of measurement data. In order to determine μ throughout the pipe, in [6], the magnetic field intensity in each element of the pipe is solved using finite-element method. In [7] the cable is divided into a large number of cells as the field is assumed to be constant within each cell and a linear integration is performed for the voltage using Finite-Difference Time Domain (FDTD) method. In [8] the parameters of the cable model are calculated by analyzing the behaviour of the short circuit impedance (z_{sc}) and open circuit impedance (z_{oc}) over a broad range of frequencies. Although the use of semiconductors in a power cable for underground transmission and distribution has been increased, the effects of these are not considered on the cable parameters, such as propagation constant and wave velocity. In [9] with some calculations and other parameters the effects of semi conducting layers has been taken into account.

Suggested equations for impedance and admittance in a pipe type cable in EMTP include infinite series formulations of the flux linkage and the proximity effects. It is due to that the conductors are positioned off centre within the pipe. With regard to CM's ability in transforming an isotropic region into a symmetrical and simpler region, in this paper the employed equations for

Z and Y within EMTP are simplified and they become more accurate. In the first instance, EMTP method of calculating Z and Y are reviewed followed by the attributes of CM and then, based on ref. [10], simplification of Z and Y is carried out, finally, a practical radial single-phase pipe type cable is analysed.

2- Single-phase cable model in EMTP:

There are a vast variety of cables in the power distribution system. Thus it is not possible to develop one generic computer program, which can calculate the parameters of all types. Because XLPE insulated cable is now well established in most European countries at low voltages and up to 35 kV in the following, the coaxial single-core cable is analysed. This type of cable consists of tubular conductors inside a metallic sheath and Armour with insulation between them. In this model, series impedances and shunt admittances per unit length are represented by the following equations [11]:

$$-\begin{bmatrix} \frac{dv_{core}}{dx} \\ \frac{dv_{sheath}}{dx} \\ \frac{dv_{armour}}{dx} \end{bmatrix} = \begin{bmatrix} z_{cc} & z_{cs} & z_{ca} \\ z_{sc} & z_{ss} & z_{sa} \\ z_{ac} & z_{as} & z_{aa} \end{bmatrix} \times \begin{bmatrix} I_{core} \\ I_{sheath} \\ I_{armour} \end{bmatrix} \quad (1)$$

Where v_{core} = voltage from core to ground,

v_{sheath} = voltage from sheath to ground and

v_{armour} = voltage from Armour to ground

According to [11], each impedance in Z matrix depend on $Z_{insulation}$, $Z_{tube\text{-}in}$, $Z_{tube\text{-}out}$ and $Z_{tube\text{-}mutual}$ as follows:

$$z_{insulation} = \frac{1}{2\pi} j\omega\mu_o\mu_r \ln\left(\frac{r}{q}\right) \quad (2)$$

μ_r = permeability of insulation

$\mu_o = 2*10^{-4}$ H/Km

r=outside radius of insulation (or tube)

q=inside radius of insulation (or tube)

$$z_{tube-in} = \frac{\rho m}{2\pi qD}\left[I_0(mq)*k_1(mr)+k_o(mq)*I_1(mr)\right] \quad (3)$$

$$z_{tube-out} = \frac{\rho m}{2\pi rD}\left[I_0(mr)*k_1(mq)+k_o(mr)*I_1(mq)\right] \quad (4)$$

$$z_{tube-mutual} = \frac{\rho}{2\pi rD} \quad (5)$$

with

$$D=I_1(mr)*k_1(mq)-I_1(mq)*k_1(mr) \quad (6)$$

$$m=\sqrt{j\omega\mu/\rho} \quad (7)$$

Where the I_0,I_1,K_0 and K_1 are Bessel functions.

For the current changes along the cable:

$$-\frac{d}{dx}\begin{bmatrix} I_{core} \\ I_{sheath} \\ I_{armour} \end{bmatrix} = \begin{bmatrix} Y_1 & -Y_1 & 0 \\ -Y_1 & Y_1+Y_2 & -Y_2 \\ 0 & -Y_2 & Y_2+Y_3 \end{bmatrix} * \begin{bmatrix} v_{core} \\ v_{sheath} \\ v_{armour} \end{bmatrix} \quad (8)$$

With $Y_i=G_i+j\omega C_i=j\,2\pi\omega\varepsilon_0\varepsilon_r/\ln(r/q)$ (9)

$$\varepsilon_r = 2.5+\frac{0.94}{\left(1+j\omega 6*10^{-9}\right)^{.315}} = \varepsilon' - j\varepsilon'' \quad (10)$$

The support routine cable constants now assume $\varepsilon''=0$ and ε' being constant. The dielectric losses are of little importance for the attenuation [11], and using a constant ε' with $\varepsilon''=0$ should therefore give reasonable answers in most cases. Compared to the geometry of the single-core cable, the geometry of the pipe-type cable is more complex for two reasons:

a) The single-core cables inside the pipe are not concentric with respect to the pipe.

b) The steel pipe is magnetic and subject to current-dependent saturation effects.

Depending on the thickness of pipe, the two states can be evaluated; infinite and finite pipe thickness. But with regard to Eq. (11), the depth of penetration in the pipe becomes:

$$d_{earth} = \frac{\sqrt{2}}{|m|} = 503*\sqrt{\frac{\rho_{earth}(\Omega m)}{\mu_r f(Hz)}} \quad (11)$$

and with typical values of $\rho_{pipe}=5*10^{-8}$, f=50 Hz and μ_r=200, d will be less than 1.5mm. Thus in this paper only infinite pipe thickness is analysed. In this case, no voltage will be induced on the outside of the pipe and consequently, the pipe is the return path instead of earth Fig(1).

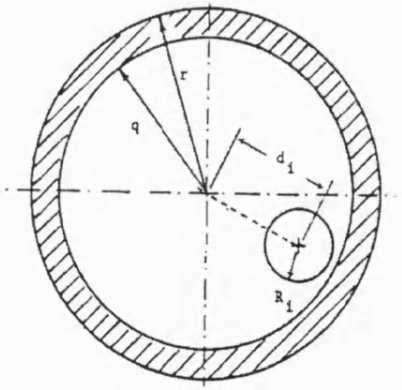

Fig.1- pipe type single phase cable

The self impedance of the loop between the Armour and the pipe consists of three terms. The first term $z_{armour\text{-}out}$ is the same as Eq.(4), but the second term becomes:

$$z_{insulation} = \frac{j\omega\mu_0}{2\pi}\ln\left[\frac{q}{R_i}*\left(1-\left(\frac{d_i}{q}\right)^2\right)\right] \quad (12)$$

And the third term is equal to:

$$z_{pipe-in} = \frac{j\omega\mu_0\mu_r}{2\pi}\left[\left(\frac{k_0(mq)}{mqk_1(mq)}\right)+\left(2*\sum_{n=1}^{\infty}\left(\frac{d_i}{q}\right)^{2n}*\frac{k_n(mq)}{n\mu_r k_n(mq)-mqk'_n(mq)}\right)\right] \quad (13)$$

With m from Eq.(7), and $\mu=\mu_o*\mu_r$=permeability of the pipe, k_i=modified Bessel function of the second kind of order I, k_i'=derivative of k_i and also:

$$\left[y_{phase}\right] = j\omega\left[P_{phase}\right]^{-1} \quad (14)$$

Where $\left[P_{phase}\right]$ is a potential coefficient matrix given as:

$$[P_{phase}]=\begin{bmatrix} p_1+p_2+p_3 & p_2+p_3 & p_3 \\ p_2+p_3 & p_2+p_3 & p_3 \\ p_3 & p_3 & p_3 \end{bmatrix}+[P_{aa}] \qquad (15)$$

With $p_i=\frac{1}{c_i}$ and c_i is the same as Eq.(9) with G=0, and also $[P_{aa}]$ in the second term is a 3*3 matrix with 9 equal elements as follows:

$$p_{aa}=\frac{1}{2\pi\varepsilon_0\varepsilon_r}\ln\left[\frac{q}{R_i}*\left(1-\left(\frac{d_i}{q}\right)^2\right)\right] \qquad (16)$$

The admittance matrix is then found by inverting $[p_{phase}]$, as has been shown in Eq.(14).

The new approach for more accurate cable model is on the basis of simplifying and amending Eqs.(12,13,16) by using CM. Aforementioned Equations have been obtained based on [10],[12].

3- The conformal mapping method

In order to modify Z and Y, in this paper Eqs. (12,13,16) are modified in single conductor pipe type cable by transforming eccentric circles into concentric circle by using CM method. It should be mentioned that, for a limited range of eccentric conductor locations, this transformation has been done by achieved by CM [13]. However, firstly the depth of penetration of pipe and the thickness of outer layer of conductor (e.g. armour) have been neglected and secondly the employed conformal transformation has some limitations, as the distance between centre of two eccentric circles depends on the radius of circles. The transformation employed is [13]:

$$W=\frac{Z-a}{Z+a} \qquad (17)$$

In this paper submitted transformation has not got two mentioned limitations. This is essentially to avoid any complexities and approximations (as in other methods) in determining Z and Y.

As a first step, a conformal transformation is found that transfers eccentric circles into concentric circles. First transformation is: $Z=Z_1/R_1$ that transforms Fig. (2) into Fig. (3), therefore:

$$x_1=\frac{d+q}{R_1} \quad \& \quad x_2=\frac{d-q}{R_1} \qquad (18)$$

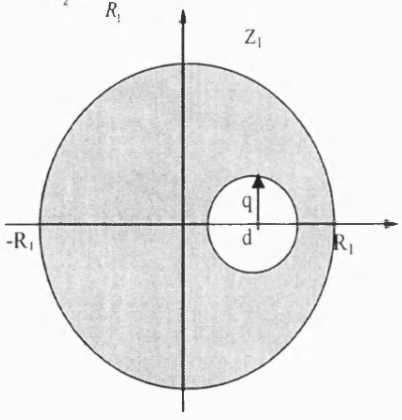

Fig.2- Pipe type single core cable

Second transformation is: $W_1=\frac{Z-a}{aZ-1}$ (19).

This transformation transforms Fig. (3) into Fig. (4).

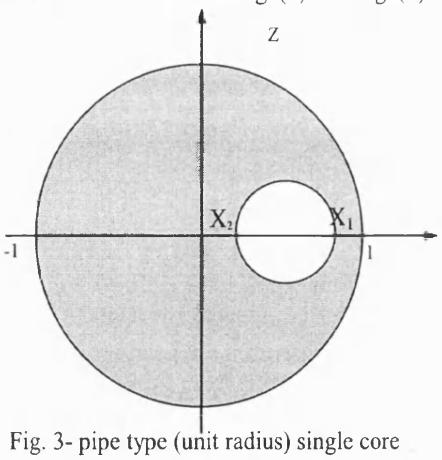

Fig. 3- pipe type (unit radius) single core

Also the transformation $W_2=\ln W_1$ transforms Fig.(4) to two parallel line.

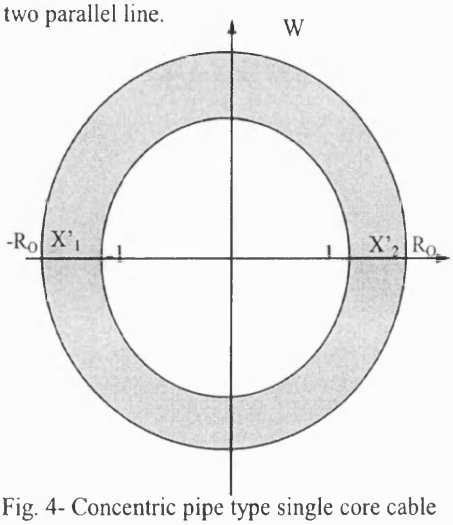

Fig. 4- Concentric pipe type single core cable

As Figs. (3) & (4) show the transformation $W_1=\frac{z-a}{az-1}$ transforms x_1 to $-R_o$ and x_2 to R_o ; Thus it follows:

$$R_o=\frac{x_2-a}{ax_2-1} \quad \text{and} \quad -R_o=\frac{x_1-a}{ax_1-1}$$

And hence:

$$a=\frac{1+x_1x_2+\sqrt{(1-x_1^2)(1-x_2^2)}}{x_1+x_2} \qquad (20)$$

$$R_o=\frac{1-x_1x_2+\sqrt{(1-x_1^2)(1-x_2^2)}}{x_1-x_2} \qquad (21)$$

And also from two parallel lines that are a cross section of two parallel plate, capacitance per unit length is:

$$C_{equal}=\frac{\varepsilon_o.A}{D}=\frac{2\pi\varepsilon_o}{\ln R_o} \text{ (F/m)} \qquad (22)$$

With regard to Fig. (5) the capacitance between circles C_1 & C_3 is deduced from Eq. (22) and the capacitance between circles C_1 & C_2 becomes: $C_{1\_2}=\frac{2\pi\varepsilon_o}{\ln(r/q)}$ (23)

As r is radius of circle C2 and q is radius of circle C1.

Therefore the capacitance between circles C_2 & C_3 becomes: (24)

$$C_{2\_3} = \frac{2\pi\varepsilon_o}{\ln\frac{R_0 q}{r}}$$

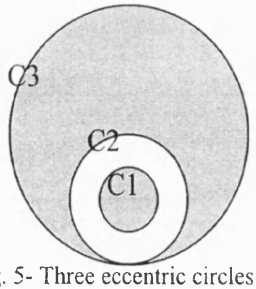

Fig. 5- Three eccentric circles

The radius of circle C_3 is unit. Since the capacitance is considered ideal, it is related to inductance at infinite frequency by[10]: $C=(\mu_o.\varepsilon_o)/L$ (25)

Thus Eqs. (12) & (16) become Eqs. (26) and (27) respectively (it should be noted that the permittivity between circles C1 and C2 is $\varepsilon_o\varepsilon_r$ and between circles C2 and C3 is ε_o):

$$Z_{insulation} = \frac{j\omega\mu_0\mu_r \ln(r/q)}{2\pi} + \frac{j\omega\mu_0 \ln(R_o.q/r)}{2\pi} \quad (26)$$

$$P = \frac{\ln[(r/q)*(R_o.q/r)^{\varepsilon_r}]}{2\pi\varepsilon_o\varepsilon_r} \quad (27)$$

If the depth of penetration of pipe and the thickness of the outside of conductor is taken into account, the aforementioned transformation transforms Fig.(6) into Fig.(7). As it can be observed, inside of pipe is transformed to outside of pipe and hence $Z_{pipe\text{-}in}$ is obtained from Eq. (4) by replacing r (the outside radius of pipe) to N (scale factor) and q (the inside radius of pipe) to N.r. r has been shown in Fig.(7). Thus $Z_{pipe\text{-}in}$ instead of Eq.(13) becomes:

$$z_{pipe-in} = \frac{\rho m}{2\pi N D}\left[I_O(mN)*k_1(mNr) + k_o(mN)*I_1(mNr)\right] \quad (28)$$

where D is: $D=I_1(mN)*k_1(mNr)-I_1(mNr)*k_1(mN)$ (29)

Also, because the inner conductor is transferred to outer conductor, thus $Z_{conductor\text{-}out}$ is obtained from the Eq.(3) by replacing q (outside radius of conductor) to $N.R_0$ and r (inside radius of conductor) to N.rr; rr has been shown in Fig.(7). Therefore $Z_{conductor\text{-}out}$ becomes:

$$z_{conductor-out} = \frac{\rho m}{2\pi N.R_0 D}\left[\begin{matrix} I_O(mN.R_0)*k_1(mN.rr) + \\ k_o(mN.R_0)*I_1(mN.rr) \end{matrix}\right] \quad (30)$$

where D is:

$D=I_1(m.N.rr)*k_1(m.N.R_0)-I_1(m.N.R_0)*k_1(m.N.rr)$ (31)

It should be noted that when Eq.(30) be used, obtained radii of CM have to be used in Eq.(5). Also the scale factor N is determined as follows.

Although we can see from Fig.(7), that all circles are not completely concentric, since the depth of penetration in pipe at power frequency is less than 1.5mm, and the thickness of the armour or sheath is much smaller than its outer radius, Fig.(7) is a good approximation of four concentric circles, and is more accurate than neglecting the effect of depth of penetration in pipe and thickness of armour (or sheath).

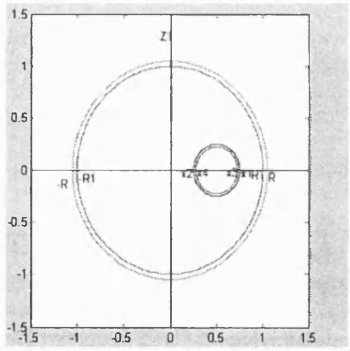

Fig. 6- Two eccentric circles (comprised thickness)

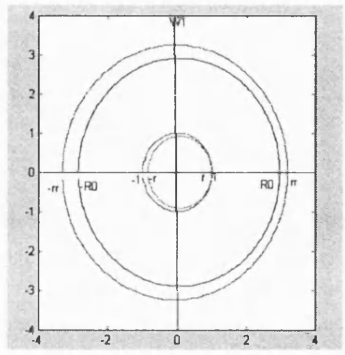

Fig. 7- CM transformation of Fig. (6)

In order to find the maximum matching between four circles in Fig.(7), and consequently the most accurate result in CM model, a coefficient k is introduced in the transformation. Thus we have: $W_1 = \frac{Z-ka}{kaZ-1}$; k causes the transformation of inner circle of conductor to be concentric with unit circle. If the thickness of conductor is b, k becomes:

$$k = M + \sqrt{M^2 - \frac{1}{a^2}} \quad (32)$$

as: $$M = \frac{(x_1-b)(x_2+b)+1}{a(x_1+x_2)} \quad (33)$$

Because of such transformations which have been used to transform Fig.(6) to Fig.(7), with an affect on scaling of Z_{pipein} [12], a scale factor or metric coefficient N should be taken into account. N is the ratio of distances in the original Z_1-plane to the corresponding distances in the transformed W_1-plane. Hence it is defined by:

$$N = \left|\frac{dZ_1}{dW_1}\right| = \left|\frac{dZ_1}{dZ}.\frac{dZ}{dw_1}\right| \quad (34)$$

In order to find the absolute value of dZ/dW_1, W_1 is expressed as: $W_1=\cos\theta + j\sin\theta$; because the radius of the pipe in W_1-plane is unit, it leads to the following:

$$\left|\frac{dZ}{dW_1}\right| = \left|\frac{(ka)^2-1}{1+(ka)^2-2ka\cos\theta}\right| \quad (35)$$

Thus: $$N = R_1\left|\frac{(ka)^2-1}{1+(ka)^2-2ka\cos\theta}\right| \quad (36)$$

N is seen to be a function of θ. With N appearing dominantly in the denominator of Eqs.(28) & (30), the average values of 1/N should appear where point by point evaluations of N are not undertaken [12]. In this

case, the cosθ term vanishes so that the N takes the form:

$$N = R_t \left| \frac{(ka)^2 - 1}{(ka)^2 + 1} \right| \quad (37)$$

In order to have a comparison between the attained Z and Y via the equations in the EMTP and CM methods, a radial network has been considered. Specifications of elements in the network are as follows:

Source: $11kV_{rms}$, f=50Hz, R_s=1Ω, X_s=0.7Ω
Switch1: closure time=.1ms (connection to source)
Switch2: closure time=1.5ms (short circuit)
Load : R_L=12Ω, X_L=10Ω
Cable: core+sheath ungrounded, length=1500m
Core: r_{in}=0, r_{out}=6.9mm, $\rho=2.3*10^{-8}$ Ω.m, μ_r=1
Sheath: r_{in}=12.5mm,r_{out}=14.5mm, $\rho=17*10^{-8}$ Ωm, μ_r=1
Insulator between core and sheath: thickness=5.6mm, ε_r=2.3
Insulator on the sheath: thickness=3mm, ε_r=8
Pipe: r_{in}=5cm, r_{out}=7cm, $\rho=5*10^{-8}$ Ω.m, μ_r=1

Because of the limitation on space as well as the importance of the voltage compare with current, only the results of voltages are shown in this paper. Figs (8,9) show voltage after the switch1 using EMTP and CM methods, respectively.

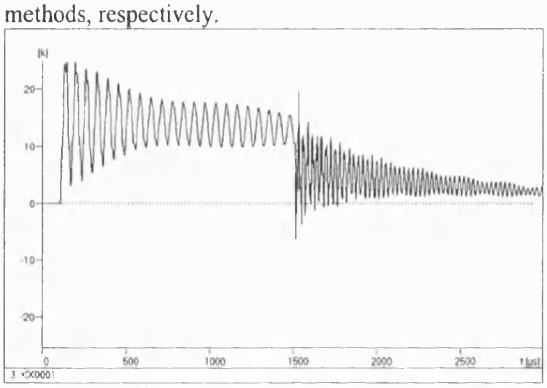

Fig. 8- voltage EMTP model

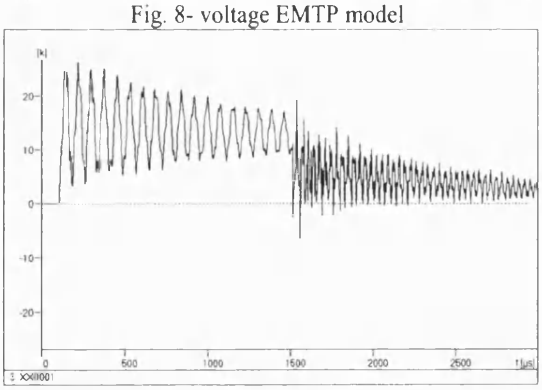

Fig. 9- voltage CM model

Table 1 shows such cable data which is employed in .lib file in ATP, as it determines cable specifications in the aforementioned network.

Table 1- mode's specification

	R modal Ω/m	Z_s modal Ω	Velocity m/s
EMTP mode1	6.4247E-04	1.4686E+01	4.90295E+07
EMTP mode2	1.4774E-04	7.09619E+01	1.71645E+08
CM mode1	5.732E-04	1.1193E+01	4.5937E+07
CM mode2	2.7003E-04	6.5265E+01	1.3660E+08

R is the modal resistance, Z_s is the modal surge impedance and v is velocity of propagation, in $vintage,1 (a function in EMTP)

It should be noted that because of the ambiguity in the eigenvectors, modal impedances and admittances only make sense if they are specified together with the eigenvectors used in their calculation. Thus the comparison between velocities of propagation in aforementioned methods in Table 1 is important. All curves of voltage in CM model are computed by replacing modal parameters of CM model in .lib file of ATP.

Since Eq.(13) is more accurate when the radius of cable is much smaller than the inner radius of the pipe, aforementioned example is repeated with $r_{pipe\text{-}in}$=.2m and $r_{pipe\text{-}out}$=.25m. The results are shown in Figs.(10) to (11) & Table 2. From a comparison between the two examples, it can be observed that the CM methods are very close to ATP model in example 2. Since the more the ratio between the inner radius of pipe and the radius of cable, the more accurate results are obtained using EMTP [11], it can be concluded that CM methods are more accurate and simpler. In totally, with being close the results, especially in second example, it can be confirmed the validity and more accuracy of new methods in single-phase pipe type cable.

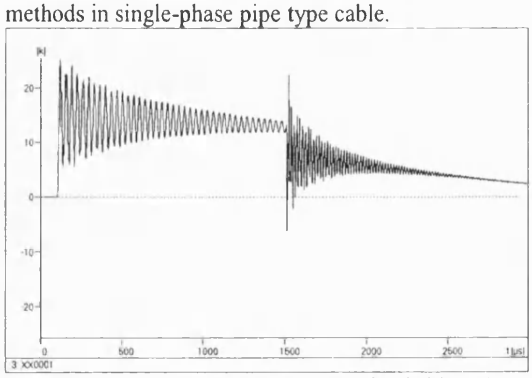

Fig. 10- voltage EMTP model (pipe is bigger)

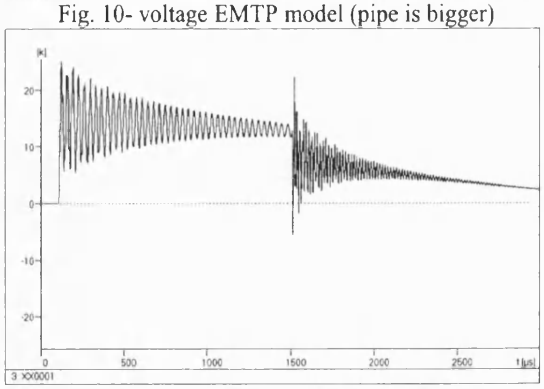

Fig. 11- voltage CM model (pipe is bigger)

Table 2- mode's specification (pipe is bigger)

	R modal Ω/m	Z_s modal Ω	Velocity m/s
EMTP mode1	5.96616E-04	1.81472E+01	5.45899E+07
EMTP mode2	1.31645E-04	1.81158E+02	2.55470E+08
CM mode1	4.54200E-04	1.38130E+01	5.45900E+07
CM mode2	1.81330E-04	2.44560E+02	2.54260E+08

The accurate representation of single-phase pipe type cable with frequency-dependent of impedances, and admittances is shown in Figs.(12) and (13). With regard to the results, the conformity and validity of results in the new model can be confirmed.

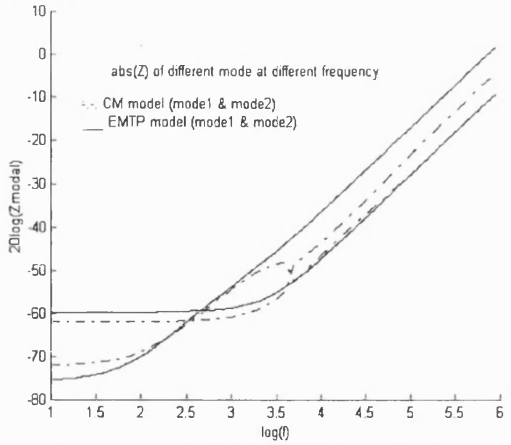

Fig. 12- Amplitude of Z in different frequencies

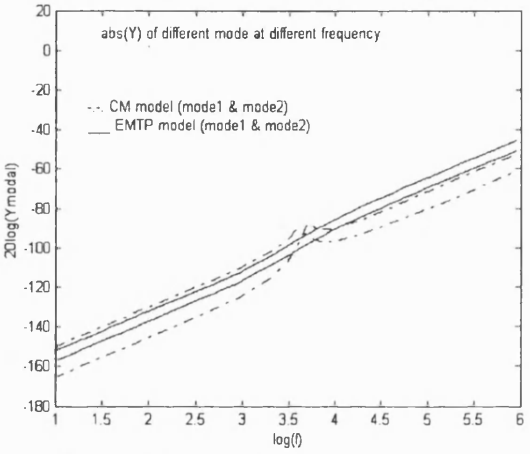

Fig. 13- Amplitude of Y in different frequencies

4-Conclusion

This paper presents a new approach to Z and Y for a single-phase pipe type cable using conformal mapping method. Z and Y in the EMTP model involve infinite series due to eccentric circles and also they are complex with some approximations. With regard to CM ability to transform eccentric circles into concentric circles some of the mentioned problems can be solved. The results show the validity and more accuracy of new method, thus CM method can be submitted as a more accurate and simpler method.

5-References

1-L.Marti, "simulation of transients in underground cables with frequency-dependent modal transformation matrices",IEEE transaction on power Delivery, July 1988

2-T.T.Nguyen & H.Y.Chan "evaluation of modal transformation matrices for overhead transmission lines and underground cables by optimization method", IEEE transaction on power Delivery, JAN.,2002

3-J.A.Tegopoulos & E.E.Kriezis, "Eddy current distribution in cylindrical shells of infinite length due to axial current", Part I: shells of one boundary, IEEE, PAS, 1971

4-J.A.Tegopoulos & E.E.Kriezis, "Eddy current distribution in cylindrical shells of infinite length due to axial current", Part II: shells of finite thickness, IEEE, PAP, 1971

5-G.Liu, "Improved modelling of the nonlinear B-H curve and its application in power cable analysis", IEEE Transaction on magnetic, JULY 2002

6-X.B.Xu & G.Liu & P.Chow, "A finite-element method solution of the zero-sequence impedance of underground pipe-type cable", IEEE transaction on power Delivery, JAN.,2002

7-D.L.Paul, C.J.Railton & I.J.Craddock, "Full-wave modelling of coaxial cables by FDTD technique", electronics letters 10_{th} Oct. 2002 vol.38 no.21

8-A.F.Moreira. T.A.Lipo, G.Venkataramanan & S.Bernet, "High-frequency modelling for cable and induction motor over voltage studies in long cable drives", IEEE Transaction on industry applications, Sep./Oct. 2002

9-W.L.Weeks & Y.M.Diao, "wave propagation characteristics in underground power cable", IEEE, PAS, Oct. 1984

10-G.W.Brown & R.G.Rocamora, "surge propagation in Three-phase cables", Part I –unsaturated pipe, IEEE ,PAS , Jun./Feb. 1976

11-EMTP Theory book

12- A. Ametani, "A general formulation of impedance and admittance of cables", IEEE, PAS, May/June 1980

13- R. Schinziger & A. Ametani, "surge propagation characteristics of pipe enclosed under ground cables". IEEE, PAS, Sept. 1978

A NEW APPROACH TO MODELLING HIGH VOLTAGE THREE-PHASE CABLE USING CONFORMAL MAPPING

J Moshtagh , R K Aggarwal
Bath University, U.K

R.K.Aggarwal@bath.ac.uk

Abstract: The increasing use of cable systems and the growing levels of capacity make the analysis of wave propagation to determine an accurate model for cables an important branch in Electrical Power Engineering. In particular, accurate determination of the per unit length cable series impedance Z and it's per unit length shunt admittance Y can play an important role. For example, the results of this analysis can lead to finding an accurate method for fault location/detection under transient fault conditions. In this respect, the EMTP is a powerful software tool for modelling the transient phenomena in power system network. However, in the modelling of underground cables, in particular the per unit length series impedance Z and the per unit length shunt admittance Y, it makes certain assumptions and approximations; this inevitably gives rise to inaccuracies when simulating the voltage and current waveforms under fault conditions. This paper presents a new approach to the modelling of the cable's Z and Y parameters using conformal mapping (CM), which avoids the assumptions and approximations associated with the EMTP software thereby increasing the simulation accuracy. In order to make a comparison between the Z and Y parameters and in the simulated transient voltage and current signals in the EMTP and CM methods, a practical radial three-phase pipe type cable is analysed. The results confirm the validity and higher accuracy of the new proposed method.
Keyword: conformal mapping, cable modelling, EMTP, pipe type cable

1- Introduction:

There has been upsurge in the usage of underground distribution systems in recent years. In this respect, increased competition due to the deregulation of the power industry and the demand to provide better service to the customers having increasingly sensitive loads, makes the development of reliable and accurate fault location methods for distribution systems an important issue. One of the most important factors in accurate fault location is to develop an accurate model of a cable which then needs to be integrated into an overall distribution system model. Essentially, there is a need to determine accurately, the per unit length impedance and admittance of a cable, which in turn determine the relationships between current, voltage, attenuation and velocity of travelling wave in the transient state.

A number of models have been proposed to date. These models can be classified into the following two main groups; time domain and frequency domain models. With regard to the advantages and disadvantages of these techniques, in reference [1], the presented model belongs to the class of time-domain, frequency-dependent models. It overcomes the main limitations of existing time-domain cable models, that is, it takes into account the frequency dependence of the modal transformation matrices. A general method based on constrained optimization for evaluating the modal transformation matrices for overhead transmission lines and underground cables has been developed and tested in reference [2]. The method guarantees in the methodology adopted, the smoothness of all the eigenvectors and modal characteristic impedances over a wide range of frequencies. In many analyses of overhead line parameters, approximations ignoring eddy currents in conductors can be assumed. However, in close conductors, such as underground cables, the AC parameters vary significantly with frequency and conductor spacing. In references [3] and [4], the distributions of current density due to proximity effect and skin effect are determined analytically by solving the differential equation for penetration of currents in the conducting material and appropriately applying boundary conditions. In the majority of methods such as these in references [3], and [4], permeability μ has been considered constant. An improved model of the nonlinear B-H curve of ferromagnetic material is introduced in reference [5]; the B-H curve is represented by a Fourier series, based on a set of measurement data. In order to determine μ throughout the pipe, in reference [6], the magnetic field intensity in each element of the pipe is solved using finite-element method. In reference [7], the cable is divided into a large number of cells as the field is assumed to be constant within each cell and a linear integration is performed for the voltage using Finite-Difference Time Domain (FDTD) method. In reference [8], the parameters of the cable model are calculated by analyzing the behaviour of the short circuit impedance (z_{sc}) and open circuit impedance (z_{oc}) over a broad range of frequencies.

It is apparent that the conductors in a three-phase cable are positioned off centre within the pipe or armour and it is Due to this that some estimations and approximations are made in the EMTP model; a direct consequence of the latter is that the mathematical representation of the impedance and admittance in a pipe type cable in the EMTP software include infinite series formulations of the flux linkage and the proximity effects. With regard to CM's ability to transform an isotropic region into a symmetrical and much simpler region, in this paper the mathematical equations for the

calculation of employed Z and Y within EMTP take a simplified form and increase the accuracy. Herein in the EMTP method for calculating Z and Y is firstly reviewed followed by out ling the attributes of CM and then, based on ref. [9], simplification of the mathematical equation for calculating Z and Y is carried out. Finally, a practical radial three-phase pipe type cable is analysed and a compared made between the results attained using the EMTP and CM models.

2- Three-phase cable model in EMTP:

There is a vast number of different cables in a power distribution system. Thus it is not possible to develop one generic computer program, which can calculate the parameters of all types. However, in view of the that an XLPE insulated cable is now widely used in most European countries at low voltages and up to 35 kV herein, only the coaxial three-phase cable is analysed. This type of cable consists of three tubular conductors inside a metallic sheath and are placed inside the Armour symmetrically with insulation between them. It is apparent that a three-phase cable is a symmetrical case of three-conductor pipe type cable, the only difference being that instead of pipe, armour is used.

The following assumptions are made in the EMTP model:

1. The displacement currents and dielectric losses are neglected.
2. The finite thickness of the pipe wall is neglected since current penetration is assumed to be confined under transient conditions.
3. The pipe is considered to have constant permeability.

Because the mutual impedances between the three outer loops are taken into account, thus according to reference [10], Z_{phase} matrix in a three-phase cable becomes:

$$[z_{phase}]=\begin{bmatrix} [z_{self-a}] & [z_{mutual-a-b}] & [z_{mutual-a-c}] \\ [z_{mutual-b-a}] & [z_{self-b}] & [z_{mutual-b-c}] \\ [z_{mutual-c-a}] & [z_{mutual-c-b}] & [z_{self-c}] \end{bmatrix} \quad (1)$$

Each impedance in $[Z_{self}]$ depends on $Z_{insulation}$, $Z_{tube\text{-}in}$, $Z_{tube\text{-}out}$ and $Z_{tube\text{-}mutual}$ as follows:

$$z_{insulation} = \frac{1}{2\pi} j\omega\mu_o\mu_r \ln(r/q) \quad (2)$$

μ_r = permeability of insulation

$\mu_o = 2*10^{-4}$ H/Km

r=outside radius of insulation (or tube)

q=inside radius of insulation (or tube)

$$z_{tube-in} = \frac{\rho m}{2\pi qD}\left[I_O(mq)*k_1(mr)+k_o(mq)*I_1(mr)\right] \quad (3)$$

$$z_{tube-out} = \frac{\rho m}{2\pi rD}\left[I_O(mr)*k_1(mq)+k_o(mr)*I_1(mq)\right] \quad (4)$$

$$z_{tube-mutual} = \rho/(2\pi rqD) \quad (5)$$

Where, $D=I_1(mr)*k_1(mq)-I_1(mq)*k_1(mr)$ (6)

And: $m=\sqrt{j\omega\mu/\rho}$ (7)

Where the I_0,I_1,K_0 and K_1 are Bessel functions.

Also: $$[z_{mutual-a-b}]=\begin{bmatrix} z_{ab} & z_{ab} & z_{ab} \\ z_{ab} & z_{ab} & z_{ab} \\ z_{ab} & z_{ab} & z_{ab} \end{bmatrix} \quad (8)$$

Where Z_{ab} is the mutual impedance between cables 1 and 2 as shown in Fig. 1.

Compared to the geometry of the single-core cable, the geometry of the three-phase or the pipe-type cable is more complex for two reasons:

a) The single-core cables inside the pipe are not concentric with respect to the pipe.

b) The steel pipe is magnetic and subject to current-dependent saturation effects.

Depending on the thickness of pipe, the two states can be evaluated as infinite and finite pipe thickness, respectively. However with regard to Eq. (9), the depth of penetration in the pipe becomes:

$$d_{earth} = \frac{\sqrt{2}}{|m|} = 503*\sqrt{\frac{\rho_{earth}(\Omega m)}{\mu_r f(Hz)}} \quad (9)$$

and with typical values of $\rho_{pipe}=5*10^{-8}$, f=50 Hz and μ_r=200, d will be less than 1.5mm. Thus in this paper, only infinite pipe thickness is analysed. In this case, no voltage will be induced on the outside of the pipe and consequently, the pipe is the return path instead of earth as shown in Fig. 1.

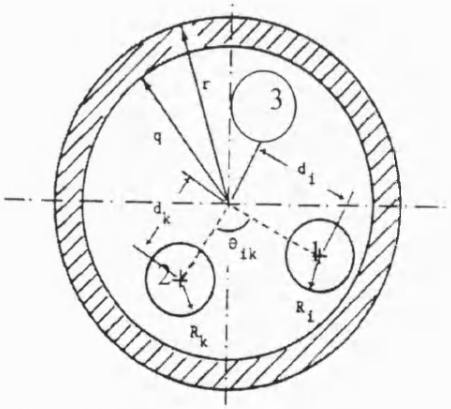

Fig.1- pipe type multi single-core cable

The self impedance of the loop between the sheath and the pipe (or armour) consists of three terms; the first term $Z_{sheath\text{-}out}$ is the same as in Eq.(4), but the second term becomes:

$$z_{insulation} = \frac{j\omega\mu_0}{2\pi}\ln\left[\frac{q}{R_i}*\left(1-\left(\frac{d_i}{q}\right)^2\right)\right] \quad (10)$$

And the third term is given as:

$$z_{pipe-in} = \frac{j\omega\mu_0\mu_r}{2\pi}\left[\left(\frac{k_0(mq)}{mqk_1(mq)}\right)+\left(2*\sum_{n=1}^{\infty}\left(\frac{d_i}{q}\right)^{2n}*\frac{k_n(mq)}{n\mu_r k_n(mq)-mqk'_n(mq)}\right)\right] \quad (11)$$

Taking m from Eq.(7), and $\mu=\mu_0*\mu_r$=permeability of the pipe, k_i=modified Bessel function of the second kind of order I, k_i'=derivative of k_i and also the mutual impedance Z_{ab} (mentioned in Eq.(8)) between two outermost loops formed by armour (pipe) and sheath becomes:

$$z_{ab}=\frac{j\omega\mu_0}{2\pi}\left[\begin{array}{l}\ln\dfrac{q}{\sqrt{d_i^2+d_k^2-2d_id_k\cos\Theta_{ik}}}+\mu_r\dfrac{k_0(mq)}{mqk_1(mq)}\\ +2^*\sum_{n=1}^{n}\left(\dfrac{d_id_k}{q^2}\right)^n\cos(n\Theta_{ik})^*(2\mu_r\dfrac{k_n(mq)}{n\mu_r k_n(mq)-mqk_n(mq)}-\dfrac{1}{n})\end{array}\right] \quad (12)$$

The admittances for pipe-type cables according to Fig. 1 configuration becomes Eq.(13).

$$[y_{phase}]=j\omega[P_{phase}]^{-1} \quad (13)$$

Where $[P_{phase}]$ is a potential coefficient matrix given as:

$$[p_{phase}]=\begin{bmatrix}[p_a] & 0 & 0\\ 0 & [p_b] & 0\\ 0 & 0 & [p_c]\end{bmatrix}+\begin{bmatrix}[p_{aa}] & [p_{ab}] & [p_{ac}]\\ [p_{ba}] & [p_{bb}] & [p_{bc}]\\ [p_{ca}] & [p_{cb}] & [p_{cc}]\end{bmatrix} \quad (14)$$

$$[P_a]=\begin{bmatrix}p_1+p_2+p_3 & p_2+p_3 & p_3\\ p_2+p_3 & p_2+p_3 & p_3\\ p_3 & p_3 & p_3\end{bmatrix} \quad (15)$$

With $$p_i=\frac{1}{c_{ii}}=\frac{\ln(r/q)}{2\pi\varepsilon_o\varepsilon_r} \quad (16)$$

and also $[p_{ii}]and[p_{ik}]$ in the second term is a 3*3 matrix with 9 equal elements as follows:

$$p_{ii}=\frac{1}{2\pi\varepsilon_0\varepsilon_r}\ln\left[\frac{q}{R_i}*\left(1-\left(\frac{d_i}{q}\right)^2\right)\right] \quad (17)$$

$$p_{ik}=\frac{1}{2\pi\varepsilon_0\varepsilon_r}\ln\left[\frac{q}{\sqrt{d_i^{\,2}-d_k^{\,2}-2d_id_k\cos\theta_{ik}}}\right] \quad (18)$$

The admittance matrix is then deduced by inverting $[p_{phase}]$, as has been shown in Eq.(13).

The new approach (presented herein) for a more accurate cable model is on the basis of simplifying and amending Eqs.(10,11,17) (ii. diagonal terms of Eqs.(1,14)) and Eqs. (12,18) (ii. mutual terms of Eqs.(1,14)) by using CM. It should be noted that the diagonal terms of Eqs. (1,14) are related to a single-core pipe type cable and hence are determined using the methodology given in ref. [11].

3- The conformal mapping method

In order to modify the equation for calculating Z and Y, in this paper Eqs. (10,11,12,17,18) are modified for a three-phase cable by transforming eccentric circles into concentric circle by using CM method. It should be mentioned that for a limited range of eccentric conductor locations, reference [12] achieves this transformation using CM. However, firstly only a single conductor pipe type cable is considered, secondly, the depth of penetration of pipe and the thickness of the outer layer of conductor (e.g. armour) is neglected and thirdly, the employed conformal transformation has some limitations, such as the distance between the centre of the two eccentric circles is dependent on the radius of circles. The transformation employed in ref. [12] is:

$$W=(z-a)/(z+a) \quad (19)$$

In this paper, the employed transformation does not have the three aforementioned limitations. This is essentially to avoid any complexities and approximations (as in other methods) in determining Z and Y. Herein, modification of five aforementioned equations associated with impedance and potential coefficient matrices are divided into two parts as follows; diagonal terms (Eqs.(10,11,17)) and off-diagonal terms (Eqs.(12,18)).

3-1- Diagonal terms of Z and P

In order to calculate the diagonal terms of Eqs.(1,14), the methodology adopted herein is similar to that single-core pipe type cable, its extension to a three-phase pipe type being simple. As a first step, a conformal transformation is determined that transforms eccentric circles into concentric circles in two stages. The first transformation is: $Z=Z_1/R_1$ that transforms Fig. 2 into Fig. 3, ie.:

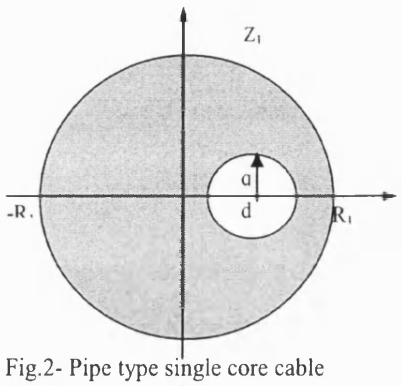

Fig.2- Pipe type single core cable

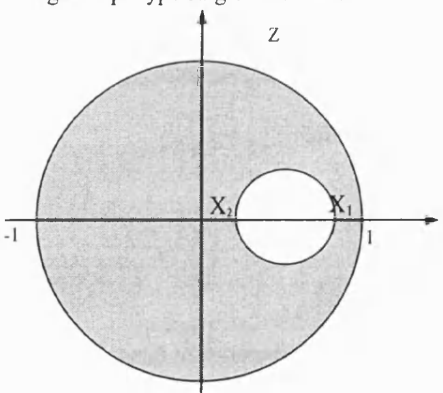

Fig. 3- pipe type (unit radius) single core

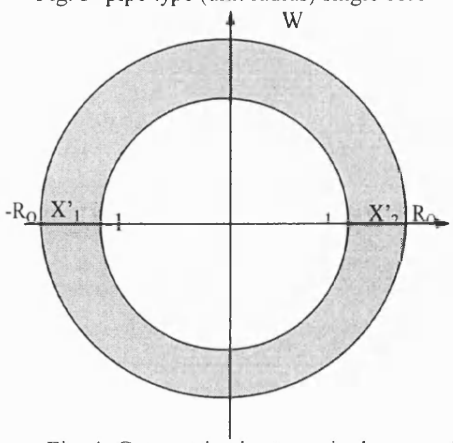

Fig. 4- Concentric pipe type single core cable

$x_1=(d+q)/R_1$ & $x_2=(d-q)/R_1$ (20)

The second transformation is:

$$W_1 = (z-a)/(aZ-1) \quad (21).$$

This transformation transforms Fig. 3 into Fig. 4.

Also the transformation $W_2=\ln(W_1)$ transforms Fig.4 to two parallel line with distance $\ln(R_o)$. As shown in Figs. 3 & 4 the transformation W_1 transforms x_1 to $-R_o$ and x_2 to R_o, thus R_o & 'a' become:

$$a=[1+x_1x_2+\sqrt{(1-x_1^2)(1-x_2^2)}]/(x_1+x_2) \quad (22)$$

$$R_o=[1-x_1x_2+\sqrt{(1-x_1^2)(1-x_2^2)}]/(x_1-x_2) \quad (23)$$

And also from the two parallel lines that are a cross section of two parallel plates, capacitance per unit length is:

$C_{equal}=\varepsilon_o.A/D=2\pi\varepsilon_o/\ln R_o$ (F/m) (24)

With regard to Fig. 5 the capacitance between circles C_1 & C_3 is deduced from Eq. (24) and the capacitance between circles C_1 & C_2 becomes:

$$C_{1\text{-}2}=2\pi\varepsilon_o/\ln(r/q) \quad (25)$$

Here r is a radius of circle C2, q is the radius of circle C1 and. the radius of circle C_3 is unity.

The capacitance between circles C_2 & C_3 becomes: $C_{2\text{-}3}=2\pi\varepsilon_o/\ln(R_oq/r)$ (26)

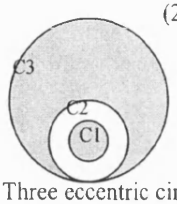

Fig. 5- Three eccentric circles

Since the capacitance is considered ideal, it is related to the inductance at infinite frequency by[10]: $C=(\mu_o.\varepsilon_o)/L$ (27)

Thus Eqs. (10) & (17) become Eqs. (28) and (29), respectively. It should be noted that the permittivity between circles C1 and C2 is $\varepsilon_o\varepsilon_r$ and between circles C2 and C3 it is ε_o in pipe type cable, but in three-phase cable, both of them are $\varepsilon_o\varepsilon_r$.

$$Z_{insulation}=\frac{j\omega\mu_0\mu_r\ln(r/q)}{2\pi}+\frac{j\omega\mu_0\ln(R_o.q/r)}{2\pi} \quad \text{(pipe type cable)}$$

$$=\frac{j\omega\mu_0\mu_r\ln R_o}{2\pi} \quad \text{(three-phase cable)} \quad (28)$$

$$P=\ln[(r/q)*(R_o.q/r)^{\sigma}]/(2\pi\varepsilon_o\varepsilon_r) \quad \text{(pipe type cable)}$$

$$=\ln R_o/(2\pi\varepsilon_o\varepsilon_r) \quad \text{(three-phase cable)} \quad (29)$$

If the depth of penetration of the pipe and the thickness of the outside of the conductor is taken into account, the transformation transforms Fig. 6 into Fig 7

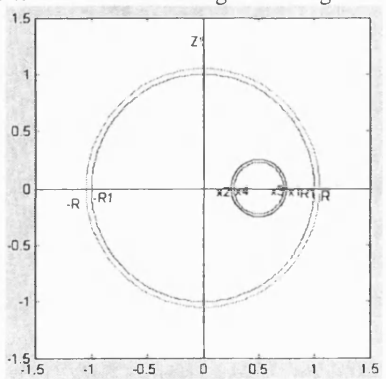

Fig. 6- Two eccentric circles (including thickness)

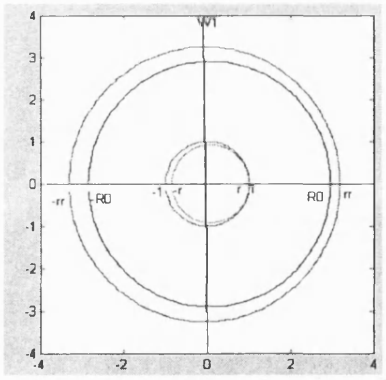

Fig. 7- CM transformation of Fig. (6)

As it can be observed, the inside of the pipe is transformed to the outside of the pipe and hence $Z_{pipe\text{-}in}$ is obtained from Eq. (4) by replacing r (the outside radius of pipe) to N (scale factor) and q (the inside radius of pipe) to N*r. r has been shown in Fig.(7). Thus $Z_{pipe\text{-}in}$ in Eq.(11) becomes:

$$z_{pipe-in}=\frac{\rho m}{2\pi ND}[I_O(mN)*k_1(mNr)+k_o(mN)*I_1(mNr)] \quad (30)$$

where D is: $D=I_1(mN)*k_1(mNr)-I_1(mNr)*k_1(mN)$ (31)

Although it can be seen from Fig. 7 that all circles are not completely concentric, since the depth of penetration in the pipe at power frequency is less than 1.5mm, and the thickness of the armour or sheath is much smaller than its outer radius, Fig.(7) is a good approximation of four concentric circles, and is more accurate than neglecting the effect of depth of penetration in pipe and thickness of armour (or sheath), as in the EMTP model.

In order to find the maximum matching between four circles in Fig. 7, and consequently the most accurate result in CM model, a coefficient k is introduced in the transformation. Thus we have:

$$W_1=\frac{Z-ka}{kaZ-1} \quad (32)$$

k causes the transformation of four circles to be more concentric. If the thickness of conductor is b, k becomes:

$$k=M+\sqrt{M^2-\frac{1}{a^2}} \quad (33) \text{ as: } \quad M=\frac{(x_1-b)(x_2+b)+1}{a(x_1+x_2)} \quad (34)$$

Because of the various transformations that have been used to transform Fig.6 to Fig.7, there is scaling on Z_{pipein} [12], and hence a scale factor or metric coefficient N should be taken into account. N is the ratio of distances in the original Z_1-plane to the corresponding distances in the transformed W_1-plane. Hence it is defined by:

$$N=\left|\frac{dZ_1}{dW_1}\right|=\left|\frac{dZ_1}{dZ}.\frac{dZ}{dw_1}\right| \quad (35)$$

In order to find the absolute value of dZ/dW_1, W_1 is expressed as: $W_1=\cos\theta+j\sin\theta$; because the radius of the pipe in W_1-plane is unit, it leads to the following:

$$N=R_1\left|\frac{(ka)^2-1}{1+(ka)^2-2ka\cos\theta}\right| \quad (36)$$

N is seen to be a function of θ. With N appearing as a dominant factor in the denominator of Eq. (30), the

average values of 1/N should appear where point by point evaluations of N are not undertaken [12]. In this case, the cosθ term vanishes so that N takes the form:

$$N = R_1\left|\frac{(ka)^2-1}{(ka)^2+1}\right| \quad (37)$$

3-2- Off-diagonal terms of Z and P matrices

This section deals with modifying the mutual terms of Z and P (or Y according to Eq. (13)) matrices. With respect to this two different states are presented as follows:

State 1: As mentioned in ref. [9], axial voltage drop depends on the flux linkage and the axial electric field at the pipe wall as follows:

$$\frac{\partial V}{\partial x} = -I(R + j\omega L) = -\frac{d\lambda}{dt} + E_x(r_1) \quad (38)$$

This section will only deal with flux linkage and modification of P (Eq.(18)) and L (first and fourth terms of Eq.(12)) and hence Y and Z, respectively. In order to obtain the mutual impedance terms, a two-conductor system is analysed as shown in Fig.8. If conductor 1 is carrying a current that is returning in the pipe, the mutual flux linkage with conductor 2 is in the region between conductor 2 and the pipe. The flux linkage becomes:

$$\frac{d\lambda_{2(1)}}{dt} = j\omega\oint A_{2(1)}.dl_2 = j\omega[A_1(r_1,\theta) - A_1(r_{12},\theta_{12})] \quad (39)$$

Where A is the vector potential within the pipe and θ_{12} has been shown in Fig. (1).

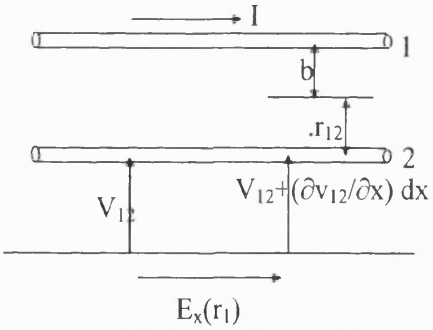

Fig.8- Two conductor system

With regard to Eq.(39) and in order to find the quantity of the mutual flux linkage between conductor 2 and the Armour associated with conductor 1, reference should be made to a three-phase cable which is shown in Fig. (9).

As can be seen, fluxes generated by conductor 1 produce a set of circles in which the centre moves from α_1 to 0 on the axis x. Thus in order to find the amount of the flux generated by conductor 1 that flows between conductor 2 and the Armour, we need to find a circle with centre α_4 and radius R_4.

Referring to Eqs.(24,38) and the CM method, the first and fourth terms of Eq.(12) become:

$$Ij\omega L = \frac{d\lambda}{dt} = Ij\omega\frac{\mu_o\mu_r}{2\pi}\ln R_o(x_{14},x_{24}) \quad (40)$$

Then, P_{12} is derived as follows:

$$P_{12} = \frac{1}{2\pi.\varepsilon_o.\varepsilon_r}\ln R_o(x_{14},x_{24}) \quad (41)$$

In order to find the circle(α_4,R_4), some calculations are done as follows:

$x_{14}=x_{11}+k.(1-x_{11})$ (42)

$x_{24}=x_{21}-k.(1+x_{21})$ (43)

$\alpha_1=(x_{11}+x_{21})/2$ (44)

$\alpha_4=\alpha_1-k.\alpha_1$ (45)

k is a percentage of the full distance between the origin to the centre as shown in Fig. 9 ; for example $x_{11}\to 1$, $x_{12}\to -1$ or $\alpha_1\to 0$.

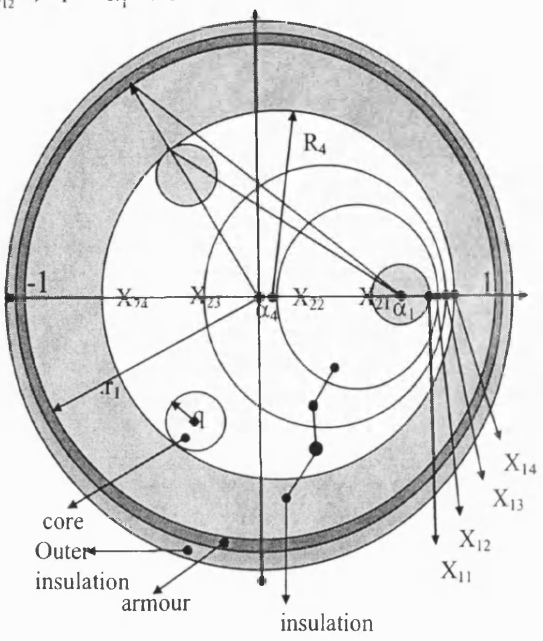

Fig. 9- Presentation of flux linkage in a three-phase cable

From Fig(9), it can be concluded that:

$$R_4 = x_{11}^2 + \alpha_4^2 - 2\alpha_4.x_{11}\cos 120 \quad (46)$$

$$R_4 = x_{14} - \alpha_4 \quad (47)$$

From Eq.(46,47) k is obtained as follows:

$$k^2 - Mk + N = 0 \Rightarrow k = \frac{M}{2} - \sqrt{\frac{M^2}{4} - N} \quad (48)$$

As :

$$M = (2d^2 + x_{11}(d-1) + d + 1)/d^2 \quad (49)$$

and

$$N = (x_{11}^2 + d^2 + x_{11}(d-1) + d)/d^2 \quad (50)$$

After calculating k, x_{14} and x_{24} can be derived from Eqs.(42) and (43) respectively. In conclusion, P_{12} and $R_o(x_{14},x_{24})$ are obtained from Eq.(41) and Eq.(23), however in latter equation, instead of x_1 and x_2, x_{14} and x_{24} should be used respectively.

State 2: In the second state, one of d_i or d_k in Eq.(12) becomes zero by using the CM method. In the first instance, a conformal transformation is determined that transforms three eccentric circles (one pipe and two conductors) into two concentric circles (pipe and one conductor) and one eccentric circle (other conductor). In

the second step, one of d_i or d_k be set to zero (for example d_k=0), and Eq.(12) is simplified as follows;

$$z_{mutual} = \frac{j\omega\mu_0}{2\pi}\left\{\ln\frac{N_1}{N_2 d_i} + \mu_r \frac{k_0(N_1 m)}{N_1 m k_1(N_1 m)}\right\} \qquad (51)$$

Where N_1 and N_2 are scaling factors as mentioned earlier and will be determined later.

Also Eq.(18) is modified as follows;

$$P_{ij} = \frac{\ln(N_1/N_2 d_i)}{2\pi\varepsilon_0} \qquad (52)$$

In order to find the aforementioned conformal transformation, reference should be made to Figs.10 to 13. Four transformations that have been used, are as follows;

W1=Z/r_1 , r_1 is inner radius of pipe

$W_2 = (W_1 - a)/(aW_1 - 1)$ a and R_0 are obtained from Eqs.(22 &23) and R_0 has been shown in Fig.(11).

$W_3 = e^{-j\theta}.W_2$ and $W_4 = (W_3 - b)/(bW_3 - 1)$

where R which is shown in the Fig.(13) and b are obtained as follows:

$$b = (1 + x_3x_4 + \sqrt{(x_3^2-1)(x_4^2-1)})/((x_3 + x_4) \qquad (53)$$

$$R = (-1 + x_3x_4 - \sqrt{(x_3^2-1)(x_4^2-1)})/((x_3 - x_4) \qquad (54)$$

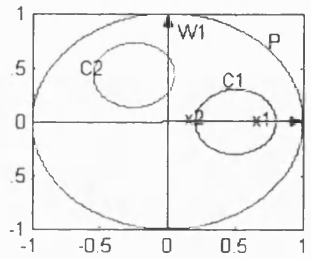

Fig. 10- Two core pipe type cable

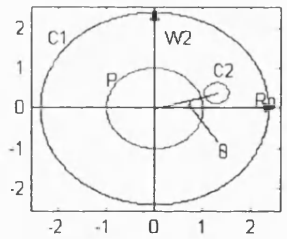

Fig. 11- First CM transformation on Fig. 37

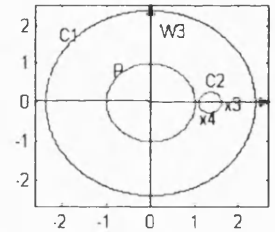

Fig. 12- Second CM transformation

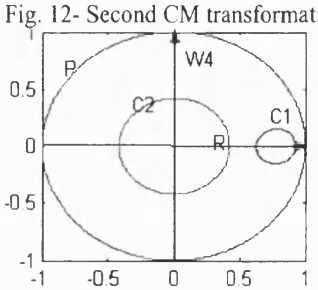

Fig. 13- Third CM transformation

Scale factors N_1 and N_2 in Eq.(51), becomes;

$$N = \left|\frac{dZ}{dW_4}\right| = \left|\frac{dZ}{dW_1}\cdot\frac{dW_1}{dW_2}\cdot\frac{dW_2}{dW_3}\cdot\frac{dW_3}{dW_4}\right| \qquad (55)$$

With regard to the aforementioned transformations and obtained results in previous section, it can be concluded that;

$\frac{dZ}{dW_1} = r_1$, $\frac{dW_1}{dW_2} = \frac{a^2-1}{(aW_2-1)^2}$, $\frac{dW_2}{dW_3} = 1$ and $\frac{dW_3}{dW_4} = \frac{b^2-1}{(bW_4-1)^2}$,

Thus N becomes; $N = \left|\frac{r_1(a^2-1)(b^2-1)}{(aW_2-1)^2(bW_4-1)^2}\right|$ (56)

In order to calculate scaling factors N_1 and N_2 from Eq.(56) and with regard to relationships, between N_1 and pipe as well as N_2 and centre of circle(c_1)(shown in Fig.(10), a suitable value should be inserted instead of W_2 and W_4 in the aforementioned equation.

Because the radii of pipe in the W_2-plane and W_4-plane are unity, in order to obtain N1, W2 and W_4 in Eq.(56) is expressed as; W_2 =W_4 =cosθ+jsinθ, this results in:

$$N_1 = \left|\frac{r_1(a^2-1)(b^2-1)}{(1+a^2-2a\cos\theta)\ (1+b^2-2b\cos\theta)}\right| \qquad (57)$$

With regard to eliminating the cosθ term (based on the same reasoning in as the previous section), N_1 is simplified as follows; $N_1 = \left|\frac{r_1(a^2-1)(b^2-1)}{(1+a^2)\ (1+b^2)}\right|$ (58).

Also in order to calculate N_2, W_2 and W_4 are replaced by zero and position of centre of circle C_1(shown in Fig.(13), respectively. Therefore N_2 is obtained as follows;

$$N_2 = \left|\frac{r_1(a^2-1)(b^2-1)}{(b.d_x-1)^2}\right| \qquad (59).$$

Where d_x is the amplitude of centre of circle C_1 in Fig.(13).

4- Data simulation:

In order to do a comparison of the Z and Y parameters between the EMTP and CM methods, a practical three-phase underground distribution network shown in Fig. 15 has been considered.

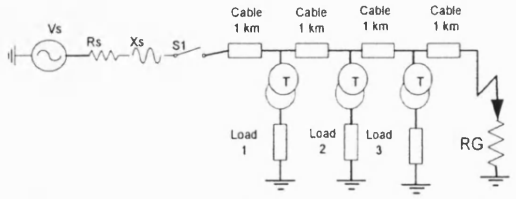

Fig. 15- Practical 3-phase underground distribution network

The specifications of the various elements in Fig (52) are as follows:

Source: V_L = 11kV, f=50Hz, X_s:R_s=10, X_s=2Ω, R_s=0.2Ω

Switch1: closer time = 0 (connection to source)

Short circuit: 3-phase, RG= 2 ohms

Fault time = 20 ms

Cables: XLPE, Three-phase pipe type cable (core + grounded sheath)

Core: r_{in}=0, r_{out}=6.1mm, $\rho=2.3*10^{-8}$ Ω.m, μ_r=100

Sheath: r_{in}=10mm, r_{out}=11mm, $\rho=17*10^{-8}$ Ω.m, μ_r=100

Insulator between core and sheath: thickness=3.9mm, ε_r=3

Insulator between pipe and sheath: ε_r=8

Pipe: r_{in}=4cm, r_{out}=4.5cm, $\rho=25*10^{-8}$ Ω.m, μ_r=100

Transformer: S=1 MVA

Winding 1 : V_L=11kV, R_p=.001pu, X_p= .0288pu

Winding 2 : V_L=380V, R_s=.001pu, X_s= .0288pu

Magnetizing Branch: R_M=500pu, X_M=500pu

Load 1=Load 3: The combination of the static and Dynamic Load: V_L=380 Vrms, f=50 Hz, P=30 HP, R_S=.0435Ω, R'_r=0.0816, L_S=.002H, L'_r=.002H, L_M=.0693H, 2 pole, inertia=.89 J(Kg.m^2).

Static Load: P=50KW, Q_L=25KVAR, Q_C=200VAR, V_L=380 Vrms

Load 2: The combination of the static and dynamic loads

Dynamic Load: V_L=380 Vrms, f=50 Hz, P=30 HP, R_S=.0435Ω, R'_r=0.0816, L_S=.002H, L'_r=.002H, L_M=.0693H, 2 pole, inertia=.89 J(Kg.m^2).

Static Load: P=100KW, Q_L=60KVAR, Q_C=10KVAR, V_L=380 Vrms

It should be noted that the Armour in three-phase cable, plays the role of pipe in pipe type cable.

Because of the limitation on space as well as the importance of the voltage compare with current, only the results of voltages are shown in this paper. Figs (15,16,17) show voltage after the switch 1 using EMTP and CM methods, associated with state 1 and 2, respectively, during 3Ph fault.

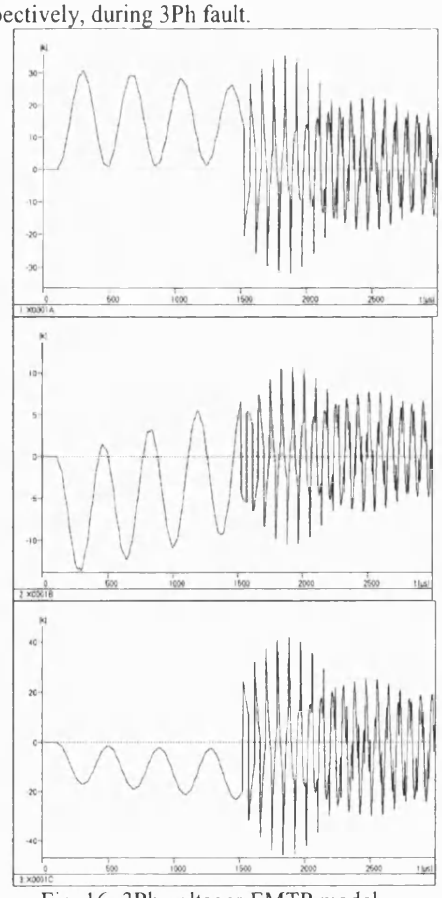

Fig. 16- 3Ph voltages EMTP model

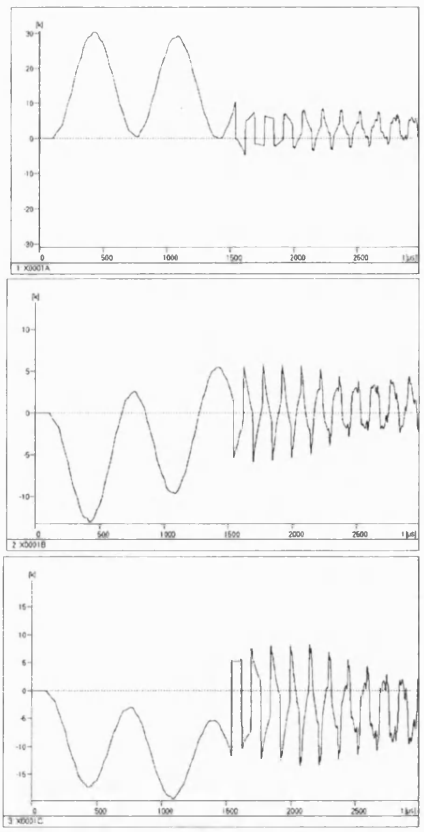

Fig. 17- 3Ph voltages CM model (state 1)

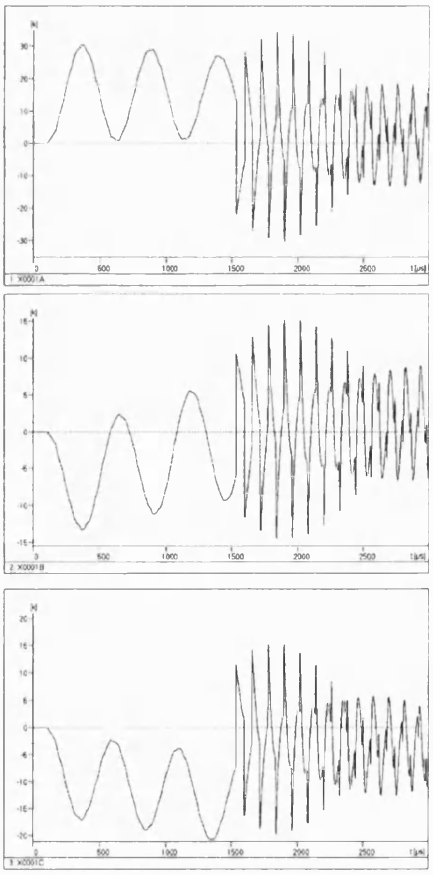

Fig. 17- 3Ph voltages CM model (state 2)

Table 1 shows the velocity of propagation for aforementioned methods.

Table 1- The velocity of propagation (m/s)

	EMTP model	CM model (state 1)	CM model (state 2)
Mode1	1.5813e+7	.75243e+7	.93717e+7
Mode2	1.9397 e+7	1.6978 e+7	.94298 e+7
Mode3	9.0674 e+7	5.3406 e+7	6.6419 e+7
Mode4	8.9673 e+7	5.9216 e+7	5.2529 e+7
Mode5	1.5613 e+7	1.6978 e+7	.94298 e+7
Mode6	9.0674 e+7	5.3406 e+7	6.6419 e+7

It should be noted that all curves of voltage in CM model are computed by replacing modal parameters of CM model in .lib file of ATP.

In order to compare frequency-dependent of new model with EMTP model and with regard to limitation on space only the accurate representation of single-phase pipe type cable with frequency-dependent of diagonal terms of Z matrix in three-phase cable, is shown in Fig. (18).

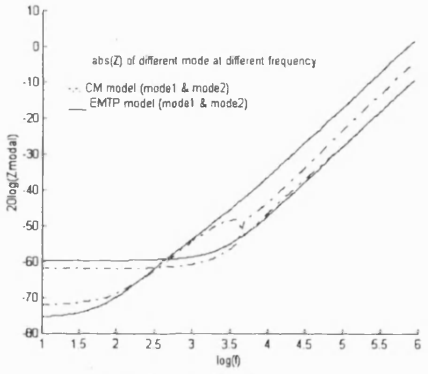

Fig. 18- Amplitude of Z in different frequencies

With regard to aforementioned maths calculation and obtained results in data simulation, the validity and larger accuracy of the new methods, can be confirmed.

4-Conclusion

This paper presents a new approach to Z and Y parameters for a three-phase cable using conformal mapping method. Because of being eccentric conductors in three-phase cable, Z and Y parameters in the EMTP model involve infinite series and also they are complex with some approximations. According to ref. [11], in practice, the level of error due to the approximations is dependent upon the radius of the outer conductor in relation to the radius of the pipe or armour in three-phase cable, as smaller the difference between the two, the error is larger. With regard to the CM's ability to transform eccentric circles into concentric circles, some of the aforementioned approximations can be neglected. On one hand, according to presented results in the reference [11], when the approximation is less in the EMTP model and as a result the error is smaller, then the obtained results from two models EMTP and CM are closer for single-phase pipe type cable or diagonal term of Z and Y matrices in three-phase cable. On the other hand, on the basis of maths calculation in this paper and obtained results in data simulation, the validity and more accuracy of the new method is confirmed, thus the CM method can be considered as a more accurate and simpler method.

5-References

1-L.Marti, "simulation of transients in underground cables with frequency-dependent modal transformation matrices",IEEE transaction on power Delivery, July 1988

2-T.T.Nguyen & H.Y.Chan "evaluation of modal transformation matrices for overhead transmission lines and underground cables by optimization method", IEEE transaction on power Delivery, JAN.,2002

3-J.A.Tegopoulos & E.E.Kriezis, "Eddy current distribution in cylindrical shells of infinite length due to axial current", Part I: shells of one boundary, IEEE, PAS, 1971

4-J.A.Tegopoulos & E.E.Kriezis, "Eddy current distribution in cylindrical shells of infinite length due to axial current", Part II: shells of finite thickness, IEEE, PAP, 1971

5-G.Liu, "Improved modelling of the nonlinear B-H curve and its application in power cable analysis", IEEE Transaction on magnetic, JULY 2002

6-X.B.Xu & G.Liu & P.Chow, "A finite-element method solution of the zero-sequence impedance of underground pipe-type cable", IEEE transaction on power Delivery, JAN.,2002

7-D.L.Paul, C.J.Railton & I.J.Craddock, "Full-wave modelling of coaxial cables by FDTD technique", electronics letters 10_{th} Oct. 2002 vol.38 no.21

8-A.F.Moreira. T.A.Lipo, G.Venkataramanan & S.Bernet, "High-frequency modelling for cable and induction motor over voltage studies in long cable drives", IEEE Transaction on industry applications, Sep./Oct. 2002

9-G.W.Brown & R.G.Rocamora, "surge propagation in Three-phase cables", Part I –unsaturated pipe, IEEE ,PAS , Jun./Feb. 1976

10-EMTP Theory book

11-J Moshtagh & R K Aggarwal, "A new approach to single-phase pipe type cable modelling using conformal mapping", UPEC 2004

12- R. Schinziger & A. Ametani, "surge propagation characteristics of pipe enclosed under ground cables". IEEE, PAS, Sept. 1978

A NEW APPROACH TO MODELLING HIGH VOLTAGE THREE-PHASE PIPE TYPE CABLE USING CONFORMAL MAPPING

Jamal Moshtagh
University of Bath
UK
eepjam@bath.ac.uk

Raj K. Aggarwal,
University of Bath
UK
r.k.aggarwal@bath.ac.uk

ABSTRACT

The increasing use of cable systems and the growing levels of capacity make the analysis of wave propagation to determine an accurate model for cables an important branch in Electrical Power Engineering. In particular, accurate determination of the per unit length cable series impedance Z and the per unit length shunt admittance Y can play an important role. For example, the results of this analysis can lead to finding an accurate method for fault location/detection under transient fault conditions. In this respect, the EMTP is a powerful software tool for modelling the transient phenomena in power system network. However, in the modelling of underground cables, in particular the per unit length series impedance Z and the per unit length shunt admittance Y, it makes certain assumptions and approximations; this inevitably gives rise to inaccuracies when simulating the voltage and current waveforms under fault conditions. This paper presents a new approach to the modelling of the cable's Z and Y parameters using conformal mapping (CM), which avoids the assumptions and approximations associated with the EMTP software thereby increasing the simulation accuracy. In order to make a comparison between the Z and Y parameters and in the simulated transient voltage and current signals attained via the EMTP and CM methods, a practical radial three-phase pipe type cable is analysed. The results confirm the validity and higher accuracy of the new proposed method.

KEY WORDS

Conformal mapping, cable modelling, EMTP, pipe type cable

1. Introduction

There has been an upsurge in the usage of underground distribution systems in recent years. In this respect, increased competition due to the deregulation of the power industry and the demand to provide better service to the customers having increasingly sensitive loads, makes the development of reliable and accurate fault location methods for distribution systems an important issue. One of the most important factors in accurate fault location is to develop an accurate model of a cable which then needs to be integrated into an overall distribution system model. Essentially, there is a need to determine accurately, the per unit length impedance and admittance of a cable, which in turn determine the relationships between current, voltage, attenuation and velocity of travelling waves in the transient state.

A number of models have been proposed to date. These models can be classified into the following two main groups; time domain and frequency domain models. With regard to the advantages and disadvantages of these techniques, in reference [1], the presented model belongs to the class of time-domain, frequency-dependent methodology. It overcomes the main limitations of existing time-domain cable models, that is, it takes into account the frequency dependence of the modal transformation matrices. This model is compatible with the time domain solution, such as the one used in the EMTP. A general method based on constrained optimization for evaluating the modal transformation matrices for overhead transmission lines and underground cables has been developed and tested in reference [2]. The method guarantees in the methodology adopted, the smoothness of all the eigenvectors and modal characteristic impedances over a wide range of frequencies. This method can be used in the EMTP software in which the eigenvalues and eigenvectors of a complex upper Hessenberg matrix are found by the modified LR-method due to Rutishauser [9]. In many analyses of overhead line parameters, approximations ignoring eddy currents in conductors can be assumed. However, in close conductors, such as underground cables, the AC parameters vary significantly with frequency and conductor spacing. In references [3] and [4], on which the EMTP model is based, the distributions of current density due to proximity and skin effects are determined analytically by solving the differential equation for penetration of currents in the conducting material and appropriately applying boundary conditions. But, for eccentric conductors such as a three-phase cable, inner conductors are replaced with an assumed small circle which is concentric with outer conductor such as pipe or armour. In all the aforementioned methods and also in EMTP model it is assumed that permeability μ for conductors and pipe is constant. Thus in order to determine μ throughout the pipe, in reference [5], the magnetic field intensity in each element of the pipe is solved using the finite-element method. In reference [6], the cable is divided into a large number of cells as the field is assumed to be constant within each cell and a linear integration is performed for the voltage using Finite-Difference Time Domain (FDTD) method.

In the modelling of a three-phase cable, the main problem arises by virtue of the fact that the three conductors are positioned off centre within the pipe or armour and it is principally due to this that some estimations and approximations are made in the EMTP model; a direct consequence of the latter is that the mathematical representation of the impedance and admittance in a pipe type cable in the EMTP software includes infinite series formulations of the flux linkage and the proximity effects; this of course is based on some approximations in the configuration of cable. However, with regard to CM's ability to transform an isotropic region into a symmetrical and much simpler region, the mathematical equations for the calculation of Z and Y take a simplified form and eliminate such approximation which changes the configuration of cable. and yet increase the accuracy, as shown in this paper.

Herein, the EMTP method for calculating Z and Y is firstly reviewed followed by outlining the attributes of CM and then, based on ref. [7], simplification of the mathematical equations for calculating Z and Y is carried out. Finally, a practical radial three-phase pipe type cable is analysed and a comparison is made between the results attained using the EMTP and CM models. It should be noted that according to reference [1], time domain method in the EMTP model is compatible with the J Marti model associated with frequency-dependent parameters. The performance of the EMTP cable model is compared with the CM model, the latter being based on the Bergeron model which is time-domain based.

2. Three-Phase Cable Model in EMTP

Cable model in EMTP is based on Brown and Rocamora's calculations and results shown in ref. [7], but these calculations are based on such assumptions which have been considered in Emanuel approach mentioned in ref. [8]. These assumptions are as follows:

1. The cylindrical conductors are replaced with infinitesimally thin sheets.
2. The displacement currents and dielectric losses are neglected.
3. The finite thickness of the pipe wall is neglected since current penetration is assumed to be confined under transient conditions.
4. The pipe is considered to have constant permeability.

First assumption is associated with the configuration of the conductors inside the pipe, as a typical configuration of a three conductor cable shown in fig. (1) is replaced with a concentric conductor shown in fig. (2)

Before dealing with eliminating this assumption as a result increasing the accuracy of cable model, following is dealt with reviewing on the EMTP model According to reference [9], Z_{phase} matrix in a three-phase cable becomes:

$$[Z_{phase}] = \begin{bmatrix} [Z_{self-a}] & [Z_{mutual-a-b}] & [Z_{mutual-a-c}] \\ [Z_{mutual-b-a}] & [Z_{self-b}] & [Z_{mutual-b-c}] \\ [Z_{mutual-c-a}] & [Z_{mutual-c-b}] & [Z_{self-c}] \end{bmatrix} \quad (1)$$

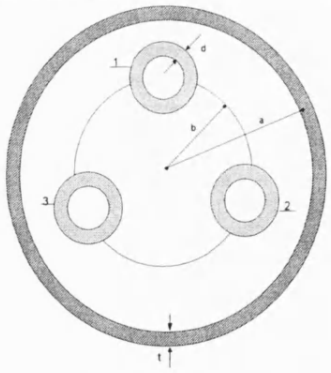

Fig. 1. Typical configuration of a three conductor's cable

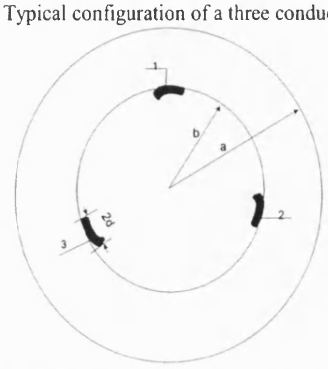

Fig. 2. Assumed configuration of three conductor's cable

Each impedance in $[Z_{self}]$ depends on $Z_{insulation}$, $Z_{tube-in}$, $Z_{tube-out}$ and $Z_{tube-mutual}$ as follows:

$$z_{insulation} = \frac{1}{2\pi} j\omega\mu_o\mu_r \ln(r/q) \quad (2)$$

μ_r = permeability of insulation

$\mu_o = 2*10^{-4}$ H/Km

r=outside radius of insulation (or tube)

q=inside radius of insulation (or tube)

$$z_{tube-in} = \frac{\rho m}{2\pi q D}\left[I_O(mq)*k_1(mr) + k_o(mq)*I_1(mr)\right] \quad (3)$$

$$z_{tube-out} = \frac{\rho m}{2\pi r D}\left[I_O(mr)*k_1(mq) + k_o(mr)*I_1(mq)\right] \quad (4)$$

$$z_{tube-mutual} = \rho/(2\pi r q D) \quad (5)$$

Where, $D=I_1(mr)*k_1(mq)-I_1(mq)*k_1(mr)$; (6)

$$m = \sqrt{j\omega\mu/\rho} \quad (7)$$

and I_0, I_1 K_0 and K_1 are Bessel functions.

Also: $$[Z_{mutual-a-b}] = \begin{bmatrix} z_{ab} & z_{ab} & z_{ab} \\ z_{ab} & z_{ab} & z_{ab} \\ z_{ab} & z_{ab} & z_{ab} \end{bmatrix} \quad (8)$$

Where Z_{ab} is the mutual impedance between conductors 1 and 2 as shown in Fig. 3.

Compared to the geometry of the single-core cable, the geometry of the three-phase or the pipe-type cable is more complex for two reasons:

a) The single-core cables inside the pipe are not concentric with respect to the pipe.

b) The steel pipe is magnetic and subject to current-dependent saturation effects.

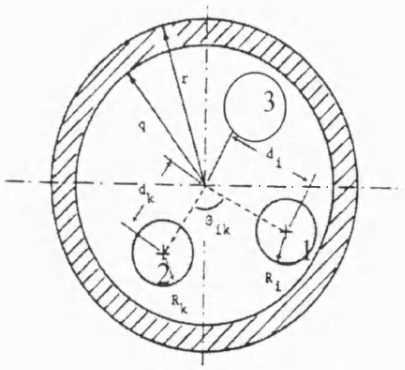

Fig. 3. Pipe type multi single-core cable

Depending on the thickness of the pipe, the two states can be evaluated as infinite and finite pipe thicknesses, respectively. However with reference to Eq. (9), the depth of penetration in the pipe becomes:

$$d_{pipe} = \frac{\sqrt{2}}{|m|} = 503 * \sqrt{\frac{\rho_{earth}(\Omega m)}{\mu_r f(Hz)}} \qquad (9)$$

and with typical values of $\rho_{pipe}=5*10^{-8}$, f=50 Hz and μ_r=200, d will be less than 1.5mm. In practice, the thickness of pipe is larger than 3 mm, and hence in this paper, only infinite pipe thickness (no earth return) is analysed. In this case, no voltage will be induced on the outside of the pipe and consequently, the pipe is the return path instead of earth as shown in Fig. 3.

The self impedance of the loop between the sheath and the pipe (or armour) consists of three terms; the first term $Z_{sheath-out}$ is the same as in Eq.(4), but the second term becomes:

$$Z_{insulation} = \frac{j\omega\mu_0}{2\pi} \ln\left[\frac{q}{R_i} * \left(1-\left(\frac{d_i}{q}\right)^2\right)\right] \qquad (10)$$

The third term is given as:

$$z_{pipe-in} = \frac{j\omega\mu_0\mu_r}{2\pi}\left[\left(\frac{k_0(mq)}{mqk_1(mq)}\right) + \left(2 * \sum_{n=1}^{\infty}\left(\frac{d_i}{q}\right)^{2n} * \frac{k_n(mq)}{n\mu_r k_n(mq) - mqk'_n(mq)}\right)\right] \qquad (11)$$

Taking m from Eq.(7), and $\mu = \mu_0 * \mu_r$=permeability of the pipe, k_n=modified Bessel function of the second kind of order n, k_n'=derivative of k_n and also the mutual impedance Z_{ab} (mentioned in Eq.(8)) between the two outermost loops formed by armour (pipe) and sheath becomes:

$$z_{ab} = \frac{j\omega\mu}{2\pi}\left\{\ln\frac{q}{\sqrt{d_i^2+d_k^2-2d_id_k\cos\Theta_{ik}}} + \mu_r\frac{k_0(mq)}{mqk_1(mq)} + 2*\sum_{n=1}^{\infty}\left(\frac{d_id_k}{q^2}\right)^n \cos(n\Theta_{ik}) * \left(2\mu_r\frac{k_n(mq)}{n\mu_r k_n(mq) - mqk'_n(mq)} - \frac{1}{n}\right)\right\} \qquad (12)$$

The admittances for pipe-type cables according to Fig.1 configuration becomes Eq.(13).

$$[y_{phase}] = j\omega[P_{phase}]^{-1} \qquad (13)$$

Where $[P_{phase}]$ is a potential coefficient matrix given as:

$$[p_{phase}] = \begin{bmatrix}[p_a] & 0 & 0\\ 0 & [p_b] & 0\\ 0 & 0 & [p_c]\end{bmatrix} + \begin{bmatrix}[p_{aa}] & [p_{ab}] & [p_{ac}]\\ [p_{ba}] & [p_{bb}] & [p_{bc}]\\ [p_{ca}] & [p_{cb}] & [p_{cc}]\end{bmatrix} \qquad (14)$$

Where:

$$[P_a] = \begin{bmatrix} p_1+p_2+p_3 & p_2+p_3 & p_3\\ p_2+p_3 & p_2+p_3 & p_3\\ p_3 & p_3 & p_3\end{bmatrix} \qquad (15)$$

With

$$p_i = \frac{1}{c_{i\,i}} = \frac{\ln(r/q)}{2\pi\varepsilon_0\varepsilon_r} \qquad (16)$$

and also $[p_{ii}]$ and $[p_{ik}]$ in the second term is a 3*3 matrix with 9 equal elements as follows:

$$p_{ii} = \frac{1}{2\pi\varepsilon_0\varepsilon_r}\ln\left[\frac{q}{R_i} * \left(1-\left(\frac{d_i}{q}\right)^2\right)\right] \qquad (17)$$

$$p_{ik} = \frac{1}{2\pi\varepsilon_0\varepsilon_r}\ln\left[\frac{q}{\sqrt{d_i^2-d_k^2-2d_id_k\cos\theta_{ik}}}\right] \qquad (18)$$

The admittance matrix is then deduced by inverting $[p_{phase}]$, as has been shown in Eq.(13).

The new approach (presented herein) for a more accurate cable model is on the basis of simplifying and amending Eqs.(10,11,17) (ii. diagonal terms of Eqs.(1,14)) and Eqs. (12,18) (ii. mutual terms of Eqs.(1,14)) by using CM. It should be noted that the diagonal terms of Eqs. (1,14) are related to a single-core pipe type cable and hence are determined using the methodology given in ref. [10].

3. The Conformal Mapping Method

In order to modify the equation for calculating Z and Y, in this paper Eqs. (10,11,12,17,18) are modified for a three-phase cable by transforming eccentric circles into concentric circle by using the CM method. It should be mentioned that for a limited range of eccentric conductor locations, reference [11] achieves this transformation using CM. However, firstly only a single conductor pipe type cable is considered, secondly, the depth of penetration of pipe and the thickness of the outer layer of conductor (e.g. armour) is neglected and thirdly, the employed conformal transformation has some limitations, such as the distance between the centre of the two eccentric circles is dependent on the radius of circles. The transformation employed in ref. [11] is:

$$W = (Z-a) / (Z+a) \qquad (19)$$

Herein, the employed transformation does not have the three aforementioned limitations. This is essentially to avoid any complexities and approximations (as in other methods) in determining Z and Y. Moreover, modifications to the five aforementioned equations associated with impedance and potential coefficient matrices are divided into two parts as follows: diagonal terms (Eqs.(10,11,17)) and off-diagonal terms (Eqs.(12,18)).

A. Diagonal terms of Z and P:I

In order to calculate the diagonal terms of Eqs.(1,14), the methodology adopted herein is similar to that of a single-core pipe type cable, its extension to a three-phase pipe type being relatively simple. As a first step, a conformal transformation is determined that transforms eccentric circles into concentric circles in two stages. The first

transformation is: $Z=Z_1/R_1$ that transforms single-core pipe type cable into Fig. 4, ie.:

$x_1=(d+q)/R_1$ & $x_2=(d-q)/R_1$ (20)

As d= distance between two centres of core and pipe

.q= the radius of core and R_1= the inner radius of pipe

The second transformation is:

$W_1 == (z-a)/(aZ-1)$ (21).

This transformation transforms Fig. 4 into Fig. 5.

Also the transformation $W_2=\ln(W_1)$ transforms Fig.5 into two parallel lines with distance $\ln(R_o)$.

As shown in Figs. 4 & 5, the transformation W_1 transforms x_1 to $-R_o$ and x_2 to R_o, thus R_o & 'a' become:

$$a=[1+x_1x_2+\sqrt{(1-x_1^2)(1-x_2^2)}]/(x_1+x_2) \quad (22)$$

$$R_o=[1-x_1x_2+\sqrt{(1-x_1^2)(1-x_2^2)}]/(x_1-x_2) \quad (23)$$

Also from the two parallel lines that are a cross section of two parallel plates, capacitance per unit length is:

$C_{equal}=\varepsilon_o.A/D=2\pi\varepsilon_o/\ln R_o$ (F/m) (24)

With regard to Fig. 6, the capacitance between circles C_1 & C_3 is deduced from Eq. (24) and the capacitance between circles C_1 & C_2 becomes:

$C_{1\text{-}2}=2\pi\varepsilon_o/\ln(r/q)$ (25)

Here r is the radius of circle C2, q is the radius of circle C1 and the radius of circle C_3 is unity.

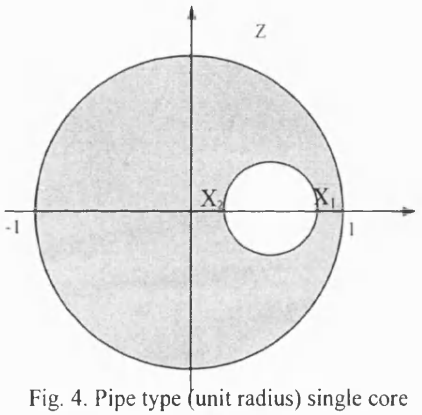

Fig. 4. Pipe type (unit radius) single core

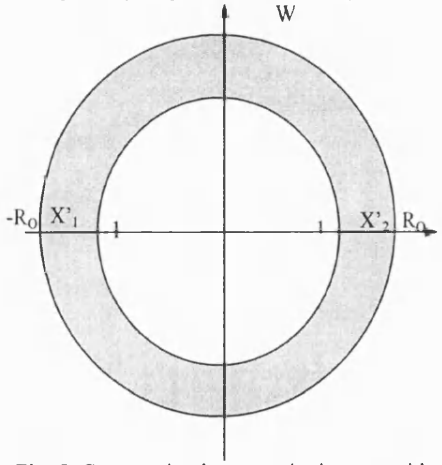

Fig. 5. Concentric pipe type single core cable

The capacitance between circles C_2 & C_3 becomes:

$C_{2\text{-}3}=2\pi\varepsilon_o/\ln(R_oq/r)$ (26)

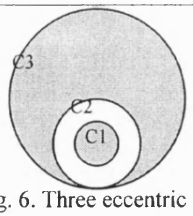

Fig. 6. Three eccentric circles

Since the capacitance is considered ideal, it is related to the inductance at infinite frequency by[9]:

$C=(\mu_o.\varepsilon_o)/L$ (27)

Thus Eqs. (10) & (17) become Eqs. (28) and (29), respectively. It should be noted that the permittivity between circles C1 and C2 is $\varepsilon_o\varepsilon_r$ and between circles C2 and C3 it is ε_o in pipe type cable, but in a three-phase cable, both of them are $\varepsilon_o\varepsilon_r$.

$$Z_{insulation}=\frac{j\omega\mu_0\mu_r\ln(r/q)}{2\pi}+\frac{j\omega\mu_0\ln(R_o.q/r)}{2\pi} \quad \text{(pipe type cable)}$$

$$=\frac{j\omega\mu_0\mu_r\ln R_o}{2\pi} \quad \text{(three-phase cable)} \quad (28)$$

$$P=\ln[(r/q)^*(R_o.q/r)^\sigma]/(2\pi\varepsilon_o\varepsilon_r) \quad \text{(pipe type cable)}$$

$$=\ln R_o/(2\pi\varepsilon_o\varepsilon_r) \quad \text{(three-phase cable)} \quad (29)$$

If the depth of penetration of the pipe and the thickness of the outside of the conductor is taken into account, the aforementioned transformation transforms Fig.7 into Fig.8. It can be observed that the inside of the pipe is transformed to the outside of the pipe and hence $Z_{pipe\text{-}in}$ is obtained from Eq. (4) by replacing r (the outside radius of pipe) to N (scale factor) and q (the inside radius of pipe) to N*r. r has been shown in Fig.(7). Thus $Z_{pipe\text{-}in}$ in Eq.(11) now becomes:

$$z_{pipe-in}=\frac{\rho m}{2\pi ND}[I_0(mN)*k_1(mNr)+k_o(mN)*I_1(mNr)] \quad (30)$$

where D is:

$D=I_1(mN)*k_1(mNr)-I_1(mNr)*k_1(mN)$ (31)

Although it can be seen from Fig. 8 that all circles are not completely concentric, since the depth of penetration in the pipe at power frequency is less than 1.5mm, and the thickness of the armour or sheath is much smaller than its outer radius, Fig. 8 is a valid approximation of four concentric circles, and is certainly more accurate than neglecting the effect of depth of penetration in pipe and thickness of armour (or sheath) altogether, as in the EMTP model.

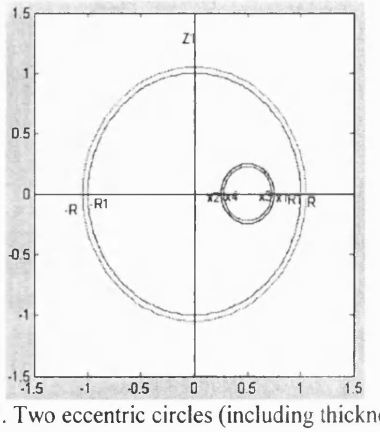

Fig. 7. Two eccentric circles (including thickness)

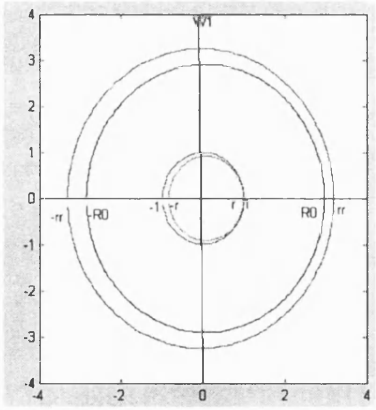

Fig. 8. CM transformation of Fig. (7)

In order to find the maximum matching between the four circles in Fig. 8, thereby maximising the accuracy of the CM model, a coefficient k is introduced in the transformation. Thus we have:

$$W_1 = \frac{Z - ka}{kaZ - 1} \qquad (32)$$

k causes the transformation of four circles to be more concentric. Thus if the thickness of conductor is b, k becomes:

$$k = M + \sqrt{M^2 - \frac{1}{a^2}} \quad (33) \text{ as: } \quad M = \frac{(x_1 - b)(x_2 + b) + 1}{a(x_1 + x_2)} \qquad (34)$$

Because of the various transformations that have been used to transform Fig.7 to Fig.8, there is scaling on Z_{pipein} [11], and hence a scale factor or metric coefficient N should be taken into account. N is the ratio of distances in the original Z_1-plane to the corresponding distances in the transformed W_1-plane. Hence it is defined as:

$$N = R_1 \left| \frac{(ka)^2 - 1}{(ka)^2 + 1} \right| \qquad (35)$$

Appendix 1 shows the various stages in the calculation of N.

B. Off-Diagonal Terms of Z and P Matrices

This section deals with modifying the mutual terms of Z and P (or Y according to Eq. (13)) matrices.

As mentioned in ref. [7], the axial voltage drop depends on the flux linkage and the axial electric field at the pipe wall as follows:

$$\frac{\partial V}{\partial x} = -I(R + j\omega L) = -\frac{d\lambda}{dt} + E_x(r_1) \qquad (36)$$

This paper will only deal with flux linkage and modification of P (Eq.(18)) and L (first and fourth terms of Eq.(12)) and hence Y and Z, respectively. In order to obtain the mutual impedance terms, a two-conductor system is analysed as shown in Fig.9. If conductor 1 is carrying a current that is returning in the pipe, the mutual flux linkage with conductor 2 is in the region between conductor 2 and the pipe. The flux linkage becomes:

$$\frac{d\lambda_{2(1)}}{dt} = j\omega \oint A_{2(1)} . dl_2 = j\omega [A_1(r_1, \theta) - A_1(r_{12}, \theta_{12})] \qquad (37)$$

Where A is the vector potential within the pipe and θ_{12} has been shown in Fig. (3).

With regard to Eq.(37), and in order to find the quantity of the mutual flux linkage between conductor 2 and the Armour associated with conductor 1, reference should be made to a three-phase cable which is shown in Fig. (10).

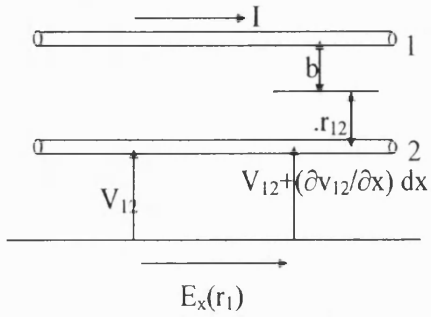

Fig.9. Two conductor system

As can be seen, fluxes generated by conductor 1 produce a set of circles in which the centre moves from α_1 to 0 on the axis x. Thus in order to find the amount of the flux generated by conductor 1 that flows between conductor 2 and the armour, we need to find a circle with centre α_4 and radius R_4.

Referring to Eqs.(28,36) and the CM method, the first and fourth terms of Eq.(12) become:

$$Ij\omega L = \frac{d\lambda}{dt} = Ij\omega \frac{\mu_o \mu_r}{2\pi} \ln R_o(x_{14}, x_{24}) \qquad (38)$$

Then, P_{12} is derived as follows:

$$P_{12} = \frac{1}{2\pi . \varepsilon_o . \varepsilon_r} \ln R_o(x_{14}, x_{24}) \qquad (39)$$

Appendix 2 shows how X_{14} and X_{24} are obtained. In conclusion, P_{12} and $R_o(x_{14},x_{24})$ are obtained from Eq.(39) and Eq.(23), however in the latter equation, instead of x_1 and x_2, x_{14} and x_{24} should be used, respectively

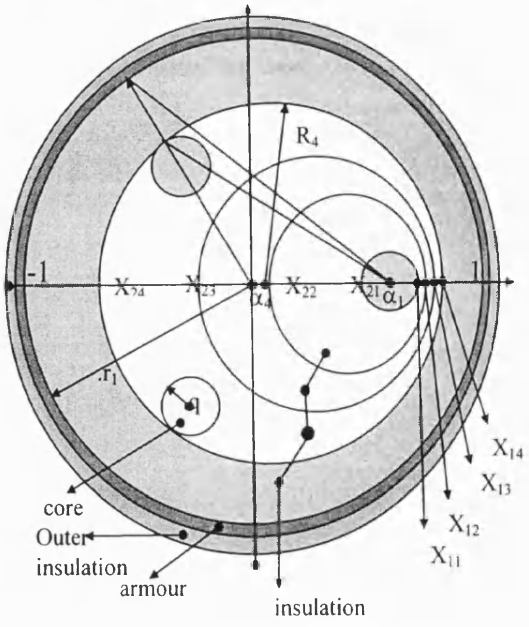

Fig. 10. Generation of flux linkage in a three-phase cable

4. Distribution System Configuration and Parameters

In order to do a comparison of the Z and Y parameters between the EMTP and CM methods, a practical three-phase underground distribution network shown in Fig. 11 has been considered.

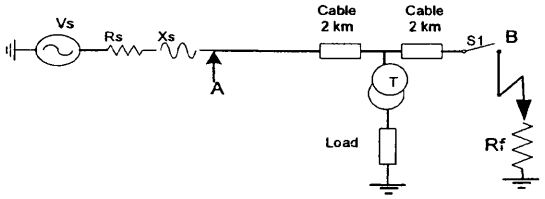

Fig. 11. Practical 3-phase underground distribution network

The specifications of the various elements in Fig (11) are as follows:

Source: V_L = 11kV, f=50Hz, X_s:R_s=10, X_s=2Ω, R_s=0.2Ω

Switch1: closing time =5 ms

Fault resistance R_f=0.1 ohms,

Step time for sampling =10 μs i.e. F=100kHz.

Cables: XLPE, Three-phase pipe type cable (core + grounded sheath)

Core: r_{in}=0, r_{out}=6.1mm, ρ=2.3*10^{-8} Ω.m, μ_r=100

Sheath: r_{in}=10mm, r_{out}=11mm, ρ=17*10^{-8} Ω.m, μ_r=100

Insulation between core and sheath: thickness=3.9mm, ε_r=3

Insulator between pipe and sheath: ε_r=8

Pipe: r_{in}=4cm, r_{out}=4.5cm, ρ=25*10^{-8} Ω.m, μ_r=100

Transformer: S=315 kVA

Winding 1 : V_L=11kV, R_p=1Ω ., X_p= 9 . Ω

Winding 2 : V_L=400V, R_s= 0.44 mΩ., X_s= 3.6 mΩ

Magnetizing Branch: R_M=1000 GΩ

Load= V_L=400 Vrms , 3phase λ, P_L=102.626 kW, Q_L=76.733 kVAR,

It should be noted that all voltage and current signals are simulated using the EMTP software.

V. Discussion of Results

This section comprises of two parts. In the first part, a comparison is made between the various cable parameters, principally to highlight the differences observed between the two types of cable models using, the EMTP and the CM models. The results shown in Table 1 typify the differences experienced in some of the important parameters of a 3-phase pipe type symmetrical cable. It should be mentioned that although the three conductors are symmetrically placed, they are nonetheless eccentric resulting in a complex and non-linear interaction amongst the various electrical variables.

First of all considering the symmetrical components (both series and shunt impedances), it is apparent that the resistive elements of the series impedances are relatively much higher in the case of the CM model compared to the EMTP model. This can be directly attributed to the fact that unlike the EMTP model, the depth of penetration in the pipe has been taken into account in the CM model; this is particularly important from a practical point of view, in view of this fact that the depth of penetration is less than the thickness of the pipe. However, there is only a small difference between the reactive elements of both the series and shunt impedances. Modal parameters are a very important indicator of the behaviour of a cable (or line) particularly under transient conditions. It is clearly evident from Table 1 that whilst the velocity of propagation of the three modes (one earth and two aerial) are little different in the two models, the attenuation is significantly higher in the case of the CM model compared to the EMTP model. The modal transformation employed is shown in ref. [9]. Although not shown here, similar differences in the cable characteristics have also been observed in the case of an asymmetrical cable.

Table 1- Characteristic of three-phase cable

	EMTP Model	CM Model
R_1 ohm/meter	6.8e-4	10.1803e-4
R_0 ohm/meter	6.78e-4	10.1584e-4
XL_1 ohm/meter	1.2654e-3	1.16085e-3
XL_0 ohm/meter	1.2734e-3	1.1652e-3
XC_1 mho/meter	1.0607e-7	1.0607e-7
XC_0 mho/meter	1.0607e-7	1.0607e-7
Velocity Mode1	2.6175e+7	2.62e+7
Velocity Mode2	2.6243e+7	2.623e+7
Velocity Mode3	2.6243e+7	2.623e+7
Attenuation Mode1	2.60193e-2	3.9027e-2
Attenuation Mode2	2.61673e-2	3.9156e-2
Attenuation Mode3	2.61673e-2	3.9156e-2

In order to ascertain the effect of the aforementioned differences in the cable parameters an both voltage and current signals under faults, an extensive series of fault studies were carried out by integrating the two cable models into a typical 11 kV distribution system as shown in Fig 11. In all cases, the point of observation of the waveforms is 'A' and all faults considered are at point 'B' in Fig 11. The sampling rate is 100 kHz and for all faults involving earth, the fault resistance is 0.1 Ω.

First of all considering an a-phase-earth fault at voltage maximum, Figs 12-15 show a comparison in the voltage and current waveforms attained via the two models. Comparing the voltage waveforms (Figs 12 and 14) it is apparent that the initial distortion on the faulted a-phase is much the same for the two models. Importantly, the transients in the case of the CM model die down much faster than in the case in the EMTP model; this clearly shows the effect of higher attenuation associated with the CM model (as discussed previously) which manifests itself into the increased damping effect. Interestingly, some distortion is also observed on the two healthy phases b and c in the case of the CM model. When considering the current waveforms (Figs 13 and 15), the transients are significantly smaller than those on the voltage waveforms and importantly, there is little difference in distortion between the two models; this is somewhat expected by virtue of the fact that in a highly inductive circuit (cable or line) current signals are predominantly power frequency and swamp over any high frequency distortions. When

considering a b-c-phase fault, Figs 16-19 depict the differences observed in the waveforms for the two models considered. First of all looking at the voltage waveforms (Figs 16 and 18), it is apparent that although the initial distortion is nearly the same for the two models, the transients take significantly longer to die down in the case of the EMTP cable model. In the absence of the earth resistivity playing a part for this type of a fault, the differences in the attenuation constants between the two models (these are higher for the CM model), manifest themselves into the increased damping effect in the case of the CM model. Here again like the single phase to ground fault, there is also distortion on the healthy 'a' phase in the case of the latter. The current waveforms are little different for the two models as shown by Figs 17 and 19.

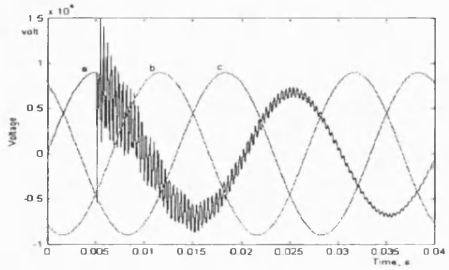

Fig. 12. Voltage signals, phase a-earth fault EMTP model

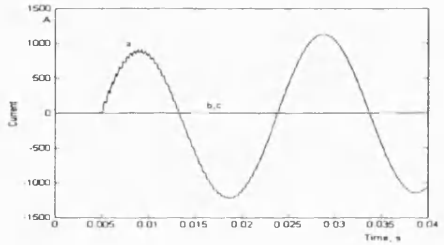

Fig. 13. Current signals, phase a-earth fault EMTP model

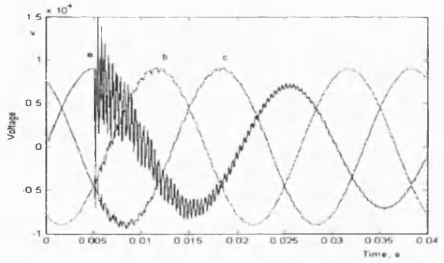

Fig. 14. Voltage signals, phase a-earth fault CM model

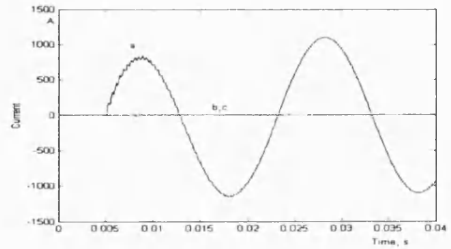

Fig. 15. Current signals, phase a-earth fault CM model

Although not shown herein, similar observations to the foregoing have been made in the case of a 3-phase fault and for faults on a system employing an asymmetrical cable i.e there is much faster attenuation on the fault phases in the case of the CM cable model in all fault cases.

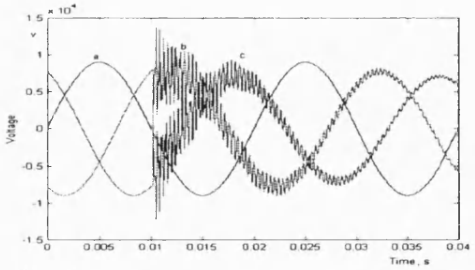

Fig. 16. 3-phase Voltage waveforms, b-c fault, EMTP model

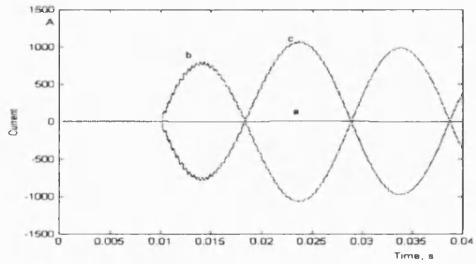

Fig. 17. 3-phase Current waveforms, b-c fault, EMTP model

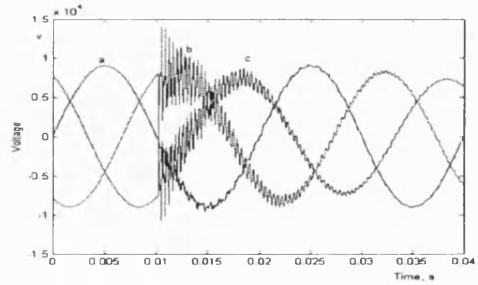

Fig. 18. 3-phase Voltage waveforms, b-c fault, CM model

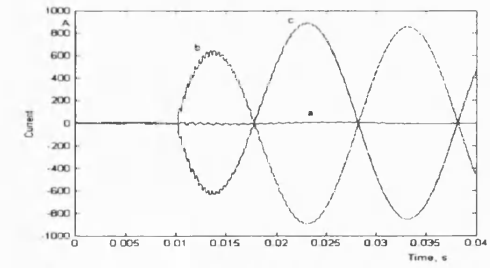

Fig. 19. 3-phase Current waveforms, b-c fault, CM model

6. Conclusion

This paper presents a new approach to the calculation of the crucially important parameters Z and Y (series impedance and shunt admittance) of a commonly employed 3-phase pipe type cable in a low voltage distribution system. It is clearly demonstrated that the conformal mapping (CM) approach adopted herein overcomes a number of approximations associated with the EMTP based cable model, which makes certain approximation in the configuration of the cable when the conductors are eccentric. The CM method overcomes this

assumption by mathematically transforming the eccentric circles into concentric circles. The results presented clearly demonstrate the differences observed in the cable parameters via the two cable models. The greatest impact is on the attenuation constant (this is a function of both Z and Y), that for the more accurate CM model being higher than that for the EMTP model. The net effect of the latter is that the high frequency transients superimposed upon the power frequency voltage and current waveforms are attenuated much faster in the case of the more accurate CM model compared to the EMTP model and this is the case for all types of faults. Equally important, some distortion is also observed on the healthy phases(s) in the case of the CM model and this is distinctly absent in the EMTP model largely due also to the approximations and their impact on the mutual coupling amongst conductors in the case of latter.

The foregoing is an important advancement in the accurate modelling of the fault transient phenomena in underground cables particularly in view of the fact that some of the developments in techniques of accurate fault detecting /location are heavily depended on extracting information from accurately modelled voltage and current signals under faults.

7. References:

[1] L.Marti, Simulation of transients in underground cables with frequency-dependent modal transformation matrices. IEEE transaction on power Delivery, July 1988,1099-1106.

[2] .T.Nguyen & H.Y.Chan, Evaluation of modal transformation matrices for overhead transmission lines and underground cables by optimization method. IEEE transaction on power Delivery, JAN.,2002,200-208.

[3] J.A.Tegopoulos & E.E.Kriezis, Eddy current distribution in cylindrical shells of infinite length due to axial current. Part I: shells of one boundary, IEEE, PAS, 1971,1278-1286.

[4] J.A.Tegopoulos & E.E.Kriezis, Eddy current distribution in cylindrical shells of infinite length due to axial current. Part II: shells of finite thickness, IEEE, PAP, 1971,1287-1294.

[5] X.B.Xu & G.Liu & P.Chow, A finite-element method solution of the zero-sequence impedance of underground pipe-type cable. IEEE transaction on power Delivery, JAN.,2002, 13-17.

[6] D.L.Paul, C.J.Railton & I.J.Craddock, Full-wave modelling of coaxial cables by FDTD technique. electronics letters 10_{th} Oct. 2002 vol.38 no.21 Sep./Oct. 2002, 1261-1262.

[7] G.W.Brown & R.G.Rocamora, Surge propagation in Three-phase cables. Part I –unsaturated pipe, IEEE ,PAS , Jun./Feb. 1976, 89-95.

[8] Emanuel, A. and Doepken Jr. H. C. Calculation of losses in steel enclosures of three-phase bus or cable. IEEE PAS-93, November 1974, 1758-1767.

[9] EMTP Theory book, section 5, 1-31.

[10] J Moshtagh & R K Aggarwal, A new approach to single-phase pipe type cable modelling using conformal mapping. UPEC 2004, 39-43.

[11] R. Schinziger & A. Ametani, Surge propagation characteristics of pipe enclosed under ground cables. IEEE, PAS, Sept. 1978,1680-1688.

APPENDIX I

Scale factor N is the ratio of distances in the original Z_1-plane to the corresponding distances in the transformed W_1-plane. Hence it is defined by:

$$N = \left|\frac{dZ_1}{dW_1}\right| = \left|\frac{dZ_1}{dZ}\cdot\frac{dZ}{dw_1}\right| \qquad \text{(A1-1)}$$

With regard to : $Z=Z_1/R_1$ therefore : $Z_1=R_1Z$ and

$$dZ_1 / dR_1 = Z \qquad \text{(A1-2)}$$

and $W_1 = \dfrac{Z-ka}{kaZ-1}$ therefore:

$$kaZW_1 - W_1 = Z - ka \Rightarrow Z = \frac{W_1 - ka}{kaW_1 - 1} \qquad \text{(A1-3)}$$

Since this is an analytic function, it can be differentiated directly with respect to W_1, as:

$$\frac{dZ}{dW_1} = \frac{(ka)^2 - 1}{(kaW_1 - 1)^2} \qquad \text{(A1-4)}$$

To find the absolute value of dZ/dW_1, W_1 is expressed as: $W_1=\cos\theta + j\sin\theta$; because the radius of the pipe in W_1-plane is unity, it leads to the following:

$$\left|\frac{dZ}{dW_1}\right| = \left|\frac{(ka)^2 - 1}{1+(ka)^2 - 2ka\cos\theta}\right| \qquad \text{(A1-5)}$$

Thus:

$$N = R_1\left|\frac{(ka)^2 - 1}{1+(ka)^2 - 2ka\cos\theta}\right| \qquad \text{(A1-6)}$$

N is seen to be a function of θ. With N appearing dominantly in the denominator of Eqs.(30) & (31), the average values of 1/N should appear where point by point evaluations of N are not undertaken [11]. In this case, the cosθ term vanishes so that the N takes the form:

$$N = R_1\left|\frac{(ka)^2 - 1}{(ka)^2 + 1}\right| \qquad \text{(A1-7)}$$

APPENDIX II

In order to find the circle(α_4,R_4), some calculations are done as follows:

$x_{14}=x_{11}+k.(1-x_{11})$, $x_{24}=x_{21}-k.(1+x_{21})$ (A2-1)

$\alpha_1=(x_{11}+x_{21})/2$, $\alpha_4=\alpha_1-k.\alpha_1$ (A2-2)

k is a percentage of the full distance between the origin to the centre as shown in Fig. 10 ; for example $x_{11}\to 1$, $x_{12}\to -1$ or $\alpha_1 \to 0$.

From Fig(9), it can be concluded that:

$$R_4 = x_{11}^2 + \alpha_4^2 - 2\alpha_4.x_{11}\cos 120 = x_{14} - \alpha_4 \qquad \text{(A2-3)}$$

From Eq.(A2-3) k is obtained as follows:

$$k^2 - Mk + N = 0 \Rightarrow k = \frac{M}{2} - \sqrt{\frac{M^2}{4} - N} \qquad \text{(A2-4)}$$

As : $M = (2d^2 + x_{11}(d-1) + d + 1)/d^2$ (A2-5)

And $N = (x_{11}^2 + d^2 + x_{11}(d-1) + d)/d^2$ (A2-6)

After calculating k, x_{14} and x_{24} can be derived from Eqs.(A2-1).

A NEW APPROACH TO UNGROUNDED FAULT LOCATION IN A THREE-PHASE UNDERGROUND DISTRIBUTION SYSTEM USING COMBINED NEURAL NETWORKS & WAVELET ANALYSIS

Jamal Moshtagh
University of Bath, UK
moshtagh79@yahoo.com

R. K. Aggarwal
University of Bath, UK
r.k.aggarwal@bath.ac.uk

Abstract

This paper presents the results of investigations into a new fault location technique based on a new modified cable model, in the EMTP software. The simulated data is then analysed using advanced signal processing technique based on wavelet analysis to extract useful information from signals and this is then applied to the artificial neural networks (ANNs) for locating ungrounded shunt faults in a practical underground distribution system. The paper concludes by comprehensively evaluation the performance of the technique developed in the case of ungrounded short circuit faults. The results indicate that the fault location technique has an acceptable accuracy under a whole variety of different systems and fault conditions.

Keywords: Fault location, ungrounded faults, underground distribution cable, wavelet, neural network

1. Introduction

In recent years, there have been many activities in using fault generated travelling wave methods for fault location and protection. The travelling wave current-based fault location scheme in which the distance to fault is determined by the time differences measured at the sending end between an incident wave and the corresponding wave reflected from the fault have been developed for permanent faults in underground low voltage distribution networks by S. Navaneethan et. al. in ref. [1]. However, due to the limitation of the bandwidth of the conventional CT (up to a few GHz) and VT (up to 50 kHz), the accuracy of fault location provided by such a scheme is not satisfactory for a power cable. Also there have been many activities in using power frequency (low frequency) for fault location and protection. Aggarwal et. al. in ref. [2] present a new technique in single-ended fault locationfor overhead distribution systems, which is based on the concept of superimposed components of voltages and currents rather than total quantities and also special filtering techniques have been utilised to accurately extract the fundamental phasors from the measured fault signals. However, in such techniques which are based on power frequency signals, some useful information associated with high frequencies in transient condition is missed.

This paper presents a new off-line method in cable ungrounded fault location based on signal processing using wavelet and ANNs. A practical 11 kV underground power distribution system (DS) with remote source is simulated using the EMTP software; the faulted current and voltage responses are then extracted from the sending end for different faults and fault conditions. The effect of transducers (CTs and VTs) and hardware errors such as anti-aliasing filters and quantisation are taken into account; the information processed throughout the fault locator algorithm is thus very close to real-life situation. Finally, the simulated data is processed in order to locate the fault point.

2. Data simulation

In order to obtain the voltage and the current signals under different faults and conditions, a practical three-phase underground distribution network shown in Fig. 1 has been considered.

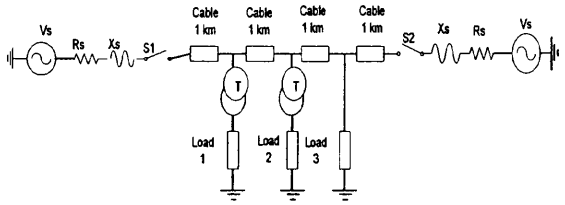

Fig. 1. Practical 3-phase underground distribution network

The specifications of the various elements in Fig (1) are as follows:

Source: V_L = 11kV, f=50Hz, X_s:R_s=10, X_s=2Ω, R_s=0.2Ω

Cables: XLPE, Three-phase pipe type cable (core + grounded sheath)

Transformer: S=1 MVA

Winding 1 : V_L=11kV, R_p=1 Ω, L_p=28.6mH

Winding 2 : V_L=380V, R_s=0.00044 Ω, L_s=0.0114mH

Load 1: Three-phase static Load: V_L=380 Vrms, f=50 Hz, P_L=92.62kW, Q_L=69.252kVAR

Load 2: The combination of a three=phase static and dynamic loads

Dynamic Load: V_L=380 Vrms, f=50 Hz, P=200 HP,

Static Load: P_L=92.62kW, Q_L=69.252kVAR, V_L=380 Vrms

Load 3: Three-phase static Load: V_L=11 kVrms, f=50 Hz, P_L=124kW, Q_L=952kVAR

In this paper, the simulation of the quantization process is based on 16-bit A/D converter with ±10V by using MATLAB program. In order to keep the voltage and current signals in range ±10V, these signals are divided by 2200 and 700 respectively, which are 1/10 of maximum amount of voltage and current signals under all conditions.

It is apparent that both the steady and transient states of the voltage and current signals can be affected by some important

parameters such as the type of fault, inception angle and distance to fault for ungrounded fault type. In order to obtain useful information from signals in the signal processing stage and mapping the extracted information to the location of fault in artificial intelligent (AI) stage, it is necessary to obtain voltage and current signals, different fault types and different conditions in the data simulation stage. In this respect, two types of fault including phase to phase short-circuit fault (3 cases ab-sc, ac-sc and bc-sc) and three-phase short-circuit fault(one case abc-sc) also three inception angles (including 90, 135 and 180 degrees) and 13 distances of fault from recording point (including 50m, 100m, 500m, 900m, 1100m, 1500m, 1900m, 2100m, 2500m, 2900m, 3100m, 3500m and 3900m) are simulated.

Figs(2 to 3) typifies the three-phase voltages and three-phase currents, respectively. Each figure contains two graphs associated with two different inception angles 90 and 180 degrees for the condition of 1100m distance in the case of bc-sc fault. Fig(2) depicts the voltage signals and as can be seen, initial distortions are much higher in the case of inception angle 180 degrees because of the maximum step change in phase voltage associated with this fault. Also the amplitude of voltage in both faulted phases b and c considerably fall after occurring the fault.

Fig(3) shows the current signals and the magnitude of current in faulted phases increase significantly. In the case of 90 degree fault (i.e. a fault near zero phase voltage), there is a large DC offset in the current signals and little distortion in the voltage signals.

Figs(4 & 5) show the three phase voltage and current waveforms for a 3-phase fault (abc-sc), fault locations= 1100m, 2100 and 3100m and without remote source connected. Fig(4) depicts voltage signals and as it can be seen that the initial distortions are much higher and the transients die down much slower in the case of the closer fault. Also, Fig(5) shows the current signals and it is clearly evident that the currents in three faulted phases increase after fault and as expected are much smaller in the case of location at 3100m.

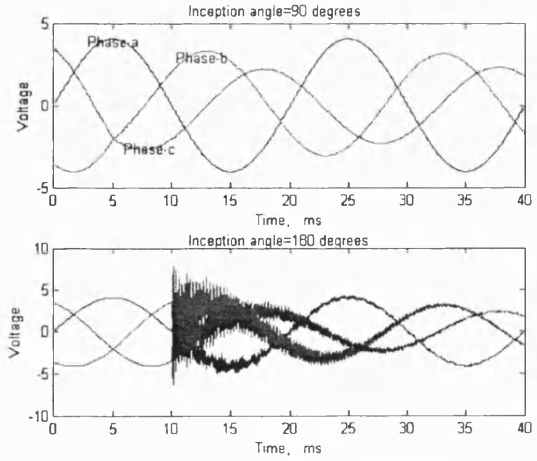

Fig. 2. Three phases of voltage signals, bc-sc fault, L=1100m

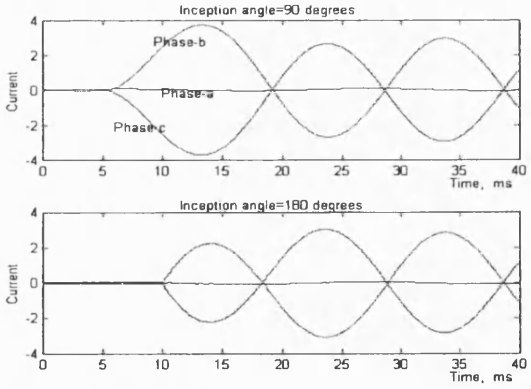

Fig. 3. Three phases of current signals, bc-sc fault, L=1100m

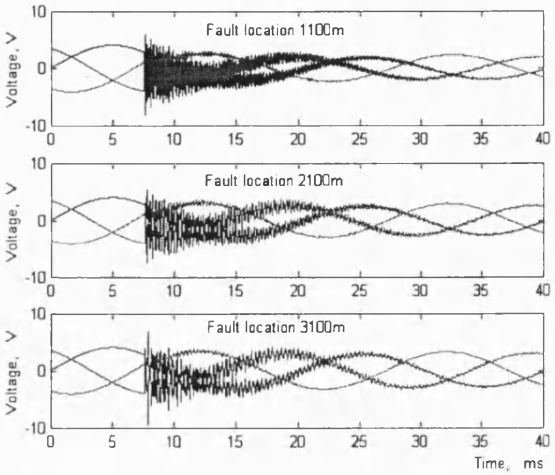

Fig. 4. Voltage signals, abc-sc, inception angle.=135degrees

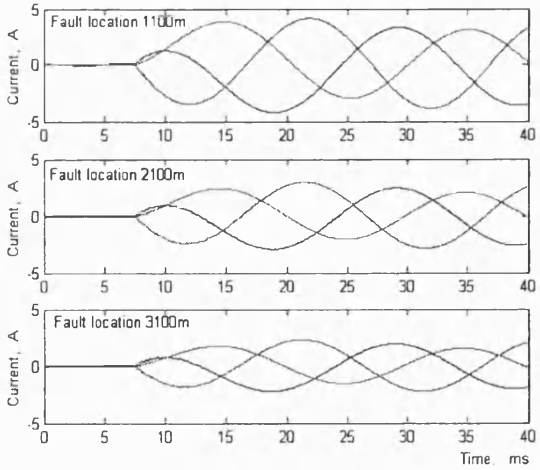

Fig. 5. Current signals, abc-sc, inception angle.=135degrees

3. Feature Extraction Using Wavelet

Transient signal analysis has been extensively used in fault location and condition monitoring of power system lines and cables. The time and frequency information can be calculated using techniques such as Fast Fourier Transform (FFT), Short-

Time Fourier Transform (STFT) and Wavelet Transform (WT). FFT and STFT techniques yield good information on the frequency content of the transient, but the time at which a particular disturbance in the signal occurred is lost.

In this paper, a new approach based on feature extraction using the WT is presented. WT possesses some unique features that make it very suitable for this particular application. It maps a given function from the time domain into time-scale domain. Unlike the basis function used in Fourier analysis, the wavelets are not only localized in frequency but also in time. This localization allows the detection of the time of occurrence of abrupt disturbances, such as fault transients.

3.1. Wavelet Transform

In the case of WT, the analysing function, which is called wavelets, will adjust their time-widths to their frequency in such a way that higher frequency wavelets will be very narrow and lower frequency ones will be broader. This property of multi-resolution is particularly useful for analysing fault transients which localize high frequency components superposed on power frequency signals (Manago & Abur [3]).

WT of sampled waveforms can be obtained by implementing the discrete WT which is given by:

$$DWT(f,m,n)=\frac{1}{\sqrt{a_0^m}}\sum_k f(k)h^*(\frac{n-ka_0^m}{a_0^m}) \qquad (1)$$

where, the parameters a_0^m and k a_0^m are the scaling and translation constant respectively, k and m being integer variables and h is the wavelet function which may not be real, as assumed in the above equation for simplicity. In a standard discrete WT (DWT), the coefficients are sampled from the continuous WT on a dyadic grid, a_0=2, yielding $a_0^0=1, a_0^{-1}=1/2$, etc. Actual implementation of the (DWT) involves successive pairs of high-pass and low-pass filters at each scaling stage of the WT. At each detail, there is a signal appearing at the filter output at the same sample rate as the input; thus, by using a sample rate F and scaling by two (a_0=2), Eq.(2) shows the association of each scale 2^m with a frequency band containing distinct components of signals.

$$\text{Frequency band of scale } 2^m = F/2^{m+2} \rightarrow F/2^{m+1} \qquad (2)$$

In this paper the original signals have been sampled at 100 kHz and passed through a DWT; thus according to Eq. (2) the frequency band for detailed and approximate signals are; 25kHz to 50kHz at detail-1, 12.5kHz t0 25kFz at detail-2, etc.

3.2. Choice of Mother Wavelet

Choosing of mother wavelets plays an important role in localizing and depends on a particular application. Researchers, in the study of underground power distribution transients are particularly interested in detecting and analysing short duration, fast decaying and oscillating type of high and low frequency voltage and current signals. One of the most popular mother wavelets suitable for a wide range of applications used is Daubichies's wavelet. In this respect, db4 wavelet with 5 level of decomposing of signals has been considered herein.

3.3. Feature Extraction in Fault Classification

The process comprises two stages including; 1- fault classification 2- fault location. At first, the original signals are passed through a DWT then 5-detailed and one approximate signals are extracted. With regard to statistics option in wavelet and data processing on approximate signals of the voltage and current phases, it was observed that some useful information can be extracted from standard deviation (SD) of approximate-5 signals in fault classification, since the amount of SD for every input data with dimension 6 (three voltage phases and three current phases) has an obvious relationship with the type of fault and faulted phases.

Figs (6 & 7) show such data which is used in the fault classification associated with the type of fault and faulted phases. Each figure comprises two graphs associated with voltage phases and current phases. Each graph shows three waveforms related to the three phases and each waveform depicts the SD of approximate-5 of signal for the all conditions dealt with in the previous section. Also, each waveform contains 3 separate the parts. Each part corresponds to the 13 locations and the same inception angle. As it can be seen, there is a significant difference between the faulted phases and healthy phase.

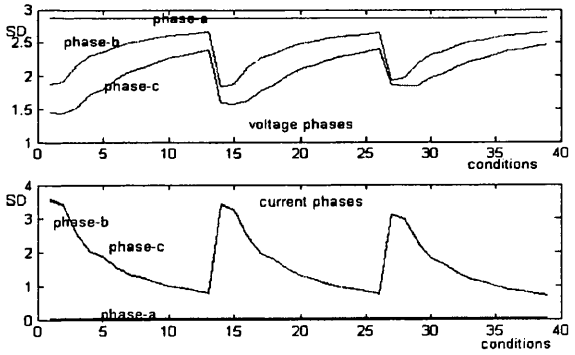

Fig. 6. SD of approximate-5 signal in the case of bc-sc fault

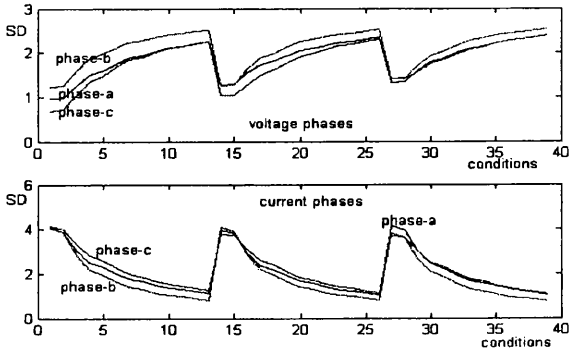

Fig. 7. SD of approximate-5 signal in the case of abc-sc fault

3.4. Feature Extraction in Fault Location

In order to locate an ungrounded fault, three important parameters are employed; 1- ratio of peak-peak voltage approximate to peak-peak current approximate at level five (a_ppv/a_ppi), 2- sine of phase-shift between current and voltage approximate at level 5 multiple by a_ppv/a_ppi, (sin(φi-φv).v/i), 3- ratio of SD of voltage approximate to SD of current approximate at level 5 (SDv/SDi). It should be mentioned that these three parameters are employed only for the faulted phases in the case of a phase to phase fault, but only phase-a is considered in the case of three-phase short circuit fault. In order to obtain more accurate results, the signals are normalized according to Eq. (3).

$$I_{normed} = (I - I_{min})/(I_{max} - I_{min}) \quad (3)$$

Figs. (8 & 9) show the results for 39 fault conditions, associated with three-phase and phase-b to phase-c faults. As can be seen, Fig. (8) comprises 3 graphs and Fig. (9) also contains 3 graphs correspond to the phase-b and here, because of similarity the graphs related to phase-c have not been considered. Each graph consists of three parts relating to three inception angles and each part corresponds to the 13 fault locations, all of which are ascending by virtue of an increase in the distance to fault location; as it can be seen, there is an apparent relationship between considered parameters and fault location for both types of fault.

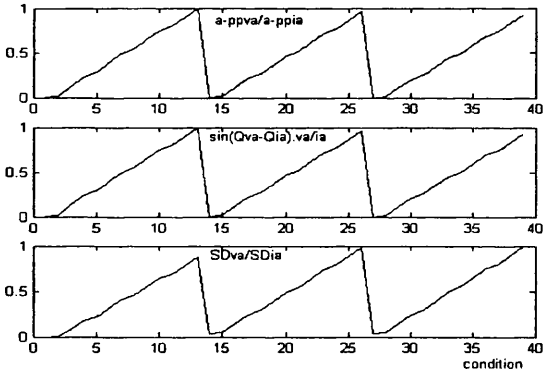

Fig. 8. Three parameters used in fault location, abc-sc fault

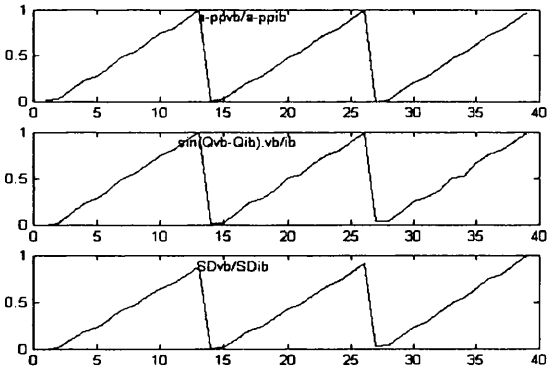

Fig. 9. Six parameters used in fault location, bc-sc fault g

4- Fault Location Based on ANNs

ANNs have emerged as a powerful pattern recognition technique and act on data by detecting some form of underlying organisation not explicitly given or even known by human experts and it possesses certain features which are not attainable by the conventional methods. In this respect, this paper describes a new method for accurate fault location based on the ANNs technique. The successful development of ANNs approaches depends on the successful learning of the correct relationship or mapping between the input and output patterns by the ANNs [4]. In order to achieve this, practical issues surrounding the design, training and testing of an ANN such as the best network size, generalization versus memorisation, feature extraction, convergence of training process and scaling of signals have been addressed and examined.

In order to find the best topology for accurate fault location, an extensive series of studies have revealed that it is not satisfactory to merely employ a single ANN and attempt to train it with a large amount of data. A much better approach is to separate the problem into two parts: firstly to employ and train an ANN to classify the faults; secondly, to use separately ANNs (one for each type of fault and faulted phases) to accurately locate the actual fault position. Fig. (10) shows the fault location scheme based on ANNs.

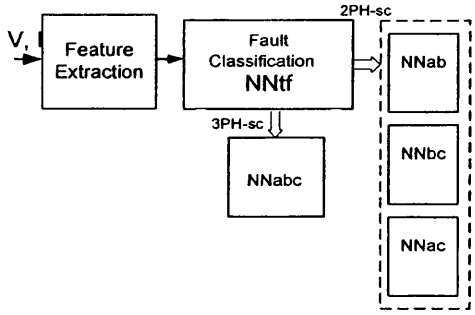

Fig. 10. Schematic diagram of fault location technique

There are many types of ANNs but the most commonly used are the multi-layer feed-forward networks, as, a three-layer network (input, one hidden and output layers). Because of this, a fully connected three-layer feed-forward ANNs with Levenberg-Marquardt (LM) learning algorithm has been used in the complete fault classification and fault location networks. Tabel-1 depicts the specifications of employed ANNs in proposed fault location technique.

Table 1. Specifications of employed ANNs

NN	N1	N2	N3	N4	f1(x)	f2(x)
NNtf	156	6	4	3	TanSig	Linear
NNab	39	6	4	1	TanSig	TanSig
NNac	39	6	4	1	TanSig	TanSig
NNbc	39	6	4	1	TanSig	TanSig
NNabc	39	3	7	1	TanSig	TanSig

Where N1=number of training data, N2=dimension of input layer, N3=number of neuron in hidden layer, N4=number of neuron in output layer, f1(x)=transfer function in hidden layer and f2(x)=transfer function in output layer.

The NNtf recognizes the type of fault and faulted phases for ungrounded faults. The output of the NNtf comprises 3 variables A, B and C; of these, a value close to unity for any of the variables corresponds to the appropriate a, b or c phases being faulted. The NNab-sc, NNac-sc, NNbc-sc and NNabc-sc architectures are shown in Table-1 and determine the location of fault in the case of phase to phase and three-phase short circuit fault.

5. Analysis of Test Results

In order to analyse the accuracy of the proposed method, seven groups of data test have been selected which are different and unseen from that used for training. Then, sensitivity of method to the system parameters such as inception angle, system elements (load taps, the length of cable, remote source) and to the external faults is evaluated. These seven groups of data test are as follows:

Group 1: This group contains such data which are obtained from normal system shown in fig (1) without remote source. 18 data are employed based on two types of fault (bc-sc & abc-sc) and 9 conditions for each fault. Table-2 depicts 9 locations, not used during training, with different inception angles.

Group 2: This group is similar to group 1 but with remote source.

Group 3: This group of data is associated with changing the location of the second load (shown in fig (1)) from 2000m to 1500m. 14 data test sets are used based on two faults and 7 conditions for each fault. Table-2 shows seven locations with different inception angles.

Group 4: In this group, data are obtained from DS shown in fig (1) based on changing the amount of three employed loads to double. This group also contains 14 data similar to group 3.

Group 5: This group contains such data which is based on doubling the amount of loads and replacing the loads 1 & 2 shown in fig (1). 14 data are obtained based on the same condition in group 3 & 4.

Group 6: This group comprises 14 data test based on the same condition shown in Table-2 and the same network shown in fig (1), but the length of cable in each section is changed from 1000m to 1500m.

Group 7: This group contains 2 data based on two faults as external fault (fault occurs before the measurement point).

Table 2. Group-1 of data test

Groups 1 & 2		Groups 3,4,5 &6	
Location	Θ (Deg.)	Location	Θ (Deg.)
80 m	117	80m	117
350 m	117	350m	117
750 m	117	1100m	90
1250 m	162	1750m	162
1750 m	162	2500m	135
2250 m	162	3250m	117
2750 m	162	3800m	117
3250 m	117		
3800 m	117		

5.1. Performance of Fault Classification

In order to quantitatively evaluate the performance of the fault classification technique, the NNtf was tested by seven aforementioned data test groups including over 92 system and fault conditions. It is evident from the results that except group-7 of data test (external fault) the number of error decision was zero in relation to the NNtf; therefore it can be concluded that this method is indead to classify the type of fault and recognizes the faulted phases.

5.2. Performance of Fault Location

The trained ANNs involved in the second stage of the fault location technique were tested by seven aforementioned groups of data test. The error for fault location is expressed as a percentage of the length of the cable, and is given as:

$$\%error=\frac{(actual\_location)-(desired\_location)}{(cable\_length)}\times 100 \qquad (4)$$

5.2.1. Effect of fault parameters. The inception angle significantly affects the fault transient voltage and current signals and it is vitally important to verify the effect of this parameter on the performance of the proposed technique. Table-3 show the accuracies attained for group-1&2 of test results. It is clearly evident from the results that the ANNs give very accurate evaluation of fault position and the maximum and mean of error correspond to the bc-sc and the abc-sc faults are (0.275 & 0.07) and (0.85 & 0.367) percent respectively. This study clearly demonstrates that the algorithm is virtually immune to any errors caused by either the higher frequency transients, which are associated with faults near voltage maximum or DC offset caused by faults near voltage zero. This feature is important since in practice, faults can occur at any point on wave i.e. the fault inception angle cannot be defined in advance.

5.2.2. Effect of remote source. It is well known that a remote infeed can adversely affect the accuracy of conventional fault locators. In this respect, the algorithm was tested based on group-2 of data test. Table-3 depicts the results. In comparison to the previous case associated without remote source, it is evident that the presence of a remote source has only a slight effect on accuracy particularly in the case of phase to phase fault, as the maximum and the mean of error associated with two faults increased very slightly to (1.957 & 0.586) and (0.735 & 0.408) respectively. These small changes can be directly attributed to the fact that with a remote source, the current changes in the healthy phase in terms of magnitude and distortion.

5.2.3. Effect of load taps. It is apparent that load taps significantly affect the fault transient waveforms. Therefore, it is vitally important to verify the effect of the load taps on the performance of the proposed technique. In this respect three groups-3,4&5 are considered and Table-4&5 depict the results. It is clearly evident from the results that the accuracy achieved in fault location is very high; being less than 1%

error in all the test cases. Thus it can be concluded that the ANNs give accurate evaluation that is largely independent on the load taps. This is a significant advantage since being different load taps at different location of DS is inevitable.

5.2.4. Effect of cable length. The cable length can vary considerably in the DS, it is vitally important to ascertain as to what extent the fault location accuracy is affected as a result of a change in the cable length. Table-5 illustrates the performance of the ANN-based technique when subjected to the cable length 1500m instead of 1000m for each section of such system shown in fig.(1) (group-6 of the data test). The results clearly demonstrate that the accuracy achieved in fault location is very high; being less than 0.85% error in all the test cases and shows that the ANNs give accurate evaluation of fault position that is largely independent on the cable length. D is real distance and L is obtained location by technique.

Table 3. Performance of fault location based on group-1&2 of data test

D (m)	bc-sc, G1		abc-sc, G1		bc-sc, G2		abc-sc, G2	
	L (m)	%e	L (m)	%e	L (m)	%e	L (m)	%e
80	79.7	.01	72.4	.19	72.5	.19	72.7	.18
350	350	.00	350	.00	339	.27	349.9	.00
750	749	.02	759	.23	738	.31	759	.21
1250	1253	.07	1263	.32	1245	.12	1266	.40
1750	1751	.02	1764	.35	1754	.12	1768	.47
2250	2252	.05	2261	.27	2273	.58	2268	.45
2750	2753	.07	2766	.4	2805	1.4	2772	.57
3250	3246	.1	3284	.85	3328	1.9	3279	.73
3800	3811	.27	3827	.67	3814	.36	3825	.64
M. E%	0.07		0.367		0.586		0.408	

Table 4. Performance of fault location based on group-3&4 of data test

D (m)	bc-sc, G3		abc-sc, G3		bc-sc, G4		abc-sc, G4	
	L (m)	%e	L (m)	%e	L (m)	%e	L (m)	%e
80	79.8	.00	72.4	.19	75.6	.08	72.0	.2
350	350	0.0	350.1	.00	356.4	.16	350.3	.01
1100	1100	0.0	1103	.08	1098	.05	1097	.08
1750	1752	.05	1765	.37	1750	.0	1757	.18
2500	2499	.02	2505	.13	2502	.05	2496	.1
3250	3242	.2	3289	.98	3243	.17	3273	.57
3800	3808	.2	3825	.62	3772	.7	3815	.37
M. E%	0.068		0.337		0.174		0.19	

Table 5. Performance of fault location based on group-5&6 of data test

D (m)	bc-sc, G5		abc-sc, G5		bc-sc, G6		abc-sc, G6	
	L (m)	%e	L (m)	%e	L (m)	%e	L (m)	%e
80	75.6	.11	72.0	.2	80.2	.00	72.4	.19
350	346.3	.09	350.3	.01	350.5	.01	350.1	.00
1100	1099	.02	1100	.0	1100	.0	1103	.07
1750	1757	.17	1760	.25	1754	.1	1766	.4
2500	2507	.17	2492	.2	2503	.07	2501	.02
3250	3246	.1	3263	.32	3253	.07	3281	.77
3800	3770	.75	3809	.22	3823	.57	3834	.85
M. E%	0.204		0.172		0.12		0.331	

5.2.5. Effect of External Faults. In any fault location technique, although a high accuracy for internal faults is of primary concern, nonetheless, it should also be stable under external faults. For the fault location technique described herein, an external fault produces an estimation which is consistently very much and negative distance. It is evident from the results that when the ANNs give such abnormally high and negative values, then it can be safely assumed that the fault is external.

6. Conclusion

In this paper at first, a new method to analyse power distribution system transient signals based-EMTP is proposed by using WT technique. This method offers important advantages over other methods such as FFT and STFT due to good time and frequency localisation characteristics. Analysis results presented clearly show that particular wavelet components can be used as the features to locate the fault in underground DS. Then an accurate fault location technique based on ANN is developed, as an ANN is trained to classify the fault type and separate ANNs are designed to accurately locate the actual ungrounded fault position on a practical underground DS. In this respect, three-layer feed-forward ANNs and the LM algorithm is used to adopt the weights and biases to achieve the desired non-linear mapping from inputs to outputs. Through a series of tests and modifications, it is shown that the ANNs can very accurately classify the type of fault under different system and fault conditions. In order to illustrate the effectiveness of fault location based-ANNs technique, each ANN is tested with a separate set of unseen data and their performance on the accuracy of the results are presented. The results presented herein, clearly show that the proposed method gives a high accuracy in fault location under a whole variety of different system and fault conditions.

Thus it can be concluded that the proposed approach based on combined WT and ANN is robust to different case studies; this is a significant advantage and can be directly attributed to the fact that WT technique effectively extracts the very crucial time-frequency features from DS transient signals and ANN approach is able to give a very high accuracy in the fault classification and fault location.

References

[1] S Navaneethan, J Soraghan, W H Siew, F Mcpherson & P F Gale, "Automatic Fault Location for Underground Low Voltage Distribution Networks", IEEE Transactions on Power Delivery, Vol. 16, No. 2, pp. 346-351, April 2001.

[2] R.K.Aggarwal, Y.Aslan, A.T.Johns, "New concept in fault location for overhead distribution systems using superimposed components", IEE Journal, Vol. 146, pp. 209-216, May 1999

[3] F H Magnago, and A Abur, 1998 IEEE, "Fault location using wavelets", Vol.13, No.4, 1475-1480

[4] Stamatios V Kartalopoulos, "Understanding Neural Network and Fuzzy Logic: Basic Concepts and Applications", The Institute of Electrical and Electronics Engineers, Inc., New York, 1996.